



**Deliverable 16.4 and 16.6: MAGIC – T2 and T3.
Report on bio-chemical processes controlling the
evolution of the microstructure and mechanical
properties of cementitious materials.**

Work Package 16



This project has received funding from the European Union's Horizon 2020 research and innovation programme 2014-2018 under grant agreement N°847593.



Document information

| | |
|-----------------------------|---|
| Project Acronym | EURAD |
| Project Title | European Joint Programme on Radioactive Waste Management |
| Project Type | European Joint Programme (EJP) |
| EC grant agreement No. | 847593 |
| Project starting / end date | 1st June 2019 – 30 May 2024 |
| Work Package No. | 16 |
| Work Package Title | Chemo-Mechanical AGIng of Cementitious materials |
| Work Package Acronym | MAGIC |
| Deliverable No. | 16.4 and 16.6 |
| Deliverable Title | Report on bio-chemical processes controlling the evolution of the microstructure and mechanical properties of cementitious materials |
| Lead Beneficiary | Andra |
| Contractual Delivery Date | Dec 2023 |
| Actual Delivery Date | May 2024 |
| Type | Report |
| Dissemination level | PU |
| Authors | Thierry Vidal (LMDC), Thomas Rougelot (LaMcube/ULille), Kyra Jantschik (GRS), Marvin Middelhoff (GRS), Johannes Kulenkampff (HZDR), Lucie Hausmannová (SURAO), Radek Vasicek (CTU), Veronika Hlavackova (TUL), Trung Duc Le (TUL), Michele Griffa (Empa), Bin Ma (PSI), Sergey Churakov (PSI), Tri Phung (SCK CEN), Erika Neeft (COVRA), Guido Deissmann (FZJ), Kristel Mijndonckx (SCK CEN), Olivier Helson (Andra), Petr Večerník (ÚJV), Tomáš Černoušek (CVŘ), Jiří Němeček (CTU), Ananya Singh (UNIMAN), Dirk Engelberg (UNIMAN), Elizabeth Evan (UNIMAN), Christopher Boothman (UNIMAN), Katherine Morris (UNIMAN), Sam Shaw (UNIMAN), Jonathan R. Lloyd (UNIMAN), Ting-Shyang Wei (HZRD), Andrea Cherkouk (HZDR), Charlotte Dewitte (IRSN), Mejdí Neji (IRSN). |

Disclaimer

All information in this document is provided "as is" and no guarantee or warranty is given that the information is fit for any particular purpose. The user, therefore, uses the information at its sole risk and liability. For the avoidance of all doubts, the European Commission or the individual Colleges of EURAD (and their participating members) has no liability in respect of this document, which is merely representing the authors' view.

Acknowledgement

This document is a deliverable of the European Joint Programme on Radioactive Waste Management (EURAD). EURAD has received funding from the European Union's Horizon 2020 research and innovation programme under grant agreement No 847593.

| Status of deliverable | | |
|------------------------------|---------------------------|--------------|
| | By | Date |
| Delivered (Lead Beneficiary) | Olivier HELSON (Andra) | 15 Dec. 2024 |
| Reviewed (internal review) | MAGIC board members | 11 Mar. 2024 |
| Verified (WP Leader) | Alexandre Dautères (IRSN) | 05 Apr. 2024 |
| Reviewed (external review) | Crina Bucur (RATEN ICN) | 15 May 2024 |
| Reviewed (external review) | John L. Provis (SCI) | 17 May 2024 |
| Reviewed | Bernd Grambow (SUBATECH) | 25 May 2024 |
| Submitted to the EC | Andra (Coordinator) | 30 May 2024 |

Executive Summary

The task 2 of the Work package MAGIC of EURAD is dedicated to study the chemo-mechanical behaviour at the macro scale considering the cement/aggregate structural behaviour. This scale permits the consolidation of the processes characterized and analysed on the nano/micro scale (task 3), and their respective description by simulation of the behaviour on the full scale (task 4).

This report provides a summary of the results and protocol development for the Task 2 and Task 3 experimental studies. It consists of a set of ongoing (started before EURAD) and new experiments with a selection of mortar/concrete samples in contact with various solutions and atmospheres (CO₂), which are representative of different host rocks, with or without microbial activity. Results show the chemical/textural changes (mineralogical evolutions, chemical changes, porosity, transport properties) and their impact on the mechanical properties (Young modulus, compressive/tensile strengths, etc).

WP leader and EURAD coordinator decided to merge the D16-6 (Subtask 3-3) and the D16-4 (final deliverable of Task 2) to group all microbiology work. This would facilitate interpreting the microbiology experiments.

Table of content

| | |
|---|-----------|
| Executive Summary | 4 |
| Table of content | 5 |
| Glossary | 18 |
| General introduction | 21 |
| 1 Key bio-chemo-mechanical processes and specifications at macro scale | 23 |
| 1.1 Specifications for long-term chemical and mechanical evolution of case studies | 23 |
| 1.2 Chemical/textural changes | 24 |
| 1.3 Mechanical behaviour of concrete at the macroscale | 26 |
| 1.3.1 Mechanical evolution of concrete under carbonation | 26 |
| 1.3.2 Impact of corrosion | 27 |
| 1.3.3 Leaching and multi-ionic attack | 27 |
| 1.4 Consideration of microbial activity | 28 |
| 1.5 Conclusion for part 1 | 29 |
| 1.6 References for part 1 | 30 |
| 2 Experimental protocols and methods | 32 |
| 2.1 Overview of materials studied: composition, curing and sampling. | 32 |
| 2.1.1 LaMcube (Task 2.1) | 32 |
| 2.1.2 LMDC (Task 2.1 and 2.2) | 32 |
| 2.1.3 PSI/Empa (Task 2.2) | 33 |
| 2.1.4 GRS (task 2.2) | 35 |
| 2.1.5 COVRA (task 2.2 and 2.3) | 36 |
| 2.1.6 SCK CEN (task 2.2 and 2.3) | 36 |
| 2.1.7 SURAO, CTU, TUL, UJV, CVREZ (Task 2.2 and 2.3) | 37 |
| 2.1.8 UNIMAN (microbiology Task 3) | 38 |
| 2.1.9 HZDR (microbiology task 3) | 39 |
| 2.2 Overview of experimental program: new experiments and ongoing experiments | 39 |
| 2.2.1 LaMcube (Task 2.1) | 39 |
| 2.2.2 LMDC (Task 2.1 and 2.2) | 41 |
| 2.2.3 PSI/Empa (Task 2.2) | 45 |
| 2.2.4 GRS (Task 2.2) | 51 |
| 2.2.5 COVRA (Task 2.2 and 2.3) | 55 |

| | | |
|------------|---|------------|
| 2.2.6 | SCK CEN (Task 2.2 and 2.3) | 57 |
| 2.2.7 | SURAO, CTU, TUL, UJV, CVREZ (Task 2.2 and 2.3) | 59 |
| 2.2.8 | SCK-CEN, COVRA and FZJ (task 2.3) | 65 |
| 2.2.9 | UNIMAN (microbiology task 3) | 68 |
| 2.2.10 | HZDR (microbiology task 3) | 70 |
| 2.3 | Conclusion for part 2 | 72 |
| 2.4 | References for part 2 | 75 |
| 3 | Chemo-mechanical evolution of unsaturated concrete | 79 |
| 3.1 | Mechanical evolution of concrete under carbonation (LaMCube/LMDC/Andra) | 79 |
| 3.1.1 | Initial mechanical characterisation | 79 |
| 3.1.2 | Mechanical behaviour after carbonation without pre damage | 82 |
| 3.1.3 | Mechanical behaviour after carbonation with pre damage | 87 |
| 3.2 | Degradation of the steel concrete bond under atmospheric carbonatation (LaMCube/LMDC/Andra) | 90 |
| 3.2.1 | Top bar effect and impact of the mechanical damage | 90 |
| 3.2.2 | Effect of corrosion according to exposure conditions and the initial state of the concrete (top bar effect and/or level of crack opening) | 94 |
| 3.3 | Conclusion for part 3 | 97 |
| 3.4 | References for part 3 | 98 |
| 4 | Chemo-mechanical evolution of saturated concrete | 99 |
| 4.1 | Concrete ageing in contact with rock (Empa, PSI, SCK-CEN) | 99 |
| 4.1.1 | Non-Destructive Evaluation (NDE) measurements of specimens aged in contact with Opalinus Claystone (OPA) | 99 |
| 4.1.2 | Physical properties of aged concrete from HADES URF | 108 |
| 4.2 | Evolution under multi-ionic chemical attack (SURAO/CTU/UJV/CVREZ, TUL, COVRA) | 113 |
| 4.2.1 | New ageing experiments under conditions representing operational disposal phase (Bukov URL) | 113 |
| 4.2.2 | Artificial ageing conditions through chemical multi-ionic attack (saline water). | 125 |
| 4.3 | Degradation under water percolation (GRS, SCK CEN) | 132 |
| 4.3.1 | Batch/percolation experiments to mimic the Belgian disposal conditions. | 132 |
| 4.3.2 | Degradation of samples percolated with a “corrosive” solution (Konrad solution) | 133 |
| 4.4 | Conclusion for part 4 | 135 |
| 4.5 | References for part 4 | 136 |

| | | |
|----------|--|------------|
| 5 | Chemo-microbial impact on chemo mechanical evolution of concrete (SURAO/CTU/UJV/CVREZ, TUL, SCK-CEN, COVRA/FZJ, UNIMAN, HZDR) | 137 |
| 5.1 | <i>Artificial ageing conditions due to salt water and microbial attack on old samples</i> | 137 |
| 5.1.1 | Mechanical characterisation | 137 |
| 5.1.2 | Chemical characterisation | 139 |
| 5.1.3 | Microbial characterisation | 139 |
| 5.2 | <i>Artificial ageing to mimic the Belgian disposal conditions with microbial attack</i> | 148 |
| 5.2.1 | Batch experiments at lab scales | 148 |
| 5.3 | <i>Artificial ageing to mimic the Czech disposal conditions with microbial attack</i> | 148 |
| 5.3.1 | Microbiology at URF Bukov | 149 |
| 5.3.2 | AIR exposure as a reference | 150 |
| 5.3.3 | Underground water environment | 152 |
| 5.3.4 | Effect of direct contact with bentonite suspension | 155 |
| 5.3.5 | Coupled multi-ionic and microbial (natural) attacks (conclusion) | 156 |
| 5.4 | <i>Interaction between low-pH cementitious material and microbes in low-carbon source groundwater</i> | 162 |
| 5.4.1 | Geochemical analysis | 162 |
| 5.4.2 | 2D-3D imaging processing analysis | 165 |
| 5.5 | <i>Microbial influenced alteration of cement phases with natural waters</i> | 169 |
| 5.5.1 | Geochemical analysis | 169 |
| 5.5.2 | Microbial diversity analysis of water and cement samples | 171 |
| 5.5.3 | Microbial colonization on cement surface | 174 |
| 5.5.4 | Analysis of the cement surface | 174 |
| 5.6 | <i>Conclusion for part 5</i> | 175 |
| 5.7 | <i>References for part 5</i> | 178 |
| 6 | Conclusion | 180 |
| 6.1 | <i>Conclusion of task 2 experimental work</i> | 180 |
| | 182 | |
| 6.2 | <i>Identification of knowledge gaps and future development needs</i> | 183 |

List of table

| | | |
|------------|--|-----|
| Table 1-1 | Strength class of materials studied (update of the table from deliverable 16.3) | 23 |
| Table 2-1 | Concrete mix | 33 |
| Table 2-2 | Composition of in-situ concrete | 37 |
| Table 2-3 | Compositions of newly made concrete | 37 |
| Table 2-4 | Phase composition by XRD of the reference LPC_SURAO sample. | 38 |
| Table 2-5 | Groundwater composition based on the Oxford clay formation, East Lincolnshire | 38 |
| Table 2-6 | CEBAMA reference cement paste formulation (Vehmas et al., 2020) | 39 |
| Table 2-7 | The oxide composition of low pH model cement paste. | 39 |
| Table 2-8 | Synthesis of number of samples and geometries, and pull-out tests at the end of each phase. | 42 |
| Table 2-9 | Number of cored specimens on which longitudinal SIMORUS was performed, for each specimen ensemble. Each ensemble's average specimen distance from the OPA interface (<i>dOPA</i>) is also indicated. | 47 |
| Table 2-10 | Boundary conditions in THMC test set up | 53 |
| Table 2-11 | Recipe for additional buffer-like sample | 57 |
| Table 2-12 | Conditions for gamma-irradiation used for preparation of the negative control with a limit of total dose of 40-100 kGy according to Černá et al. (2023). | 61 |
| Table 2-13 | Physical-chemical parameters of source S25 groundwater prior and during experiments | 61 |
| Table 2-14 | Chemical composition of source S25 groundwater prior and during experiments (mg/l) | 61 |
| Table 2-15 | BCV bentonite – the semiquantitative XRD analysis of randomly oriented powder mounts (wt. %); bql – below quantification limit, nd – not detected. | 62 |
| Table 2-16 | Chemical composition of BCV bentonite suspension porewater obtained by centrifugation (mg/l) | 62 |
| Table 2-17 | Conditions in different systems in the microcosm experiment | 69 |
| Table 2-18 | Conditions and analyses of microcosm setups. | 70 |
| Table 3-1 | Elastic properties (<i>E</i> , <i>v</i>) and failure strength (<i>R_c</i>) for different carbonation states. | 85 |
| Table 3-2 | Elastic properties (<i>E</i> , <i>v</i>) and failure strength (<i>R_c</i>) for different carbonation states (with discarded samples). | 85 |
| Table 3-3 | Comparison of triaxial and uniaxial compression results according to carbonation. | 86 |
| Table 3-4 | Elastic properties (<i>E</i> , <i>v</i>) and failure strength (<i>R_c</i>) for sound samples with or without pre-damage (with discarded sample). | 90 |
| Table 4-1 | Results of Young's modulus (<i>E</i>) and hardness (<i>H</i>) of the samples exposed to air ventilation measured by nanoindentation at the surface and core locations. | 114 |
| Table 4-2 | Phase composition of the samples by XRD and their percentages after 6, 12 and 18 months. | 115 |
| Table 4-3 | Evolution of pH values of the concrete samples from air environment. | 116 |
| Table 4-4 | Results of Young's modulus (<i>E</i>) and hardness (<i>H</i>) of the samples exposed to underground water measured by nanoindentation at the surface and core locations. | 118 |
| Table 4-5 | Phase composition by XRD of the LPC samples exposed to water representing their weight percentages after 6, 12, 18 months | 120 |
| Table 4-6 | Evolution of pH values of the concrete samples from URL Bukov groundwater environment | 121 |

| | | |
|------------|---|-----|
| Table 4-7 | Results of Young's modulus (E) and hardness (H) of the samples exposed to bentonite suspension measured by nanoindentation at the surface and core locations. | 122 |
| Table 4-8 | Phase composition by XRD of the LPC samples exposed to bentonite suspension, representing their weight percentages after 6, 12 and 18 months. | 124 |
| Table 4-9 | Evolution of pH values of the concrete samples from BCV bentonite suspension environment. | 124 |
| Table 4-10 | Compressive strength measurements and weight of buffer-like materials (cement: CEM-III/B, coarse aggregate: 2-8 mm) after 52/3 years exposure to saline synthetic clay pore water. Measured on 11 April 2022 (cubical specimens with an edge of 150 mm and 100 mm) and casted on 13 July 2016. | 125 |
| Table 4-11 | Compressive strength measurements and weight of buffer-like materials (cement: CEM-III/B, coarse aggregate: 2-8 mm) after 51/3 years exposure to saline synthetic clay pore water. Measured on 8 January 2021, 11 April 2022 and 23 October 2023, casted on 13 July 2016 and sawn after some months of exposure to tap water. | 126 |
| Table 4-12 | Compressive strength measurements and weight of certified backfill materials (cement: CEM-III/B, only fine aggregate: 0-2 mm) after 51/3 years exposure to saline synthetic clay pore water. Measured on 13 April 2022, casted on September 2016 and sawn after some months of exposure to tap water. | 127 |
| Table 4-13 | Compressive strength measurements and weight of certified backfill-like materials (cement: CEM-III/B, only fine aggregate: 0-2 mm) after 5 and 51/2 years exposure to saline synthetic clay pore water. Measured on 11 and 13 April 2022 (cubical specimens with an edge of 150 mm and 100 mm) and casted on 6, 8 and 9 September 2016 and 14 June 2017. | 128 |
| Table 4-14 | Compressive strength measurements and weight of backfill-like materials (cement: CEM-III/B, only fine aggregate: 0-2 mm) after 52/3 years exposure to saline synthetic clay pore water. Measured on 13 April 2022 (cubical specimens) and casted in May 2016. | 129 |
| Table 4-15 | Compressive strength measurements and weight of backfill-like materials (cement: CEM-I, only fine aggregate: 0-2 mm) after 5 ^{2/3} years exposure to saline synthetic clay pore water. Measured on 13 April 2022 (cubical specimens) and on 17 May 2016. | 130 |
| Table 5-1 | Compressive strength measurements and weight of certified backfill materials (cement: CEM-III/B, only fine aggregated: 0-2 mm) after 5 years submersion in saline synthetic clay pore water. Measured on 28 September 2022 and casted on 14 June 2017. The edges of the samples is 5 cm. In brackets, the weight and compressive strength as measured on 23 October 2023. | 137 |
| Table 5-2 | Compressive strength measurements and weight of backfill materials (cement: CEM-I, only fine aggregated: 0-2 mm) after 61/3 years exposure to saline synthetic clay pore water. Measured on 28 September 2022 and casted on 17 May 2016. Edge of cubical samples is 5 cm. In brackets, the weight and compressive strength as measured on 23 October 2023. | 137 |
| Table 5-3 | Compressive strength measurements and weight of backfill materials (cement: CEM-III/B, only fine aggregated: 0-2 mm) after 61/3 years exposure to saline synthetic clay pore water. Measured on 28 September 2022 and casted in May 2016. Edge of cubical samples is 5 cm. In brackets, the weight and compressive strength as measured on 23 October 2023. | 138 |
| Table 5-4 | Compressive strength measurements and weight of buffer-like materials (cement: CEM-III/B, coarse aggregate: 2-8 mm) after 6 years exposure to saline synthetic clay pore water. Measured on 28 September 2022 and casted | |

| | | |
|------------|--|-----|
| | on 13 July 2016a and on 30 June 2015b or 1 July 2015b. Edge of samples is 5 cm. In brackets, the weight and compressive strength as measured on 23 October 2023. | 138 |
| Table 5-5 | Overview of the classification of the different colonies isolated from the water samples on R2A in aerobic conditions. Similar classifications are represented with matching colours for corresponding samples. | 142 |
| Table 5-6 | Relative quantity (RQ) of bacterial biomass inside (RQ_LPC) and on the surface (RQ_biofilm) of the SURAO LPC samples exposed to underground air at indicated time points after 6 (T1), 12 (T2) and 18 (T3) months in comparison to input samples (T0). | 151 |
| Table 5-7 | Relative quantity (RQ) of bacterial biomass inside (RQ_LPC) and on the surface (RQ_biofilm) of the SURAO LPC samples exposed to underground water at indicated time points after 6 (T1), 12 (T2) and 18 (T3) months in comparison to input samples (T0). | 154 |
| Table 5-8 | The geochemical data from natural groundwater of Cernon, France collected in 2022 and 2023 (*data under detection limits from one replicate). | 169 |
| Table 5-9 | Microbial diversity of natural groundwater of Cernon, France collected in 2022 and 2023. Only genera with relative abundance >1 % in each year are shown in the table. | 171 |
| Table 5-10 | Details of sample codes for microbial diversity analysis. | 172 |

List of figures

| | | |
|-------------|---|----|
| Figure 2-1 | Curing of cored cylindrical samples (on the left) and prismatic beams for 3-point bending test | 32 |
| Figure 2-2 | Fails in concrete fabrication: a) sample is porous, b) sample with agglomerations and c) sample with shrinkage holes. d) Low-pH S5 sample, which is useable for experiments. | 35 |
| Figure 2-3 | SEM measurement and EDX element maps of the cement matrix with aggregates of the reference LPC sample. | 37 |
| Figure 2-4 | Non-carbonated surface detected on mortar specimen after pre-drying at 20 °C / 65 % HR and 5 days of accelerated carbonation (diameter of the specimens is 4 mm) | 41 |
| Figure 2-5 | Geometry of prism and different operations to provide pull-tout tests specimens after three-point bending test | 43 |
| Figure 2-6 | Geometry of wall to create some defects at SCI by top bar effect, and sawing operation to provide prisms | 44 |
| Figure 2-7 | Configuration of the three-point bending test | 44 |
| Figure 2-8 | Tunnel segments of the underground laboratory (CMHM) in the left and tunnel segments blocks in the right (ageing ~10 years) | 45 |
| Figure 2-9 | Implementation of the longitudinal Single MOde Resonant Ultrasound Spectroscopy (SIMORUS) measurement inside a glove box, to measure longitudinal resonance frequencies of the cored specimens (in this example, one of the 2274-A ensemble) under the same temperature (20°C) and relative humidity (90%) conditions, at which the cores were continuously kept in the storage climatic chamber. The inset provides a zoom-in view of the specimen in contact with the pin transducer acting as the longitudinal vibration source. | 48 |
| Figure 2-10 | Implementation of SIMORUS for the preferential excitation of torsional vibration eigenmodes of cylindrical specimens. (a): an example of surface distribution of the X- and Y-displacement fields at a time point during the 1st | |

order torsional vibration of the 2274-B6 specimen, as computed with the Finite Element Analysis. The straight arrows provide a qualitative example of displacement vector direction on the surface. To be noted are the symmetries responsible for the torque imposed to the specimen at its end (black arrows). (b): example of implementation of the vibration source as a series of custom-built shear piezoelectric transducers, glued on the edge of one specimen's end, each forcing the specimen tangentially (i.e., in-plane) to the contact surface. The arrows indicate each transducer's direction of straining, while the driving voltage signal is applied along its thickness.

| | | |
|-------------|---|----|
| | | 50 |
| Figure 2-11 | Schematic depiction of the percolation cell | 52 |
| Figure 2-12 | Set-up of percolation tests | 52 |
| Figure 2-13 | Configuration of the triaxial cell with fluid percolation and heater | 53 |
| Figure 2-14 | Set up of the HMC-test. Five samples can be investigated in parallel. | 54 |
| Figure 2-15 | Experimental specific for microbial research. The plastic boxes (Araven, 1.5 litre) in which the cylinders and samples have been put are made from polypropylene. | 56 |
| Figure 2-16 | Test setups for batch (left) and percolation (right) experiment | 58 |
| Figure 2-17 | A schematic representation of the batch experiment set up. | 60 |
| Figure 2-18 | A) Preparation of the in-situ experiment at URF Bukov. B) Arrangement of the experimental setups for studying interactions of LPC samples under in-situ conditions (air, groundwater, bentonite suspension) | 60 |
| Figure 2-19 | Example of the punch test record and rigidity determination | 63 |
| Figure 2-20 | A) A scheme of the SURAO LPC sample processing workflow. B) Effect of UV treatment on intact SURAO LPC samples. C) Sample processing of samples exposed to bentonite suspension. D) Test of microbial calcium precipitation | 64 |
| Figure 3-1 | Preliminary uniaxial compression results on 3 saturated samples after 7.5 months of curing. | 79 |
| Figure 3-2 | Mass evolution of 4 samples from saturated state to pre-conditioning before carbonation then after 100%+ carbonated state. | 80 |
| Figure 3-3 | Sound and 100% + carbonated samples (left), sample at an intermediate state of carbonation (50 % carbonation state, right figure). | 80 |
| Figure 3-4 | Examples of samples after failure in uniaxial compression. | 81 |
| Figure 3-5 | Stress-strain curves in uniaxial compression for sound samples. | 81 |
| Figure 3-6 | Stress-strain curves in uniaxial compression for samples with 100 % + carbonation. | 82 |
| Figure 3-7 | Stress-strain curves in uniaxial compression for samples with 50 % carbonation. | 83 |
| Figure 3-8 | Stress-strain curves in uniaxial compression for samples #1, 51, 61 and 63 (different carbonation states). | 84 |
| Figure 3-9 | Stress-strain curves in triaxial compression ($P_c = 3$ MPa) according to carbonation | 86 |
| Figure 3-10 | Stress-strain curves in triaxial compression according to confining pressure (3 or 10 MPa) on samples with 100%+ carbonation. | 87 |
| Figure 3-11 | Comparison of relative variation of mass for different sound specimens with or without pre-damage. | 88 |
| Figure 3-12 | Axial stress-strain behaviour of samples with pre-damage under uniaxial compression. | 89 |
| Figure 3-13 | Comparison of axial stress-strain curves for different samples under different conditions in uniaxial compression. | 89 |
| Figure 3-14 | Evolutions of CMOD measurements vs bending moment. | 91 |
| Figure 3-15 | Residual crack width values for each prism, each degradation type of SCI, and each future storage conditions. | 92 |

| | | |
|-------------|---|-----|
| Figure 3-16 | Evolution of shear stress vs slip of steel rebar for each reference pull-out test samples without carbonation and for each degradation type of SCI. | 93 |
| Figure 3-17 | Evolution of shear stress vs slip of steel rebar and for each degradation type of SCI after phase A. | 95 |
| Figure 3-18 | Comparison of the mean value of maximum shear stress (with standard deviation) for each degradation type of SCI (w1, w2 and top bar effect group "TP"), for reference samples (in grey) and after phase A (in orange). | 96 |
| Figure 4-1 | Complex-valued, dynamic Young's modulus values (vertical axes) of the ESDRED (mix design Nr. 2274) concrete specimens, as a function of the specimen distance ($dOPA$, horizontal axis) from the interface with the Opalinus Claystone (OPA). Each marker refers either to a single specimen or to the average value over the whole specimen ensemble. The 2274-A specimens all had a $dOPA$ value of 0 mm. Thus, their markers are artificially displaced horizontally, to improve their visibility. The 2274-B specimens had on average a $dOPA$ value of 47.2 mm. (a): real part of the complex-valued Young's modulus (E_{dyn}). (b): longitudinal wave amplitude attenuation coefficient (αL), proportional to the imaginary part of the complex-valued Young's modulus and expressed in Neper per meter (Np/m). | 100 |
| Figure 4-2 | Same as in Figure 4-1 but for the LAC concrete specimens (mix design Nr. 2275). In both (a) and (b), the dashed and solid horizontal lines indicate the lower and upper bounds, respectively, of the corresponding values for the ESDRED specimens (see Figure 4-1). For the 2275-B specimens, the average distance from the Opalinus Claystone's (OPA) interface was 49.9 mm. In both (a) and (b), when the vertical lines are not visible, it means that the range is smaller than the marker size. | 101 |
| Figure 4-3 | Same as in Figure 4-1 but for the OPC concrete specimens (mix design Nr. 2276). For the 2276-B specimens, the average distance from the Opalinus Claystone's (OPA) interface was 49.2 mm. In both (a) and (b), the black, dashed and solid, horizontal lines indicate the lower and upper bounds, respectively, of the corresponding values for the ESDRED specimens (see Figure 4-1). The red, dashed and solid, horizontal lines indicate the lower and upper bounds, respectively, of the corresponding values for the LAC concrete specimens (see Figure 4-2). In both (a) and (b), when the vertical lines are not visible, it means that the range is smaller than the marker size. | 102 |
| Figure 4-4 | Same as in Figure 4-1 but for the OPC mortar specimens (mix design Nr. 2277). For the 2277-B specimens, the average distance from the Opalinus Claystone's (OPA) interface was 29.11 mm. For the 2277-C specimens, it was 49 mm. In (a), when the vertical lines are not visible, it means that the range is smaller than the marker size. | 103 |
| Figure 4-5 | Same as in Figure 4-1 but for the ESDRED mortar specimens (mix design Nr. 2278). For the 2278-B specimens, the average distance from the Opalinus Claystone's (OPA) interface was 29.2 mm. For the 2278-C specimens, it was 52.9 mm. Notice that repeated measurements on single specimens were not available at the time of this report. In (b), the dashed horizontal line indicates the lower bound of values for the OPC mortar (see Figure 4-4 (b)), while the solid one refers to the respective upper bound. | 104 |
| Figure 4-6 | (a): quasi-static, compressive Young's modulus values ($EQ - S$, vertical axis) of the three concrete specimen ensembles (2274, 2275 and 2276), as a function of the specimen surface distance ($dOPA$, horizontal axis) from the interface with the Opalinus Claystone (OPA). (b): correlation between E_{dyn} and $EQ - S$ values (markers), with some indicative theoretical models (lines) provided for reference. | 106 |

| | | |
|-------------|---|-----|
| Figure 4-7 | X-ray tomogram of one LAC concrete specimen (2276-A6), showcasing the presence of damage. The right inset shows a cross-section from the tomogram along the core's longitudinal direction. Notice that the tomogram covered 121 mm of the total core's length (161 mm). The region highlighted by the red rectangle is shown in the left inset as a zoom-in, to better highlight the presence of a mesoscopic scale crack (left arrow) running through half of the core's horizontal size. Such crack is interconnected with a disbanded Interfacial Transition Zone for one aggregate (right arrow). | 107 |
| Figure 4-8 | Autoradiography porosity map of the concrete-Boom Clay interface - Frequency histograms obtained from the rectangles plotted on the autoradiography. | 108 |
| Figure 4-9 | Localization of the mapped areas on the autoradiograph: The green, orange, and red outlines on the maps correspond to their positions on the autoradiography, and at the bottom, BSE images and quantitative chemical maps are presented. Atomic weight % is used for calibration, ensuring a consistent scale for the analyzed elements across all maps. | 109 |
| Figure 4-10 | BSE image and a quantitative mineral map of the concrete. The Si-Ca-AlFeMg ternary diagram provides a projection of the elements examined within the mapped area. | 110 |
| Figure 4-11 | Mineral maps of the concrete adjacent to Boom Clay, featuring Si-Ca-AlFeMg ternary plots that encompass all the pixels within the map. Various segmentation steps were employed to distinguish the hydrates, with labels such as Stev. (stevensite), Ill. (illite), MX 80 (smectite MX80), Chlor. (chlorite), and Montm. (montmorillonite) corresponding to different mineral phases. | 111 |
| Figure 4-12 | Increase in water sorptivity at the concrete interface. | 112 |
| Figure 4-13 | Overview of the complete concrete core (left); the concrete-clay interface (middle) and the clay on the concrete core (right) | 113 |
| Figure 4-14 | Total number of CFU/mL after 1 week of growth on R2A at 30°C in aerobic conditions from a swab taken from the concrete and from the remainder of the clay. | 113 |
| Figure 4-15 | Results of punch tests - Load at break and rigidity evolution in time; air environment; average values (left); example of min/ max range of k2; k4+ and load at break datasets (right) | 113 |
| Figure 4-16 | Scanning electron micrographs of the surface of samples exposed to air after 18 months (left) and showing penetration of the carbonation area observed only after 18 months (right). | 115 |
| Figure 4-17 | GIXRD analysis at an angle of 0.5° of the sample surface after 1.5 years. | 116 |
| Figure 4-18 | Evolution of pH values from casting to experimental time T0 of LPC SURAO material | 116 |
| Figure 4-19 | pH determination of LPC_SURAO by rainbow indicator (T3 – 18 months aged samples; broken discs after punch tests). | 117 |
| Figure 4-20 | Results of punch tests - Load at break and rigidity evolution in time; water environment; average values (left); example of min/ max range of k2; k4+ and load at break datasets (right) | 117 |
| Figure 4-21 | Scanning electron micrographs of the surface of samples exposed to water after 18 months. | 118 |
| Figure 4-22 | SEM measurement of LPC sample exposed to water environment indicating presence of organic matter and element sulphur after 12 months. | 119 |
| Figure 4-23 | Scanning electron micrograph showing penetration of the carbonation area in water environment after 18 months. | 120 |
| Figure 4-24 | GIXRD analysis at an angle of 0.5° of the sample surface in water after 1.5 years. | 120 |

| | | |
|-------------|--|-----|
| Figure 4-25 | pH determination of LPC_SURAO by rainbow indicator (T3 – 18 months aged samples; broken discs after punch tests). | 121 |
| Figure 4-26 | Results of punch tests - Load at break and rigidity evolution in time; bentonite suspension environment; average values (left); example of min/ max range of k2; k4+ and load at break datasets (right). | 122 |
| Figure 4-27 | Evolution of Young's modulus (left) and hardness (right) of main hydration product over the different exposure time, measured by nanoindentation at the surface location. | 123 |
| Figure 4-28 | SEM showing the LPC samples cross-sections exposed to the bentonite suspension after 12 (left) and EDS elemental mapping of Mg (right). | 123 |
| Figure 4-29 | GIXRD analysis at an angle of 0.5° of the sample surface in bentonite suspension after 1.5 years. | 124 |
| Figure 4-30 | pH determination of LPC_SURAO by rainbow indicator (T3 – 18 months aged samples; broken discs after punch tests). | 125 |
| Figure 4-31 | Re-assembled certified backfill-like concrete (left in box, 5_HS_79_50) and buffer-like concrete (right in box, 7_COV_59, and held by hand in right photo). Both casted and sawn samples. | 126 |
| Figure 4-32 | Chiselled cubical CEM III/B specimen with an edge of 10 cm without (left) and with sprayed phenolphthalein solution. | 131 |
| Figure 4-33 | Chiselled cubical CEM I specimens with an edge of 10 cm without (left) and with sprayed phenolphthalein solution. | 131 |
| Figure 4-34 | Mechanical properties of reference concrete. | 132 |
| Figure 4-35 | Water permeability of reference concrete. | 133 |
| Figure 4-36 | Primary results of the THMC-testing. The results refer to the thermal phase with load steps of 35°C and 70°C under nearly isotropic stress. | 133 |
| Figure 4-37 | Left: CT scan of low-pH S5 sample (voxel size = 20µm) Middle: Segmented pores (porosity = 0.04) Right: Thickness map (pore size distribution) | 134 |
| Figure 5-1 | Irradiated sample sticking to the irradiated sample holder (left), irregular surface of the sample (right). | 139 |
| Figure 5-2 | Bar plots representing a) total cell concentration determined with flow cytometry; b) microbial activity based on intracellular ATP. Values of flow cytometry measurements represent average and standard deviation of two technical replicates. | 139 |
| Figure 5-3 | Bar plot showing the number of CFU/mL counted on R2A agar plates. Samples P_S50_26/27 and P_S50_29/30 are also shown in the small graph represented with a different scale. | 140 |
| Figure 5-4 | Example of different colonies from the water samples grown on R2A agar plates in aerobic conditions. | 141 |
| Figure 5-5 | Bar plots showing the number of CFU/mL in water samples (blue) compared to the number of CFU originating from a swap taken from the concrete surface (red). | 141 |
| Figure 5-6 | Distance matrix based on pairwise multiple sequence alignments of 16S rRNA amplicon sequences from colonies isolated from the water (marked with *) and concrete cubes. Samples from which the same genus was identified in the water and on the concrete cubes are designated in dark and light orange, respectively. The scale represents the dissimilarities between the sequences. | 143 |
| Figure 5-7 | a) Total cell concentration determined with flow cytometry and b) intracellular ATP measured at the start of MAGIC (blue) and after 1.5 year (red). Samples without a value after 1.5 year were sterilized with γ-radiation. | 143 |
| Figure 5-8 | Bar plots showing the number of CFU/ml in water samples (blue) compared to the number of CFU originating from a swap taken from the concrete surface (red) at the start of the experiment (full bars) and after 1.5 year (blocked boxes). | 144 |

| | | |
|-------------|--|-----|
| Figure 5-9 | Bar plots representing a) total cell concentration determined with flow cytometry; b) microbial activity based on intracellular ATP of water originating from large boxes with certified CEM specimens; water from large boxes with blend CEM; tap water and sand to prepare the concrete cubes. Values represent average and standard deviation of three replicates. | 144 |
| Figure 5-10 | Bar plot showing the number of CFU/mL counted on R2A agar plates for water from large boxes with blend CEM; tap water and sand to prepare the concrete cubes. Values represent average and standard deviation of three replicates. | 145 |
| Figure 5-11 | Microbial community profiles based on 16S rRNA amplicon sequencing showing the relative abundance (> 0.1%) of the different phyla in the different samples. | 146 |
| Figure 5-12 | Microbial community profiles based on 16S rRNA amplicon sequencing showing then relative abundance (> 0.1%) of the 20 most varying genera in the samples. | 146 |
| Figure 5-13 | Rarefaction curves for the 16S rDNA gene amplicon sequencing data showing for each sample the number of OTUs in function of the number of reads. The dashed line represents the number of subsampled reads. | 147 |
| Figure 5-14 | PCoA analysis based on weighted unifrac distances that show the dissimilarities between the bacterial community present in the different samples. | 148 |
| Figure 5-15 | Intracellular ATP (left) and the number of CFU/mL on R2A in aerobic conditions after 1 week at 30°C (right) at the start and after 111 days of the experiments for the biotic (green) and abiotic (blue) sample. Results are the average and standard deviation of two technical replicates. | 148 |
| Figure 5-16 | Relative abundance (> 1%) of microbiota present in the source water S25 and water in experimental boxes after 3 months of exposition to the underground in-situ conditions. | 149 |
| Figure 5-17 | A) Relative abundance (>1%) of bacterial community on surface and interior of SURAO LPC samples exposed to underground air ventilation for 6, 12 and 18 months. B) Periodic changes of chosen microbes detected in and on the concrete exposed to the underground air ventilation. C) Surface SEM analysis of 1 (up) and 1,5-years-old (bottom) samples indicating Streptomyces genus and chains of fungal spores. | 150 |
| Figure 5-18 | A) Relative abundance (> 1%) of fungal community on surface and interior of SURAO LPC samples exposed to underground air ventilation for different time points. CT – extraction control, SW – swab. B) Cultivation of fungi and their classification using microscopic analysis | 151 |
| Figure 5-19 | A) 16S sequencing heatmap of S25 underground water in anaerobic conditions for different time points (T0-T3). For sampling T2 (1 year) the water was taken directly from the borehole (S25_T2) and tested before entering the experimental box (S25_aerobic_T2). B) Alpha diversity of S25 source water at different time points. | 152 |
| Figure 5-20 | A) Relative abundance (> 1%) of microbial community on surface and interior of SURAO LPC samples exposed to underground water S25 for 6, 12 and 18 months, respectively. B) Periodic changes of chosen microbes detected in and on the concrete exposed to the underground water. C) SEM analysis of the biofilm after 1.5 years of exposure. | 154 |
| Figure 5-21 | Relative abundance of present microbiota in biofilm of water box (1.5-years exposure), biofilm formed around the inlet tube and biofilm of the containers exposed to underground air, respectively. | 154 |
| Figure 5-22 | A) Relative abundance (> 1%) of microbial community interior of the SURAO LPC samples (LPC) exposed to bentonite suspension for 6 (T1), 12 (T2) and 18 (T3) months, respectively and microbial analysis of bentonite suspension | |

| | | |
|-------------|---|-----|
| | at different time points. Each time three different concrete discs were used for separate extraction. BCV – Bentonite Cerny Vrch, CT – control extraction without input material; IRR – irradiated samples; UV – UV-treated LPC samples. B) Periodic changes of chosen microbes detected in bentonite (BCV) and in the concrete exposed to the bentonite suspension (LPC). | 155 |
| Figure 5-23 | Determination of bacterial viability in bentonite extracts prepared from (A) top and B) bottom (mostly in contact with LPC samples) of the bentonite suspension mass relative to the position in the experimental box (scale bar = 10 µm, red fluorescence = light clay fraction and dead cells, green fluorescence = living cells). | 156 |
| Figure 5-24 | pH evolution in all three environments. | 157 |
| Figure 5-25 | pH visualisation by rainbow indicator - cube cut edge (surface exposed to air for 3 years URL Bukov at 100% RH + 2 years at CTU lab with 30-50% RH). | 157 |
| Figure 5-26 | Specific characteristic surface changes for individual environments air, water and bentonite suspension after 6, 12 and 18 months. | 158 |
| Figure 5-27 | Scanning electron micrograph showing the penetration of magnesium into the cement matrix after 6, 12 and 18 months | 159 |
| Figure 5-28 | Time evolution of mechanical parameters in all three environments ((in %; strength left; rigidity k2 and k4+ right) | 160 |
| Figure 5-29 | Relative quantification of bacterial biofilm (RQ_BF) on air- and water-exposed samples and biomass inside SURAO LPC samples (RQ_LPC) in time (0 - 18 months) and different environments (A – air, W – water, B – bentonite suspension). B) detection of biofilm on air-exposed samples using SEM cross section analysis | 161 |
| Figure 5-30 | Growth kinetics of urease positive clone B62 at different pH. | 162 |
| Figure 5-31 | pH change in (a) no-nitrate system (GW, GL, GY) and (b) nitrate system (GWN, GYN, GLN). | 162 |
| Figure 5-32 | VFAs concentration and electron acceptor (sulphate, nitrate, nitrite) concentration for (ai & aii) Groundwater & Groundwater + Nitrate (GN), (bi & bii) Groundwater + Lactate (GL) & Groundwater + Lactate + Nitrate (GLN), (ci & cii) Groundwater + Yeast extract (GY) & Groundwater + Yeast extract + Nitrate (GYN) treatment of microcosm. For GL & GLN system, two axes represent lactate, which decomposes in acetate. The dotted line (....) represents no-nitrate, and the solid line (-----) represents the nitrate system. | 163 |
| Figure 5-33 | (a) Calcium ion concentration, (b) Sodium ion concentration, and (c) Magnesium ion concentration for the no-nitrate and nitrate system for 6 months. | 165 |
| Figure 5-34 | BSE image of crack healing material after three months in (a) Groundwater (G), (b) Groundwater + Nitrate (GN), (c) Groundwater + Lactate (GL), (d) Groundwater + Lactate + Nitrate (GLN), (e) Groundwater + Yeast extract (GY), and (f) Groundwater + Yeast extract + Nitrate (GYN). (g) & (h) Formation of calcite and aragonite minerals on the surface of cement tablets belongs to GYN system. (j) SEM-EDS for qualitative analysis of elements present on the surface cement tablet from GYN system. | 166 |
| Figure 5-35 | (a) Ortho slice of a volume section of GLN system. The different grey scales represent different phases present in the sample, Segmentation of the carbonate phase deposited on the surface of the GLN system in (b) 1 month and (c) 6 months. | 167 |
| Figure 5-36 | 1- and 6-month 3D XCT image and semi-log graph of pore diameter v/s count for (a) groundwater + Lactate (GL), (b) Groundwater + Lactate + Nitrate (GLN), (c) groundwater + Yeast extract (GY), and (d) Groundwater + Yeast extract + Nitrate (GYN) | 168 |

| | | |
|-------------|---|-----|
| Figure 5-37 | The evolution of sulphate concentration (A), total organic carbon (TOC) (B), and total inorganic carbon (TIC) (C) in water samples collected from condition 1 and 2 (Table 2-12) after different time frames analysed by High Performance Ionic Chromatography or Multi N/C 2100S. | 169 |
| Figure 5-38 | The evolution of elemental composition ((Ca (A), Mg (B), K (C), Si (D), Ba (F) and Na (F)) in waters collected from microcosms incubated with natural groundwater (blue) and additional 2 mM of lactate (orange) for up to 3 months and analysed by Inductively Coupled Plasma Mass Spectrometry. Fresh: fresh natural groundwater collected from source. | 170 |
| Figure 5-39 | Microbial diversity of fresh natural groundwater collected in 2022 and 2023 (Fresh), water samples from 20 and 41 days of incubation with natural groundwater (W2 & W3), and with groundwater and additional lactate (W6 & W7), and surface of cement samples incubated with natural groundwater (C2 & C3), and with groundwater and additional lactate (C6 & C7) for 86 days at phylum level (A), genus level of Gammaproteobacteria (B) and genus level of Alphaproteobacteria (Classification based on Silva database). The red boxes highlight the dominant or common microbial taxa in all communities. Details about the sample codes are listed in Table 5-10. | 173 |
| Figure 5-40 | Scanning electron microscopic images of surface structure from cement samples incubated with groundwater supplied with 2 mM of lactate (A) and natural groundwater (B) for 3 months. | 174 |
| Figure 5-41 | EDS mapping of calcium of low-pH cement samples incubated in a tank with constant flow of natural groundwater, in a microcosm with 300 ml of natural groundwater, and in a microcosm with 300 mL of groundwater supplied with 2 mM of Na-lactate. The rainbow colourmap denotes the high content (red) and low content (blue) of calcium. | 174 |
| Figure 5-42 | X-Ray diffractograms of surface of low-pH cement samples incubated in a tank with constant flow of natural groundwater, in a microcosm with 300 ml of natural groundwater, and in a microcosm with 300 ml of groundwater supplied with 2 mM of Na-lactate. | 175 |

Glossary

| | |
|------------------|--|
| ASV | Amplicon sequence variants |
| ATP | Adenosine triphosphate |
| BCV | Bentonite Cerny Vrch |
| BFS | Blast furnace slag |
| BSE | Backscattered electron |
| C ₂ S | Belite |
| C ₃ S | Alite |
| C-A-S-H | Calcium alumino silicate hydrates |
| CEBAMA | Cement-based materials, properties, evolution, barrier functions |
| CI | Cement-clay Interface |
| CMOD | Crack mouth opening displacement |
| COx | Callovo-Oxfordian |
| C-S-H | Calcium silicate hydrate |
| DGR | Deep geological repositories of RW |
| DNA | Deoxyribonucleic acid |
| DSC | Differential Scanning Calorimetry |
| EBS | Engineered barrier system |
| EDS | Energy dispersive X-ray spectroscopy |
| EDX | Energy dispersive X-ray spectroscopy |
| EPMA | Electron probe microanalysis |
| ESDRED | Engineering Studies and Demonstrations of Repository Designs |
| FA | Fly ash |
| FEA | Finite element eigenfrequency analysis |
| FIB | Ion Beam |
| FOV | Field of view |
| GDF | Geological disposal facilities |
| GIXRD | Grazing incidence X-ray diffractometry |
| GL | Groundwater Lactate |
| GLN | Groundwater Lactate Nitrate |
| GY | Groundwater Yeast extract |
| GYN | Groundwater Yeast extract Nitrate |
| HADES | High-Activity Disposal Experimental Site |
| HMDS | Hexamethyldisilazane |
| HPIC | High Performance Ionic Chromatography |

| | |
|-----------|---|
| IC | Ion Chromatography |
| ICP-AES | Inductively Coupled Plasma Atomic Emission Spectroscopy |
| ICP-MS | Inductively coupled plasma mass spectrometry |
| ICP-OES | Inductively Coupled Plasma Optical Emission Spectroscopy |
| IDPC | Interactive Data Platform on Cement |
| ITZs | Interfacial Transition Zones |
| LAC | Low-Alkali Cement |
| LPC | Low-pH concrete |
| MCP | Microbial calcium precipitation |
| MEA | Malt-Extracting Agar |
| M-S-H | Magnesium silicate hydrate |
| OPA | Opalinius |
| OPC | Ordinary Portland cement |
| PBS | Phosphate Buffer Saline |
| PCA | Potato Carrot Agar |
| PCoA | Principal Coordinates Analysis |
| PCR | Polymerase chain reaction |
| PERMANOVA | Permutational multivariate analysis of variance |
| PET | Positron Emission Tomography |
| PTZ | Piezoelectric ceramic lead-zirconate-titanate |
| RILEM | International Union of Laboratories and Experts in Construction Materials, Systems and Structures |
| rRNA | Ribosomal ribonucleic acid |
| RUS | Resonant Ultrasound Spectroscopy |
| SCI | Steel-concrete interface |
| SEGA | Soil agar with rose Bengal |
| SEM | Scanning Electron Microscope |
| SF | Silica fume |
| SIMORUS | Single MOde Resonant Ultrasound Spectroscopy |
| SOTA | State-of-the-art |
| SRB | Sulfate reducing bacteria |
| TC | Triaxial compression |
| TGA | Thermal Gravimetric Analysis |
| TIC | Total inorganic carbon |
| TN | Total nitrogen |
| TOC | Total organic carbon |
| TP | Top bar effect |

| | |
|-----|------------------------------------|
| URF | Underground Research Facility |
| URL | Underground Research Laboratories |
| WDS | Wavelength dispersive spectroscopy |
| XCT | X-ray computed tomography |
| XRD | X-ray diffraction |

General introduction

This report concerns the results of experiments carried out in Task 2 of the MAGIC WP. In addition, it includes the microbiology work performed in Task 3 to group all the results related to microbiology. The work performed focuses on the macro-scale chemical-mechanical behaviour of different mortars and concretes (OPC and low pH cements). The choice of materials for the Task 2 studies depends on the disposal concept. What makes the experimental programme so rich is that the geological conditions, the state of progress and design vary from one country to another.

The cementitious materials studied are representative of several components within the geological disposal sites or concepts, i.e. concrete tunnel linings, sealing plugs, backfill materials and buffer materials. During the operating period and early post closure, their chemical degradation depends on exposure to drying and atmospheric carbonation. Even if it takes considerably longer, because it depends on the resaturation period, cementitious materials are also chemically degraded under water, by leaching, carbonation, sulphatic, multi-ionic attacks, etc. The expected evolutions are related to the geological environment and the sealing principle, particularly the influence of the type of host rock (crystalline rock, Opalinus clay, Boom clay, Callovo-Oxfordian clay), the in-situ chemical composition of the water (granitic, clay, saline and bentonite waters).

The aim of Task 2 is to quantify the impact of these alteration processes independently, but also by assessing their influence if they are coupled to mechanical damage (corrosion or loading), application of pressure and combined with microorganisms attacks. The experimental program includes several chemo-hydro-mechanical characterisations that take advantage of experiments already underway or new experiments set up in the project involving the development of specific experimental devices. In the first case, the aim is to be able to collect samples that have aged for several years or decades in the conditions of underground laboratories (Bure URL, Mont Terri URL, Bukov URL, HADES URL). In the second case, the equipment adopted aims to mimic the exposure conditions encountered in a disposal configuration and, in most cases, to accelerate degradation. The characterisation tests aim to identify chemical (mineralogical changes, decalcification, magnesium ingress...) changes and the evolutions of the porous media (porosity, transfer properties...) in these conditions. The aim is to study the impact of these evolutions on mechanical properties (static and dynamic Young's modulus, compressive/tensile strength, punch test, ...). Pull-out test were performed to characterize the steel-concrete bond.

The aim of Chapter 1 is to review the main bio-chemical-mechanical processes and specifications. The main findings of the SOTA are exploited to provide a basis for the deliverable and to provide some context for the experimental studies in Task 2. Chapter 2 then describes the experimental protocols and the methods developed, but also the modifications made to the protocol compared with deliverable 16.3 which described experiments for assessing the evolution of concrete, their mechanical safety function and performance targets. This chapter includes a description of the preparation of the samples and/or their in-situ collection.

To facilitate reading, the results are then presented by sub-task:

- In task 2-1 (Chapter 3), the contribution of the various partners highlights the effect of atmospheric carbonation and corrosion on the degradation of the concrete studied. The results specifically focus on residual performance in different states of carbonation (accelerated conditions), including on previously damaged samples. It also includes degradation of the steel-concrete bond due to corrosion of the steel with/without top bar effect and including two levels of mechanical damage.

- In task 2-2 (Chapter 4), a first group of partners studied the evolution of existing samples buried or drilled as part of on-going experiments, with the specimens in contact with the host rock or existing metal structures. The second group carried out artificial ageing with water to assess the chemical-mechanical evolution under multi-ionic chemical attack, i.e. depending on the type of groundwater (granitic, clay, saline and bentonite waters) and whether or not it is circulating. A third group investigated the degradation of cementitious materials percolated with a solution that is 'corrosive' or representative of the water in situ (decalcification/leaching and carbonation) using underground salt solution or clay slurry.
- In sub-task 2-3 and 3-3 (Chapter 5), the additional impact of microorganisms is analysed. Changes in chemical, hydric and mechanical properties are monitored for sterilised samples and samples exposed to micro-organisms. The conditions studied are the same as in task 2.2, i.e. the effect of percolation or contact with water (multi-ionic chemical attack) or slurry representative of the deep geological disposal environment. One part also concerns the chemo-mechanical stability of concrete in consideration of the microbial activity under aerobic and anaerobic conditions.

These sub-tasks provide knowledge of the degradation factors and kinetics, i.e. the degree and speed of degradation processes according to the cementitious material and its environment, to be considered in the numerical simulations (model validation). These must be used to assess whether the mechanical functions of the Engineered Barrier System (EBS) in unsaturated/saturated conditions are guaranteed for the geological disposal of radioactive waste. This task 2 enables the processes characterised and analysed in task 3 to be upscaled (nano/micro scale) and enables full-scale behaviour to be described by simulation in task 4.

1 Key bio-chemo-mechanical processes and specifications at macro scale

1.1 Specifications for long-term chemical and mechanical evolution of case studies

Geological disposal facilities (GDF) and deep geological repositories of RW (DGR) are planned to ensure the isolation of radioactive waste through a multiple-barrier protection system consisting of the natural barrier system (NBS) and an engineered barrier system (EBS) (Tyupina, et al., 2023). In MAGIC, the case studies concern different types of host rock, mainly clay and granite that form the geological barrier. For EBS, cementitious materials play a key role which depends on the component (e.g. liners, buffers, backfills, plugs and seals, containers...).

Concrete is usually designed according to the prescriptive method in standard EN 206 (CEN, 2013), which specifies a water/binder ratio, a cement content and a strength class based on exposure categories. In France, since October 2022, the new FD P18-480 (documentation file), allows the durability of concrete to be demonstrated using a performance-based approach. As indicated in D16.3, the partners involved in Task 2 investigate the ageing of concretes with strength classes ranging from C35/45 to C80/95 but some buffer and backfill materials with much lower resistance are also being studied (Table 1-1).

Table 1-1 Strength class of materials studied (update of the table from deliverable 16.3)

| Kind of samples | Belgian samples | Czech samples | Dutch samples | | French samples | | German samples | Swiss samples | |
|-----------------|-----------------|---------------|----------------|-------------|----------------|----------------|------------------|---------------|-------------|
| Strength class | 80-95 MPa ♦ | 65 MPa ■ | 35-45 MPa ♣ | 10 MPa ♣ | 60-75 MPa • | 40-50 MPa • | - 80 MPa ♥ | 34 MPa ♥ | 30 MPa ♥ |

♦: similar to the concrete used in HADES.

♣: 15 cm, 10 cm and 5 cm cubes, 28 days of hardening.

■: low pH concrete, 3-years compressive strength values, 15 cm cubes.

•: Andra's methodological reference formula (C60/75) and the concrete studied in the WP MAGIC (C40/50), autogenous curing at 20 °C, 4 cylinders 112.8 mm in diameter and 220 mm high.

♥: for the concretes only, 90-day compressive strength values, measured on 150x150x150 mm³ cubes according to the EN 12390-3 standard, average value of 3 specimens. Curing under water at 20°C.

The cementitious materials studied in MAGIC have different initial properties due to their function in the deep geological disposal. There are three main categories of materials selected for the experiments:

- Concrete linings of tunnels ensure safety during the operating phase and must therefore guarantee mechanical stability for over a hundred years. Liners need to support the convergence of the geological environment in the case of clay rocks. This component is exposed to atmospheric carbonation and drying under the effect of ventilation. In the long term the failure of this component can have an impact on the extension of the damaged zone of the host rock (Armand, et al., 2014). The expected extension is not the same whether the void between containers and liners is empty or filled with material (e.g. sand). It is therefore important to study the influence of chemical degradation, induced by multi-ionic attacks caused by the environment through contact with water/rock. This can lead to degradation by leaching, carbonation, sulphate attack, etc. This type of structure is also subject to degradation by corrosion of the reinforcement, the propagation of which is not well known, depending on cracking and the initial quality of the steel/concrete interface (Castel, et al., 2006).

- Sealing plugs have a mechanical function, which consists of containing the swelling pressures of the clay core (bentonite) (Lebon, et al., 2013). In this case, the re-saturation of the swelling clay core can charge the groundwater with sulphates and chlorides and therefore alter the concrete components in contact with the bentonite pore water (Alonso et al., 2017). In the case of closure structures, the use of low pH concrete is a solution to prevent chemical alteration of clay materials with time (host rock and bentonite) (Pernicova, et al., 2023). The advantage is twofold in the case of plugs, as low pH concretes have the advantage of low heat of hydration and therefore avoid reaching excessively high temperatures during setting that could alter mechanical and transfer properties. Depending on the geometry of the closure structure, the plugs are cast directly in contact with the host rock, and the swelling of the clay core can apply an axial force that mechanically solicits the interface (Stavropoulou, et al., 2020). Chemical degradation of concrete can affect the mechanical behaviour of the interface between the concrete and the host rock by altering the first few centimetres of the component.
- Backfill and buffer-like materials are also studied in MAGIC. Backfill fills voids and helps dissipate heat providing a material with a higher thermal conductivity than concrete, while buffer provides alkaline environment to limit the corrosion rate of the carbon steel overpack (Li, et al., 2023), under anaerobic conditions (Tyupina, et al., 2023). The buffer's protection against corrosion includes a period during which the waste emits heat in amounts that the host rock is heated by the wastes. The buffer also contributes to the radiological shielding facilitating handling during the operational phase (Bel, et al., 2006).

1.2 Chemical/textural changes

○ Introduction

The mechanical behaviour of cementitious materials is strongly influenced by the physical and chemical boundary conditions imposed by the host rock and its evolution (geotechnical conditions and physico-chemical environment (i.e. water saturation, temperature, etc.)), during the operating phase, the post-closure transient period (water saturation evolution) and the long term (back to a physical equilibrium with the host rock). This mechanical evolution is significantly influenced by coupled chemo-mechanical evolutions. To assess the evolution of the cementitious component's properties, studies must be extended over long periods of time, considering various operating conditions, with data acquisition focussed on the cementitious material properties. This allows, to perform modelling to describe the long-term evolutions of the structures.

Cementitious materials are planned to be used as disposal components (e.g. tunnel segments, buffer, plugs) in the underground engineering structure, as well as conditioning materials (waste packages and waste matrices). These multiple uses require further understanding of their long-term behaviour, considering the influence of the different relevant physical, chemical and bio-geochemical processes on their physical and chemical evolution. Furthermore, over a long period of time, groundwaters, with aggressive chemical ions are a key driving factor for cementitious materials degradation. The chemical (i.e. mineralogical) and microstructural changes generated by these aggressive environments might have consequences on the mechanical behaviour of the cementitious materials.

Full details are given in the D16.1 report, which provides a state of the art (SOTA) report in the context of the coupled chemo-mechanical cementitious materials evolution.

○ Key processes

Two key periods have to be taken into account:

- During the operating period and early post closure, cementitious materials evolve under unsaturated conditions. In this context, the main chemical process identified is atmospheric carbonation. This chemical reaction can lead to a chemical gradient from the surface to the steel reinforcements. An uncontrolled evolution can lead to an increase of the corrosion rate and may have an impact on the mechanical properties of the structure. The conception phase takes this evolution into account and technical decisions can prevent such an evolution (formulations, steel embedding).
- During the re-saturation period and for the time thereafter, back to hydraulic equilibrium, chemical evolution is strongly linked to the chemical composition of the host-rock porewaters. Whatever the geological medium, it will be seen as an acidic medium by cementitious materials. Thus, due to this huge chemical disequilibrium, the very first process is hydrolysis (water is the vector as well as the main reactive species). The consequences are closely linked to the chemical stability of calcium-bearing phases (i.e. cement hydrates). Porewaters ionic content can promote chemical reactions especially with sulphate anions or magnesium cations. Associated to neutralization, such reactive species can change the mineralogical content of the cementitious materials and lead to significant physical evolutions. Carbonation, by precipitating calcium carbonates, starting under unsaturated conditions, can continue under saturated conditions enhancing the neutralization of the hydrated cement.

Chloride anions of host-rock porewaters can influence steel corrosion, especially in oxic conditions and participate to increase corrosion kinetics.

Alkali-silica reaction is not directly related to the interactions of concrete with clay or crystalline rock.

It is an intrinsic reactivity of concrete and is therefore not considered in the present context. Indeed, deleterious alkali-silica reactions can be prevented with a proper choice of cement and aggregates to manufacture concrete.

- **Key consequences**

Chemical evolutions can be assessed relative to processes with an impact on transfer properties and to processes with an impact on mechanical properties. Whatever the processes, the evolution with time and the consequences do not vary linearly. Chemical and mechanical evolutions exhibit different zones according to the chemical evolution and lead to the creation of distinct successive layers (from the surface to the core) with their own properties.

- Influence on evolution of transport properties.

The main consequence of the hydrolysis/neutralization chemical process is a significant change of the mineralogical content. If the medium does not allow a water flux, this neutralization reaction is very limited and does not change the calcium content of the material. The microstructure evolution (and then the transfer properties) is in accordance to the molar volume of the phases precipitated compared to the ones dissolved. In a leaching configuration with access of large quantities of water the consequence is a decalcification of the material with a loss of the cement hydrates and then an increase of the porosity and a significant increase of the transfer properties.

Carbonation (whatever unsaturated or saturated medium) leads to the precipitation of calcium carbonate as well as to a partial neutralisation of the cement. In the main affected volume, this process leads to a partial porosity closure, locally decreasing the transport properties with a neutralisation of the medium (decrease of the pH of the pore water down to a value below 10). In some specific cases, the atmospheric carbonation of the blended cement, due to carbonation shrinkage, can initiate and promote microcracks on the surface on the materials leading to an increase of the transport properties. Physical evolution then evolves non-linearly from the surface to the sound material.

□ Influence on mechanical evolution

If the former chemical evolutions may have an impact on the mechanical behaviour of the material due to a significant chemical evolution, some other processes have direct and huge impact on the mechanical properties. Sulphate attack is the main well known chemical degradation identified over the last few decades to have a major impact on the mechanical properties. The expansive properties of calcium sulpho-aluminates initiate and promote cracks, leading at the end to major mechanical damages. This so-called Delayed Ettringite Formation can be prevented with a careful selection of cement to manufacture concrete and considering the exposure environment of concrete.

Combined with sulphate ions, magnesium can weaken the cementitious material through dissolution of calcium-bearing hydrates and precipitation of sulphates (e.g. gypsum) and magnesium bearing phases (i.e. M-S-H or $Mg(OH)_2$). These coupled processes generate cracks and a decrease of the mechanical properties in the affected volume.

In relation to neutralisation (hydrolysis/carbonation) and chloride ingress, significant changes in the physico-chemical properties of the cementitious material at steel/concrete interfaces can change the corrosion rate and initiate mechanical constraints locally far exceeding the tensile strength of the concrete. Consequently, cracks initiate, and progress through the material from the reinforcements to the surface of the structure. The final impact could be the loss of the structure due to mechanical damage.

1.3 Mechanical behaviour of concrete at the macroscale

1.3.1 Mechanical evolution of concrete under carbonation

The carbonation process on cementitious materials has multiple impacts on the mechanical behaviour of concrete associated to mineralogical and microstructural changes as stated previously and in the state of the art for MAGIC program (Deliverable 16.1, §1.1.1 and 2.3.2). The reaction of carbon dioxide with portlandite and C-S-H (Bary and Sellier, 2004) leads to calcite production associated with pore filling by calcite and carbonation shrinkage, as well as modifications of mechanical characteristics of C-S-H which isare experiencing decalcification.

These different effects may lead to opposite evolutions in the mechanical behaviour of concrete under carbonation. The densification due to pore, or even initial pre-existent microcracks, filling tends to increase the strength of concrete and the Young's modulus (Merah and Krobbba, 2017) whereas C-S-H decalcification and subsequent shrinkage (Kangni-Foli et al., 2021) in a heterogeneous material (cementitious matrix, aggregates, air voids) could generate new micro-cracks and a decrease in mechanical properties (Cheng et al., 2016).

In addition, concrete materials used in deep geological repositories are frequently submitted to (partial) drying, at least during a period of their lifetime, which could lead to drying shrinkage (Bisschop and Van Mier, 2002) even before any carbonation or loading process. This shrinkage is linked to potential microcracking between constituents of concrete (mainly shrinking matrix around "rigid" aggregates) but also due to heterogeneous hydraulic gradients. For example, in tunnel linings, the intrados side would be submitted to a drying environment but due to the low transportfer properties of concrete, the progression of the desaturation front towards the core of the lining will be very slow. As a result, a shrinking concrete near the intrados around a non-shrinking core would lead to "structural" microcracking. In the same way, this structural effect could appear for differential carbonation shrinkage between the exposed side and the inner part of a concrete lining.

These material and structural shrinkages, due to drying and carbonation, could affect in a different way the mechanical behaviour and could also enhance the kinetics of carbonation towards the core of a structure

(or sample). Therefore, all these chemo-thermo-hydro-mechanical phenomena act in a complex manner with couplings and competitive effects at different scales which still need to be better accounted.

1.3.2 Impact of corrosion

Steel corrosion is one of the main degradation phenomena of reinforced concrete structures. The stability of a metal in contact with concrete interstitial solution depends on the pH of the solution and also on the electrical potential of the metal (Pourbaix, 1963). The concrete pore water exhibits high pH values thanks to its alkalinity, but the pH could decrease to a value below 9 during carbonation and dissolution of portlandite, provided a large quantity of water is available. In the presence of water and oxygen, reinforcement bars can be depassivated leading to steel corrosion. Concrete carbonation induces generalised corrosion which provokes a reduction of the reinforcement section and steel-concrete bond. Thus, the mechanical reinforced concrete behaviour is degraded (stiffness, ductility, and load bearing capacity). The formation of expansive corrosion products induces pressure on the concrete surrounding the reinforcement. When stress is higher than the tensile strength, cracking occurs. This cracking affects the mechanical behaviour of the structural elements and represents new penetration paths for aggressive agents. In the context of the French geological disposal program CIGEO, simulation of atmospheric carbonation of intermediate-level long-lived radioactive waste (ILW) concrete packages (Thouvenot et al., 2013) shows that the concrete alteration might be as much as about 2 to 3 cm over a period of 100 years, which is non-negligible considering the thickness of the concrete cover required to protect steel rebars.

The quality of the steel-concrete interface (SCI) is considered a major parameter controlling the degree of steel rebar corrosion. Previous researchers concluded that SCI defects are required to initiate corrosion by favouring oxygen and aggressive agents such as chlorides to reach the rebars (Page, 2009; Angst et al., 2017). Two main relevant origins of defects in the SCI are known. The first is imperfections during concrete placing and formation of gaps caused by plastic settlement and collection of bleeding water, a phenomenon known as the top bar effect (Soylev and François, 2005). The second one corresponds to mechanical damage which occurs during mechanical loading when cracking occurs due to high tensile stress (Castel and François 2011). This damage is located in the area of the SCI around crack tips.

The couplings between steel-concrete bond and the spread of steel reinforcement corrosion require to be studied under conditions representative of those of geological repository structures leading to either atmospheric carbonation or carbonation under water. The analysis must focus on the couplings between the degradation of the SCI, of mechanical origin or due to defects linked to the concrete material settlement, on the initiation and propagation of corrosion, and the behaviour of the resulting steel-concrete bond.

An experimental programme has been set up to study the degradation of the steel-concrete bond due to steel corrosion in conditions representative of reinforced structures of repository projects such as the CIGEO project in France. The objectives are to analyse the coupled effects of the degradation of the steel-concrete interface by mechanical means or by top bar effect, on corrosion initiation and propagation. The effects of corrosion on steel-concrete bonds are studied, through pull-out tests.

1.3.3 Leaching and multi-ionic attack

In the experiments performed by the Czech Team the main interaction process expected is a multi-ionic attack, where carbonation and leaching could occur Simultaneously. Leaching and multi-ionic attack are two important processes that can affect cementitious materials, particularly concrete. These processes can lead to the deterioration and degradation of such materials over time. Multi-ionic attack refers to the simultaneous or sequential action of various (aggressive) ions like chlorides, sulphates, carbonates and chemical species on cementitious materials. Multi-ionic attack is a common phenomenon in real environments, so the Czech

Team focused on studies of interaction of low pH concrete (LPC) with real groundwater, whose composition was recorded prior and during in-situ experiments.

One of the leaching processes in concretes is the leaching of portlandite. Portlandite ($\text{Ca}(\text{OH})_2$), is one of the primary hydration products formed during the cement hydration process, and it is highly soluble in water undersaturated in portlandite, where it is dissolved and leached out of the concrete matrix. In case of low-pH cementitious materials, the amounts of portlandite are usually minor. Leaching of C-S-H phases occurs when water infiltrates the concrete and comes into contact with the C-S-H gel. Water acts as a solvent, dissolving the calcium (Ca), silicon (Si), and oxygen (O) containing ions present within the C-S-H structure. These dissolved ions are carried away by the infiltrating water.

Sulphate attack occurs by reaction between cementitious phases and sulphate anions in the presence of calcium ions in an aqueous environment and a new mineral phase, ettringite, is formed. The transformation from a high-density phase to a low density but larger volume phase can cause the material to expand and crack. Cracks make continuous porosity more accessible and thus accelerate the transport of sulphate ions into the cement matrix and its degradation. The ingress of magnesium sulphate or magnesium chloride are specific forms of sulphate or chloride attack. In contact with magnesium rich groundwaters, calcium bearing phases could be dissolved and replaced by magnesium bearing phases without binding properties.

The effect of chlorides is particularly evident in the corrosion of steel reinforcements in concrete when the passivating film on their surface is broken. This is not a case of Low pH Cement (LPC) samples, there is no steel reinforcement present.

During carbonation of concrete, the pH of the matrix decreases because of the reaction between dissolved CO_2 and phases of the matrix containing calcium. Carbonation occurs on the surface and the zone of carbonation products penetrate the internal structure of the concrete. The distance to which carbonation products penetrate corresponds to the porosity of the cement mixture. Degradation of basic structural phases can thus lead to a loss of material strength, however, the formation of carbonates can, on the contrary, also increase the strength.

Negative consequences of leaching and multi-ionic attack could be loss of alkalinity, increased porosity, decreased durability, reduced strength, increased permeability, cracking, and mechanical damage.

1.4 Consideration of microbial activity

Microbes can exert a dual influence on cementitious materials. They release metabolic by-products that are either detrimental, leading to bio-deterioration, or beneficial, contributing to the healing of concrete cracks through calcium carbonate precipitation.

Microbial degradation of cementitious materials has been observed in various settings such as sewage pipes, marine structures and wastewater treatment systems (reviewed in Wei et al., 2013). Initially, the highly alkaline conditions established by the cement upon construction inhibit microbial activity. However, various processes alter the chemical environment of cementitious materials, causing localised reductions in pH, thus enabling microbial activity. Additionally, concrete's limited capacity to withstand tensile stress results in the formation of (micro)cracks through which microorganisms can infiltrate. Microbially induced concrete degradation occurs due to the secretion of metabolic intermediates or end products, as well as exoenzymes (De Graef et al., 2005). Typically, these metabolic by-products can react with the cement hydration products, leading to the formation of soluble calcium salts. The leaching of these salts from the cement increases porosity and reduces pH values at the surface layer. Consequently, degradation gradually extends into the inner concrete matrix, affecting the entire structure. The rate and extent of concrete biodegradation depend on physical and geochemical factors that govern microbial growth and activity.

These factors include carbon flow, the availability and abundance of energy sources such as compounds involved in sulphur, iron, and nitrogen oxidation, as well as microbial bioavailability (Turick and Berry, 2016).

Early studies reported that almost all bacteria have the capability to precipitate CaCO_3 as a by-product of their metabolic processes, which is beneficial for healing of concrete cracks (Siddique et al., 2011). Microbial carbonate precipitation can be induced through various metabolic pathways including ureolysis, denitrification, sulphate reduction, iron reduction and methane oxidation. Microbial-induced calcite precipitation results in reduced concrete permeability and limits the penetration of corrosive substances, ultimately enhancing concrete durability (Wang et al, 2016). However, carbonation, which lowers pH values, can increase the corrosion rate of reinforcing bars (Phung et al, 2017).

While extensive research has examined microbial interactions with cementitious materials, studies related to nuclear waste disposal are limited. One crucial consideration in the study of microbial effects is the use of appropriate abiotic controls.

1.5 Conclusion for part 1

Boundary conditions imposed by geological waste disposals vary according to the host rock and with time, in relation to the operating, closure or post closure period. Pathologies encountered are those identified by the civil engineering industry in various environments. Key parameters initiating the processes are not always perfectly controlled and well known. Moreover, in civil engineering, the time scale is up to one hundred years, the same time scale is only the operating period for the waste disposals, then too short for a full description. All evolutions must be assessed over a broader time scale.

These physical and chemical processes may initiate deleterious reactions. At the origin of these evolution there is most of the time, a chemical reaction. Under unsaturated conditions drying could initiate cracks, enhancing the ingress of chemically reactive species. The main chemical reaction is then the atmospheric carbonation. This reaction leads to a partial neutralization of the cementitious materials and could initiate (in the worst case) the steel depassivation. Steel reinforcement corrosion leads to cracks and the loss of mechanical properties of the structure. A bacterial activity could enhance such an evolution.

Under saturated conditions, the list of the chemically reactive species is larger and aqueous ionic species such as carbonate, sulphate, chloride, magnesium, ammonium, added to a potential microbial activity, can have a strong impact on the chemical degradation of cementitious materials and promote a significant decrease of the physical properties as well as an increase of steel corrosion rate. Regarding a very long-term evolution, the final state of evolution differs significantly from the sound one with major changes of the physical properties of the structures.

Within the context of the MAGIC project, the aim is to study key parameters and specific boundary conditions according to physical degradation of reinforced concrete materials. The materials studied cover the variability of those planned to build geological waste disposals.

1.6 References for part 1

- A. Castel, R. François, Modeling of steel and concrete strains between primary cracks for the prediction of cover-controlled cracking in RC-beams, *Engineering Structures*, Volume 33, Issue 12, 2011, Pages 3668-3675, ISSN 0141-0296, <https://doi.org/10.1016/j.engstruct.2011.08.001>.
- A. Castel, T. Vidal, K. Viriyametanont, R. Francois. (2006). Effect of reinforcing bar orientation and location on bond with self-consolidating concrete. *ACI STRUCTURAL JOURNAL*. 103. 559-567.
- A. Merah, B. Krobba, Effect of the carbonation and the type of cement (CEM I, CEM II) on the ductility and the compressive strength of concrete, *Construction and Building Materials*, Volume 148, 2017, Pages 874-886, ISSN 0950-0618, <https://doi.org/10.1016/j.conbuildmat.2017.05.098>.
- B. Bary, A. Sellier, Coupled moisture—carbon dioxide—calcium transfer model for carbonation of concrete, *Cement and Concrete Research*, Volume 34, Issue 10, 2004, Pages 1859-1872, ISSN 0008-8846, <https://doi.org/10.1016/j.cemconres.2004.01.025>.
- B. De Graef, V. Cnudde, J. Dick, N. De Belie, P. Jacobs and W. Verstraete, 2005. A sensitivity study for the visualization of bacterial weathering of concrete and stone with computerized X-ray microtomography. *Science of the total environment*, 341(1-3), pp.173-183
- Bisschop, J. and Van Mier, J. (2002). Drying shrinkage microcracking in cement-based materials. *Heron*, 47 (3), 2002.
- C. E. Turick, C. J. Berry. Review of concrete biodeterioration in relation to nuclear waste. *Journal of Environmental Radioactivity* 151, 12–21, 2016. <https://doi.org/10.1016/j.jenvrad.2015.09.005>
- C.L. Page, Initiation of chloride-induced corrosion of steel in concrete: role of the interfacial zone. *Materials and Corrosion*, 2009, 60: 586-592. <https://doi.org/10.1002/maco.200905278>
- CEN, European standard EN 206:2013 + A2:2021. Concrete - Specification, performance, production and conformity, European Committee for Standardization, 2013
- E. Kangni-Foli, S. Poyet, P. Le Bescop, T. Charpentier, F. Bernachy-Barbé, A. Dauzères, E. L'Hôpital, J.-B. d'Espinose de Lacaillerie, Carbonation of model cement pastes: The mineralogical origin of microstructural changes and shrinkage, *Cement and Concrete Research*, Volume 144, 2021, 106446, ISSN 0008-8846, <https://doi.org/10.1016/j.cemconres.2021.106446>.
- E. Stavropoulou, M. Briffaut, F. Dufour, G. Camps, Time-dependent behaviour of the Callovo-Oxfordian claystone-concrete interface, *Journal of Rock Mechanics and Geotechnical Engineering*, Volume 12, Issue 1, 2020, Pages 89-101, ISSN 1674-7755.
- E.A. Tyupina, P.P. Kozlov, V.V. Krupskaya. Application of Cement-Based Materials as a Component of an Engineered Barrier System at Geological Disposal Facilities for Radioactive Waste - A Review. *Energies* 2023, 16, 605. <https://doi.org/10.3390/en16020605>.
- EN 1992-1-1, Eurocode 2: Design of concrete structures - Part 1-1: General rules and rules for buildings (2004)
- G. Armand, F. Leveau, C. Nussbaum, et al. Geometry and Properties of the Excavation-Induced Fractures at the Meuse/Haute-Marne URL Drifts. *Rock Mech Rock Eng* 47, 21–41 (2014). <https://doi.org/10.1007/s00603-012-0339-6>.
- J. Wang, Y.C. Ersan, N. Boon, et al. Application of microorganisms in concrete: a promising sustainable strategy to improve concrete durability. *Appl Microbiol Biotechnol* 100, 2993–3007, 2016. <https://doi.org/10.1007/s00253-016-7370-6>.

- J.J. Bel, S.M. Wickham and R.M. Gens, 2006. Development of the Supercontainer Design for Deep Geological Disposal of High-Level Heat Emitting Radioactive Waste in Belgium. MRS Proceedings. 2006; 932:122.1. doi:10.1557/PROC-932-122.1
- M. Pourbaix, Atlas of Electrochemical Equilibria. Gauthier-Villars, 1963, Paris.
- M.C. Alonso, J.L.G. Calvo, J. Cuevas, M.J. Turrero, R. Fernández, E. Torres, A.I. Ruiz, Interaction processes at the concrete-bentonite interface after 13 years of FEBEX-Plug operation. Part I: Concrete alteration, Physics and Chemistry of the Earth, Parts A/B/C, Volume 99, 2017, Pages 38-48, ISSN 1474-7065.
- P. Lebon, J. M. Bosgiraud, R. Foin, and G. Armand The Full Scale Seal Experiment - A Seal Industrial Prototype for Cigéo – 13106, WM2013 Conference, February 24 – 28, 2013, Phoenix, Arizona, USA.
- P. Thouvenot, O. Bildstein, I. Munier, B. Cochapin, S. Poyet, X. Bourbon, E. Treille, Modeling of concrete carbonation in deep geological disposal of intermediate level waste. EPJ Web of Conferences, 2013, International Workshop NUCPERF 2012: Long-Term Performance of Cementitious Barriers and Reinforced Concrete in Nuclear Power Plant and Radioactive Waste Storage and Disposal (RILEM Event TC 226-CNM and EFC Event 351), 56, pp.05004.10.1051/epjconf/20135605004
- Pernicova, R.; Citek, D.; Dobias, D.; Kolisko, J.; Mandlik, T.; Hausmannova, L. Development of a Low-pH Concrete Intended for Deep Geological Repository for Radioactive Waste. Buildings 2023, 13, 182. <https://doi.org/10.3390/buildings13010182>.
- Q.T. Phung, N. Maes, and D. Jacques Current concerns on durability of concrete used in nuclear power plants and radioactive waste repositories, in CIGOS 2017: Proceedings of the 4th Congrès International de Géotechnique - Ouvrages -Structures. 2017, Springer.
- S. Wei, Z. Jiang, H. Liu, D. Zhou, M. Sanchez-Silva. Microbiologically induced deterioration of concrete--a review. Braz J Microbiol. 2014 Mar 10;44(4):1001-7. doi: 10.1590/S1517-83822014005000006. PMID: 24688488; PMCID: PMC3958164.
- Siddique, R. and N.K. Chahal. Effect of ureolytic bacteria on concrete properties. Construction and Building Materials - CONSTR BUILD MATER. 25. 3791-3801, 2011. 10.1016/j.conbuildmat.2011.04.010.
- T. A. Soylev, R. François, Quality of steel–concrete interface and corrosion of reinforcing steel, Cement and Concrete Research, Volume 33, Issue 9, 2003, Pages 1407-1415, ISSN 0008-8846, [https://doi.org/10.1016/S0008-8846\(03\)00087-5](https://doi.org/10.1016/S0008-8846(03)00087-5).
- U.M. Angst, M.R. Geiker, A. Michel, C. Gehlen, H. Wong, O.B. Isgor, B. Elsener, C. M. Hansson, R. François. K. Hornbostel, R. Polder, M. C. Alonso, M. Sanchez, M.J. Correia, M. Criado, A. Sagües, N. Buenfeld, Materials and Structures (2017) 50: 143, 1-24. DOI 10.1617/s11527-017-1010-1
- X. L. Li, B. Neerdael, D. Raymaekers, and X. Sillen, “The construction of the HADES Underground Research Laboratory and its role in the development of the Belgian concept for a deep geological repository”, Geological Society of London Special Publications, vol. 536, no. 1, 2023. doi:10.1144/SP536-2022-101.
- Y. Cheng, Y. Zhang, Y. Jiao, J. Yang, Quantitative analysis of concrete property under effects of crack, freeze-thaw and carbonation, Construction and Building Materials, Volume 129, 2016, Pages 106-115, ISSN 0950-0618, <https://doi.org/10.1016/j.conbuildmat.2016.10.113>.

2 Experimental protocols and methods

2.1 Overview of materials studied: composition, curing and sampling.

2.1.1 LaMcube (Task 2.1)

All samples used by LaMcube are based on the concrete formulation elaborated by LMDC (see section 2.1.2). To reduce the variability during the fabrication and allowing better comparisons between experimental results in LMDC and LaMcube, the concrete for French specimens is always mixed and cast by LMDC. A batch of concrete is devoted to LaMcube samples: prismatic beams 70x70x280 mm for 3-point bending tests and several bigger beams in which cylindrical samples Ø37x74 mm are cored (and their ends sawn to ensure better parallelism).



Figure 2-1 Curing of cored cylindrical samples (on the left) and prismatic beams for 3-point bending test

Beams are kept for 28 days in endogenic conditions then sent to LaMcube where they are stored under lime-saturated water (temperature $20\pm 2^{\circ}\text{C}$) for an extended period to ensure a sufficient hydration and saturated state (duration > 6 months) before any conditioning for tests. The coring of cylindrical samples has been performed between 40 and 60 days after casting and samples are also kept under the same conditions (Figure 2-1).

Each conditioning process (pre-damage, carbonation...) applied to samples after this curing period will be explained in §2.2.1.

2.1.2 LMDC (Task 2.1 and 2.2)

The concrete studied within the framework of subtask 2.1 and for a part of subtask 2.2 by the two laboratories, LMDC and LaMcube, had to meet several criteria:

- be representative of some mixes of structures of the repository project CIGEO;
- incorporate constituents identical to those mixes of the repository project CIGEO;
- be characterized by compressive strength of concretes used structures but not high performances concrete to favor the top bar effect and then to improve the understanding of the link between rebar corrosion onset and steel-concrete decohesion. In real structures, SCI decohesion can appear even in case of High Performance Concrete without top bar effect, induced by other reasons as defects during of concrete pouring in narrow formworks or/and with high reinforcement density.

Thus, a mean compressive strength of around 40 MPa was targeted, without superplasticizer to increase the potential settlement and bleeding leading to SCI defects.

Several concrete mixes have been designed and tested. The elected mix is presented in Table 2-1. It is a “degraded” version of HPC mix studied in different theses led at LMDC with Andra. Concrete is made up of limestone gravel and sand, and a cement CEM I 52.5 N. The effective water to cement ratio of the concrete, W_{eff}/C , is 0.579.

Table 2-1 Concrete mix

| Materials and mix parameters | kg/m ³ |
|------------------------------|-------------------|
| Limestone Sand 0/4 | 895.5 |
| Limestone Gravel 4/12 | 986.3 |
| CEM I 52.5 N | 350.0 |
| Total water | 214.1 |
| Effective water | 202.7 |
| W_{eff}/C | 0.579 |
| Total mass | 2446 |

Concrete samples

For the experimental program of LaMcube and LMDC, all samples were cast at the LMDC. Some samples were sent to the LaMcube at the end of the curing period. Considering the reinforced concrete samples intended to the study of steel-concrete bond with concrete carbonation, an autogenous curing at $20^{\circ}\text{C} \pm 1^{\circ}\text{C}$ was performed, instead of water curing to avoid any steel corrosion during the hydration. The duration of this curing was 28 days minimum to stabilize the hydration of cement before initiating the carbonation ageing phase.

Reinforced concrete specimens

Two different geometries have been chosen for reinforced concrete samples intended to the study of steel-concrete bond with concrete carbonation: 100×100×400 mm prism and 1000×100×400mm wall. All samples were stored in autogenous curing at $20^{\circ}\text{C} \pm 1^{\circ}\text{C}$ during 28 days minimum to stabilize the degree of cement hydration. It was impossible to apply a water curing for such large dimensions, and autogenous conditions also limit any steel corrosion initiation during cement hydration. The design of such geometries will be described further below.

2.1.3 PSI/Empa (Task 2.2)

Sample origin and curing conditions

The PSI/Empa team has worked with mortar and concrete specimens of different types stemming from the CI (Cement-clay Interface) experimental campaign at the Mont Terri Underground Research Laboratory (URL). As a brief reminder of what is described in detail in Section 9 of the EURAD Deliverable 16.3 Report (“Selected experiments for assessing the evolution of concrete, their mechanical safety function and performance targets”), the CI campaign is a long-term, ongoing experiment aiming at investigating the reactive transport processes occurring between the host rock type, the Opalinus Claystone (also abbreviated as OPA, in what follows), and distinct types of cementitious composites considered for realizing the concrete liner components of the Engineered Barrier System (EBS) of the Swiss deep underground disposal site for radioactive waste (Bossart et al, 2017, Mäder et al, 2017). Important to be remarked here is that the CI campaign was not originally designed for investigating the chemo-mechanical couplings of such interactions.

The mortar/concrete specimens investigated in MAGIC Subtask 2.2 were not obtained directly on-site from the boreholes into the OPA bedrock, filled with the distinct cementitious composites to realize interfaces, but rather from mock-ups of such interface systems, realized at the same time when the boreholes were filled up. Each mock-up consisted of a plastic barrel, containing at its center an OPA cylindrical core obtained from a borehole. The core-surrounding volume was filled with a cast cementitious composite of a single type for each distinct barrel. The details about the realization of such barrels can be found in Section 9.2 of the Deliverable 16.3 Report. Here, we recall of a few relevant features of such mock-up interface systems: (1) they were realized either in 2007 (3 mock-ups with concretes) or in 2012 (2 mock-ups with mortars); (2) the barrels were tightly closed (but not air-sealed) with plastic lids and stocked till 2018 in the same tunnel, where the CI boreholes are located, then moved to NAGRA's storage site in Mellingen (Switzerland); (3) in July 2021, they were moved to Empa, where they were stored in a climatic chamber at 70% relative humidity (RH) and 20°C; they were then opened and sliced through to create a surface for sampling (see the next Section for details). After the slicing, they were left in the same climatic chamber.

Details about the curing conditions as well as about the sampling by coring from the sliced barrels are provided in Section 9.2 of the Deliverable 16.3 Report. For the sake of the measurement result interpretation, we highlight here a few key details. We update, in the following, the number of cored specimens used for each measurement type.

First, the definition of the “material age” is based upon the date of casting and the date when the cores were drilled out. The slicing of and coring into each barrel occurred in July/August 2021, corresponding to an age of 14 and 9 years, for the 3 concrete types and the 2 mortars, respectively.

Second, the materials were considered as “saturated” in that, till the coring time, they remained inside the closed barrels, sealed from the external environment, although, as mentioned above, the sealing was not perfectly airtight. Nevertheless, desiccation due to evaporation in the outside atmosphere was largely avoided. However, it is important to remark that each cementitious composite, being in contact with the OPA, was subjected to an “internal drying” process. The latter was driven not only by gradients in RH across the OPA interface, due to different saturation degrees. It was also driven by the difference in pore size distribution (PSD). Indeed, the OPA is a repository rock with pore sizes mainly in the range of tens of nm (Keller et al, 2013). On the contrary, the investigated cementitious composites have pore sizes spanning a much wider range, from the nm length scale up to the mm one of air voids and porous patches. In addition, the water-to-cement ratio (w/c) of the cast cementitious composites (always larger than or equal to 0.47, see Section 9.2.2 of the D16.3 Report) may have very likely guaranteed a higher free water content on the cementitious side of the interface than on the OPA one (water content in the range 0.058 - 0.12, see Table A10.4 in (Pearson et al, 2003), “Silty-Shaly Facies” segment). Thus, capillary suction of water across the OPA interface, towards the OPA core, may have very likely occurred.

During the slicing of each barrel and the subsequent coring of specimens, water was used, further increasing the water saturation degree of the cementitious composites. Since the measurements on the cores occurred between 2021 and the time of this report, special measures were taken to minimize the water content loss at any measurement stage. Such measures are described in detail in Section 2.2.1 below in relation to each measurement. Beyond such measures, the specimens were continuously (and are still) stored in a climatic chamber at 90% RH and 20°C.

Composition of mortars/concretes

Tables 9.1, 9.4, 9.7, 9.10 and 9.13 Section 9.2 of the Deliverable 16.3 Report provide the mix designs of the 3 concretes and 2 mortars, respectively. A numerical ID is associated to each mix design. They are used to label the results reported in Section 4 of this Report. More details about the realization, curing and mix designs of each single barrel can be found in the same section of the Deliverable 16.3 Report.

From the measurement result interpretation viewpoint, the following details need to be remarked:

- Very different cement types were used to realize the 5 composite types (CEM I 42.5 N, CEM III/B 42.5 L and CEM I 42.5 R HS), making the comparison between the composites of the same type (concrete and mortar) more complicated; the cements used to cast the two mortars were identical to those of two concretes;
- The aggregates for the 3 concrete types were of the same type, stemming from the same source, although not necessarily from the same batch (information not retrieved from the Mont Terri URL's Technical Reports); they were rounded river sediment particles, mainly consisting of limestone and quartz;
- One of the concretes (ESDRED) was cast with aggregate sieve size range 0 – 8 mm, while the other two with 0 – 16 mm; this difference may be relevant for the viscoelastic properties interpretation, as a different aggregate sieve size range may lead to distinct degrees of aggregate spatial packing, thus of local aggregate vol.-%; the actual aggregate vol.-% in a specific specimen plays a significant role in the bulk viscoelastic moduli; the sieve size grading was the same for the two concretes with 0 – 16 mm range ;
- The sand for the 2 mortar types was of the same exact type;
- As evinced by the X-ray tomography measurements, the silica fume used for the ESDRED mortar (mix design Nr. 2278) was not sieved; as such, the material contained large amounts of silica fume clumps, potentially acting as very porous and soft artificial aggregates, thus potentially contributing to lowering the viscoelastic properties.

2.1.4 GRS (task 2.2)

The fabrication of the low-pH concrete S5 was carried out with a handheld electric mixer. The components were added in the following order:

1. Addition of sand (0-2 mm), gravel sand (2-8 mm) and micro silica – mixing 5 minutes
2. Addition of EFA-Fuller and CEM I 42.5 N – mixing 5 minutes
3. Addition of water and superplasticiser – mixing 15 minutes

Micro silica, EFA-Fuller and CEM I 42.5 N were added in small amounts of around 50 g while continuous mixing. Water and superplasticiser were added in volumes of around 20 ml.

Upon mixing concrete was filled in cylindrically shaped plastic tubes (Typ I: 1000 mm length / 50 mm diameter; Typ II: 250 mm length / 100 mm diameter) and shaken at a vibration plate for 1 minute. Eventually, the tubes were covered with a plastic lid and concrete cured for at least 28 days.

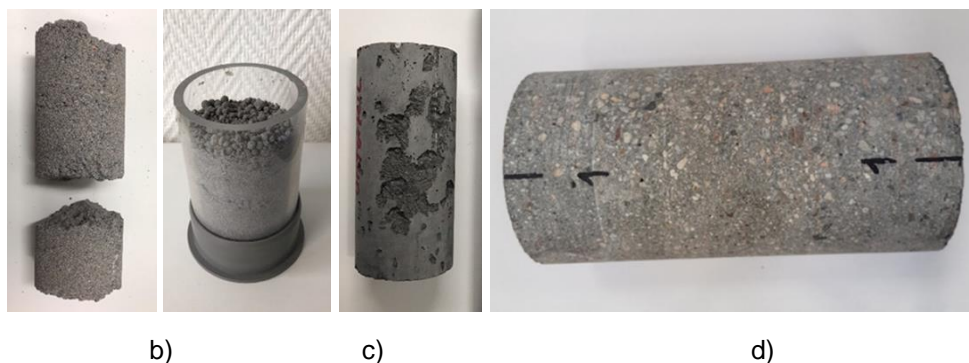


Figure 2-2 Fails in concrete fabrication: a) sample is porous, b) sample with agglomerations and c) sample with shrinkage holes. d) Low-pH S5 sample, which is useable for experiments.

Missing information regarding the concrete fabrication process accounted for major difficulties and several attempts were required to yield homogeneous concrete samples. One example of a fabrication failure is shown in Figure 2-2 (picture a, b, c). Figure 2-2 (picture d) shows a well cured and homogenous sample, which is used in experiments.

2.1.5 COVRA (task 2.2 and 2.3)

2.1.5.1 Sample characteristics and short description of experiment

The Dutch cubical concrete samples have been submerged in synthetic clay pore water as saline as seawater (for composition of the pore water see Table 6-1 in Deliverable 16.3) since September 2016 at around room temperature. This solution is envisaged to be representative for the clay host rocks considered in the Netherlands to host a geological disposal facility. Magnesium is present in this pore water. Ingress of magnesium in concrete reacts with cementitious minerals into brucite and magnesium silicate phases. These formed magnesium phases have been identified as non-bonding phases (Atkinson et al., 1985) and are therefore expected to have a negative impact on the strength of concrete. Sulphate is also present in this saline water but only sulphate resistant cements had been used for the manufacturing of the Dutch samples. No impact of ingress of sulphate on the mechanical strength is therefore foreseen. Bicarbonate is also present in such saline water but no detrimental effect on the mechanical strength is envisaged.

The cement content for all samples was about 400 kg/m³. These cubical samples are mortars made with CEM I (Portland cement) and CEM III/B (a blend of Portland (20-35 wt%) and Blast furnace Slag (66-80 wt%). Two types of hardened mortars with CEM III/B are so-called certified mortar samples i.e. the minimum in compressive strength is guaranteed after 28 days hardening. Also, the variation in density (porosity) between the samples is sufficiently small by which the moisture storage function of the mortars could be obtained. The porosity of these two mortars is 13 % (buffer-like) and 21 % (backfill-like). The size of the coarse aggregates in the buffer-like mortars was 2 mm to 8 mm (content about 900 kg/m³) and fine aggregates 0 mm to 4 mm (content about 800 kg/m³). The size of the aggregates in the backfill mortars was 0 mm to 2 mm (content about 1000 to 1100 kg/m³). The other two mortars are not certified samples and are made with the same size of aggregates as the certified backfill mortar as explained in Deliverable 16.3 (Neeft et al., 2021). A porosity of the not-certified mortar samples representative for samples cannot be given due to the large variation in density.

The porosity of the (certified) mortars of 21 % is smaller than poorly indurated clay such as Boom Clay with porosity of 35 % (Aertsens et al., 2023). The permeability of the mortars is also smaller than poorly indurated clay such as Boom Clay. In this case, exposure of concrete to a saline solution is representative for concrete interfacing a clay host rock.

2.1.6 SCK CEN (task 2.2 and 2.3)

Aged concrete

A Boom Clay-concrete interface was sampled at the HADES underground research facility (in Mol, Belgium), following the procedure described in deliverable 16.3. The HADES located at – 225 m below the surface and surrounded by Boom Clay, which contains high partial CO₂ pressure (see D 16.3). The sample was taken from the Connecting Gallery, in which low-permeability high-pH concrete wedge-blocks have been in contact with Boom Clay for 14 years. The composition of the concrete is given in Table 2-2. The concrete was made of cement CEM I.

Table 2-2 Composition of in-situ concrete

| For 1 m ³ Concrete | Cement CEM I | Fly ash (FA) | Coarse aggregate | Fine aggregate | Admixture | | Water |
|-------------------------------|--------------|--------------|------------------|----------------|------------------|-------------|---------|
| | | | | | Superplasticizer | Silica fume | |
| | 335 (kg) | 115 (kg) | 1252 (kg) | 540 (kg) | 4.5 (l) | 90 (kg) | 135 (l) |
| Solid fraction (%) | 14 | 5 | 54 | 23 | | 4 | |
| Binder fraction (%) | 50 | 17 | | | | 13 | 20 |

Newly made interface.

The concrete composition mimicking the lining concrete is shown in Table 2-3. This formulation is similar to the one used for lining concrete at the HADES. The concrete was cast in PVC tube and cured for 28 days in sealed conditions. Consequently, concrete was sawn into discs with 45 mm thickness. The concrete discs were then lime saturated before percolation and batch experiments.

Table 2-3 Compositions of newly made concrete

| Mix components | Weight (kg/m ³) | | | | | |
|----------------|-----------------------------|------------------|--------------------------|----------------------------|--------|-----------------|
| | OPC cement | Silica fume (SF) | Blast furnace slag (BFS) | Aggregates (coarse + fine) | Water | Chemical admix. |
| Wt | 417 | 62 | 36 | 1792 | 151.67 | 4.83 |

2.1.7 SURAO, CTU, TUL, UJV, CVREZ (Task 2.2 and 2.3)

Table 5-1 of the Deliverable 16.3 Report provides the mix designs of the specially-designed concrete with a reduced pH – SURAO low-pH concrete (LPC). Concrete is made of CEM I 42.5 R, micro silica, slag, water, aggregates, and additives. These are concrete cubes measuring 15 cm on each side, stored at the Underground Research Facility (URF) at a relative humidity of 95±5% and a temperature of 15±2°C.

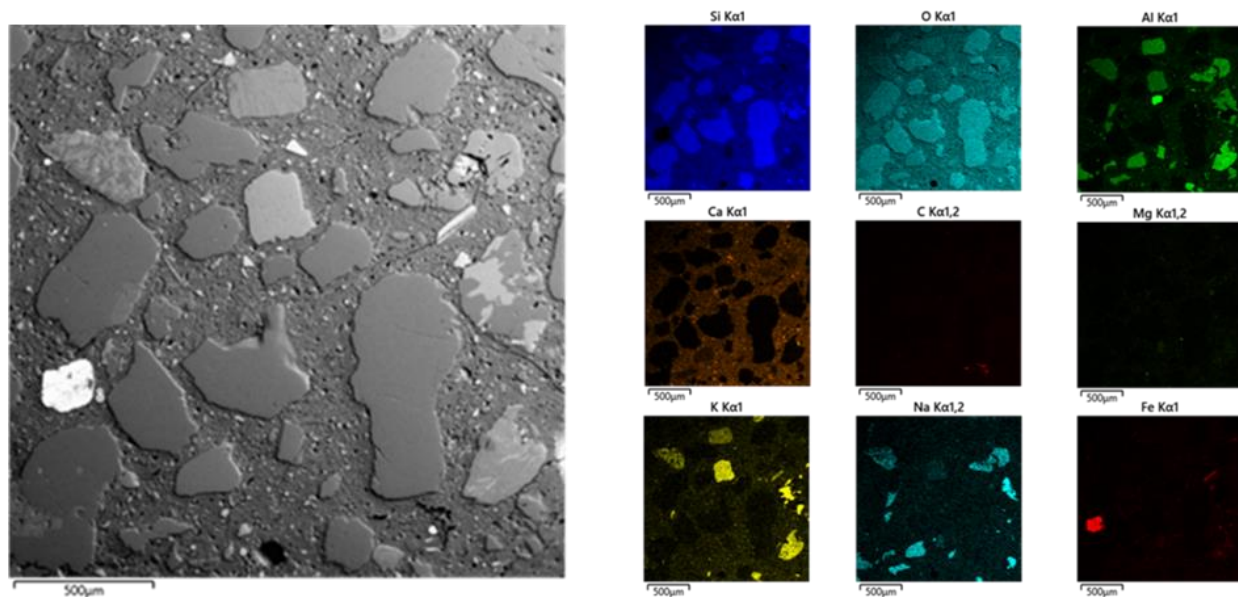


Figure 2-3 SEM measurement and EDX element maps of the cement matrix with aggregates of the reference LPC sample.

SEM analysis of the reference SURAO LPC sample show that the cement matrix is mainly formed by calcium aluminoferrite. The initial phase composition of the reference SURAO LPC sample as a percentage determined by XRD is in Table 2-4. The aggregates in the reference LPC sample are mainly silica sand with aggregates of acidic magmatic rocks contains potassium and sodium calcium feldspars (Figure 2-3).

Table 2-4 Phase composition by XRD of the reference LPC_SURAO sample.

| Phase | Wt% |
|---------------|------|
| Silica | 71.6 |
| Albite | 11.6 |
| Microcline | 2.8 |
| Sanidine | 3.4 |
| Chlorite-IIb | 1.4 |
| Muskovite 2M1 | 5.3 |
| Calcite | 2.6 |
| Hornblende | 1.0 |
| Hematite | 0.13 |

2.1.8 UNIMAN (microbiology Task 3)

2.1.8.1 Sediment

Sediment slurry was collected from a calcite-rich legacy lime working site in Harpur Hill in Derbyshire, UK (Rizoulis et al., 2012) and stored in a cold, dark place prior to use in the microcosm experiment. Volatile fatty acids, VFAs, (lactate, acetate, and formate), sulphate, nitrate and nitrite concentrations in the slurry were analyzed by using Ion Chromatography (IC) (see below for details on equipment used). The pH of the slurry was 11.7 at the time of use.

2.1.8.2 Groundwater

The synthetic groundwater composition (Table 2-5) used was based on geochemical analyses of waters from the Oxford clay formation in the East Lincolnshire area (BGS reference groundwater report, 2022). The TDS reported in this groundwater was approximately 29,102 mg/l. The pH of the synthetic groundwater was 8.3.

Table 2-5 Groundwater composition based on the Oxford clay formation, East Lincolnshire

| Composition | CaCl ₂ | MgCl ₂ 6H ₂ O | NaCl | KCl | NaHCO ₃ | Na ₂ SO ₄ | Na ₂ SiO ₃ 5H ₂ O |
|--------------|-------------------|-------------------------------------|--------|-------|--------------------|---------------------------------|--|
| Amount (g/l) | 1.207 | 7.461 | 18.339 | 0.627 | 0.428 | 4.997 | 0.0229 |

2.1.8.3 Cement tablets

Cement tablets were cast using the low-pH CEBAMA reference mix (Table 2-6) (Vasconcelos et al., 2020; Vehmas et al., 2020). The formulation of the concrete mix composed of low alkaline ordinary Portland cement CEM I 42.5R (Mannokbuild, Ireland), densified silica fume (SF) from Hsamaterial China (as supplementary pozzolanic material) and blast furnace slag (BFS) (as hydraulic material, which self-hydrates or reacts with the hydration product that controls the pH and composition of cement pore solution). Naphthalene sulfonate (Pantrahit LK FM from Ha-Be Betonchemie GmbH) was used as a superplasticizer to achieve desired workability. The water-to-solid ratio was approximately 0.6 by weight. To make the cement mix, silica fume, OPC, and superplasticizer were mixed for 3 minutes with water at a slow speed in a mixer. The sides and bottom were scraped occasionally to ensure mixing before adding BFS (Vehmas et al., 2017; Vasconcelos et al., 2020). The slurry was then mixed in a high-speed mixer for 1 hour before use.

EURAD (Deliverable n° 16.4 and 16.6) - Report on bio-chemical processes controlling the evolution of the microstructure and mechanical properties of cementitious materials.

Dissemination level: PU

Date of issue of this report: 30/05/2024

The cement slurry was cast into tablet shape using a silicon mould containing wells of 6 mm depth and 10 mm diameter. The tablets were air-dried for one day and then cured for an additional 30 days in a zip-lock bag to lock moisture. The cement tablets were then rinsed under a continuous stream of deionized water for 2 minutes with gentle rubbing on the surface to remove any extra particles. They were soaked in deionized water for at least seven days until they reached a stable pH and then soaked in groundwater for another four days until the pH reached approximately 10 before use in the microcosm experiments.

Table 2-6 CEBAMA reference cement paste formulation (Vehmas et al., 2020)

| Material | CEM I 42.5R (OPC) | Silica fume (SF) | Blast furnace slag (BFS) | Plasticizer | Water |
|----------|----------------------|---------------------|-----------------------------|-------------|---------|
| Amount | 954 g | 1000 g | 590 g | 11.24 mL | 1138 mL |

2.1.9 HZDR (microbiology task 3)

2.1.9.1 Groundwater

Natural groundwater from the flow of Cernon at the Tournemire Experimental Station of IRSN in France was collected several times (22nd of June in 2022 and 9th of May in 2023) for analyses of geochemistry and microbial diversity. In addition, the water was used for the aerobic microcosms set ups.

2.1.9.2 Cementitious material

The low-pH model cement paste was produced by mixing Ordinary Portland Cement (CEM I, 590.5 g) with colloidal silica (310.9g), superplasticizer (35.2g) and water (585.9 g), resulting in SiO₂, CaO as major oxide composition based on calculations (Table 2-7). After one year of hydration in a sealed bag, the paste was cut into slices with a depth of 1 cm. A layer of resin (Resoltech 3030) was applied to each slice to enforce unidirectional diffusion in IRSN. The solid cement paste was then divided into square shape (4x4x1cm) for microcosm setups.

Table 2-7 The oxide composition of low pH model cement paste.

| Oxide | SiO ₂ | CaO | Al ₂ O ₃ | SO ₃ | Fe ₂ O ₃ | K ₂ O | Na ₂ O |
|------------------------|------------------|---------|--------------------------------|-----------------|--------------------------------|------------------|-------------------|
| Concentration (mmol/l) | 8009.43 | 7535.64 | 353.89 | 292.13 | 108.5 | 66.77 | 8.9 |

2.2 Overview of experimental program: new experiments and ongoing experiments

2.2.1 LaMcube (Task 2.1)

Overview of unchanged experimental protocol and method

For actions 1, 2 and 4, experimental protocols and methods for uniaxial, triaxial and creep remain globally identical. In the following paragraphs, main technical precisions are provided.

- Action 1

Uniaxial tests are performed on an Instron® electromechanical testing machine (load capacity 250 kN). Several preliminary results have been obtained on an Instron® hydraulic testing machine (capacity 500 kN). Each cylindrical sample Ø37x74 mm is instrumented with 2 longitudinal and 2 lateral gages. The reference loading path is 3 cycles between 3 and 6 MPa, 1 cycle between 6 and 15 MPa (to measure the Young's modulus E and the Poisson's ratio ν) then a load increase until failure. The rate of actuator displacement is fixed at 2 μ m/s. The values are recorded through a data acquisition system (load and strains).

Triaxial tests are performed in a triaxial cell (to ensure the confining pressure of 3 or 10 MPa) under the same Instron® electromechanical testing machine to apply the deviatoric pressure. Each cylindrical sample Ø37x74 mm is instrumented with 2 longitudinal and 2 lateral gages and placed in a rubber sleeve to prevent

any oil intrusion from the confining pressure. The reference loading path is 3 cycles between 6 and 15 MPa, 15 and 30 MPa, and 30 and 45 MPa (to measure the Young's modulus E and the Poisson's ratio ν) then a load increase until failure. The rate of actuator displacement is fixed at 0.5 $\mu\text{m/s}$. The values are recorded through a data acquisition system (load and strains).

- Action 2

For creep tests, the experiment has yet to begin. For uniaxial creep tests, 6 samples will be used (0 %, 50 % and 100 % of carbonation, 2 samples each time), placed in a frame with an axial load of 20 MPa (50 % of the aimed compressive strength at 28 days), only the axial strain will be recorded through analog indicators. For triaxial creep, tests will be performed on 1 sound sample, 1 sample at 50% and 1 sample at 100% of carbonation under a confining pressure of 3 MPa for 2 weeks (deviatoric load: 35 MPa), then under a confining pressure of 10 MPa (deviatoric load: 50 MPa) for additional 2 weeks.

- Action 3

The protocol of uniaxial and triaxial compression is the same as for action 1. The pre-damaging protocol has been updated (see §2.2.2).

Experiment design and protocol modification

- Climatic chamber development

Adaptations have been proposed and done in the conversion of an ordinary climatic chamber into a carbonation chamber, mainly to reduce the CO_2 leakage by creating a box inside the chamber.

- Carbonation process

The carbonation process has been modified, compared to the description in deliverable 16.3. A pre-drying at 20 °C/ 65 % RH (same temperature and relative humidity conditions as during carbonation) before carbonation at 20 °C/ 65 %RH /50 % CO_2 was initially planned but preliminary results have shown that this pre-drying was not sufficient to achieve in a limited period of time (less than 1 month) a fully-carbonated state. This could result in a limited gaseous diffusion of CO_2 due to too much condensed water in the pore network. In addition, the accelerated carbonation generates water that will also increase the water saturation of concrete. The Figure 2-4 shows the state of carbonation of a mortar (same cement as for concrete, diameter 4 mm) after drying at 20 °C/ 65 % RH until equilibrium (2 days) then 5 days of carbonation (20 °C / 65 % RH / 50 % CO_2): no carbonation has been detected by phenolphthalein.

The process of carbonation is therefore modified to obtain a less saturated material before carbonation and improve the gaseous diffusion of CO_2 : the pre-drying is an oven-drying at 45°C until mass stabilization.

During the carbonation process in the climatic chamber with CO_2 injection, samples are regularly moved inside the chamber to ensure a homogenous state of carbonation for all samples.

- Reference state for sound samples

Before the beginning of a test, the samples are supposed in a state corresponding to the end of the curing period described previously (saturated and hydrated material kept under lime-saturated water for more than 6 months). Then, the reference for sound state (no carbonation, no pre-damage) is an oven-dried specimen at 45 °C (around 13% RH) until equilibrium then stored at 20°C / 65 % RH. This reference state allows comparisons between the different samples that underwent different conditionings and tests.



Figure 2-4 Non-carbonated surface detected on mortar specimen after pre-drying at 20 °C / 65 % HR and 5 days of accelerated carbonation (diameter of the specimens is 4 mm)

– States of carbonation

To assess the detection of carbonation, sprayed phenolphthalein (in solution with water and ethanol) has been used. The fraction of carbonation is calculated as the carbonated surface (i.e. colourless surface after phenolphthalein spraying) of a cross-section in the middle of the sample divided by the whole surface of the cross-section.

It must be noted that the 100 % carbonated state is ambiguous as carbonation process may still continue even if the whole sample remains colourless after phenolphthalein spraying (which only stands for a pH value under around 9, not the end of the carbonation of C-S-H for example). In the results (§3), it will be indicated if the 100% of carbonation corresponds to the first time where the sample is totally colourless after phenolphthalein spraying (so called “100 %” carbonation state, achieved after 21 days of carbonation on cylindrical samples Ø37×74 mm) or if additional days of carbonation have been added after this state (“100 %+” carbonation state, achieved after 40 days of carbonation on cylindrical samples Ø37×74 mm).

– Mechanically induced damage before carbonation

The objective was to obtain a sufficient level of damage before carbonation to assess the effect of a pre-damage on mechanical behaviour of carbonated or non-carbonated samples. Initially, the pre-damage would have been generated through a compression test up to 75 % of average peak strength. However, even at this level, the damage may have only few effects on transport properties of the concrete and the (micro)cracks would have preferential orientations.

The degradation is finally performed by thermal shock. Differential thermal strains between the cementitious matrix and aggregates, but also between the core and external part of the sample, would lead to a more diffuse crack network with less preferential orientation. The method is as follows. Saturated samples (end of curing under lime-saturated water) are protected with aluminium foil (to prevent water exchange) and immersed in boiling water for 5 min (temperature around 96-97°C) then in water with ice for 5 min (temperature around 4-5°C). This thermal cycle is applied a second time.

2.2.2 LMDC (Task 2.1 and 2.2)

2.2.2.1 Experimental program and experiment design

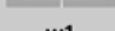
○ Concrete samples

The compressive strength and the modulus of elasticity were respectively measured on 4 and 3 cylinders 112.8 mm in diameter and 220 mm height at the end of the curing. Porosity was measured at 28 days after the same 28-day autogenous curing on cylinders 112.8 mm and 60 mm high extracted from cylinders 112.8 mm in diameter and 220 mm height.

- Reinforced concrete specimens

The walls allow to create some defects of SCI by top bar effect and by sawing to provide prisms of same geometry than the others. The prisms are tested by three-point bending to create two different levels of mechanical damages at the SCI. The prisms are then subjected to different storage conditions: reference one without carbonation, or a phase A of accelerated atmospheric carbonation, or after phase A and a second phase B of cycles of immersion in CO_x (Callovo-Oxfordian claystone) synthetic pore solution and atmosphere. After each storage conditions, the prisms are sawn in 2 parts to provide 2 pull-out tests samples, and the pull-out tests are carried out. The types and numbers of samples are presented in Table 2-8.

Table 2-8 Synthesis of number of samples and geometries, and pull-out tests at the end of each phase.

| Type of initial steel-concrete interface degradation | Type of initial cast samples | Nb and type of samples | Nb of pull-out tests before corrosion | Nb of pull-out tests after the phase A of corrosion condition | Nb of pull-out tests after the phases A and B of corrosion condition |
|--|---|--------------------------------|---------------------------------------|---|--|
| Effects of 2 levels of mechanical damage | w1  | 9 prisms = 18 pull-out samples | 3 prisms = 6 pull-out tests | 3 prisms = 6 pull-out tests | 3 prisms = 6 pull-out tests |
| | w2  | 9 prisms = 18 pull-out samples | 3 prisms = 6 pull-out tests | 3 prisms = 6 pull-out tests | 3 prisms = 6 pull-out tests |
| Effects of material defects = top bar effect  | w1  | 9 walls = 18 pull-out samples | 3 prisms = 6 pull-out tests | 3 prisms = 6 pull-out tests | 3 prisms = 6 pull-out tests |

- Carbonation phases for reinforced concrete specimens

The reinforced concrete samples used to characterize the steel-concrete bond with concrete and SCI defects are submitted to two successive phases inducing concrete carbonation.

- phase A. It corresponds to accelerated atmospheric carbonation with 3 % ±0.5 % CO₂, 57 % RH ±3 % RH and 20 °C ±1 °C following (EN 12390-12, 2020). This condition is representative of the intrados of the reinforced concrete tunnel segments. Its duration is 70 days. The carbonation depth is measured on blocks cast with the other samples.

- phase B. It consists of cycles of immersion in CO_x synthetic pore solution during 1 month followed by a period of 2 weeks in atmosphere 50 % RH ±5 % RH and 20 °C ±1 °C to accelerate the diffusion of CO₂. This condition is representative of the extrados of the reinforced concrete tunnel segments. 3 or 4 cycles are applied. The pH of 7.2 is balanced by monitoring the partial pressure of CO₂. The potential gradient is mapped at the end of each immersion period for each cycle.

The phase A corresponds to unsaturated concrete conditions (Task 2.1) and phase B to saturated concrete (Task 2.2).

- Design of reinforced concrete samples

To study the evolution of steel-concrete bond with evolution of steel corrosion due to concrete carbonation, the classical samples are pull-out tests ones as defined by the RILEM recommendations for this test. However, it is impossible to store such samples with steel rebars partially outside of the concrete considering the phase B of carbonation under CO_x water (dissolved CO₂) with humidification-drying cycles. So, the reinforcement rebar had to be protected inside the concrete. To be able to pull on the rebar to carry out the

pull-out test, their ends were threaded and protected from the concrete contact by plastic sleeves. After sawing reinforced concrete samples to free the threaded rebars ends, a coupler has been used to associate the rebar to another, which be the one to apply the tensile force during the pull-out test.

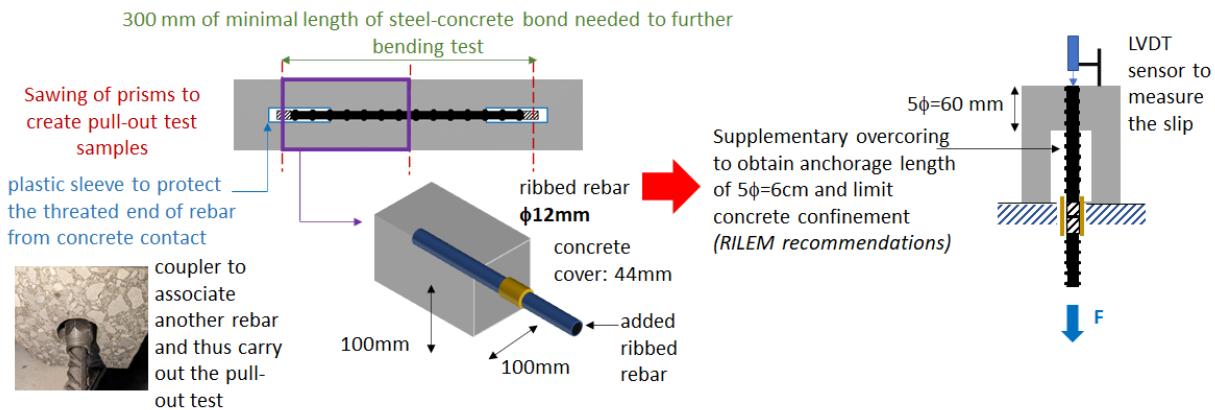


Figure 2-5 Geometry of prism and different operations to provide pull-out test specimens after three-point bending test

The sample geometry was chosen prismatic to get the required geometry for pull-out test specimens, and also in order to carry out bending tests before carbonation phases and create a cracking which will lead concrete carbonation around the crack tip and generate steel corrosion. The dimension of the reinforced concrete prisms was designed following several criteria. A rebar diameter d_s of 12 mm classically used in reinforced concrete has been chosen. RILEM (RILEM, 1994) recommends a length of the side of the square section equal to $10d_s$, but not below 200 mm. The 200 mm side was too large, taking into account the carbonation process and the objective to obtain steel corrosion during the research project. Thus, the side of the square section was taken equal to 100 mm, close to $10d_s$, with a concrete cover of 44 mm. The length of the prism is 400 mm with a length of steel rebar of 300 mm. It is a compromise with a concrete cover for steel of 50 mm at the ends of the prism, relatively similar to that of the cross-section, and a sufficient length considering the three-point bending test configuration, presented further. To ensure a bonding length between steel and concrete respecting the $5d_s$, i.e. 60 mm, a supplementary overcoring is carried out to obtain this length and to limit concrete confinement with the support of the hydraulic press during pull-out tests. The Figure 2-5 presents the geometry of prisms and the different processes to obtain two pull-out test specimens from a prism, after the three-point bending test used to crack the prism.

- Degradation types of SCI

Defects of SCI due to concrete

To create defects at SCI due to the top bar effect (bleeding, settlement of fresh state concrete), 1000x100x400 mm walls were cast with 12 mm diameter in the upper part of the wall, in order to provide exactly the same reinforced concrete prisms after a sawing. The Figure 2-6 presents the wall geometry and the sawing operation.

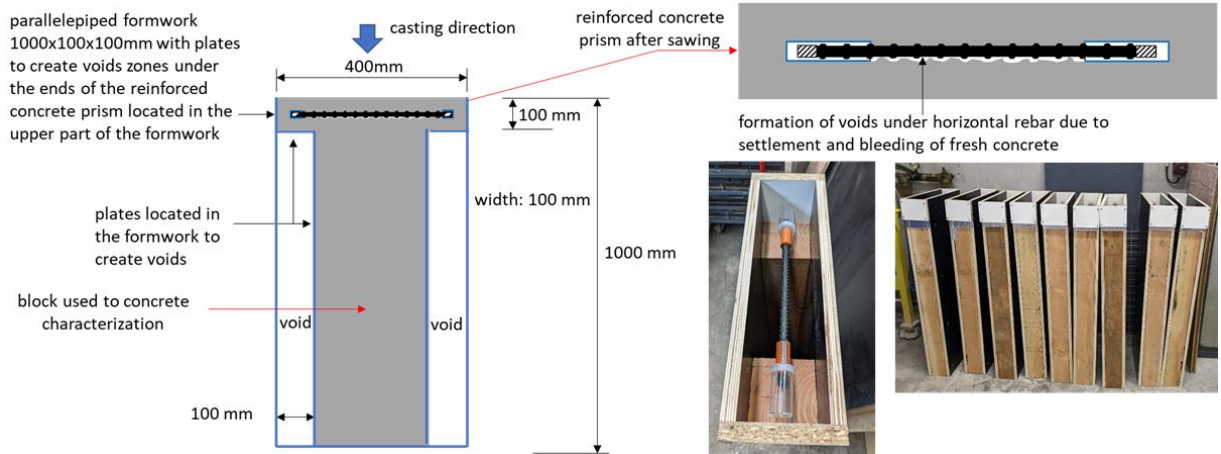


Figure 2-6 Geometry of wall to create some defects at SCI by top bar effect, and sawing operation to provide prisms

Mechanical damage of SCI

Before storing the prisms in the carbonation phase, they are tested by three-point bending to create a crack which allowed to carbonate concrete around the crack tip. Two levels of SCI mechanical degradation were tested by applying different loading forces. To distinguish this level, two residual crack widths were targeted after unloading:

- $w_1 \approx 200-300 \mu\text{m}$ (targeted)
- $w_2 \approx 400 \mu\text{m}$ (targeted)

These values correspond to classical values defined at the Serviceability Limit State (SLS) of Eurocode 2 (Eurocode 2, 2005).

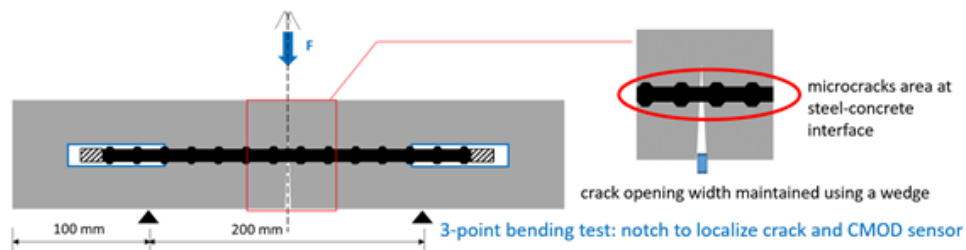


Figure 2-7 Configuration of the three-point bending test

The configuration of the three-point bending test is represented in Figure 2-7. A notch of 3 mm width and 6 mm height is carried out to localize the flexural crack. A crack mouth opening displacement (CMOD) sensor is placed to record the crack width evolution. The test is controlled by crack opening with a rate of $1 \mu\text{m/s}$. Before unloading, some wedges of several slightly different widths were placed on the bottom side of the crack to maintain the residual crack width, w_1 or w_2 , for the next carbonation phases as desired by LMDC.

- Configurations of SCI degradation and chronology of the different operations

As explained in Table 2-8, there are 3 groups of prisms to characterize the steel-concrete bond:

- without carbonation, they can be called “reference” prisms
- after phase A
- after phases A and B

EURAD (Deliverable n° 16.4 and 16.6) - Report on bio-chemical processes controlling the evolution of the microstructure and mechanical properties of cementitious materials.

Dissemination level: PU

Date of issue of this report: 30/05/2024

For each group, 3 types of degradation of SCI were tested:

- prisms with w1 residual crack width, lowest mechanical damage of SCI
- prisms with w2 residual crack width, highest mechanical damage of SCI
- prisms with w1 residual crack width and top bar effect

The three-point bending test was applied for all the prisms at the same date just before the phase A. The sawing operation to provide pull-out test samples from prisms is carried out just before the pull-out test (after phase A, phase B, or after bending test for reference prisms). The pull-out test is carried out following the RILEM recommendations (RILEM RC6, 1994). The test is controlled by force with a loading of 75 N/s ($0.5d_s^2$, with d_s the diameter of the rebar in mm) and the slip between the steel rebars and the concrete is measured using an LVDT fixed to concrete as illustrated in Figure 2-1.

2.2.2.2 Reinforced concrete from Bure underground laboratory

LMDC received reinforced concrete (blocks of tunnel segments and core samples) collected at the Bure underground laboratory (Figure 2-8). The aim was to carry out pull-out tests and chemical analyses on these decommissioned structures. The samples were collected while taking advantage of an experiment designed to assess the feasibility of removing the tunnel segments, a step that ensures the closure system works properly. Tunnel segments removed spaced out by 3 tunnel segments not removed.

The removal process includes preparatory work:

- Segment zone reinforcement (installation of metal and protective rings)
- Dismantling of the reinforced concrete slab and management of the networks and ventilation (dust)
- Segments removed in 2 pieces by drilling and then a trellis is put in place to secure the area, leaving the bare rock for at least 3 weeks

The steel/concrete interface will also be analysed to assess the presence or absence of top bar effect and the presence of corrosion products. The relevance of testing concrete segments, i.e. decommissioned structures without corrosion, will be assessed.

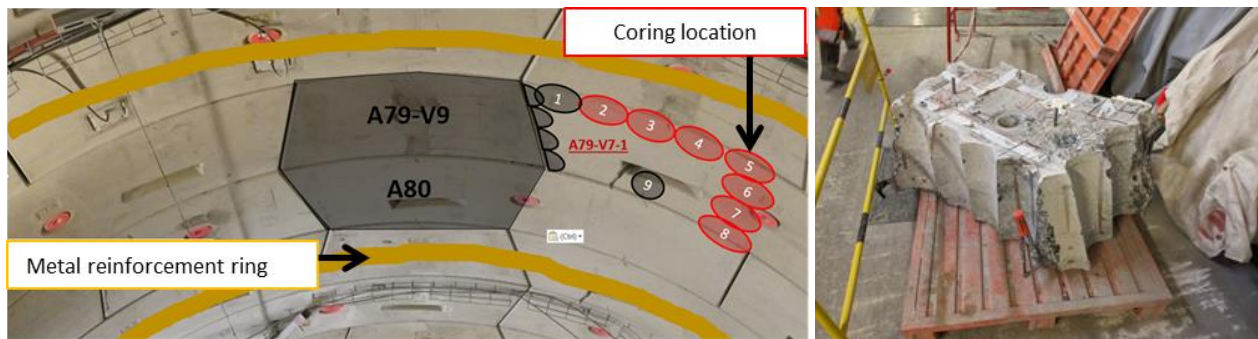


Figure 2-8 Tunnel segments of the underground laboratory (CMHM) in the left and tunnel segments blocks in the right (ageing ~10 years)

2.2.3 PSI/Empa (Task 2.2)

To support the interpretation of the results shown in Section 4.1.1, it is reminded here that the poromechanical characterization by the PSI/Empa team aimed at (1) comparing the viscoelastic, meso- and microstructural properties of the distinct cementitious composites as well as at (2) assessing, for each composite by itself, their eventual dependences on the distance from the interface with the OPA. The latter goal was addressed by measuring on cores obtained either in contact with the OPA surface or at further

distances along the radial directions of the barrels. See, for example, in Figure 9-6 of the D16.3 Report, the coring positions for the OPC mortar specimens.

Further, it is key to remind the reader that this team focused on the use of fully non-destructive measurement methods, except for the quasi-static Young's modulus and compressive strength measurements as well as the SEM/EDX analysis. The reason for such focus was, on the one side, the advanced degradation age of the investigated cementitious composites, on the other side, the lack of prior knowledge about the properties of identical or similar composites analysed after such long ages. Indeed, within the CI experimental campaign at the Mont Terri URL, no poromechanical characterization of specimens as old as those investigated here has been so far reported. The sampled cores are thus unique. The team needed, on the one side, to perturb specimens as little as possible, let alone to sacrifice them for measurements requiring destructive preparation, while, on the other side, to preserve as many specimens as possible for further investigation beyond the MAGIC project itself.

Since the whole experimental campaign did not vary significantly compared with what was described in Chapter 9 of the D16.3 Report, in the following, only key technical details about the distinct measurement implementations as well as the actual number of specimens for each measurement are provided, while the differences compared with what was originally planned and described in the D16.3 Report are detailed in the Section 2.2.3 below.

2.2.3.1 Dynamic, complex-valued elastic moduli measurements by Single M₀de Resonant Ultrasound Spectroscopy (SIMORUS)

The PSI/Empa team implemented a specific version of Resonant Ultrasound Spectroscopy (RUS), called Single M₀de RUS (SIMORUS in short), by which a specific type of vibration *eigenmode* is preferentially excited. Two distinct configurations were implemented: one for exciting preferentially longitudinal *eigenmodes*; one for torsional ones. Figure 2-9 shows the implementation for the longitudinal *eigenmodes*. In both configurations, the vibration signal was an out-of-plane component of the surface velocity vector at the measurement position, measured in non-contact mode by a single point Laser Doppler Vibrometer (LDV). The two configurations just differed in terms of (1) the vibration source implemented and (2) the holding of the specimen, suspended in space.

It is needed to remind the reader that the implementation, in both configurations, included performing these measurements inside a glove box conditioned at the same RH (90 %) and temperature (20 °C) as those of the climatic chamber hosting continuously the cores, when not subjected to measurements. The rationale was to minimize as much as possible water content changes, as dynamic moduli are significantly sensitive to them. Such conditioning was realized by placing, at the bottom of the glove box and at least a couple of days before each measurement session, a super-saturated aqueous solution of K₂SO₄ with a concentration slightly above 0.66 M (DIN EN ISO 12571) and, further, by using an air conditioner the night before the measurement session.

The longitudinal SIMORUS measurement provides a resonance spectrum, containing the first longitudinal resonance peak. Two parameters of such peak are estimated: the 1st longitudinal resonance frequency, being the peak frequency, because the signal measured is the longitudinal vibration velocity; that peak's Q-factor. The 1st longitudinal resonance frequency is directly proportional to the Young's modulus, E^{dyn} (Spinner et al., 1960, Kolluru et al., 2000, ASTM C215-19), i.e., to the real part of the complex-valued Young's modulus (Lakes 2009), while the longitudinal Q-factor is the inverse of the ratio between the imaginary and the real parts, also known as the loss tangent (or $\tan(\delta)$) in rheology (Lakes, 2009). As a reminder, in rheology and viscoelasticity, the real part is also called the storage modulus while the imaginary part is called the loss modulus (Lakes, 2009). While the data made available to all the EURAD MAGIC

partners include values for the storage and loss Young's moduli as well as for the longitudinal Q-factor and the wave amplitude attenuation coefficient, α_L , the results reported in Section 4.1.1 below show only α_L values, expressed in Neper *per* m (Np/m). As a reminder, α_L is directly proportional to the loss Young's modulus (see Section 9.5.1.1 in the D16.3 Report) and represents the exponential decay rate of the wave amplitude per unit of propagation distance. It is more meaningful and more commonly reported than the loss Young's modulus itself, as it is physically more meaningful for dynamic measurements with elastic waves. It is dependent both on the material's bulk viscosity as well as on its structural heterogeneity at the scale of the wavelength range, in which the measurement is performed. Such wavelength range corresponded to a temporal frequency range approximately equal to 8 – 13 kHz. This frequency range falls, nominally, still within the sound range (between 20 Hz and 20 kHz).

Table 2-9 Number of cored specimens on which longitudinal SIMORUS was performed, for each specimen ensemble. Each ensemble's average specimen distance from the OPA interface (d_{OPA}) is also indicated.

| Specimen ensemble ID | Average d_{OPA} [mm] | Nr. of specimens |
|----------------------|------------------------|------------------|
| 2274-A | 0 | 3 |
| 2274-B | 47.2 | 3 |
| 2275-A | 0 | 2 |
| 2275-B | 49.9 | 3 |
| 2276-A | 0 | 2 |
| 2276-B | 49.2 | 2 |
| 2277-A | 0 | 3 |
| 2277-B | 29.11 | 3 |
| 2277-C | 49 | 3 |
| 2278-A | 0 | 3 |
| 2278-B | 29.2 | 3 |
| 2278-C | 52.9 | 3 |

Section 4.1.1 does not provide any results from the torsional SIMORUS measurements, since they are still ongoing at the time of this report. However, they were implemented similarly to the longitudinal ones, except for a distinct vibration source implementation, which needed to be newly designed and implemented specifically for the MAGIC project. From the 1st torsional resonance peak, the complex-valued shear modulus can be estimated based upon the same principles and workflow used for estimating the complex-valued Young's modulus (Pickett 1945, Spinner et al 1958, ASTM C215-19). Such measurements are performed on the same exact cores used for the longitudinal SIMORUS measurements as well as on additional ones. Table 2-9 provides information about the number of specimens of each *ensemble*, on which both SIMORUS measurements have been performed.

2.2.3.2 Quasi-static Young's modulus and compressive strength measurements

Quasi-static Young's modulus measurements were performed, for each specimen *ensemble*, on a set distinct from the one on which the longitudinal SIMORUS measurements were performed. That is because such measurements introduce irreversible modifications to a specimen, including eventual micro- and/or meso-scale damage (see Section 9.5.1.1 of the D16.3 Report). The measurements were performed according to an adaptation of the EN 12390-13 standard, consisting of shortening the cored specimens till having an aspect ratio (length-to-diameter) of about 3 and 5.5, for the concrete and mortar specimens, respectively. The standard itself requires a value between 2 and 4. Further, it suggests working with cylindrical specimens 300 mm long and 150 mm in diameter. For the concrete cores, the average length

was about 120 mm and the average diameter about 40 mm. For the mortar specimens, the average length was about 155 mm and the average diameter about 28 mm. This difference from what the standard suggests and prescribes was motivated by the need for the cored specimens to have a sufficiently high aspect ratio to allow performing both SIMORUS measurements as well as allowing sufficient sampling from the available cross-section of the barrels. For each specimen *ensemble*, either 2 or 3 specimens were sacrificed for such measurements. The sole exception was the 2275-A *ensemble*, from which only a single specimen was available.

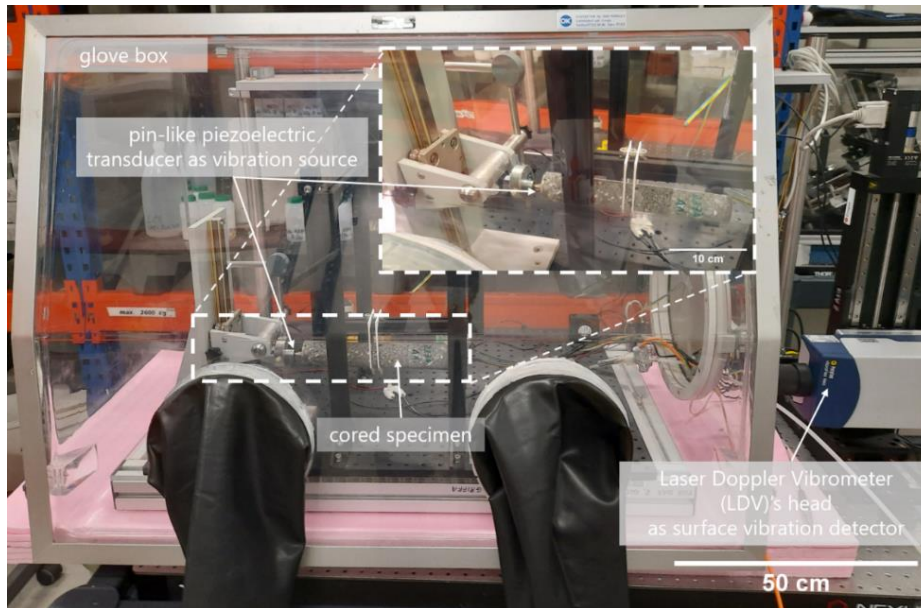


Figure 2-9 Implementation of the longitudinal Single MOde Resonant Ultrasound Spectroscopy (SIMORUS) measurement inside a glove box, to measure longitudinal resonance frequencies of the cored specimens (in this example, one of the 2274-A ensemble) under the same temperature (20°C) and relative humidity (90%) conditions, at which the cores were continuously kept in the storage climatic chamber. The inset provides a zoom-in view of the specimen in contact with the pin transducer acting as the longitudinal vibration source.

Since the quasi-static Young's modulus measurements were performed on specimens distinct from those used for the dynamic ones, the correlation analysis between the two Young's modulus types, reported in Section 4.1.1 below, needs to be intended only in terms of average values, with respective uncertainty ranges.

Uniaxial compressive strength (UCS or f_c) measurements were performed according to the EN 12504-1 standard on yet additionally cored specimens cut to an aspect ratio of 2, i.e., about 80 and 56 mm long cores, for the concrete and mortars *ensembles*, respectively. The number of specimens for each ensemble were typically either 1 or 2.

2.2.3.3 X-ray tomography for the mesostructure characterization

X-ray tomography was performed, for each *ensemble*, on at least one of the specimens subjected to the SIMORUS measurements. The goal was to assess the structure at the composite's mesoscopic scale, in search of typical damage features, e.g., cracks and delamination of Interfacial Transition Zones (ITZs). At the time of this report, the tomography results have been analysed only qualitatively, i.e., by human visual

inspection. 3D image analysis is planned for eventual following articles, to quantify features of interest for the SIMORUS results interpretation, e.g., air voids volumes as well as their size distribution.

These measurements were performed with one of the tomographs of [Empa's Center for X-ray Analytics](#), equipped with a reflection-based, micro-focus X-ray source with 230 keV maximum photon energy and a 2D flat panel detector relying on the double conversion detection process (X-ray-to-light photon conversion by a CsI scintillator layer covering each pixel, the latter made of amorphous Si and converting the light photon into electrical current). Each pixel has a physical size, p , of 127 μm .

The measurement settings differed for the concrete and for the mortar specimens.

In the concrete case, the source-to-detector distance, d_{S-D} , was 542.145 mm, while the source-to-specimen distance, d_{S-S} , was 134.067 mm. With such a configuration, the geometrical magnification factor, $M \equiv \frac{d_{S-D}}{d_{S-S}}$, of the cone-shaped X-ray beam is approximately 4, leading to a radiographic pixel size of 31.4 μm . The tomographic voxel size is equal to \tilde{p} , not to be confused with the tomographic spatial resolution, which is a multiple of \tilde{p} (approximately twice, in the case of the performed measurements). In the mortar case, $d_{S-D}=348.658$ mm and $d_{S-S}=59.842$ mm, leading to $M \cong 5.8$ and $\tilde{p} \cong 21.8$ μm .

The X-ray source was operated at 160 kV and 170 μA in the concrete case, while at 120 kV and 100 μA in the mortar one.

A helical tomographic acquisition protocol needed to be used in the concrete case, instead of a traditional circular one, where the specimen is rotated over 360° around an axis parallel to the detector's vertical axis. In the helical protocol, the specimen is rotated and simultaneously displaced, at constant velocity, along the rotation axis itself. Such a protocol allows measuring specimens long enough not to fit fully within the detector's Field Of View (FOV), at the set geometrical magnification, without the need to perform multiple, independent tomographic acquisitions of different vertical regions of the specimen and stitch together the resultant tomograms. The helical protocol consisted of 4 turns over 360°. 1152 radiographs were acquired during each turn, each being the result of a pixel-wise averaging of 25 successive raw radiographs, acquired at a frame rate of 11 Hz. The corresponding tomograms covered on average a total length of 103 mm along the symmetry axis of the cored specimens.

In the case of the mortar specimens, a smaller range of core length was covered by the tomographic volume, via a standard circular tomographic acquisition with a singular, 360° rotation with not vertical specimen displacement. In such case, 3600 radiographs were acquired for each tomogram, each radiograph being the result of a 13-frame averaging, with a raw acquisition rate of 9.25 Hz.

2.2.3.4 SEM/EDX analysis

SEM/EDX analysis on polished cross-sections obtained from one additionally sacrificed specimen of each *ensemble* is used to assess, on the one side, any eventual damage feature at the microscopic scale within the hydrated binder regions (SEM in back-scatter electron mode), on the other side, the elemental spatial distributions in specimens directly in contact with the OPA interface *versus* in those farther away. Such comparison should provide information about the reactive transport process and the respective degradation of the hydrated binder, as obtained at earlier ages from other specimens in work already reported within the literature (Jenni et al 2014, Dauzeres et al 2016, Mäder et al 2017, Lerouge et al 2017). In turn, this information should empower a clearer interpretation of the poromechanical characterization results reported in Section 4.1.1.

2.2.3.5 Dynamic, complex-valued shear modulus measurements by torsional SIMORUS

The estimation of the complex-valued shear modulus from measured torsional resonance peaks requires, in the case of cylindrical specimens, a distinct vibration source rather than the pin transducer used for measuring longitudinal peaks (see Figure 2-9 above). While a pin transducer still allows exciting torsional vibration eigenmodes of prismatic specimens, when positioned at specific locations on the specimen surface, prescribed by the ASTM C215-19 standard, the same does not apply in the case of cylindrical specimens, especially of highly attenuating materials as concrete and mortars as well as rocks (Chen et al 1989, Jackson et al 2011, Remillieux et al 2016, Saltiel et al 2017).

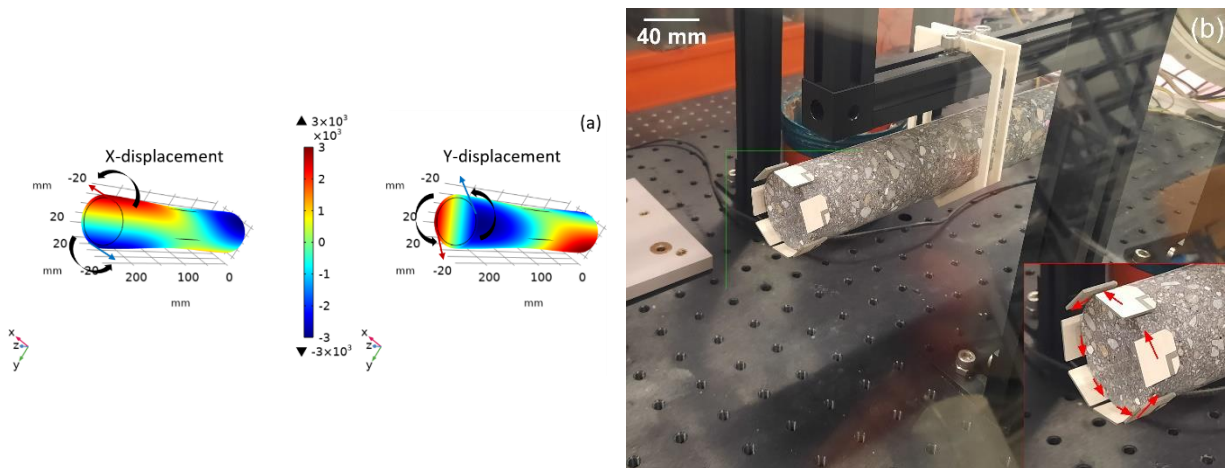


Figure 2-10 Implementation of SIMORUS for the preferential excitation of torsional vibration eigenmodes of cylindrical specimens. (a): an example of surface distribution of the X- and Y-displacement fields at a time point during the 1st order torsional vibration of the 2274-B6 specimen, as computed with the Finite Element Analysis. The straight arrows provide a qualitative example of displacement vector direction on the surface. To be noted are the symmetries responsible for the torque imposed to the specimen at its end (black arrows). (b): example of implementation of the vibration source as a series of custom-built shear piezoelectric transducers, glued on the edge of one specimen's end, each forcing the specimen tangentially (i.e., in-plane) to the contact surface. The arrows indicate each transducer's direction of straining, while the driving voltage signal is applied along its thickness.

An alternative possibility consists of applying a sinusoidal torque at one specimen's end. As shown in Figure 2-11(a) by the results of a Finite Element *eigen*frequency Analysis (FEA) implemented in Comsol Multiphysics™, the first torsional vibration eigenmode of a cylinder is characterized by a surface displacement vector field, which has maximum magnitude at the specimen's ends and, there, consists of purely tangential surface components. Equivalently, such displacements can be imposed to one specimen's end. The approach proposed by Simonetti et al. (2004) and Remillieux et al. (2016) was implemented, consisting of using a series of plate-like shear piezoelectric transducers, glued at the specimen's edge at one of its end sides (see Figure 2-10 (b)). In this MAGIC project, customized transducers were designed at Empa, then manufactured by APC International Ltd. Each plate has a size of 15×15×1 mm³ (length×width×thickness) and is made of a type of piezoelectric ceramic lead-zirconate-titanate (PZT). During the torsional SIMORUS measurement, the same sinusoidal voltage is applied to each plate via a distribution amplifier (by Stanford Research Systems, model FS730/4), in order for each transducer to apply synchronously in-phase tangential displacements to the specimen at the contact surface.

2.2.3.6 Protocol modification

X-ray tomography was originally planned to be performed on cylindrical cores 40 mm-long and 10 mm in diameter (see Tables 9.2, 9.5, 9.8, 9.11 and 9.14 in the D16.3 Report), additionally sampled to those used for the other measurement types. During the execution of the experimental campaign, it was decided to perform X-ray tomography first on the cored specimens used for the SIMORUS measurements. On the one side, being the latter larger specimens, they could be tomographed at lower spatial resolution, compared with what could have been achieved with 10 mm-diameter specimens. This choice implied reducing the amount of eventual mesoscale damage features detected. On the other side, given the large spatial heterogeneity of the investigated specimens and materials, the tomograms of the same exact specimens, whose dynamic moduli were measured, allowed a more meaningful interpretation and comparison of the latter measurement results.

2.2.3.7 Summary of remaining measurements

At the time of writing of this report, two main sets of measurements/characterizations are not yet completed: the shear modulus measurements based upon the torsional SIMORUS configuration and the SEM/EDX characterization of sampled cross-sections. Thus, corresponding results from these two measurement types are not contained in the corresponding results Section (4.1.1).

2.2.4 GRS (Task 2.2)

GRS' experiment program aimed to determine the mechanical strength of low-pH concrete S5 samples depending on the degree of degradation under specific chemical boundary conditions. It was planned to percolate concrete samples with a corrosive solution (Konrad solution) for 3, 6 and 12 months (Part A). The underground salt solution (Konrad) has a pH of 7.9 and consists mainly of sodium and chloride, more details are available in D16.3. Afterwards, samples are removed from the percolation test cells and are installed in the triaxial compression test (Part B). In addition, it was planned to complement GRS' experimental program by performing similar percolation experiments in the GeoPET (Positronen Emission Tomographie) at HZDR. The method is based on the employment of a radioactive tracer in the corrosive solution and enables to visualize the percolation and degradation processes inside the concrete (Part C).

2.2.4.1 Part A: Flow through of corrosive solutions through low-pH concrete

Figure 2-11 shows the schematic set up of the percolation cell used at the GRS lab. The challenge is removing the sample from the percolation cell after percolation without mechanical damage caused by the removing process and installation of this sample in the triaxial test set up. Hence, the sample is cased in a double jacket and the dimensions of the jacket are adapted to the requirements of the triaxial cell. The sample plus double jacket is inserted in the percolation cell and the annular gap between sample and cell is filled with resin. After percolation, the cell, the resin, and the outer jacket shall be cut and the sample with the inner jacket can be installed in the triaxial test set up.

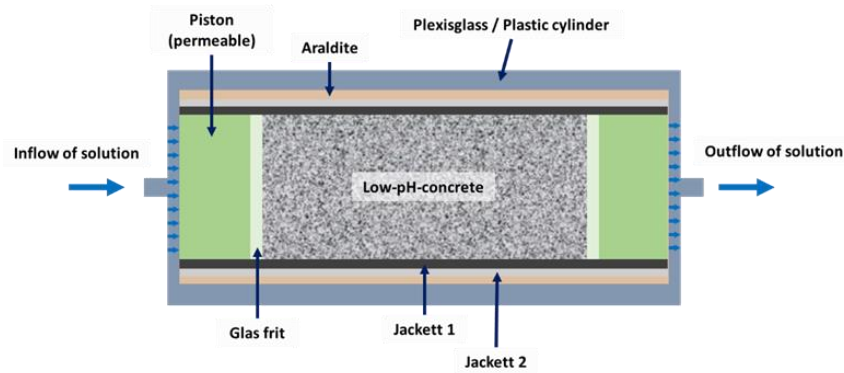


Figure 2-11 Schematic depiction of the percolation cell

The samples are percolated by using a peristaltic pump in combination with an overflow valve. The peristaltic pump generates a constant flow rate of the solution at the inflowing surface of the percolations cells. To ensure a constant injection pressure of the solution, in front of the sample surface an overflow valve, regulated to 0.1 MPa, is installed. The inflowing pressure is monitored by a pressure sensor. At the outflowing surface and behind the overflow valve the outflowing solution is collected and the volume per time is determined. The solution at the outflowing surface, which percolated the sample, will be analysed regarding to its composition. The general test setup is shown in Figure 2-12.

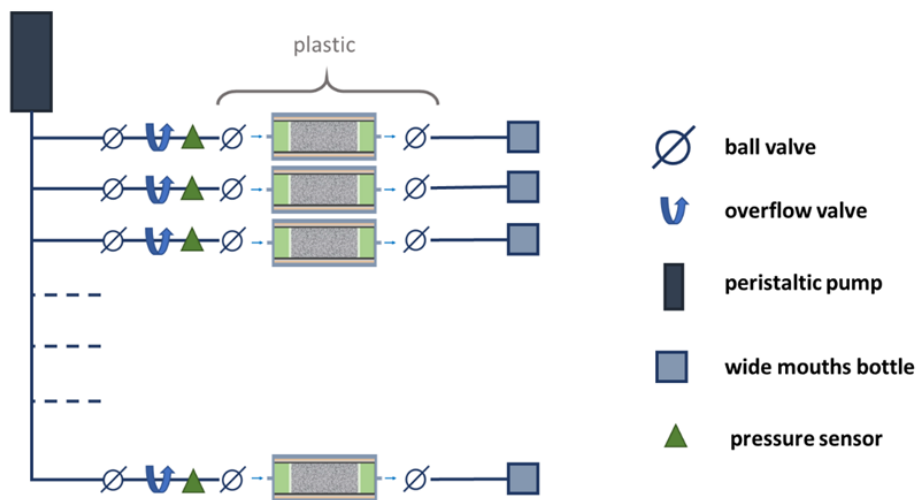


Figure 2-12 Set-up of percolation tests

2.2.4.2 Part B: Determination of material strength dependent on degree of degradation

Triaxial compression (TC) experiments are performed on concrete samples upon terminating the percolation with corrosive solution after about 3, 6, and 12 months. Three samples are accordingly analyzed in one TC experiment series per time step. Cylinders and resin are removed from the samples by means of a turning lathe. Prepared samples are placed in the triaxial cell and subsequently subjected to an isotropic stress state. The adjusted lateral stress of 1, 3, or 5 MPa is kept constant during the shear phase. A strain-rate of 0.25%/min is then adopted to deform the samples in axial direction. Upon reaching an axial strain of 1%, the samples are unloaded until they recover 0.25%. The subsequent strain-controlled reload eventually induces failure. Results can be exploited to derive the Young's modulus, the Poisson's ratio and parameters defining a failure criterion. Variations in those parameters can be directly linked to the degree of degradation.

Part C: Concrete percolation with radioactive tracer and GeoPET (HZDR)

The GeoPET method offers the possibility of the visualisation of transport processes in non-transparent media. Therefore, a solution with a radioactive tracer is induced in the sample. The photon radiation is detected in spatial resolution. From this, the current distribution of the tracer can be calculated. With the data of GeoPET preferred pathways, the effective pore space and diffusion coefficients can be estimated. The general process of sample percolation is comparable with the percolation test described in Part A.

2.2.4.3 The modified set up divides in a THMC- and an HMC-set up.

- THMC-set up

This approach combines the percolation of the concrete with the mechanical load. In addition, the concrete is exposed to increased temperatures corresponding to the expected temperatures at the tunnel lining in the German repository concept. The test methodology is subdivided into two phases: at first a time frame of temperature load under constant, nearly isotropic stress and secondly a deviatoric loading of stress under constant temperature. The thermal phase aims at a pre-treatment of the concrete sample to consider the temperature impact resulting from the heat-generating waste to the concrete lining before concrete is exposed to mechanical load.

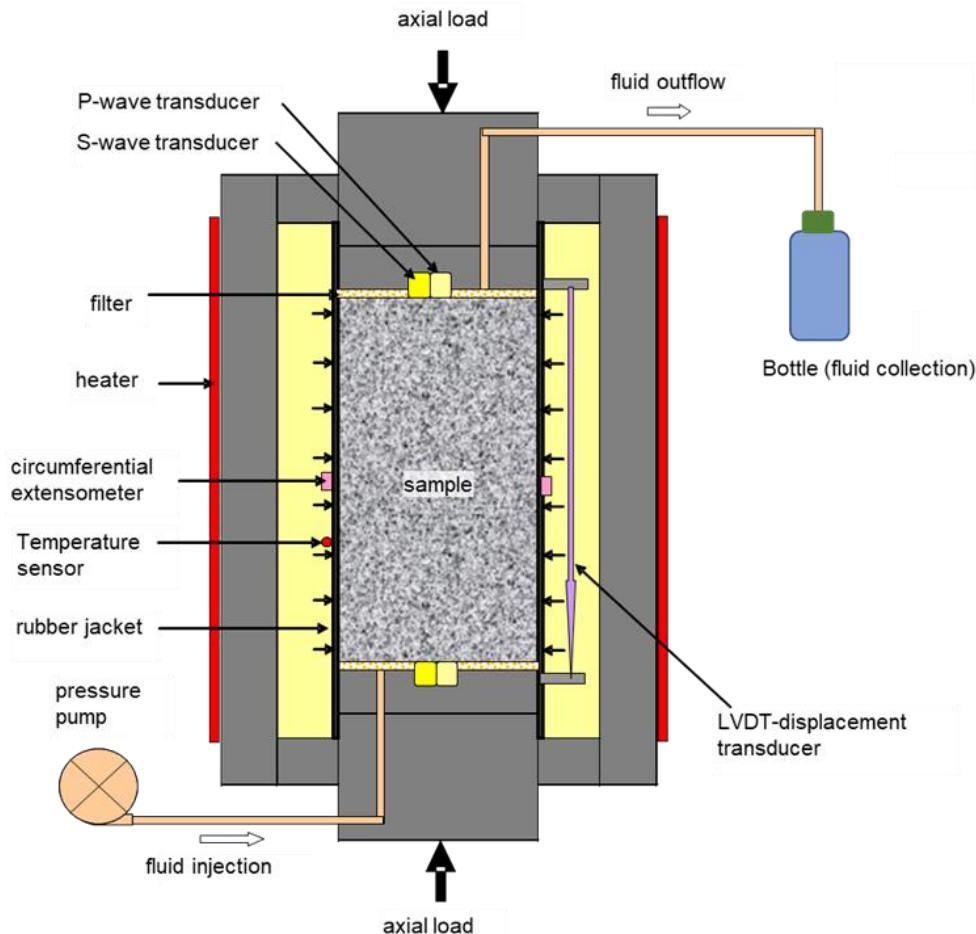


Figure 2-13 Configuration of the triaxial cell with fluid percolation and heater

Table 2-10 Boundary conditions in THMC test set up

| Thermal phase (pre-treatment) | |
|--|---|
| Constant boundary conditions: <ul style="list-style-type: none"> axial / radial stress injection pressure | $\sigma_x = 0,5 \text{ MPa} / \sigma_z = 0,764 \text{ MPa} (6,0 \text{ kN})$ $p_{in} = 0,1 \text{ MPa}$ |
| Variable boundary conditions: <ul style="list-style-type: none"> temperature | Step 1: 35°C (30 days) Step 2: 70°C (30 days) Step 3: 105°C (30 days) |
| Mechanical phase | |
| Constant boundary conditions: <ul style="list-style-type: none"> radial stress injection pressure temperature | $\sigma_x = 5.0 \text{ MPa}$ $p_{in} = 0.5 \text{ MPa}$ $t = 40^\circ\text{C}$ |
| Variable boundary conditions: <ul style="list-style-type: none"> axial stress | Step 1: $\sigma_z = 10 \text{ MPa} \rightarrow 78.54 \text{ kN} (\sigma_{div} = 5 \text{ MPa})$ Step 2: $\sigma_z = 15 \text{ MPa} \rightarrow 117.81 \text{ kN} (\sigma_{div} = 10 \text{ MPa})$ Step 3: $\sigma_z = 18 \text{ MPa} \rightarrow 141.37 \text{ kN} (\sigma_{div} = 13 \text{ MPa})$ |

While an experiment is running, the temperature inside the cell, the axial and radial pressure, the injection pressure of the fluid so as the axial and radial deformations and the inflow rate of the fluid are measured. The configuration of the triaxial cell is showed in Figure 2-13.

- HMC-set up

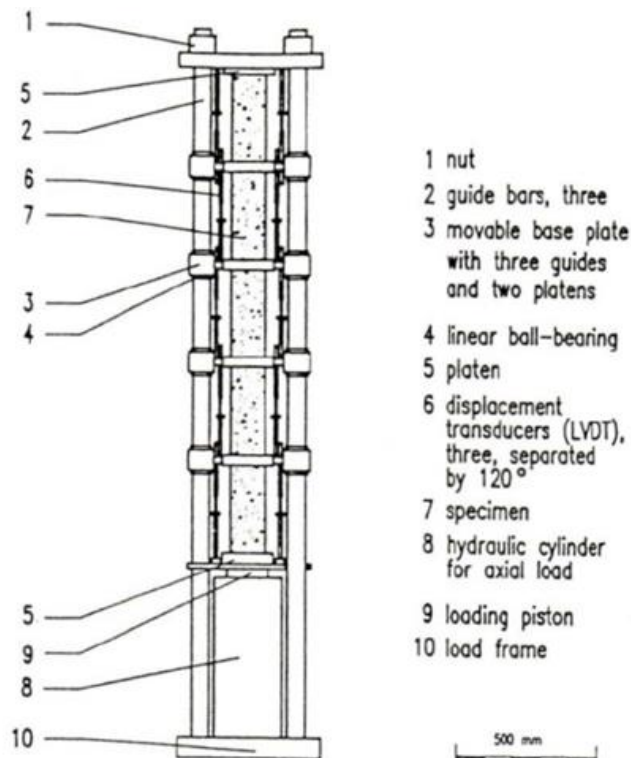


Figure 2-14 Set up of the HMC-test. Five samples can be investigated in parallel.

In this set up, percolation experiments with confining pressure are performed. 5 samples can be investigated in parallel (Figure 2-14). The test aims at the estimation of the hydraulical and chemical impacts to the mechanical strength of the concrete. Therefore, 3 samples will be percolated with Konrad solution and are loaded with an axial and radial pressure and 2 samples are only loaded with axial and radial stress without percolation. Like the former set up of percolation experiments, the samples will be percolated by a peristaltic pump in combination with an overflow valve (see part A for more details). The injection pressure is 0.1 MPa. The stress will be nearly isotropic and constant in the primary test phase. Based on the constant flow rate and the determination of the volume of solution, which leaves the incident flow to the sample by the overflow valve, the volume of solution which enters the sample can be calculated. Complementary, the outflow of solution at the second surface of each sample is determined. At a certain timestep, which needs to be identified by the inflow and outflow of solution to the samples respectively, all samples, including the only mechanical loaded samples, shall be subjected to a deviatoric stress state. The deviatoric stress state after the solution entry intrusion to a part of the samples, aims to investigate the hydraulical and chemical impact on the mechanical strength of the concrete.

However, this test set up was not planned in the beginning of MAGIC and was firstly initiated after the failure of the former set up. Consequently, some materials, especially the special measuring chains, which fit in the annulus, needs to be developed and constructed. Following, the test will primarily start in the end of 2023.

- Protocol modification

Indeed, against earlier test set ups of part A, a pathway between the inner and outer jacket was generated a few days after experimental start. The generation of the pathway between the jackets in this experimental set up may be caused by the high viscosity of the Konrad solution, which is used in combination with the low-pH concrete. In former experiments, highly saline solutions with high viscosities were used, which presumably prevented the generation of a pathway between the jackets. Hence, the test set up of part A needs to be modified for the present materials to ensure a percolation of the sample itself.

The new set up offers the possibility of the combination of thermal, hydraulic, mechanical, and chemical testing in the same set up without removing the sample. In a second set up hydraulical, mechanical, and chemical impacts can be investigated in the same aperture. Following, part B “Determination of material strength dependent on degree of degradation”, is also modified.

2.2.5 COVRA (Task 2.2 and 2.3)

2.2.5.1 Artificial ageing conditions due to salt water and microbial attack on old samples

Additional information of the samples

The Dutch cubical concrete samples have been submerged in synthetic clay pore water as saline as seawater (see Table 6-1 in Deliverable 16.3) since September 2016 at around room temperature. The backfill is a type of cellular concrete. Cement, water, aggregates are mixed with a preformed foam. The purpose of the foam is to supply a relatively high proportion of stable air voids upon curing. The size of the pores of backfill-like specimens is considered sufficiently large to allow microbial activity. The concrete samples made of CEM III/B have a reducing environment for microbes within the samples. This reducing environment becomes lost near the surface of the samples. The samples made with CEM I lack reducing chemical species and have a slightly oxidizing environment for microbes. The buffer-like samples have a too small connecting pore-throats to allow microbial activity.

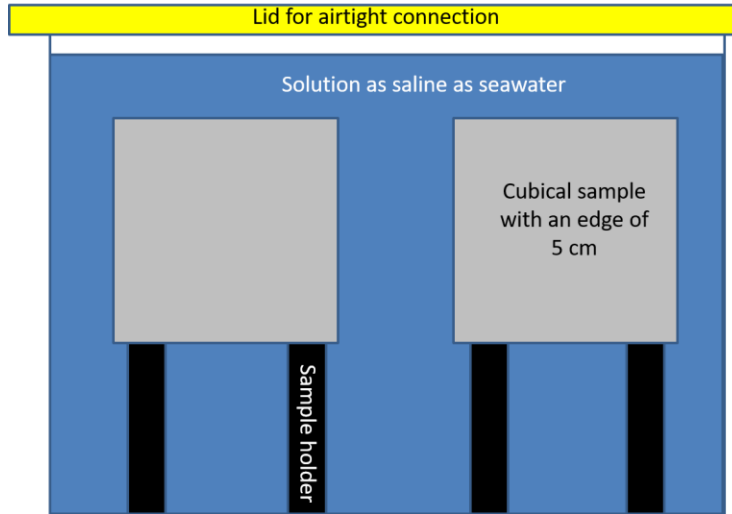


Figure 2-15 Experimental specific for microbial research. The plastic boxes (Araven, 1.5 litre) in which the cylinders and samples have been put are made from polypropylene.

An important manufacturing detail for microbial research was not mentioned in Deliverable 16.3. The moulds for casting cubical specimens are covered with a casting oil (CUGLA, base paraffine, density $0,854 \pm 0,02$ kg/l) before pouring concrete. The application of this oil is necessary in order to be able to remove the concrete after one day hardening. This oil can be a nutrient for microbes. The set-up of the samples for microbial research is shown in Figure 2-15.

Microbial activity was measured in the synthetic clay pore water. Two sets of samples were envisaged to be gamma irradiated in order to make the samples and the pore water sterile. For each type of concrete eight samples were available.

The suggested programme for the microbial part was therefore:

- In the beginning of MAGIC: two samples not gamma-irradiated for destructive analysis, two gamma irradiated samples for destructive analysis;
- At the end of MAGIC: two samples not gamma-irradiated for destructive analysis, two gamma irradiated samples for destructive analysis.

Unfortunately, two samples of each set have become lost by post. It was therefore decided to re-measure the compressive strength of the same samples in the beginning and end of MAGIC. The application of the load on the samples was immediately stopped after the peak strength was achieved. The samples were gamma-irradiated when submerged in synthetic clay pore water as shown in Figure 2-15 till a dose of 57.6 kGy (dose rate 6.4 kGy per hour).

The load rate is kept uniform at about 0.6 MPa/s but can be easily adjusted. Changes in the load rate occur just before the peak strength is achieved so that the operator can start preparing removing the load. COVRA's experience on re-measuring the compressive strength on the same samples after the load has been immediately stopped after achieving the peak strength, is that the re-measured strength can never be as large as the first measured strength, but its re-measured strength can be close to the strength measured initially, see for example section 5.1.2. Re-measured strengths are always between brackets.

After the first measurement of the strength, the irradiated samples have been cleaned with 70% ethyl alcohol to sterilise the samples again. Samples for other analysis have been taken from other samples for example those with an edge of 10 cm (see section 4.2.2.1).

Additional certified buffer-like specimen and its exposure history

An additional buffer-like specimen with an edge of 15 cm and made with CEM III/A has also been mechanically tested, again. CEM III/A is a blend of Portland cement (35-64 wt%) and Blast Furnace Slag (36-65 wt%). This specimen was stored from 1993 until July 2018 in COVRA's waste processing facility. It was one of the mortar cubes from a wall for the working area for the radiation protection unit in this facility. A number of these cubes had been manufactured in October 1993 to check the mechanical strength of the mortar used for the conditioning of waste. The air is controlled in this facility and adjusted to a relative humidity between 45-50% and a temperature of 21°C. In 2018, during the refurbishment of this protection unit, a number of these mortar cubes became superfluous. These cubes had been mechanically tested again more than 25 years later. One of these mechanically tested cubes had no pulverized edges and was saved for further analysis. This cube was put in a separate plastic box without a lid in a larger plastic box from July 2018. That larger plastic box was filled with synthetic clay pore solution that was aimed to be kept at a temperature of 20°C. The heating of the synthetic clay pore solution caused some evaporation of the water. The lid of the larger plastic box minimized the water leaving the plastic box but also caused droplets falling into the plastic box in which the cube manufactured in 1993 was emplaced. This cube was completely destructed in April 2022. Its strength was too large to chisel by hand, the machine to measure the compressive strength was therefore used for its destruction.

The exact recipe used to manufacture the waste package mortar fabricated on 13 July 2016 has been registered but this recipe for 6 October 1993 would take some time since these data are only available on paper. The variation in recipes hardly differ between the different batches and therefore the recipe published in a report (Roovers, 1994) has been included in Table 2-11.

Table 2-11 Recipe for additional buffer-like sample

| Component | Type casted 6 October 1993 | kg.m⁻³ |
|------------------|-----------------------------------|--------------------------|
| Cement | CEM III/A | ≈ 410 |
| Dutch tap water | | ≈ 176 |
| Superplasticiser | OFT-2 84/39 Tillmann | ≈ 3 |
| Fine aggregate | Sand: 0-4 mm | ≈ 858 |
| Coarse aggregate | Gravel: 2-8 mm | ≈ 930 |

The measured strength of the cube with the recipe in Table 2-11 after exposure for 25 years to the dry environment of the waste processing facility was 81 N/mm². A strength of 76.8 N/mm² was measured 3.5 years later after exposure to the more humid environment supporting COVRA's experience that the initially measured strength can never exceed the second one. The strength measured for a second time, is large.

2.2.6 SCK CEN (Task 2.2 and 2.3)

2.2.6.1 Overview of unchanged experimental protocol and method

SCK CEN used the same experimental protocol described in D 16.3 (Figure 2-16). They performed batch/percolation experiments to mimic the Belgian disposal conditions. These experiments concern pastes

(task 3) and mortars (task 2).



Figure 2-16 Test setups for batch (left) and percolation (right) experiment

In the case of percolation tests, a difference of 3 bar is applied to the sample and a solution having a composition representative of the Boom clay pore water injected (use of Boom Clay plugs). For batch type experiments a backfill material disc was immersed into a Boom clay slurry. For both types of experiment, 0.4% CO₂ was bubbled into the chambers to reproduce the in-situ CO₂ concentration.

2.2.6.2 Characterization of microstructure and mineralogy – aged interface

- Quantitative porosity mapping

To obtain spatialized quantitative porosity maps, autoradiography was employed using the technique developed by Pret (2003) specifically for clay materials. The process involved subjecting the sample to a 7-day oven-drying period at 70°C under vacuum conditions. Subsequently, the sample was impregnated through diffusion for 60 days with ¹⁴C Methylmethacrylate (MMA) containing a tracer activity of 10 µCi/mL. Polymerization was initiated through gamma irradiation, with a total dose of 120 kGy.

- Quantitative chemical maps

Quantitative X-ray intensity maps and a backscattered electron (BSE) image were acquired using a Cameca SX Five electron probe microanalysis (EPMA) instrument equipped with five wavelength dispersive spectrometers (WDS), operating at 15 keV and 30 nA. These maps were aimed at investigating the distribution of the nine major elements present in the concrete (Si, Ca, Al, Mg, Fe, Na, K, S, Cl). A standard based PHIRHOZ matrix correction method (Merlet, 1994) was subsequently applied to determine the weight percentage for each element per pixel. The elemental maps, consisting of 512 by 512 pixels, were recorded using stage mastering with a stationary beam, offering a spatial resolution of 2 µm per pixel.

- Quantitative mineral maps

Mineralogical maps were generated to illustrate the spatial distribution of minerals across a 1 x 1 mm² surface area, with a resolution of 2 µm, following the methodology established by Gaboreau et al. (2017) and utilizing the µMAPphase software (Pret et al., 2010). This approach involves the identification of mineral phases within the analyzed area through step-by-step projections of the elemental composition points, converting them into ternary plots that allow visualization of the varying chemical compositions of all minerals and phases.

- Backscattered electron microscopy

All images were acquired using a Zeiss Neon40 ESB dual-beam microscope coupled with a Focused Ion Beam (FIB) column. Backscattered electron images (BSE) were captured at a low accelerating voltage of 1.5 kV to achieve an electron probe size of 5 nm.

2.2.6.3 Microbial analysis of batch and percolation experiments

To obtain abiotic controls, half of the mortar samples were irradiated at SCK CEN for 9 hours with a dose rate of 6.4 kGy/h corresponding to a total dose of 57.6 kGy. In addition, the Boom Clay pore water used in the abiotic conditions was filter sterilized and autoclaved. In order to estimate microbial presence and activity in the experiments, analyses were performed on obtained water samples.

To analyse the microbial community present at the interface between Boom Clay and concrete from the HADES URF, a concrete core was investigated. In detail, the remainder of the clay that was present on the concrete core was collected, diluted 10 times in PBS and horizontally mixed for 1h. Afterwards, 2 swabs were taken from the concrete surface and further analysed. All preparations were carried out in an anaerobic glovebox.

The following microbial analysis were carried out:

- Flow Cytometry (total cell count)
- Intracellular ATP measurement (estimate of microbial activity)
- Cultivation in different conditions

These techniques were selected as standard techniques such as measuring the optical density are not suitable for these samples as the detection limit of those techniques is too high. To be as accurate as possible a combination of different techniques was carried out.

In addition, small pieces of the concrete core were collected and were used to perform SEM analysis and DNA extraction.

Details on the used techniques are presented in section 2.2.8.

2.2.7 SURAO, CTU, TUL, UJV, CVREZ (Task 2.2 and 2.3)

The ageing concept in three environments in URF Bukov

In the experimental programme of the Czech partners, the influence of three experimental environments on LPC SURAO material were tested and studied: *In-situ* air environment, *in-situ* groundwater environment and BCV bentonite suspension environment (in experimental boxes placed into in-situ conditions). All three types of experiments were located at the Bukov URF (Underground Research Facility) at the 12th underground floor at a depth of approximately -500 m below surface. Four experimental boxes were connected to borehole S25, which served as source of natural groundwater, four boxes were filled with BCV bentonite suspension, and four boxes were opened covered with a protecting net to avoid large impurities to interfere with the samples and keep samples in contact with the *in-situ* air ventilation (Figure 2-17 and Figure 2-18). The air environment represents an ordinary condition of the underground environment of the former uranium mine. Very high humidity, depending on ventilation and affected by season of the year, is typical for this environment with temperatures close to 15 °C.

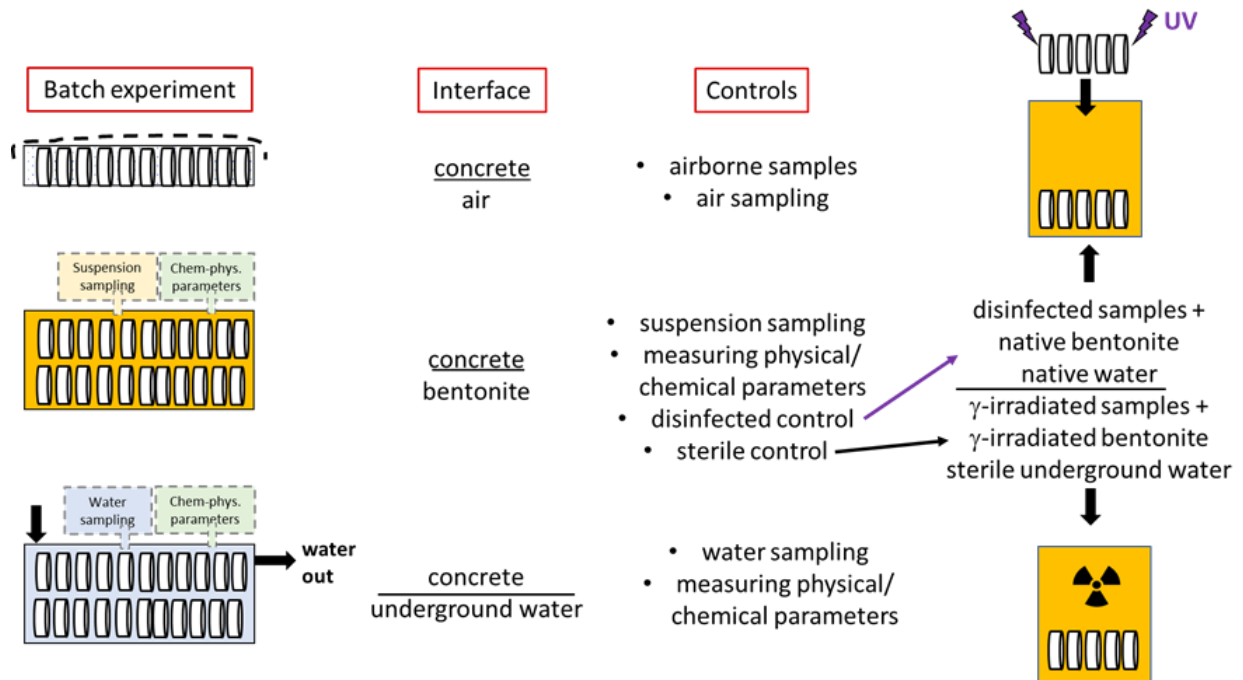


Figure 2-17 A schematic representation of the batch experiment set up.

Second, interface of concrete and groundwater was set up as an open system with water continuously flowing from the source (borehole S25) into four experimental boxes. As such it simulates the underground conditions realistically and avoids spoiling the water by insufficient circulation leading to robust outgrowth of fermentative species.



Figure 2-18 A) Preparation of the in-situ experiment at URF Bukov. B) Arrangement of the experimental setups for studying interactions of LPC samples under in-situ conditions (air, groundwater, bentonite suspension)

Third, the interface of concrete and bentonite suspension was set up into closed boxes. The bentonite suspension was prepared one week before setting up the in-situ experiment. The barrel of prepared bentonite suspension was profoundly mixed using a manual mortar-mixer with sterilized whisk extender and transferred into clean boxes with concrete discs in holders to avoid their mutual contact (Figure 2-20).

Finally, there were two smaller batches of irradiated and UV-treated controls prepared as controls for microbiological analyses. The conditions of irradiated concrete discs and bentonite powder were chosen in accordance with the previous results (Černá et al., 2023) and details are given in Table 2-12. Alternatively, to distinguish between microbial activity on surface or inside the samples, 5 SURAO LPC discs were treated with UV light for 6 hours from each side to ensure the proper disinfection of the surface. These samples were exposed to native bentonite suspension for a given time (18 months) and stored at URF Bukov.

Table 2-12 Conditions for gamma-irradiation used for preparation of the negative control with a limit of total dose of 40-100 kGy according to Černá et al. (2023).

| | |
|--------------------------|---------------|
| Material | discs and BCV |
| γ-irradiation supply | Co-60 |
| Date | 3.-6.12.2021 |
| Dose/discs | 19.55 Gy/min |
| Dose/BCV | 14.62 Gy/min |
| Exposure time | 3996.4 min |
| Total dose/discs | 78.14 kGy |
| Total dose/BCV | 58.44 kGy |
| Insecurity of dose (k=2) | ±5 % |
| Temperature | 22 ± 1.5 °C |

Prior and during the MAGIC experiments the geochemical parameters of S25 groundwater were studied. Both physical and chemical parameters, and results from chemical analyses are listed in Table 2-13 and Table 2-14, respectively.

Table 2-13 Physical-chemical parameters of source S25 groundwater prior and during experiments

| experimental time | date | temperature (°C) | pH | conductivity (μS/cm) | dissolved O ₂ (mg/l) | ORP (mV) |
|-------------------|------------|------------------|-------|----------------------|---------------------------------|----------|
| - | 20.12.2022 | 13.3 | 9.82 | 336 | 9.5 | -126 |
| - | 05.01.2022 | 14.1 | 9.50 | 372 | 9.0 | -110 |
| - | 08.03.2022 | 14.0 | 10.00 | 370 | 3.9 | -80 |
| 0 | 16.03.2022 | 13.4 | 9.61 | 351 | 0.1 | -330 |
| - | 14.06.2022 | 14.1 | 8.23 | 331 | 6.0 | -90 |
| 0.5 year | 04.10.2023 | 14.0 | 9.53 | 353 | 8.0 | -80 |
| 1 year | 28.03.2023 | 13.5 | 9.53 | 347 | 6.5 | -35 |
| 1.5 year | 19.09.2023 | 13.9 | 9.53 | 336 | 7.2 | -50 |

Table 2-14 Chemical composition of source S25 groundwater prior and during experiments (mg/l)

| time | date | Cl ⁻ | SO ₄ ²⁻ | SiO ₃ ²⁻ | HCO ₃ ⁻ | CO ₃ ²⁻ | NO ₃ ⁻ | F ⁻ | PO ₄ ³⁻ |
|------|------------|-----------------|-------------------------------|--------------------------------|-------------------------------|-------------------------------|------------------------------|----------------|-------------------------------|
| - | 20.12.2021 | 15.8 | 33.8 | 28.0 | 74.5 | 19.4 | --- | --- | --- |
| - | 05.01.2022 | 20.4 | 45.5 | 21.0 | 89.0 | 14.0 | --- | --- | --- |
| - | 13.01.2022 | 20.4 | 44.7 | 22.3 | 104 | 8.16 | < 2.0 | --- | --- |
| 0 | 08.03.2022 | 20.0 | 42.7 | 24.0 | 72.0 | 19.9 | < 2.0 | 0.403 | < 0.04 |

| - | 16.03.2022 | 19.2 | 40.8 | 22.8 | 76.2 | 16.2 | < 2.0 | --- | --- | | |
|----------|------------|------|-------|--------|------|--------|--------|---------|--------|------------------------------|------|
| 0.5 year | 04.10.2023 | 18.9 | 40.7 | 23.5 | 81.3 | 15.6 | < 2.0 | 0.421 | < 0.04 | | |
| 1 year | 28.03.2023 | 18.9 | 40.6 | 21.6 | 88.0 | 12.0 | < 2.0 | 0.42 | < 0.04 | | |
| 1.5 year | 19.09.2023 | 18.8 | 41.4 | 21.3 | 86.4 | 12.3 | < 2.0 | 0.426 | < 0.04 | | |
| time | date | Na | K | Mg | Ca | Fe | Al | Mn | Sr | NH ₄ ⁺ | TOC |
| - | 20.12.2021 | 82.3 | 0.657 | 0.0476 | 1.94 | 0.0653 | 0.0514 | 0.0011 | 0.0234 | --- | 1.01 |
| - | 05.01.2022 | 56.6 | 0.702 | 0.215 | 1.57 | 0.434 | 0.345 | --- | --- | --- | 1.89 |
| - | 13.01.2022 | 72.2 | 0.744 | 0.0566 | 1.96 | 0.0278 | 0.0522 | --- | 0.0279 | --- | 0.92 |
| 0 | 08.03.2022 | 76.5 | 0.663 | 0.0665 | 1.83 | 0.111 | 0.0967 | 0.0018 | 0.0248 | < 0.05 | 0.72 |
| - | 16.03.2022 | 74.8 | 0.685 | 0.0561 | 1.58 | 0.082 | 0.0213 | <0.0005 | --- | --- | 1.16 |
| 0.5 year | 04.10.2023 | 69.6 | 0.673 | 0.0274 | 1.66 | 0.0025 | <0.01 | <0.0005 | 0.025 | < 0.05 | 1.31 |
| 1 year | 28.03.2023 | 69.5 | 0.622 | 0.0231 | 1.64 | <0.002 | 0.0104 | <0.0005 | 0.026 | < 0.05 | 0.98 |
| 1.5 year | 19.09.2023 | 71.2 | 0.631 | 0.0278 | 1.6 | <0.002 | 0.0096 | <0.0005 | 0.0245 | 0.079 | 0.92 |

The bentonite suspension was prepared in laboratory from S25 groundwater and Czech BCV bentonite at the S/L ratio = 1/2 kg/l. The bulk mineralogical composition of the BCV bentonite is shown in Table 2-15. Moreover, BCV bentonite is rich in amorphous phases, the content of which can be as high as 10 wt.% (Villar et al., 2020). The chemical composition of suspension porewater obtained by centrifugation is shown in Table 2-16.

Table 2-15 BCV bentonite – the semiquantitative XRD analysis of randomly oriented powder mounts (wt. %); bql – below quantification limit, nd – not detected.

| | |
|--------------|-----|
| Smectite | 72 |
| Quartz | 10 |
| Kaolinite-1A | 6 |
| Illite-2M1 | 2 |
| Sanidine | 2 |
| Goethite | 3 |
| Anatase | 2 |
| Calcite | 1 |
| Aragonite | 1 |
| Siderite | 1 |
| Ankerite | bql |
| Augite | nd |
| Analcime | nd |
| Total | 100 |

Table 2-16 Chemical composition of BCV bentonite suspension porewater obtained by centrifugation (mg/l)

| Cl ⁻ | SO ₄ ²⁻ | SiO ₃ ²⁻ | HCO ₃ ⁻ | CO ₃ ²⁻ | NO ₃ ⁻ | Na | K | Mg | Ca | Fe | Al | Sr | TOC |
|-----------------|-------------------------------|--------------------------------|-------------------------------|-------------------------------|------------------------------|-----|------|------|------|--------|--------|--------|------|
| 32.2 | 154 | 13.7 | 344 | 4.32 | <2.0 | 162 | 13.7 | 16.9 | 9.75 | 0.0468 | 0.0624 | 0.0895 | 5.35 |

The punch test

The punch tests are carried out on specimens 8 mm thick and 50 mm diameter by pressing with punches in the middle of the discs. During compression with the punch, the entire volume of the specimen is thus loaded gradually in four steps until failure (loading to 2 kN; 4 kN; 4 kN; over 4 kN; i.e. 1/3; 2/3; 2/3; max load capacity). The result is also influenced by micro/macro cracks, pores and aggregates. During the test, the displacement of the punch is recorded. Load at break (N) and rigidity k (N/mm) is evaluated; four loading phases (and three unloading to 200 N) provide values of rigidity k_2 , k_{4-1} , k_{4-2} , k_{4+} . In fact, k is derived from the sections of 35-80% of loading maximum; at least above 700 N due to technical reasons (Figure 2-19).

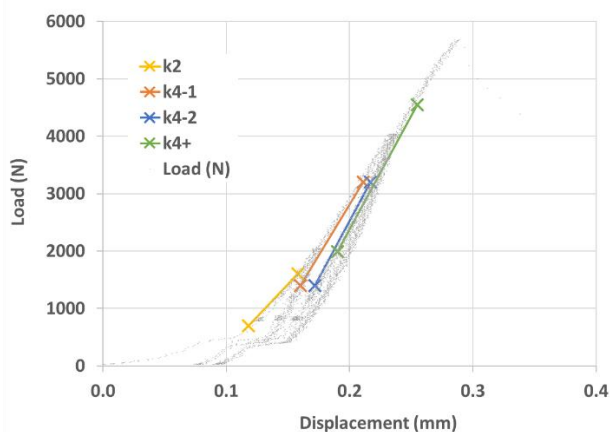


Figure 2-19 Example of the punch test record and rigidity determination

SEM, XRD

The LPC_SURAO samples were examined in their respective environments, both on the surface and in the cross-sectional areas of the samples. This examination was performed using a LYRA3 scanning electron microscope from Tescan in the Czech Republic. Additionally, Energy dispersive X-ray spectroscopy (EDS) was used to determine the local chemical composition of the LPC samples. Before SEM measurement, a thin layer of gold was applied to the samples.

In the case of XRD measurements, the method used for each sampling campaign was X-Ray Powder Diffraction and Grazing Incidence X-Ray Diffraction (angle of 0.5° and 2θ scan mode). The measurements were performed using an Empyrean 3rd generation diffractometer (Malvern-PANalytical). The identification of crystalline phases was performed using the High Score Plus software (PANalytical) that includes the PDF-4+ database.

Sample processing for microbiological analyses

First, SURAO LPC samples exposed to air and water environments were swabbed to collect the biofilm and water samples (source, underground water at input and output) were collected directly at URF Bukov, Samples exposed to bentonite suspension were taken into the laboratory and processed under controlled sterile conditions using laminar flow box and sterile equipment as illustrated in the Figure 2-20 C. Second, the intact LPC samples were exposed to UV treatment administered for 2 hours and 20 minutes to each site of the concrete disk. We proved that this time of surface disinfection was sufficient (Figure 2-20 B). Such

treated samples were consequently manually and aseptically broken and crushed to obtain powder. This material was used for cultivations and for isolation of DNA (Figure 2-20 A).

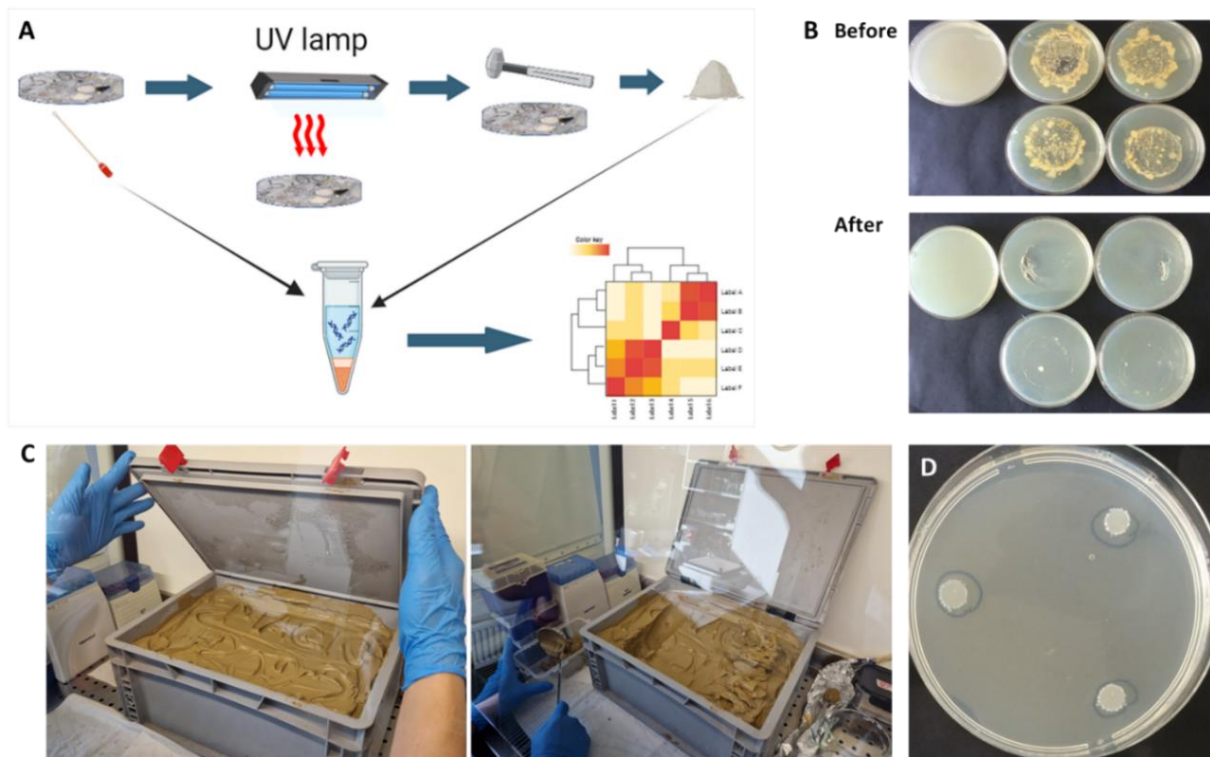


Figure 2-20 A) A scheme of the SURAO LPC sample processing workflow. B) Effect of UV treatment on intact SURAO LPC samples. C) Sample processing of samples exposed to bentonite suspension. D) Test of microbial calcium precipitation

The powder was incubated in PBS (Phosphate Buffer Saline, pH 7.4) in ratio 1:10 for 24 hours at 30 °C and this suspension was used as an inoculum for solid media plates. Three types of media differing in amount of organic matter to cultivate heterotrophic bacteria specific for the concrete environment (Soya casein digest agar, nutrient agar and R2A agar) were used. To isolate and cultivate fungi, three media (Potato Carrot Agar (PCA), Malt-Extracting Agar (MEA) and Soil agar with rose Bengal (SEGA)) were used. The addition of antimicrobial compounds (tetracycline, chloramphenicol, streptomycin sulphate) was used to avoid bacterial growth and enabled to obtain pure fungal cultures.

To check the ability of microbial calcium precipitation (MCP), the urease (EC 3.5.1.5) activity of isolated clones was determined. Bacterial clones were plated on Christensen agar (Peptone 1 g, Dextrose 1 g, Sodium chloride 5 g, Potassium phosphate monobasic 2 g, Urea 20 g, Cresoll red 0.012 g, Agar 15 g) and incubated for 7 to 14 days in 37 °C. The urea served as a substrate degraded by bacteria to ammonia. Increase in concentration of ammonia leading to increase of pH resulted in a colour change of the pH indicator to pink-red colour. Positive urease-expressing strains were selected and subjected to test calcium precipitation ability. To that aim, nutrient agar plates supplemented with 5 mM CaCl₂ were prepared, inoculated with bacterial spots and incubated overnight. Positive evaluation was based on the formation of the nucleation sites of calcium precipitates visible around the colonies (Figure 2-20 D). The urease positive clone was assessed in pH tolerance. In this experiment, 120 µL of nutrient broth with a pH ranging from 9.5 to 12.5 was inoculated with 80 µL of the urease positive clone. The plate was measured OD at 600 nm in spectrometer every 30 minutes of an overnight incubation at 37°C.

Those three types of samples - swabs, water, and LPC powder – were used to obtain genetic material representing surface biomass, water biomass, and inner concrete biomass, respectively. DNA was isolated using commercially available kits for DNA extraction from water and swabs (DNeasy PowerWater Kit, Qiagen, USA). DNA extraction from concrete samples is the most critical point to ensure good-quality data for sequencing, because the high pH of crushed concrete and the DNA uptake by concrete negatively affect the efficiency of extraction. Different DNA extraction approaches including chloroform extraction method and commercially available DNA extraction kit for soil samples - DNeasy PowerMax Soil Kit (Qiagen, USA) were applied on the processed samples after 6 months of incubation. 2.5 g of SURAO LPC powder was consistently used for each DNA extraction and each sample was extracted from three different SURAO LPC discs. Chloroform extraction was performed with some modifications as described earlier (Cattaneo et al., 1995; Maresca et al., 2016). DNeasy PowerMax Soil Kit extraction was performed according to manufacturer protocol and the obtained eluate was concentrated and cleaned using DNA clean & Concentrator TM-25 kit (Zymo Research, USA). DNA concentration was determined using a Qubit® 2.0 Fluorometer (Thermo Fischer Scientific, USA). Comparable results from quantitative PCR (qPCR) for concrete samples from bentonite and water environment were observed using both approaches proving sufficient amplification of extracted DNA. Hence, DNeasy PowerMax Soil Kit was chosen for extraction of DNA from SURAO LPC samples mainly because of easier handling and replicability.

Extracted DNA was used for molecular-genetic analyses including qPCR and sequencing; methods are described in D16.3. Primers used to determine the quantity of bacteria are described in D16.3. Preparation of sequencing library was performed in house using 515F (3'-TGCCAGCMGCNGCGG-5') and 802R (3'-TACNVGGGTATCTAATCC-5") primers for amplification of V4 region of 16S rRNA gene (Claesson et al., 2010; Dowd et al., 2008) or ITS3-F (3'-GCATCGATGAAGAACGCAGC-5') and ITS4-R (3'- TCCTCCGCTTATTGATATGC-5') primers (White et al., 1990) to detect bacteria and fungi, respectively. Library was sequenced on Genexus™ platform (Thermo Fischer Scientific, USA) using commercially available kits. Viability of the bentonite community was verified using epi-fluorescent microscopy as described earlier (Hlavackova et al., 2023).

2.2.8 SCK-CEN, COVRA and FZJ (task 2.3)

2.2.8.1 Experimental design of microbial analysis on aged concrete and mortar in contact with poorly indurated clay simulants

At the start of the MAGIC project, the water and concrete surface were analysed of 8 1.5 L boxes containing 2 concrete cubes each supported by a cylinder with a high resistance against degradation in salt and alkaline environments. Afterwards, 4 boxes were sterilized by γ -irradiation (6.4 kGy per hour for 9 hours: 57.6 kGy). Finally, at the end of the project, we analysed the water and concrete surfaces of the remaining 4 boxes. In addition, analysis was performed on water originating from large boxes containing multiple specimens of certified or blend cement, tap water and sand used for preparing the concrete cubes.

For the analysis of the water samples, 5 mL of each was taken from each sample for microbial analysis. Prior to this, the water was mixed as thoroughly as possible to make sure homogeneity was obtained. For analysis of the concrete surface, swabs were taken from each side of the concrete cubes (QUANTISWAB, VWR, Belgium). The microbial community of the sand was studied by adding 9 mL phosphate buffered saline (PBS) to 1 g of sand and stirring the mixture for 30 min.

To estimate microbial presence and activity in the water surrounding the concrete cubes, the following microbial analyses were performed:

- Flow Cytometry (total cell count)
- Intracellular ATP measurement (estimate of microbial activity)
- Cultivation in different conditions

These techniques were selected as standard techniques since measuring the optical density are not suitable for these samples as the detection limit of those techniques is too high. To be as accurate as possible a combination of different techniques was carried out.

In addition, the complete bacterial community was identified through amplicon sequencing based on the 16S rRNA amplicon.

2.2.8.2 Flow Cytometry

Flow cytometry was used to count the total amount of microbial cells present in the water. Total cell count is based on SYBR® Green I, which has a strong affinity for dsDNA but also a low affinity for ssDNA and RNA and enters and stains all cells with nucleic acids independent of membrane integrity. To this end, samples were diluted in filter sterilized (0,22 μ m) Evian potable water and stained with SYBR® Green I (10 000 x concentrate in 0.22 μ m filtered dimethyl sulfoxide) (ThermoFisher Scientific, Belgium) (final concentration of 1x concentrate). All samples including filter sterilized samples as control samples were stained and incubated in the dark for 20 min at 37 ° C. Flow cytometry was performed using a NovoCyte Quanteon Flow Cytometer (BioSPX, Belgium), which was equipped with two scatter detectors, four lasers (405/488/561/637 nm) and 25 fluorescence channels. Samples were analysed in a fixed volume mode of 100 μ l and the minimal threshold was fixed on the green fluorescence (FL1-H at a relative intensity of 1000). Flow cytometry data were analyzed with the NovoExpress software.

2.2.8.3 ATP analyses

The metabolic activity as intracellular ATP was measured with the Microbial ATP Kit HS of Biothema (Isogen Life Science, The Netherlands (Lundin 2000)). This kit makes use of an internal standard to exclude any bias due to sample heterogeneity. In addition, filter sterilized samples were included to have a representative negative control sample. In a first step, extracellular ATP (e.g. from dead cells) is neutralized by adding 50 μ l of sample to an equal amount of ATP eliminating reagent for 10 min. Next, 50 μ l of a cell lysis solution was added that inactivates the ATP eliminating reagent and releases the ATP of the viable cells. Afterwards, the total volume was mixed with 400 μ l of ATP reagent HS (containing D-luciferin). Immediately, light intensity (I_{smp}) was measured with a Lumitester C-100 (Kikkoman). Then, 10 μ l of 100 nmol L⁻¹ ATP standard was added and light intensity was measured again ($I_{smp+std}$). The amount of ATP (pmol) in a sample was calculated as the ratio of I_{smp} to the difference between $I_{smp+std}$ and I_{smp} . If the difference between $I_{smp+std}$ and I_{smp} was not 10 times higher than the I_{smp} value, samples were diluted and analyzed again, to stay below the upper detection limit.

2.2.8.4 Cultivation

To further confirm the presence of viable cells, 100 μ l of each water sample was spread on R2A agar medium. This medium is typically used to monitor heterotrophic bacterial populations present in water samples (Reasoner and Geldreich 1985). Samples were incubated at 30°C in aerobic conditions for 1 week. Colonies with phenotypical differences were purified by dissolving them in MgSO₄ (10 mM) and spreading them on R2A agar plates. Plates were incubated at 30°C for 3 days. Purified colonies were identified based on the 16S rRNA gene. To this end, a single colony was dissolved in the PrepMan™ Ultra Sample Preparation Reagent (ThermoFisher Scientific, Belgium) and treated according to the manufacturer's procedure. The 16S rDNA amplicon was generated by performing a PCR reaction in which the reaction mixture contained 5 μ l sample, primers 8F (5'- AGAGTTTGATCCTGGCTCAG-3') and 1492R (5'- TACGGTTACCTTGTTACGACTT-3') and Phusion High-Fidelity Polymerase (ThermoFisher Scientific, Belgium). PCR conditions were the following: 2 min at 94°C followed by 30 cycles of 30 s at 94°C, 30 s at 56°C and 2 min at 72°C, followed by a final extension of 2 min at 72°C. The obtained PCR product was subjected to Sanger Sequencing (Eurofins Genomics, Germany). Taxonomy of the obtained sequences

was obtained with the command “assignTaxonomy” in the R package DADA2 with the Silva taxonomic training dataset (version 132) as a reference (Callahan *et al.* 2016).

To screen for sulphate reducing bacteria (SRB) in the water, samples were 10 times diluted in liquid Postgate medium (Postgate 1979). This medium is optimized to grow SRB and is composed of the following components: K₂HPO₄ 0.5 g, NH₄Cl 1.0 g, Na₂SO₄ 1.0 g, CaCl₂•2H₂O 0.1 g, MgSO₄•7H₂O 2.0 g, Na-DL-lactate 2.0 g, Yeast extract 1.0 g, Resazurin 1.0 mg, distilled water 980.0 ml (Solution A); FeSO₄•7H₂O 0.5 g, distilled water 10.0 ml (Solution B); Na-thioglycolate 0.1 g, Ascorbic acid 0.1 g, distilled water 10 ml (Solution C). Solution A is boiled for a few minutes, then cooled down to room temperature while gassing with oxygen-free N₂ gas. Solutions B and C are added, the pH is adjusted to pH 7.8 with NaOH, transferred to the glove box and distributed in anaerobic tubes. During distribution the medium is continuously swirled to keep the grey precipitate suspended. Finally, the tubes are autoclaved for 15 min at 121°C. Samples were incubated at 30°C for 4 weeks.

2.2.8.5 DNA extraction

To extract the total DNA from the water samples, microorganisms were collected on a 0.22 µm filter membrane through filtration of 25 ml of water from the small boxes, the remainder of the fluid from the swap or x ml of the tap water or water from the large boxes. Afterwards, the filter was washed with 50 ml of a sterile phosphate buffered saline (PBS) solution. DNA was extracted following the procedure of Povedano-Priego *et al.* (2021) but with some modifications. More in detail, the filter membranes were placed in a Lysis matrix E tubes (MP Biomedicals, The Netherlands) and then the phosphate and lysis buffers were added for chemical lysis and lysozyme and proteinase as enzymatic lysis. Then, mechanical lysis was performed using a TissueLyser II (Qiagen, Belgium) for 10 min at 30 Hz. To all samples, one volume of phenol:chloroform:isoamylalcohol (25:24:1 v/v) was added and the tubes were mixed gently by inverting the tubes. After centrifugation at 1500 g for 10 min at 4°C, the upper (aqueous) phase was transferred to a new tube and washed by adding one volume of chloroform:isoamylalcohol (1:1 v/v). Tubes were again centrifuged at 1500 g for 10 min at 4°C and the supernatant was transferred to a new tube. Afterwards, DNA was precipitated by adding 1 volume of 75 % isopropanol and 1/10 volume of 3 M sodium acetate (pH 5.3) and overnight incubation at -20°C. Afterwards, the sample was centrifuged 30 min at 5000 g at 4°C, the pellet was washed with 5 ml of an 80 % ice-cold ethanol solution (stored at -20°C) and centrifuged for 5 min at 10000 g. The supernatant was discarded and the pellet was dried overnight at 30°C. Finally, all DNA pellets obtained for 1 replicate were pooled and dissolved in 500 µl milli-Q water. Subsequently, the sample was applied on a 100 kDa amicon filter unit (Merck, Belgium) and centrifuged for 10 min at 14000 g. The pellet was washed twice with 500 µl milli-Q water. Finally, the pellet was eluted by centrifugation for 2 min at 1 500 g. DNA concentration was measured with the Quantifluor dsDNA sample kit (Promega, the Netherlands).

The method was also used to try to extract DNA from 0.5 g sand. However, this was too little so no DNA could be extracted. Therefore, DNA extraction from the sand was carried out from 10 g sand using the DNeasy® PowerMax® Soil Kit (Qiagen, Belgium) with some minor modifications. In brief, 15 ml PowerBead solution was added to the sand and the sample was vortexed during 1 min. After addition of the lysis solution, samples were vortexed at maximum speed for 10 min and placed in a water bath at 65°C for 30 min. In addition, samples were homogenized by vortexing the tubes 10 min at maximum speed with a Vortex adapter cat 13000-V1 (Qiagen, the Netherlands). Then, we followed the recommended protocol. Purified DNA was eluted in 2.3 ml of the provided elution buffer (10 mM Tris). Nucleic acids were precipitated using 4 µl/ml Genelute-LPA (25 mg/ml; Sigma-Aldrich, Belgium), 0.1 volumes of 5 M NaCl, 1 volume of isopropanol, gently mixed by inverting the tubes and stored at -20°C overnight. Precipitated DNA was pelleted by centrifugation at 13 000 g for 30 min at 4°C and then washed with 80% ice-cold ethanol (stored at -20°C). Finally, pellets were air-dried in a laminar flow for 15 min and suspended in 125 µl of elution buffer

(10 mM Tris). DNA concentration was measured with the Quantifluor dsDNA sample kit (Promega, the Netherlands).

2.2.8.6 Identification of the bacterial community

To identify the bacterial community, high-throughput amplicon sequencing of the V3– V4 hypervariable region of the 16S rRNA gene was performed. To this end, DNA was amplified with primers 341F (5'-CCTACGGGNGGCWGCAG-3') and 785R (5'-GGACTACHVGGGTATCTAATCC-3') containing Illumina adapter sequences 5'-ACACTCTTCCCTACACGACGCTCTTCCGATCT-3' and 5'-GACTGGAGTTCAGACGTGTGCTCTTCCGATCT-3', respectively. PCR conditions were the following: 2 min at 98°C followed by 30 cycles of 30 s at 98°C, 30 s at 62°C and 1 min at 72°C and a final extension of 5 min at 72°C. The amplified products were visualized with gel electrophoresis and purified with the Wizard® SV Gel and PCR Clean-Up System (Promega, Netherlands) according to the manufacturer's procedure. Purified products were sent to Eurofins Genomics (Germany), where they were sequenced with the Illumina MiSeq platform according to the manufacturer's guidelines.

First, primers were removed using cutadapt (Martin 2011). Subsequently, raw reads were processed according to the DADA2 pipeline with recommended settings (Callahan et al. 2016). Briefly, reads with ambiguous, poor-quality bases and more than two expected errors were discarded. The paired reads were merged, chimeras were identified and removed. Only amplicon sequence variants (ASV) with more than two reads were retained. Taxonomy was assigned to the ASV using the naive Bayesian classifier method implemented in DADA2 with the Silva taxonomic training dataset (version 132) as a reference (Callahan 2018).

The 16S rRNA amplicon sequencing data were further analysed in R version 4.3.0 with the R package phyloseq (McMurdie and Holmes 2013). Subsampling was performed based on the lowest number of reads obtained over the different samples amended with a mock community, i.e., a coverage of 23519 reads. A further subsampling was performed based on the relative abundance of the different ASV and ASV with a relative abundance higher than 0.1 % were included in the analysis. The β -diversity was calculated by Principal Coordination Analysis (PCoA) with weighted Unifrac distances with the command "ordinate."

2.2.9 UNIMAN (microbiology task 3)

2.2.9.1 Microcosms setup

Three batches of 30 mL groundwater were prepared in triplicate in 50 mL capacity serum bottles. Sulphate was present in the groundwater as an electron acceptor, and an additional set of experiments was set up using nitrate (20 mM) as an additional electron acceptor. To explore the impact of low concentrations of organic matter representative of deep groundwaters in the UK, 15 mg/L yeast extract was added to one set of microcosms. Negative control microcosms contained no added carbon, while positive control microcosms contained 15 mM sodium lactate as an electron donor. Parallel experiments without nitrate were also set up as a control for all three batches. The microcosm media were autoclaved at 120°C for 20 minutes to sterilize the system before adding 5 g of Harpur Hill sediment as a microbial inoculum and four cement tablets in each serum bottle in an anaerobic chamber. The headspace of the bottles containing lactate and no electron donor was then filled with N₂, while the headspace of the low carbon yeast extract media bottles was filled with H₂, which was flushed every 14th day to ensure enough H₂ was available as an electron donor in that system. The system conditions are summarized in Table 2-17. The bottles were incubated in the dark for 6 months.

Table 2-17: Conditions in different systems in the microcosm experiment

| System | Abbreviation | Lactate | Yeast Extract | Hydrogen | Nitrate |
|---------------------------------------|--------------|---------|---------------|----------|---------|
| Groundwater | G | | | | |
| Groundwater + nitrate | GN | | | | X |
| Groundwater + lactate | GL | X | | | |
| Groundwater + lactate + nitrate | GLN | X | | | X |
| Groundwater + yeast extract | GY | | X | X | |
| Groundwater + yeast extract + nitrate | GYN | | X | X | X |

2.2.9.2 Geochemical analysis

Sediment slurry with groundwater was extracted every 15th day initially for 2 months and then every 30th day for the remaining 4 months under anaerobic conditions. The pH was measured using a Denver Instrument digital meter and Fisherbrand FB68801 electrode, calibrated before measuring each time using pH 7, 10 and 12 buffers. Samples were centrifuged at 14,000 g for 10 minutes to separate out the sediments. The supernatant was then diluted 200 times with deionised water to measure the concentration of anionic species (nitrate, sulphate, nitrate, volatile fatty acid) using a Dionex ICS5000 Dual Channel on Chromatograph fitted with a Dionex AS-AP auto sampler, connected to a CD20 conductivity detector. The chromatograph was equipped with a Dionex Capillary (50 mm x 0.4 mm) AG11-HC 4 µm analytical column. For background reduction, a Dionex ACES300 Chemical Suppressor was used. To assess the cation concentrations, filtered supernatants were diluted 100 times in a 2% nitric acid solution, followed by ICP-AES measurement on acid-digested samples (Perkin Elmer Optima 5300).

2.2.9.3 Mineralogical analysis

2.2.9.3.1 Scanning Electron Microscopy (SEM)

The cement tablets from bottles incubated for one, two, three and six months were analysed by using low vacuum scanning electron microscopy. The tablets were taken out from microcosm bottles in an anaerobic cabinet using a sterilized steel wire and gently rinsed using deionized water to remove unadhered particles on the surface. They were then dried at room temperature for at least a week. Dried samples were then gold coated for 60 seconds at 20 mA/1.5 kV. The coated samples were imaged using FEI Quanta 650 FEG(E)SEM at 15 kV in a 1 mbar vacuum.

2.2.9.3.2 Micro X-ray Computed Tomography (µ-XCT)

Treated cement tablets extracted from microcosms after the first, third and sixth months were analyzed by X-ray Computed Tomography using Zeiss VersaXRM620-DCT at the Henry Moseley X-ray Imaging Facility at the University of Manchester. The magnification for the scanning was 0.4 times with a resolution of 5 µm pixel size. Reconstruction of the 3D volume was performed after correcting the slices for center shift and beam hardening. The images were saved as TXM files and were opened in the Avizo software package (Thermo Fisher Scientific). The images were of sufficient resolution to work with, so no filter was applied. Segmentation of pores, carbonate on the surface and cement phases was performed using a histogram range tool and interactive thresholding. With the help of label analysis, the diameter of the pores was determined. Using a sieve analysis tool, the pores were separated into four groups according to their equivalent diameter. Identical processing methods were applied to all sample data.

2.2.10 HZDR (microbiology task 3)

2.2.10.1 Microcosm setup

The microcosms were set up under two different conditions on 29th of March, 2023 at Tournemire Experimental Station of IRSN. First, two cement samples placed into two holders were incubated with natural groundwater of Cernon (~300 mL) in a wide-mouth beaker sealed by AeraSeal film (MERCK) for gas exchange. Second, to further stimulate microbial growth 2 mM of sodium lactate were added to the water in the beaker. The groundwater was collected (~100 mL) for geochemical and microbial diversity analysis every 3 weeks and the remaining water in the microcosms of both conditions was discarded. Subsequently, fresh groundwater (~300 mL) was supplied to the microcosms without or with 2 mM of sodium lactate every 3 weeks until the end the experiment.

The cement samples in each microcosm were collected individually at 3 and will be collected after 9 months of the incubation period (Table 2-18). Up to 4 microcosms under one condition (8 cement samples in total) were set up, and the cement samples from 3 months of incubation were applied for SEM-EDX, XRD and micro-indentation (n=1), μ -CT (n=1) and microbial diversity analysis (n=2) (Table 2-18).

Table 2-18 Conditions and analyses of microcosm setups.

| | Condition 1 | | | | Condition 2 | | | |
|-----------------|---------------------------------|---|--------------------------------|---|--|---|---|--------------------------------|
| Groundwater | Natural groundwater of Cernon | | | | Groundwater of Cernon with 2mM of Na-lactate | | | |
| Microcosm | 1 | 2 | 3 | 4 | 5 | 6 | 7 | 8 |
| Cement (3 mon.) | 1 | 1 | 1 | 1 | 1 | 1 | 1 | 1 |
| Cement (9 mon.) | 1 | 1 | 1 | 1 | 1 | 1 | 1 | 1 |
| Analyses | SEM-EDX, XRD, micro-indentation | Microbial diversity analysis of water & surface | μ -CT, SEM-EDX for surface | | SEM-EDX, XRD, micro-indentation | Microbial diversity analysis of water & surface | | μ -CT, SEM-EDX for surface |

2.2.10.2 Geochemical analysis

The geochemistry of collected water samples (10 mL) were analysed for anions (nitrate, nitrite, sulphate, phosphate, Br-, Cl- & F-) by High Performance Ionic Chromatography (HPIC, Dionex Integriion, Thermo Fisher Scientific, USA) and for the total nitrogen (TN), total organic carbon (TOC) and total inorganic carbon (TIC) by Multi N/C 2100S (Analytik Jena, Germany). Additional volumes of water samples (10 mL were then acidified with 1% of nitric acid (HNO₃) for quantifying cations (Ca, Mg, Na and K for example) by Inductively Coupled Plasma Mass Spectrometry (ICP-MS, ELAN 9000, PerkinElmer, Germany)).

2.2.10.3 Microscopic and mineralogical analysis

After the three-month incubation in the groundwater, a cube of 1x1x2 cm was sampled from each cement for a chemo-mechanical characterization by SEM-EDS and XRD. Additional cement sample incubated with constant flow of natural groundwater was also carried out by IRSN to compare the static effect and limited volume of groundwater (microcosm 1 & 5) on the cement degradation.

SEM-EDS analyses were carried out on carbon metallized polished sections of cement samples. The acquisition was performed on SEM Hitachi S3500N with two EDS Brüker 5030 XFlash at 15 keV with x100 magnification. The pixel size is 2.4 μ m, at the limit of the interaction pair for this type of material. The average number of photons per pixel is greater than 4000, allowing rework of signals from hyperspectral images.

To observe microbial colonization (biofilm) on the cement surface via a scanning electron microscope (SEM, Carl Zeiss AG - NVision 40), firstly the pieces of cement samples were fixed with 2.5% glutaraldehyde in

EURAD (Deliverable n° 16.4 and 16.6) - Report on bio-chemical processes controlling the evolution of the microstructure and mechanical properties of cementitious materials.

Dissemination level: PU

Date of issue of this report: 30/05/2024

0.1 M phosphate buffer. Secondly, the samples were gradually dehydrated with gradient ethanol (10%, 20%, 40%, 60%, 80% and 99%) and Hexamethyldisilazane (HMDS) was used for the final dehydration step. Lastly, after the dehydration process, the samples were gold coated using a sputter-coater at 30 mA for 40 seconds. An acceleration voltage of 15.0 kV was applied during the entire measurement.

The XRD analyses presented were carried out with an Aeris Research Edition diffractometer from Malvern-Panalytical in θ - 2θ configuration, under CuK α radiation ($\lambda = 1.54 \text{ \AA}$) with a divergence slot of 0.5° and a rotation platform.

2.2.10.4 Microbial diversity analysis in water and cement samples

Prior to DNA extraction for water samples, an autoclaved Bottle Top Filter (Nalgene) with $0.22 \mu\text{m}$ of MCE membrane (Millipore) was used to filter the biomass. Subsequently, the filter was applied to DNeasy PowerWater Kit (QIAGEN) following manufacturers' protocol. For cement samples the biomass from the surface was recovered using FLOQSwab (Copan), and the swab was also applied to DNeasy PowerWater Kit (QIAGEN) for DNA extraction. The DNA was quantified using Qubit 1X dsDNA HS Assay kit (Thermo Scientific).

Microbial diversity was analysed using 16S amplicon sequencing. The V4 region of 16S rRNA genes of extracted DNA from both water and cement samples was amplified using bacterial V4 primer set (515f modified: 5'-GTGYCAGCMGCCGCGGTAA-3' and 806r modified: 5'-GGACTACNVGGGTWTCTAAT-3') (Walters et al., 2016), and KAPA HiFi HotStart ReadyMix (Roche) (Table 3) with 30 thermal cycles of PCR. The PCR reaction mixture contained DNA ($2.5 \mu\text{L}$), 515f primers ($5 \mu\text{L}$), 806r primers ($5 \mu\text{L}$) and KAPA ReadyMix ($12.5 \mu\text{L}$). The PCR was performed under the following conditions: 95°C for 5 min, and 30 cycles of 95°C for 30 s, 55°C for 30 s and 72°C for 30 s, followed by 72°C for 10 min.

The 16S amplicons were purified using QIAquick PCR & Gel Cleanup Kit (QIAGEN), and sequenced on a next-generation sequencer, MiSeq platform, at Eurofins Genomics (Germany). The raw sequence data were analysed using DADA2 (Callahan et al., 2016) to generate amplicon sequence variants (ASVs), and the bacterial taxonomy of ASVs were assigned against the Silva SSU database (Quast et al., 2013). The microbial diversity data was normalized and visualized using phyloseq (McMurdie & Holmes, 2013).

2.3 Conclusion for part 2

Task 2 focuses on the chemo-mechanical behaviour of mortars and concretes at the macro scale. The aim of this chapter was to provide a reminder but also an update on the materials studied and the partners' experimental program. This information was provided in D16.3, but to make the document self-supporting we felt it was important to remind the composition of cementitious materials, their curing conditions, and their sampling method (laboratory production or collection in situ). Some mortar/concretes have been developed since the publication of D16.3 and feedback has been obtained from sampling and sample preparation. These elements are thus included to make the results easier to understand. A section is also dedicated to the description of experimental programs, knowing that some partners have elaborated protocols and developed experimental devices.

In task 2.1, the LMDC developed a OPC concrete with a compressive strength of 40 MPa. LaMcube conducted its experiments on concrete samples produced at the LMDC, to reduce the variability of the results and facilitate the cross-interpretation of the results compared with the LMDC study. The experimental program involves mechanical characterisation tests on prismatic (70×70×280 mm) and cylindrical (Ø37×74 mm) cored samples. The aim is to determine the strength (compression and indirect traction), elastic properties (E and ν), and post-peak behaviour of concrete. The mechanical tests were carried out on partially or fully carbonated samples, with and without pre-damage caused by thermal shock. The LMDC investigates steel/concrete bond after an accelerated carbonation phase (70 days). The 3-point bending tests carried out allow the reinforced concrete prisms (100×100×400 mm) to be cracked at mid-span to promote the propagation of carbonation along the steel-concrete interface. After the bending test, the prisms are sawn in two parts to provide two pull-out test samples. The concrete recipe and wall design also enabled to study the additional effect of a top bar effect on pull-out behaviour. In addition, blocks of tunnel segments and core samples were taken from Andra's underground laboratory at Bure (Cigeo project). The aim for the LMDC is to carry out pull-out tests and chemical analyses on these decommissioned structures.

In task 2.2, after the carbonation phase in Task 2.1, the LMDC exposes the reinforced concretes samples to cycles involving immersion in a synthetic CO_x solution for 1 month and a 2-week period in an atmosphere. The potential gradient is the indicator used to assess the level of corrosion and evaluate the number of cycles required before mechanical testing (bending test then pull-out). EMPA/PSI measured the poro-chemical-mechanical properties of 2 mortars and 3 concretes cores collected at different distances from the surface of the OPA core (barrels containing OPA blocks). The Swiss team mainly uses non-destructive measurement methods, implementing a specific version of Resonant Ultrasound Spectroscopy, called SIMORUS. Measurements are carried out on cylindrical samples of mortar (Ø28×155 mm) and concrete (Ø40×120 mm), made with OPC or blended cement. GRS/HZDR investigates the degradation of low pH concrete percolated with a saline solution (Konrad mine). The cylindrical samples are (Ø50×1000 mm) and (Ø100×250 mm). The residual mechanical properties must be determined after different percolation times (3, 6 and 12 months), using a triaxial compression test. In parallel, the GeoPET system should make it possible to visualise the percolation and degradation processes inside the concrete. Several experimental difficulties were encountered, especially problems of homogeneity during preparation, sample damages during removal from the percolation cell, and pathway between the inner and outer jacket. SCK CEN experimentally investigates the combined effect of carbonation and leaching. They developed batch/percolation experiments to reproduce Belgian disposal conditions and investigates the evolution of the interface in contact with Boom clay over a period of 14 years (HADES URL). The materials studied are OPC mortars/concretes. COVRA focuses on the evolution of chemo-mechanical behaviour of mortars under artificial ageing conditions through saline water since September 2016.

This solution is supposed to be representative of the clay host rock suitable for a geological disposal facility in the Netherlands. The study aims to determine the compressive strength of cubic samples (5 to 15 cm sides) of aged OPC and CEM III/B mortars. Chemical characterisation of mortars is planned to improve understanding of degradation processes (SEM-EDS, XRD, XRF, TGA-DSC). The Czech team is carrying out artificial ageing experiments on three-year-old low pH concrete (LPC SURAO). The influence of three environmental conditions is investigated: samples are placed in BCV bentonite suspension, or in-situ environment (Bukov URF) immersed in groundwater or exposed to air. The aim is to characterise the mechanical evolution of concrete in these 3 environments after 6, 12, 18 and 24 months of exposure. At these various stages, macroscale mechanical properties are assessed by punch test and ultrasonic measurement (pundit). Chemical analyses using EDX-EDS and XRD should help to explain the mechanical changes. The punch test is carried out on cored and sawn discs ($\varnothing 50 \times 8$ mm) and provides an indication of the material's rigidity. The Impulse ultrasound method is used to measure the modulus of elasticity on cored and sawn cylindrical specimens ($\varnothing 42 \times 84$ mm).

In task 2.3, the Czech team investigates the microbial evolution of the 3-year-old LPC samples artificially aged and stored under in situ conditions in three different environments (water, BCV bentonite, air), combining the genetics approach with cultivation experiments. The aim is to determine the microbial community in concrete samples, bentonite, water, and swabs by determining the relative abundances and if possible, quantities of the dominant bacterial genera. The experimental program includes DNA extraction using swabs taken from the surface of the low pH concrete ($\varnothing 50 \times 8$ mm discs), to examine the formation of a biofilm, but also the extraction of DNA and 16S rRNA amplicon sequencing from the concrete matrix to analyse micro-organisms in low pH concrete ($\varnothing 50 \times 8$ mm discs). The extraction of DNA and cells from the water/bentonite must also provide knowledge of the micro-organisms in the environment of the concrete samples. An irradiation and UV treatment method provides reference samples without microorganisms. The SCK CEN experimental program includes batch and *in situ* percolation experiments (HADES URL) to study the mechanical evolution of OPC materials under the combined effect of chemical and microbial exposure. Several boundary conditions (partial pressure of CO₂, hydraulic pressure, microbial biofilm) relevant to the context of geological disposal are considered. The techniques used involve quantifying mineralogical changes (TGA, XRD, FTIR) and mechanical changes (elastic modulus, compressive strength, tensile strength, triaxial compression tests in collaboration with LaMcube) in mortars degraded by the chemo-bio-mechanical processes. They also monitor the microbial communities in percolated solution, biofilm formation and analysis on cementitious material and identification of mineral phases precipitated by microbes via flow cytometry, ATP, IC. STEM/HAADF, SEM/EDX, fluorescence microscopy, Field Emission Electron Microscope associated with Raman Spectroscopy (EEM/RS), and sequencing technologies. The SCK CEN microbiology group is also involved in research focusing on the chemical-mechanical behaviour of cementitious materials on a meso/macro scale, in close collaboration with COVRA. and FZJ.

This deliverable also includes the microbiology work performed in task 3. Here, the group of UNIMAN explored the potential for microbial alterations of low-pH cement under post-closure GDF-relevant conditions. Anaerobic microcosm experiments were set up using a synthetic groundwater representative of Oxford clay groundwaters, low pH cement tablets, and a moderately alkaliphilic microbial inoculum from a cementitious GDF analogue site. Two organic amendments were compared: low levels of complex organics (15 mg/L yeast extract) representative of groundwater organic loadings and a positive control containing sodium lactate (15 mM). A negative control treatment was also analyzed, containing no added electron donor/carbon source. Hydrogen was added to the headspace of the low-level organic incubation as an additional electron donor to mimic the gas accumulation in a GDF (due to steel corrosion). Nitrate (20 mM) was used as an electron acceptor in all the treatments. A parallel setup was also run without nitrate as controls for each treatment.

evolution of the microstructure and mechanical properties of cementitious materials.

Dissemination level: PU

Date of issue of this report: 30/05/2024

However, sulphate was present in both nitrate and no nitrate systems. The microcosm experiments lasted for six months. SEM imaging was used to study the cement surface. Pore distribution in the low and high-carbon systems was also determined using μ -XCT. PCR-based 16S rRNA gene sequencing is pending in this work to monitor the accompanying changes in microbial communities.

HZDR evaluated whether microorganisms of natural groundwater of Cernon, France, lead to degradation or calcite precipitation of low-pH cements. To this end, microcosms incubating cement samples with two conditions of groundwater (with and without 2 mM of lactate) were conducted at the Tournemire Underground Research Laboratory of IRSN for up to 9 months with water renewing every 3 weeks. SEM-EDS was used to study the cement surfaces. Microbial communities were monitored with 16S rRNA gene sequencing.

2.4 References for part 2

- A. Dauzeres, G. Achiedo, D. Nied, E. Bernard, S. Alahrache, B. Lothenbach, Magnesium perturbation in low-pH concretes placed in clayey environment—solid characterizations and modeling, *Cement and Concrete Research*. 79 (2016) 137–150.
- A. Jenni, U. Mäder, C. Lerouge, S. Gaboreau, B. Schwyn, In situ interaction between different concretes and Opalinus Clay, *Physics and Chemistry of the Earth, Parts A/B/C*. 70–71 (2014) 71–83.
- A. Lundin. Use of firefly luciferase in ATP-related assays of biomass, enzymes, and metabolites. *Methods Enzymol*. 2000;305:346-70. doi: 10.1016/s0076-6879(00)05499-9. PMID: 10812612.
- ASTM C09 committee, ASTM C215-19: Test Method for Fundamental Transverse, Longitudinal, and Torsional Resonant Frequencies of Concrete Specimens, (2019).
- B.J. Callahan, P. McMurdie, M. Rosen, et al. DADA2: High-resolution sample inference from Illumina amplicon data. *Nat Methods* 13, 581–583, 2016. <https://doi.org/10.1038/nmeth.3869>.
- C. Cattaneo, D.M. Smillie, K. Gelsthorpe, A. Piccinini, A.R. Gelsthorpe, R.J. Sokol. A simple method for extracting DNA from old skeletal material. *Forensic Sci Int*. 1995 Jul 28;74(3):167-74. doi: 10.1016/0379-0738(95)01758-b. PMID: 7557753.
- C. Coll, J. Desrues, P. Bésuelle, G. Viggiani, 2004. Characterizing in the Laboratory Permeability Changes Induced by Deviatoric Stress in Clayey Rocks, in: Stephanson, O. (Ed.), Elsevier Geo-Engineering Book Series. Elsevier, pp. 547-552.
- C. Lerouge, S. Gaboreau, S. Grangeon, F. Claret, F. Warmont, A. Jenni, V. Cloet, U. Mäder, In situ interactions between Opalinus Clay and Low Alkali Concrete, *Physics and Chemistry of the Earth, Parts A/B/C*. 99 (2017) 3–21.
- C. Merlet, An accurate computer correction program for quantitative electron probe microanalysis. *Mikrochim Acta* 114, 363–376 (1994). <https://doi.org/10.1007/BF01244563>
- C. Povedano-Priego, F. Jroundi, M. Lopez-Fernandez, R. Shrestha, R. Spanek, I. Martín-Sánchez, *et al.* Deciphering indigenous bacteria in compacted bentonite through a novel and efficient DNA extraction method: Insights into biogeochemical processes within the Deep Geological Disposal of nuclear waste concept. *Journal of Hazardous Materials* 408: 124600, 2021.
- C. Quast, E. Pruesse, P. Yilmaz, J. Gerken, J., T. Schweer, P. Yarza, J. Peplies, F.O. Glöckner. The SILVA ribosomal RNA gene database project: improved data processing and web-based tools. *Nucleic Acids Research*. 41. D590-D596. 10.1093/nar/gks1219, 2013.
- C.P. Chen, R.S. Lakes, Apparatus for Determining the Viscoelastic Properties of Materials Over Ten Decades of Frequency and Time, *Journal of Rheology*. 33 (1989) 1231–1249.
- Černá, K., Šachlová, Š., Bedrníková, E., Bartak, D., Kašpar, V., Říha, J., Hlaváčková, V., Dobrev, D., Večerník, P., Zuna, M., 2023. TAČR TK02010169: Závěrečná zpráva. Technická univerzita v Liberci.
- D. Pret, 2003. Nouvelles méthodes quantitatives de cartographie de la minéralogie et de la porosité dans les matériaux argileux : application aux bentonites compactées des barrières ouvragées, PhD thesis. Université de Poitiers, France, Poitiers, p. 257.
- D. Pret, Sammartino, D. Beaufort, A. Meunier, M. Fialin, L.J. Michot, 2010. A new method for quantitative petrography based on image processing of chemical element maps: Part I. Mineral mapping applied to compacted bentonites. *Am Mineral* 95, 1379-1388.

- D.J. Reasoner, E.E. Geldreich. A new medium for the enumeration and subculture of bacteria from potable water. *Appl Environ Microbiol.* 1985 Jan;49(1):1-7. doi: 10.1128/aem.49.1.1-7.1985. PMID: 3883894; PMCID: PMC238333.
- DIN EN ISO 12571, Hygrothermal performance of building materials - Determination of hygroscopic sorption properties - German version of EN ISO 12571:2000, (2000).
- E. Jacobs, Q.T. Phung, L. Frederickx, S. Levasseur, Diffusive Transport of Dissolved Gases in Potential Concretes for Nuclear Waste Disposal. *Sustainability* 2021, 13, 10007. <https://doi.org/10.3390/su131810007>
- E.W. Washburn, Note on a Method of Determining the Distribution of Pore Sizes in a Porous Material. *Proceedings of the National Academy of Sciences of the United States of America* 7(4): 115-116. doi: 10.1073/pnas.7.4.115. PMID: 16576588; PMCID: PMC1084764.
- EN 12390-12, Testing hardened concrete Determination of the carbonation resistance of concrete. Accelerated carbonation method (2020).
- F. Simonetti, P. Cawley, A guided wave technique for the characterization of highly attenuative viscoelastic materials, *J. Acoust. Soc. Am.* 114 (2003) 9.
- F.J. Pearson, D. Arcos, A. Bath, J.-Y. Boisson, A.M. Fernandez, H.-E. Gäbler, A. Gautschi, L. Griffault, P. Hernan, H.N. Waber, Mont Terri Project – Geochemistry of Water in the Opalinus Clay Formation at the Mont Terri Rock Laboratory, Swiss Federal Office for Water and Geology (FOWG), Bern, 2003.
- G. Pickett, Equations for Computing Elastic Constants from Flexural and Torsional Resonant Frequencies of Vibration of Prisms and Cylinders, *Proceedings of the American Society for Testing Materials.* 45 (1945) 846–865.
- I. Jackson, H. Schijns, D.R. Schmitt, J. Mu, A. Delmenico, A versatile facility for laboratory studies of viscoelastic and poroelastic behaviour of rocks, *Review of Scientific Instruments.* 82 (2011) 064501.
- J. A. Maresca, P. Moser, T. Schumacher, Analysis of bacterial communities in and on concrete. *Mater Struct* 50, 25 (2017). <https://doi.org/10.1617/s11527-016-0929-y>
- J.R. Postgate, 1979. The sulphate-reducing bacteria, CUP Archive
- L.M. Keller, P. Schuetz, R. Erni, M.D. Rossell, F. Lucas, P. Gasser, L. Holzer, Characterization of multi-scale microstructural features in Opalinus Clay, *Microporous and Mesoporous Materials.* 170 (2013) 83–94.
- M. MARTIN, Cutadapt removes adapter sequences from high-throughput sequencing reads. *EMBnet.journal*, [S.I.], v. 17, n. 1, p. pp. 10-12, may 2011. ISSN 2226-6089. doi: <https://doi.org/10.14806/ej.17.1.200>.
- M.C. Remillieux, R.A. Guyer, C. Payan, T.J. Ulrich, Decoupling Nonclassical Nonlinear Behaviour of Elastic Wave Types, *Phys. Rev. Lett.* 116 (2016) 115501.
- M.J. Claesson, Q. Wang, O. O'Sullivan, R. Greene-Diniz, J.R. Cole, R.P. Ross, P.W. O'Toole. Comparison of two next-generation sequencing technologies for resolving highly complex microbiota composition using tandem variable 16S rRNA gene regions. *Nucleic Acids Res.* 2010 Dec;38(22): e200. doi: 10.1093/nar/gkq873. Epub 2010 Sep 29. PMID: 20880993; PMCID: PMC3001100.
- P. Bossart, F. Bernier, J. Birkholzer, C. Bruggeman, P. Connolly, S. Dewonck, M. Fukaya, M. Herfort, M. Jensen, J.-M. Matray, J.C. Mayor, A. Moeri, T. Oyama, K. Schuster, N. Shigeta, T. Vietor, K. Wiczorek, Mont Terri rock laboratory, 20 years of research: introduction, site characteristics and overview of experiments, *Swiss J Geosci.* 110 (2017) 3–22.

- P.J. McMurdie, S. Holmes, Phyloseq: An R Package for Reproducible Interactive Analysis and Graphics of Microbiome Census Data. PLOS ONE 8(4): e61217, 2013. <https://doi.org/10.1371/journal.pone.0061217>.
- Phung, Q. T., et al. (2019). Preliminary experimental results on the changes in microstructure, mineralogy and transport properties of Boom Clay-concrete interface. Proceedings of the Second Workshop of the HORIZON 2020 CEBAMA Project (KIT Scientific Reports; 7752), KIT Scientific Publishing.
- Q.T. Phung, N. Maes, D. Jacques, G. De Schutter, G. Ye, Investigation of the changes in microstructure and transport properties of leached cement pastes accounting for mix composition, Cement and Concrete Research, Volume 79, 2016, Pages 217-234, ISSN 0008-8846, <https://doi.org/10.1016/j.cemconres.2015.09.017>.
- Q.T. Phung, N. Maes, F. Claret, S. Gaboreau, J. Leysen, (2017). Methodology to study the changes in microstructure and transport properties of the Boom Clay - concrete interface. 1st Annual CEBAMA Workshop Proceedings, Barcelona, Spain, KIT Scientific Publishing.
- Q.T. Phung, N. Maes, F. Claret, S. Gaboreau, J. Leysen, 2017. Methodology to study the changes in microstructure and transport properties of the Boom Clay - concrete interface, 1st Annual CEBAMA Workshop Proceedings. KIT Scientific Publishing, Barcelona, Spain, pp. 37-48.
- Q.T. Phung, N. Maes, G. De Schutter, D. Jacques, G. Ye, Determination of water permeability of cementitious materials using a controlled constant flow method, Construction and Building Materials, Volume 47, 2013, Pages 1488-1496, ISSN 0950-0618, <https://doi.org/10.1016/j.conbuildmat.2013.06.074>.
- R.G. Vasconcelos, B. Walkley, S. Day, C.C. Tang, H. Paraskevoulakos, L.J. Gardner and C.L. Corkhill, 2020. 18-month hydration of a low-pH cement for geological disposal of radioactive waste: The Cebama reference cement. *Applied Geochemistry*, 116, p.104536.
- R.S. Lakes, Chapter 3. Dynamic behaviour, in: Viscoelastic Materials, Cambridge University Press, Cambridge, 2009: pp. 55–90.
- RILEM RC6 Bond test for reinforcement steel. 2.Pull-out test, Rilem Technical Recommendations for the Testing and Use of Construction Materials: International Union of Testing and Research Laboratories for Materials and Construction, 1994.
- S. Gaboreau, D. Prêt, V. Montouillout, P. Henocq, J.-C. Robinet, C. Tournassat, 2017. Quantitative mineralogical mapping of hydrated low pH concrete. *Cement and Concrete Composites* 83, 360-373.
- S. Saltiel, P.A. Selvadurai, B.P. Bonner, S.D. Glaser, J.B. Ajo-Franklin, Experimental development of low-frequency shear modulus and attenuation measurements in mated rock fractures: Shear mechanics due to asperity contact area changes with normal stress, *GEOPHYSICS*. 82 (2017) M19–M36.
- S. Spinner, R.C. Valore, Comparison of theoretical and empirical relations between the shear modulus and torsional resonance frequencies for bars of rectangular cross section, *Journal of Research of the National Bureau of Standards*. 60 (1958) 459.
- S. Spinner, T.W. Reichard, W.E. Tefft, A comparison of experimental and theoretical relations between Young's modulus and the flexural and longitudinal resonance frequencies of uniform bars, *Journal of Research of the National Bureau of Standards Section A: Physics and Chemistry*. 64A (1960) 147.
- S.E. Dowd, T.R. Callaway, R.D. Wolcott, et al. Evaluation of the bacterial diversity in the feces of cattle using 16S rDNA bacterial tag-encoded FLX amplicon pyrosequencing (bTEFAP). *BMC Microbiol* 8, 125 (2008). <https://doi.org/10.1186/1471-2180-8-125>.

- S.V. Kolluru, J.S. Popovics, S.P. Shah, Determining Elastic Properties of Concrete Using Vibrational Resonance Frequencies of Standard Test Cylinders, *Cement, Concrete, Aggr.* 22 (2000) 81.
- T. Vehmas, V. Montoya, M.C. Alonso, R. Vašíček, E. Rastrick, S. Gaboreau, P. Večerník, M. Leivo, E. Holt, N. Fink and N.A. Mouheb, 2020. Characterization of Cebama low-pH reference concrete and assessment of its alteration with representative waters in radioactive waste repositories. *Applied geochemistry*, 121, p.104703.
- T.J. White, T. Bruns, S.J.W.T. Lee, J. Taylor, 1990. Amplification and direct sequencing of fungal ribosomal RNA genes for phylogenetics. *PCR Protoc. Guide Methods Appl.* 315–322.
- U. Mäder, A. Jenni, C. Lerouge, S. Gaboreau, S. Miyoshi, Y. Kimura, V. Cloet, M. Fukaya, F. Claret, T. Otake, M. Shibata, B. Lothenbach, 5-year chemico-physical evolution of concrete–claystone interfaces, Mont Terri rock laboratory (Switzerland), *Swiss Journal of Geosciences*. 110 (2017) 307–327.
- U. Mäder, A. Jenni, C. Lerouge, S. Gaboreau, S. Miyoshi, Y. Kimura, V. Cloet, M. Fukaya, F. Claret, T. Otake, M. Shibata, B. Lothenbach, 5-year chemico-physical evolution of concrete–claystone interfaces, Mont Terri rock laboratory (Switzerland), *Swiss Journal of Geosciences*. 110 (2017) 307–327.
- V. Hlavackova, R. Shrestha, E. Hofmanova, P. Kejzlar, J. Riha, D. Bartak, A. Sevcu, K. Cerna, A protocol for the extraction of viable bacteria for identification of bacterial communities in bentonite, *Applied Clay Science*, Volume 232, 2023, 106809, ISSN 0169-1317, <https://doi.org/10.1016/j.clay.2022.106809>.

3 Chemo-mechanical evolution of unsaturated concrete

3.1 Mechanical evolution of concrete under carbonation (LaMCube/LMDC/Andra)

The following paragraphs recapitulate the main results obtained on cylindrical samples Ø37x74 mm in actions 1 and 3 (§ 2.2.1). For the sake of simplicity as tests presented are in compression, all values given below are according to this rule: compression is positive, extension/tension is negative.

3.1.1 Initial mechanical characterisation

A first uniaxial compression test has been performed on three hydrated samples (7.5 months of curing under lime-saturated water) to get an indicative strength value on a material without any thermal or drying process. That could be of interest by comparing this value to sound samples in a reference state (mature samples with initial drying at 45 °C then equilibration at 20 °C / 65 % RH) and help identifying potential changes due to this process. Figure 3-1 presents the mechanical behaviour of 3 tested samples, drawing axial stress versus displacement of the machine actuator.

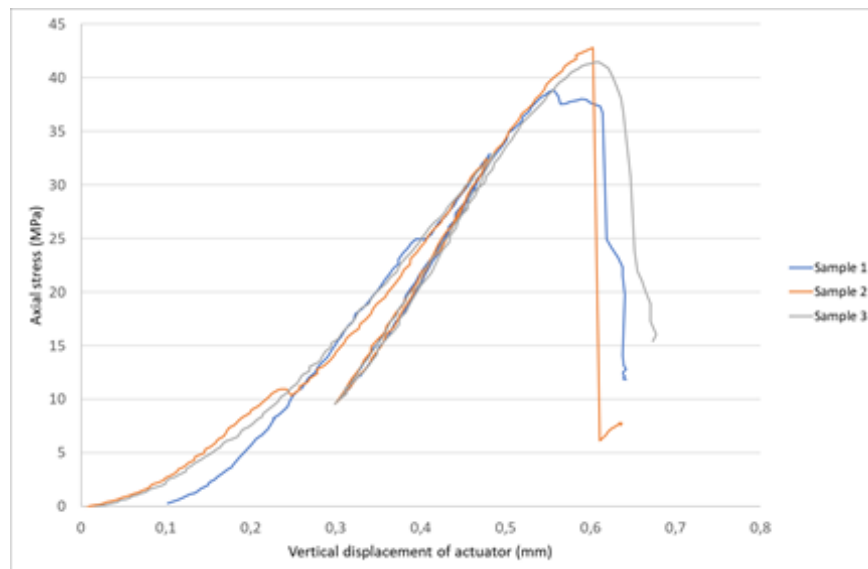


Figure 3-1 Preliminary uniaxial compression results on 3 saturated samples after 7.5 months of curing.

The average of compressive strength on this 3 samples is 41.0 MPa and the behaviour is similar with low dispersion of values (coefficient of variation of 4.9 %). The elastic properties were not measured as samples were not instrumented with gages, and only the vertical displacement of the actuator was recorded but cannot be directly linked to axial strains inside samples (rigidity of the loading machine...).

Another characterization would be useful to better understand changes in mass of samples during the pre-drying process before carbonation. Figure 3-2 shows the mass evolution (in respect with time) on 4 samples from the saturated state after curing under lime-saturated water to a state of carbonation where pH is below 9 as indicated by phenolphthalein. As it can be seen, samples were initially aimed to be dried at 20 °C / 65% RH to have the same conditions as during carbonation, but carbonation protocol was not successful and a more intense pre-drying was required to allow a sufficient CO₂ gaseous diffusion. Therefore, samples were further dried at 45°C: a clear mass decrease is observed with a water loss of more than 4 g (i.e. more than 2% of the mass at saturation) in a week (higher than the water loss during 19 days at 20 °C / 65 % RH). The carbonation can be performed and, after 40 days, the mass of samples reached almost the same value as before pre-drying, indicating that carbonation has been effective. A unique period of 14 days at 45

°C (adopted as the pre-drying before carbonation) would be adequate to get a water saturation compatible with an accelerated carbonation process according to these results.

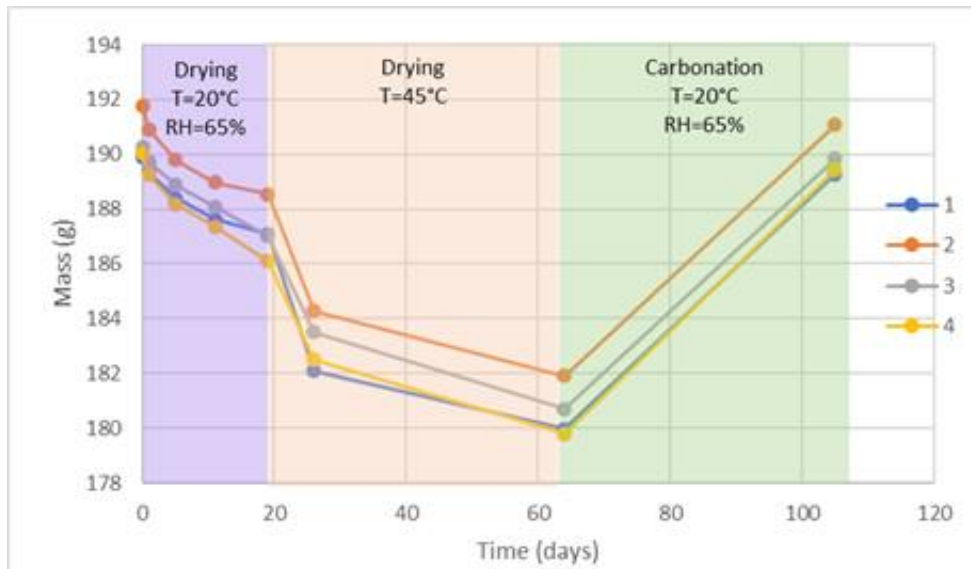


Figure 3-2 Mass evolution of 4 samples from saturated state to pre-conditioning before carbonation then after 100%+ carbonated state.

A visual confirmation of the carbonation state achieved after pre-drying without or with 40 days under 50% CO₂ atmosphere can be seen in Figure 3-3 (left). The left sample exhibits a purple cross section after application of phenolphthalein (pH>9, no carbonation) whereas the right one remains colourless (pH<9, defined as a 100 %+ carbonation state). Figure 3-3 (right) shows the carbonation state of a sample after 8 days of carbonation. The remaining purple sound area is not easy to measure, but the method described in standard NF XP P18-458 provides a procedure ensuring a good measurement accuracy and repeatability. The depth of carbonation appears to be between 5 and 6 mm, corresponding to around 50 % of the area carbonated (depth should be around 5,3 mm). This intermediate level of carbonation is called “50 % carbonation” thereafter.



Figure 3-3 Sound and 100% + carbonated samples (left), sample at an intermediate state of carbonation (50 % carbonation state, right figure).



Figure 3-4 Examples of samples after failure in uniaxial compression.

Uniaxial compression tests can now be conducted according to the protocol defined in §2 on sound, 50% and 100 %+ carbonated cylindrical samples. Figure 3-4 presents photos of various samples after failure under uniaxial compression tests. Cracking patterns are visible and are mainly axially orientated as expected. Lateral strain gages have a bigger probability to be non-functional once cracks are nucleating (due to their orientation): the post-peak behaviour should be taken with caution as the measured values are no more linked to material values under compression but may be affected by localization of cracks.

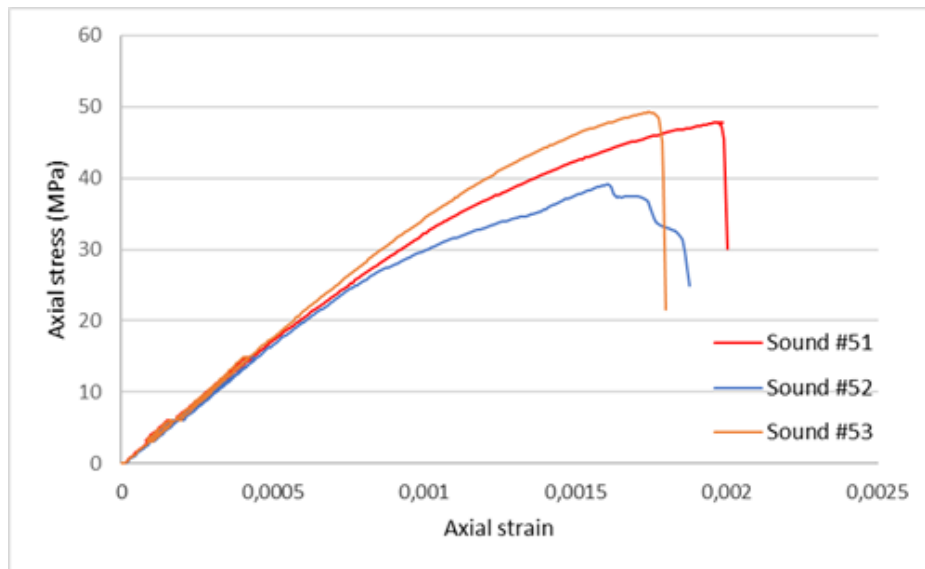


Figure 3-5 Stress-strain curves in uniaxial compression for sound samples.

Figure 3-5 presents the axial stress-strain curve for 3 sound samples (only dried at 45 °C then 20 °C / 65 % RH). Curves have an almost linear part up to about 20 MPa and are superposed for all samples, where an

elastic behaviour could be assumed. The loading-unloading cycles are performed in this zone to obtain the Young's modulus (E) and Poisson's ratio (ν) of the sound material. The hysteretical behaviour during these cycles remains very low, for example with a value of $E = 37.1$ GPa for sample #51 in the unloading cycle to be compared to 36.5 GPa in the reloading branch.

Following this initial linear part, a slightly nonlinear part between 20 MPa and failure strength may be observed, probably linked to friction in existing microcracks and creation of new ones. Other potential irreversible behaviours could also be at the origin of such a behaviour: nevertheless, one can note an increasing discrepancy in the behaviour between specimen what could be linked to local creation of cracks and, depending of the position of strain gages compared to these cracks, the recorded measures may be more variable. The failure strength of samples #51 and #53 is of the same order of magnitude whereas for #52, it is clearly lower. As the failure process is highly linked to cracks and their position that could be greatly affected by aggregates or air bubbles or defects inside the sample, the representativity of this last sample could be questioned. This will be discussed later.

3.1.2 Mechanical behaviour after carbonation without pre damage

In the same way as for sound samples, Figure 3-6 gives the stress-strain curve for 3 samples with 100%+ carbonation (i.e. fully carbonated state obtained after 40 days). In a first analysis, if the sample #4 is discarded, the linear behaviour seems, contrarily to sound samples, to exist until the peak stress of the sample (and not up to around 20 MPa). Carbonation may play a role in this observation. Indeed, the creation of solid calcite inside the existing porous network (that can include microcracks due to pre-drying) may help filling the gaps and both reduce friction of cracks (solid phase continuity between the edges of cracks) and limit the creation of new ones (decreasing porosity and therefore higher strength). In terms of strength, a clear increase compared to sound samples is noted as expected due to calcite creation. In addition, a potential carbonation shrinkage may act as a "confining" pressure: the outer part of the sample contains more likely more decalcified C-S-H (so, more carbonation shrinkage) than the inner part. This differential shrinkage may result in a confined inner part where crack nucleation and opening would be more difficult. This could lead to a contribution to a strength increase even if it remains secondary compared to pore filling by CaCO_3 precipitation.

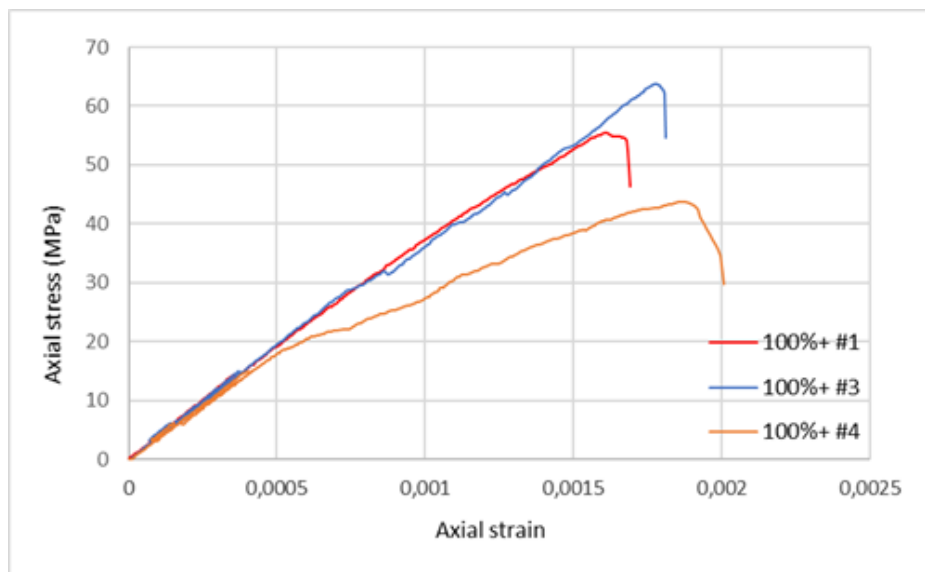


Figure 3-6 Stress-strain curves in uniaxial compression for samples with 100 % + carbonation.

The sample #4 has a comparable initial linear behaviour but had probably a heterogeneity which led to a localized cracking zone and an inhomogeneous and nonlinear behaviour starting from around 18 MPa. The effect of discarding this sample or not will be discussed later, as for sample #52.

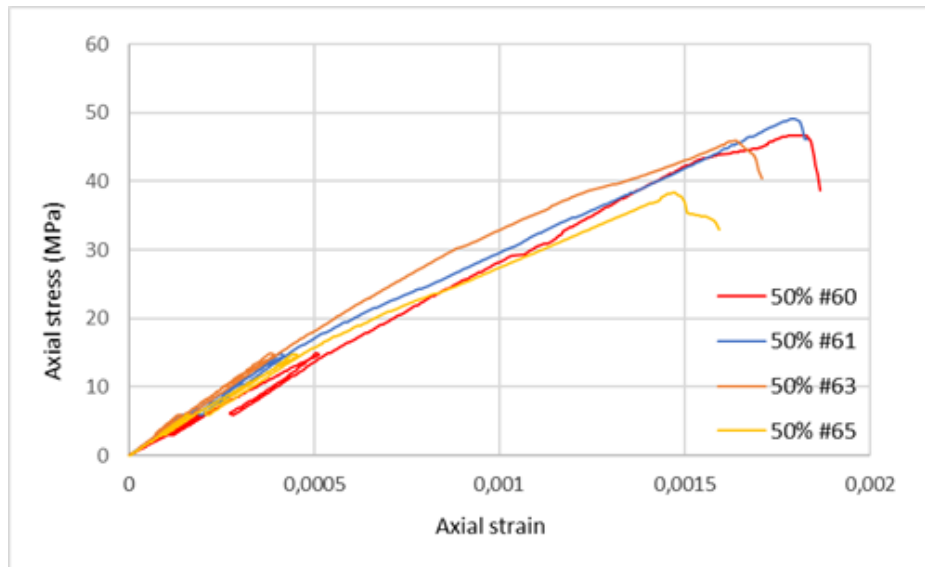


Figure 3-7 Stress-strain curves in uniaxial compression for samples with 50 % carbonation.

Finally, for uniaxial compression, Figure 3-7 plots strain-stress curves for four samples with 50 % carbonation. Unlike for sound and 100 %+ carbonated samples, the behaviour appears to be more variable even at low axial stresses and with a nonlinear behaviour closer to sound samples for sample #63, or closer to fully carbonated ones for sample #61 (linear, nonlinear then again linear until failure). The existing sound inner part in these partially carbonated sample could explain this intermediate behaviour. The sample #65 has a lower failure strength than the other specimens and could also be discarded.

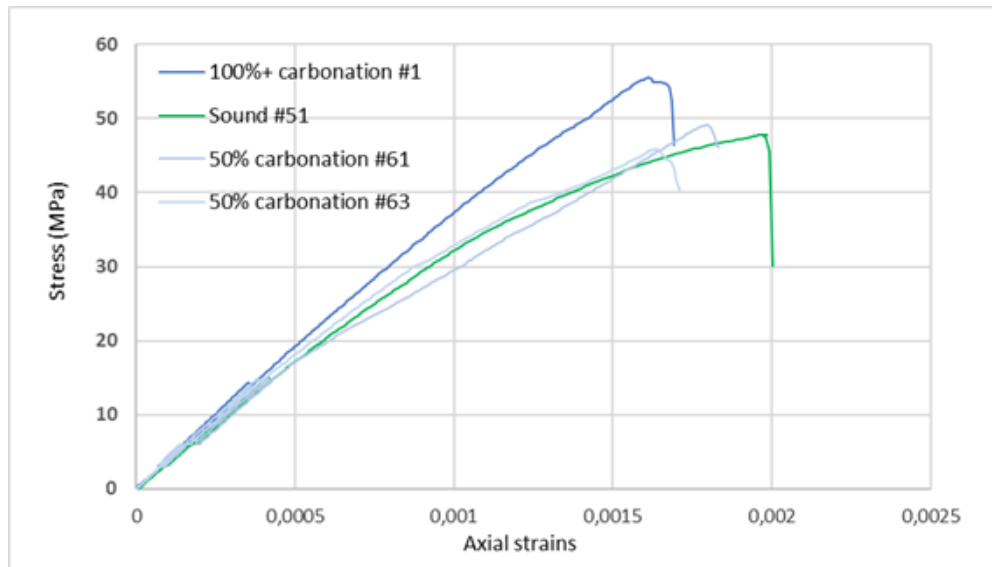


Figure 3-8 Stress-strain curves in uniaxial compression for samples #1, 51, 61 and 63 (different carbonation states).

To help comparing stress-strain curves for different carbonation states and supporting the previous analysis, curves from 4 “representative” samples are plotted in Figure 3-8. The behaviour of 100 %+ carbonated sample #1 has a higher strength and a more linear behaviour than sound or partially carbonated samples. Samples #51 (sound) and #61/#63 (50 % carbonation) seem more or less similar in strength and in shape of the stress-strain curve. A quantitative comparison is proposed in Table 3-1. It sums up individual properties (E, ν , failure strength R_c) for each sample under uniaxial compression and grouped by carbonation states. Average failure strength of sound samples is 43.5 MPa, higher than for saturated samples without pre-drying (41 MPa). A 50 % carbonation increases this value to 45 MPa (+4 % compared to sound samples) and a strength of 54,3 MPa is measured on 100 % + carbonated samples (+25 % compared to sound samples). As discussed before, if one would discard samples #4, #65 and #53, Table 3-2 proposes to calculate averages without these samples. Samples with 50 % of carbonation have a slightly lower failure strength than sound ones (47.3 vs 48.6 MPa) whereas a same +25 % increase exists between 100 %+ carbonation and sound samples.

The same kind of average is performed for E with or without discarding samples. An increase in E of +3 % is calculated between sound and 50 % carbonation, and +10 % for 100 %+ carbonation. These increases remain equivalent with or without discarding samples.

Several main conclusions in uniaxial compression tests may be drawn:

- Failure strength is more impacted by individual results than Young’s modulus which is therefore more reliable.
- It seems that carbonation clearly tends to increase E, slightly for 50 % carbonation (+3 %) and +10 % at 100 %+carbonation state.
- For failure strength, conclusions are less evident for 50 % carbonation: no influence or very tiny increase has been detected. At 100 %+ carbonation, a notable strength increase is seen (+25 %).
- For the Poisson’s ratio, more affected by cracks due to strain gage orientation perpendicular to main crack orientation (axial), a notable range between 0.21 up to 0.29 has been measured. It would be more reliable to compare averages in Table 3-2 to reduce impact of individual variability by discarding samples. ν appears to be around 0.24-0.26 with no tendency with respect to carbonation.

Table 3-1 Elastic properties (E, ν) and failure strength (R_c) for different carbonation states.

| Sample state | Sample # | R_c (MPa) | E (GPa) | ν (-) |
|------------------------------------|----------------|-------------|-------------|-------------|
| 100 %+ carbonation (no pre damage) | 1 | 55.5 | 40.7 | 0.25 |
| | 3 | 63.7 | 41.0 | 0.26 |
| | 4 | 43.7 | 38.6 | 0.24 |
| | Average | 54.3 | 40.1 | 0.25 |
| 50 % carbonation (no pre damage) | 60 | 46.7 | 36.7 | 0.25 |
| | 61 | 49.2 | 39.1 | 0.23 |
| | 63 | 45.9 | 39.2 | 0.25 |
| | 65 | 38.3 | 35.8 | 0.21 |
| | Average | 45.0 | 37.7 | 0.24 |
| Sound (no carbonation) | 52 | 47.8 | 37.1 | 0.26 |
| | 53 | 39.1 | 36.1 | 0.29 |
| | 54 | 49.3 | 38.7 | 0.25 |
| | Average | 43.5 | 36.6 | 0.28 |

Triaxial compression tests are conducted in order to check the influence of a confining pressure on the behaviour of carbonated materials. A first batch of tests was performed with a confining pressure of $P_c = 3$ MPa at three different states (sound, 50 %, 100 %+ carbonation) to compare with uniaxial compression test results and help reinforcing conclusions drawn. Due to time constraints (1 sample requires 1 day of preparation, installation in the triaxial cell and test), only one sample for each state has been tested.

Table 3-2 Elastic properties (E, ν) and failure strength (R_c) for different carbonation states (without discarded samples).

| Sample state | Sample # | R_c (MPa) | E (GPa) | ν (-) |
|------------------------------------|----------------|-------------|-------------|-------------|
| 100 %+ carbonation (no pre damage) | 1 | 55.5 | 40.7 | 0.25 |
| | 3 | 63.7 | 41.0 | 0.26 |
| | 4 | | | |
| | Average | 59.6 | 40.9 | 0.26 |
| 50 % carbonation (no pre damage) | 60 | 46.7 | 36.7 | 0.25 |
| | 61 | 49.2 | 39.1 | 0.23 |
| | 63 | 45.9 | 39.2 | 0.25 |
| | 65 | | | |
| | Average | 47.3 | 38.3 | 0.24 |
| Sound (no carbonation) | 52 | 47.8 | 37.1 | 0.26 |
| | 53 | | | |
| | 54 | 49.3 | 38.7 | 0.25 |
| | Average | 48.6 | 37.9 | 0.25 |

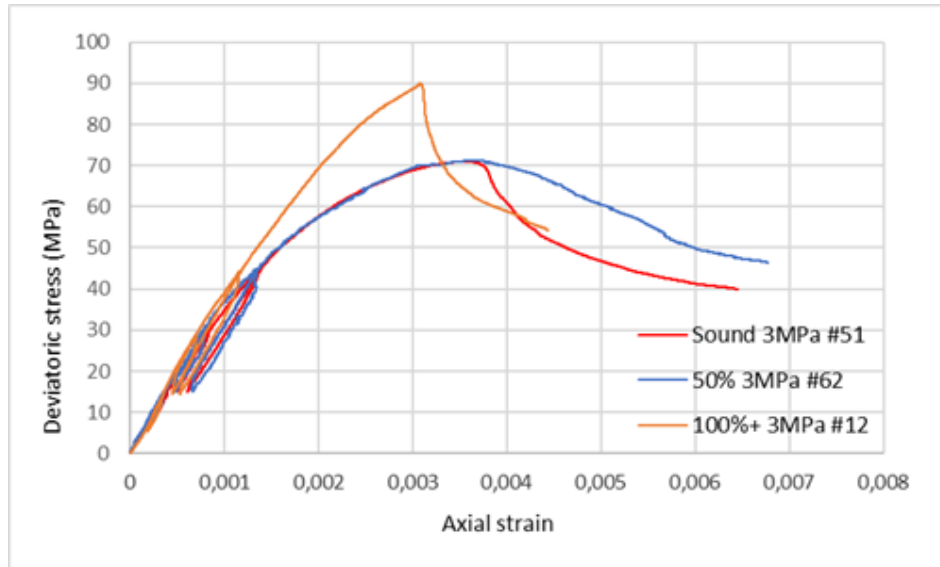


Figure 3-9 Stress-strain curves in triaxial compression ($P_c = 3 \text{ MPa}$) according to carbonation

The deviatoric stress-axial strain curve for each sound, 50 % carbonated and 100 %+ carbonated samples are presented in Figure 3-9. One can note the similarity of the measured behaviour between sound and 50 % carbonated samples up to peak strength. This would tend to confirm a small effect of intermediate level of carbonation on the mechanical behaviour (even if it is only a measure on one sample and additional samples need to be tested). As in uniaxial compression, a rather linear trend is observed up to around 45 MPa. It is followed by a clear nonlinear behaviour that could be associated to creation of friction of cracks. The threshold is increased from 20 MPa in uniaxial tests to 45 MPa in triaxial tests. The confining pressure could help closing existing cracks. There will be fewer crack edges sliding. More energy is also required to create new cracks. The post peak behaviour may be more sample dependent. In addition, the 100 %+ carbonated sample exhibits a notable change with a quite linear behaviour up to around 60 MPa, followed by a slightly nonlinear one up to peak strength. This finding is consistent with observations in uniaxial compression and explanations tied to an important number of gaps (pores, cracks) filled by solid calcite as well as densification of the material.

Table 3-3 Comparison of triaxial and uniaxial compression results according to carbonation.

| Confining pressure | Sample state | Sample number | Rc (MPa) | E (GPa) | ν (-) |
|--------------------|--------------------|-------------------|----------|---------|-----------|
| Pc = 3 MPa | 100 %+ carbonation | 12 | 93.0 | 40.5 | 0.25 |
| | 50 % carbonation | 62 | 74.2 | 37.4 | 0.25 |
| | Sound | 51 | 74.0 | 37.0 | 0.26 |
| Pc = 0 MPa | 100 %+ carbonation | Average 2 samples | 59.6 | 40.9 | 0.26 |
| | 50 % carbonation | Average 3 samples | 47.3 | 38.3 | 0.24 |
| | Sound | Average 2 samples | 48.6 | 37.9 | 0.25 |

In Table 3-3, quantitative properties on samples under triaxial and uniaxial compression are listed, according to the sample state of carbonation. Values for uniaxial compression tests are averages from Table 3-2 (with discarded samples). The Poisson's ratio ν seems unaffected neither by the confining pressure nor the state of carbonation (between 0.24 and 0.26). The Young's Modulus E remains similar at sound state and 50 % of carbonation both with or without confining pressure (37-38 GPa). However, a same increase due to 100 %+ carbonation is observed and tends to confirm the findings in uniaxial compression. The confining

pressure does not change the value of this elastic modulus (perhaps a slight decrease but conclusions cannot be drawn as only one sample has been tested).

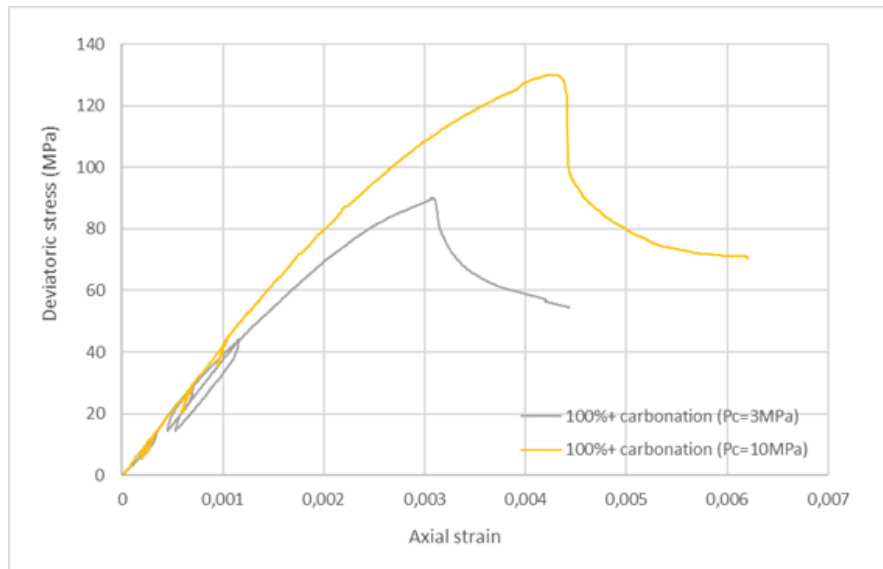


Figure 3-10 Stress-strain curves in triaxial compression according to confining pressure (3 or 10 MPa) on samples with 100%+ carbonation.

The most important change due to the addition of a confining pressure concerns the peak strength which is about 55 % higher in comparison with uniaxial compression, whatever the level of carbonation. This large effect of confining pressure would indicate that it may exist a potential “structural confining” of the inner part of a specimen due to an important carbonation shrinkage in the outer part (at high level of C-S-H decalcification), leading to an increase in strength.

Finally, Figure 3-10 is a first comparison between two sound samples under two different confining pressures of 3 and 10 MPa. It has to be noted that the sample under $P_c = 10$ MPa has only one functional gage and that the displacement rate of the actuator (applying the deviatoric stress) was of $2 \mu\text{m/s}$ (and not $0.5 \mu\text{m/s}$ as in the proposed protocol, loading-unloading cycles are greatly impacted by this rate). This sample was only a preliminary sample used to test a tentative protocol. Nevertheless, the result is presented for indicative purpose and allows to underline the effect of higher confining pressure on the peak strength increase.

3.1.3 Mechanical behaviour after carbonation with pre damage

This second part is devoted to study the influence of an existing damage before carbonation. As explained in the §2, the pre-damaging protocol relies on a thermal shock applied to saturated samples to try obtaining a homogenous and isotropic cracking pattern. The experimental campaign is still ongoing and only results on sound samples are presented in the following paragraphs.

Firstly, to try to ensure the effectiveness of the pre-damaging protocol, relative variations of mass of different sound samples (i.e. no carbonation) during the pre-drying phase at 45°C are given in Figure 3-11. Two samples without pre-damage (cylindrical sample $\text{Ø}37 \times 74$ mm and prismatic beam $70 \times 70 \times 280$ mm) and one with pre-damage (cylindrical sample $\text{Ø}37 \times 74$ mm) are studied. As expected, relative variation of mass for samples without pre-drying is affected by the dimensions of samples: the cylindrical sample has lost mass faster than the more massive prismatic beam.

For the cylindrical sample with pre-damage, it can be observed that the relative mass loss is higher than for the sound cylinder, but the gap between the two curves is reducing as time goes by. This could be linked to a better-connected porous network in the sample with pre-drying, increasing the transport properties of the concrete and allowing faster kinetics of drying at early age. After 36 days, the relative variation of mass is almost the same indicating that the pre-damage is mainly an accelerator of drying without modifying the global water mass that can be lost. The protocol appears to be suitable without modifying free water mass inside the specimen.

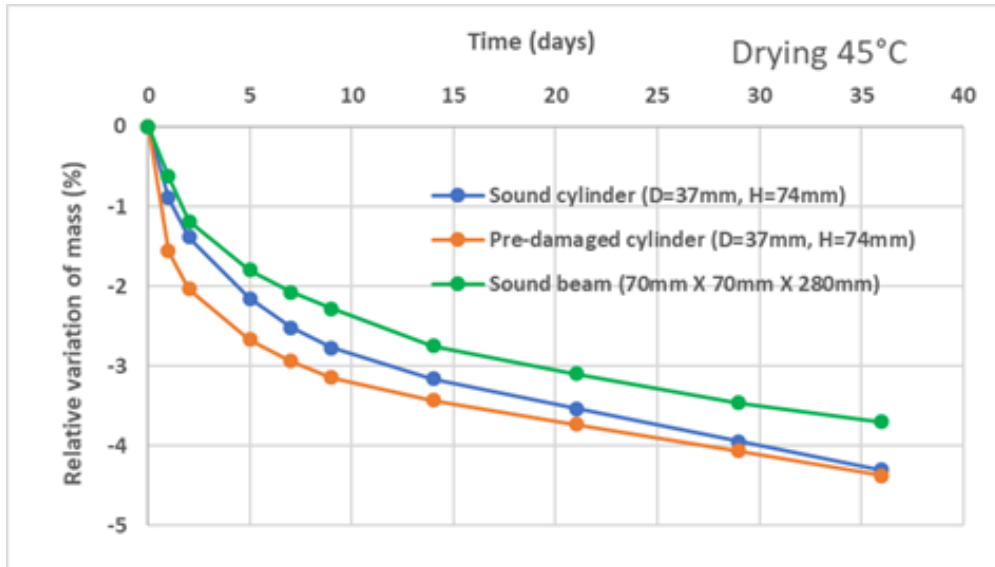


Figure 3-11 Comparison of relative variation of mass for different sound specimens with or without pre-damage.

Uniaxial compression tests are therefore performed on 2 pre-damaged samples (#E1 and #E8) and the axial stress-strain curves are plotted below (Figure 3-12). The behaviour of both samples is similar and almost linear up to 25 MPa. If this behaviour is compared to previous experiments on samples without pre-damage at different states of carbonation (Figure 3-13), one can note a clear decrease in the failure strength of the pre-damaged sample. Its behaviour is more comparable to the one observed on the 100 %+ carbonated sample (predominance of a linear behaviour up to peak strength). However, the pre-damaged sample is not carbonated so the gap filling cannot be an explanation. Hence, this could be an indication that the presence of existing cracks will limit the extent of creation of new cracks during the uniaxial compression test. The non-linearity could be more tied to this creation of new cracks rather than sliding between edges of existing cracks. Additional tests are needed to address this potential explanation.

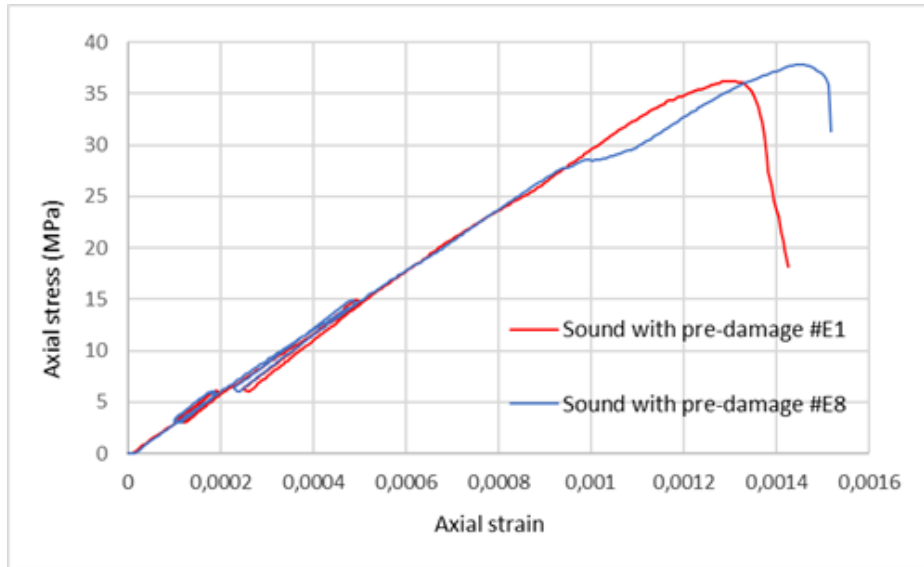


Figure 3-12 Axial stress-strain behaviour of samples with pre-damage under uniaxial compression.

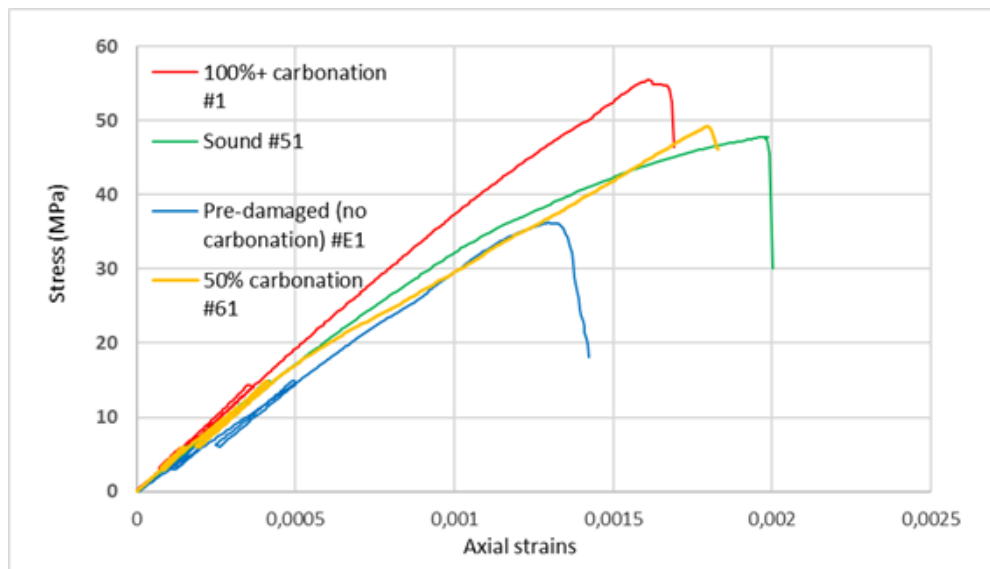


Figure 3-13 Comparison of axial stress-strain curves for different samples under different conditions in uniaxial compression.

Finally, a quantitative comparison of material properties between sound samples with or without damage is presented in Table 3-4. It confirms that the pre-damaging protocol decreases by -23% the strength of concrete and by -6% its Young's modulus. Therefore, the effectiveness of this protocol is confirmed. The Poisson's ratio remains in the same range as in previous tests (0.24-0.26) without any clear effect.

Table 3-4 Elastic properties (E, ν) and failure strength (R_c) for sound samples with or without pre-damage (with discarded sample).

| Sample state | Sample # | R_c (MPa) | E (GPa) | ν (-) |
|-------------------------------------|----------------|-------------|-------------|-------------|
| Sound (no carbonation) | 52 | 47.8 | 37.1 | 0.26 |
| | 53 | | | |
| | 54 | 49.3 | 38.7 | 0.25 |
| | Average | 47.8 | 37.1 | 0.26 |
| Pre-damaged sample (no carbonation) | E1 | 36.2 | 35.6 | 0.24 |
| | E8 | 37.8 | 34.0 | 0.24 |
| | Average | 37.0 | 34.8 | 0.24 |

3.2 Degradation of the steel concrete bond under atmospheric carbonation (LaMCube/LMDC/Andra)

The concrete was characterized at the end of an autogenous curing period at $20^\circ\text{C} \pm 1^\circ\text{C}$. The compressive strength and the modulus of elasticity were respectively measured on 4 and 3 cylinders 112.8 mm in diameter and 220 mm in height. The mean value of the compressive strength is $46.3 \text{ MPa} \pm 1.7 \text{ MPa}$. The mean value of the modulus of elasticity is $38.3 \text{ GPa} \pm 0.7 \text{ GPa}$. The porosity was $16.7 (\pm 0.3 \%)$.

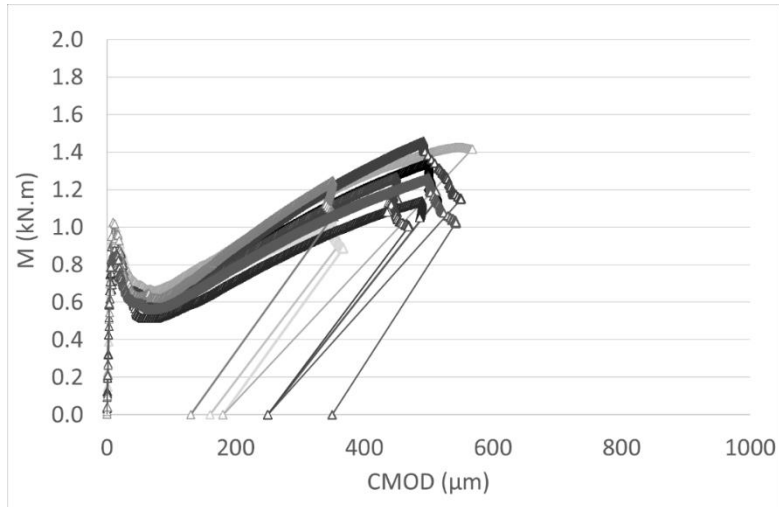
3.2.1 Top bar effect and impact of the mechanical damage

The Figure 3-14 presents the evolutions of CMOD measurements vs bending moment applied for the three families of prisms:

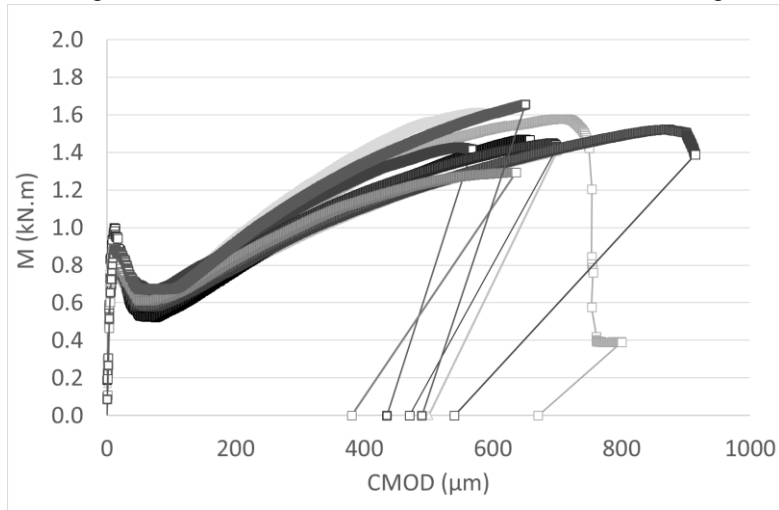
- prisms with residual targeted crack width “w1”, i.e. the SCI with the lowest mechanical damage
- prisms with residual targeted crack width “w2”, i.e. the SCI with the highest mechanical damage
- prisms with top bar effect with residual targeted crack width “w1”

These graphs can be divided in two phases. The first phase represents a linear behaviour of the reinforced concrete prism until a value of the bending moment inducing a flexural cracking. This crack appears when the stress reaches the tensile strength of concrete in the central part of the prism, in the lower fibre. The second phase corresponds to the composite behaviour of a cracked reinforced concrete element, with the softening post-cracking behaviour of the concrete coupled with the steel reinforcement contribution. Thus, the curve decreases and then increases thanks to reinforcement action. In case of prisms with top bar effect, bending moment values to reach the targeted crack width value are smaller than the value leading to cracking. This reveals that rebar anchorage length on the support in this configuration of three-bending test is not sufficient. The rebar probably slips because of the lower bond with concrete due to the top bar effect.

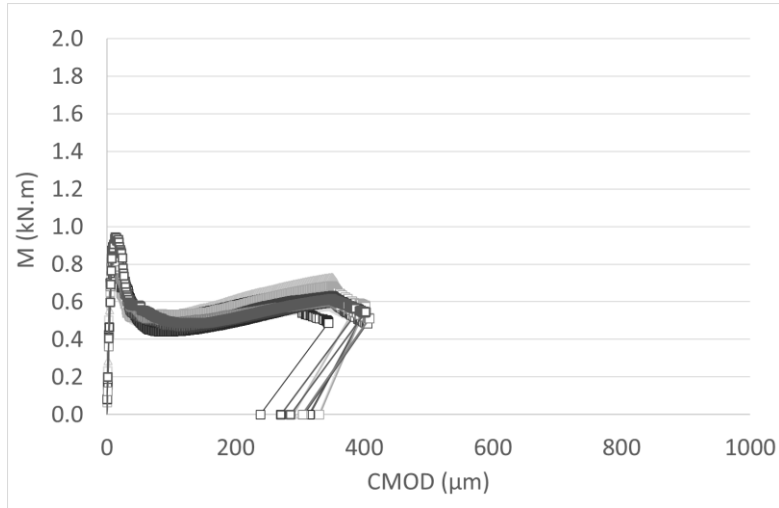
The objective was to reach a crack width higher than the targeted value ($w_1 > 200\text{-}300 \mu\text{m}$ and $w_2 > 400 \mu\text{m}$) considering the elastic reversible behaviour when unloading. The wedges were placed just before unloading to maintain the desired crack width after unloading. However, even with the placement of wedges, some variability on the residual crack width values is observed, whatever the prism family. It was rather difficult to place the wedges, because of the tortuosity and the variability of the crack width along the depth of the prism, on its lower side. Then, residual crack width can be different even with the same value before unloading.



w1 residual targeted crack width: SCI with lowest mechanical damage



w2 residual targeted crack width: SCI with highest mechanical damage



top bar effect with residual targeted crack width w1

Figure 3-14 Evolutions of CMOD measurements vs bending moment.

The Figure 3-15 presents the values of the residual crack width for:

- each prism: n°1 to 3
- for each family: w1, w2, or w1 with top bar effect (TP)
- for prisms used for reference pull-out tests without carbonation, for prisms which were stored in the only Phase A, and for prisms which were stored successively under Phases A and B.

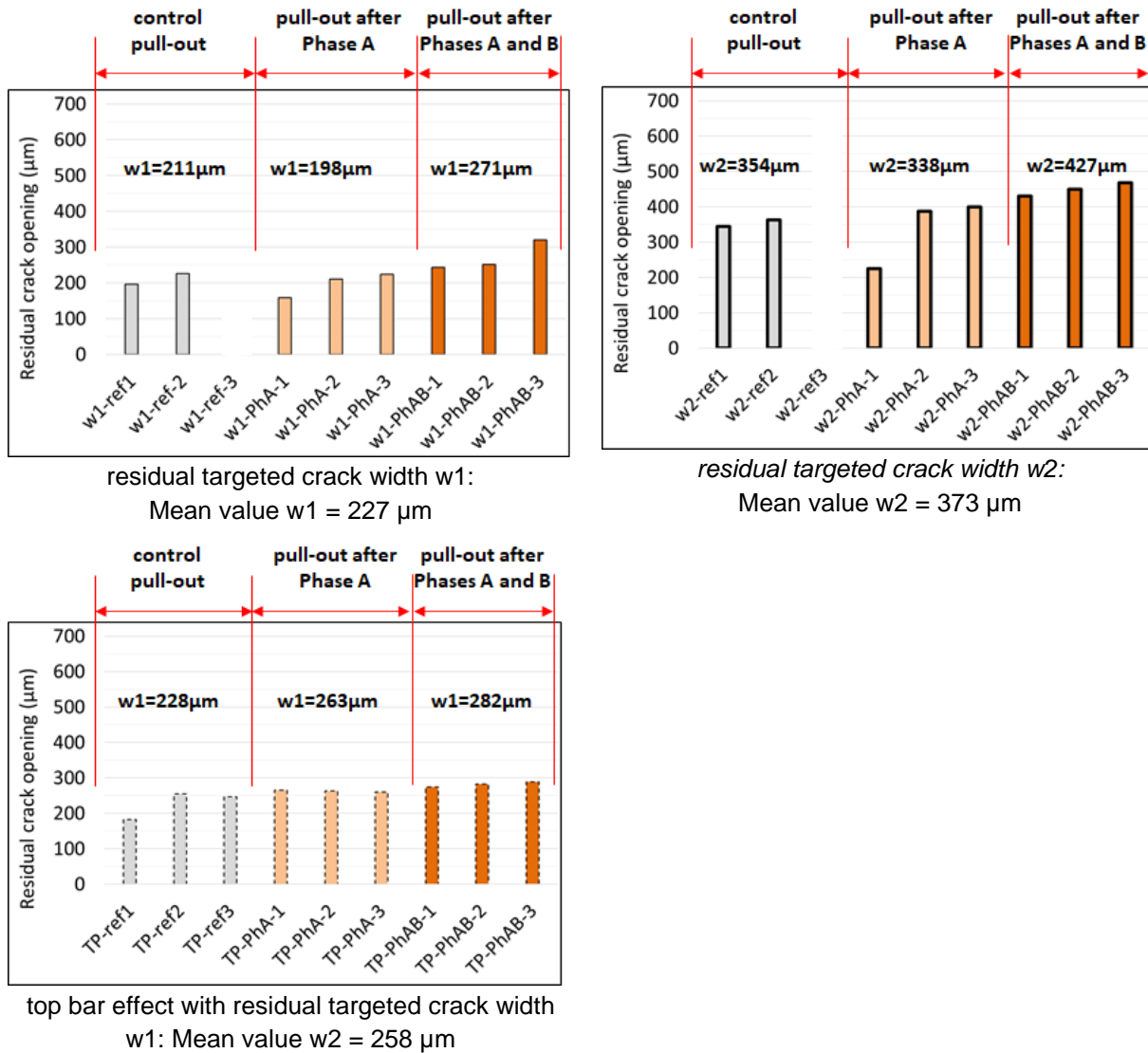
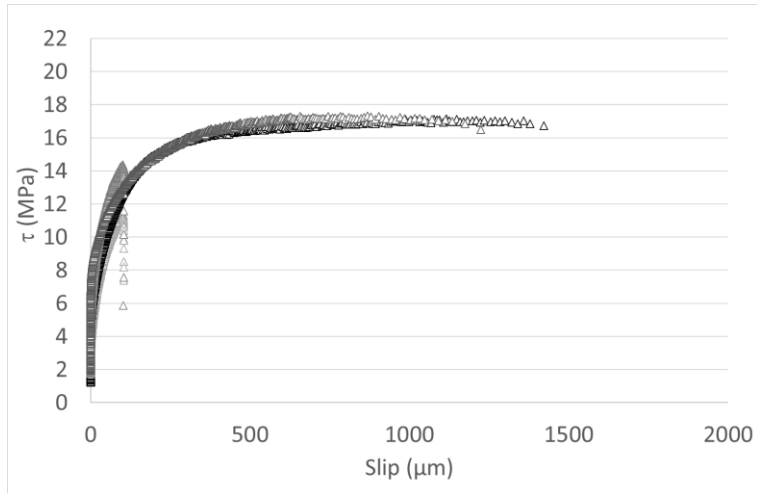
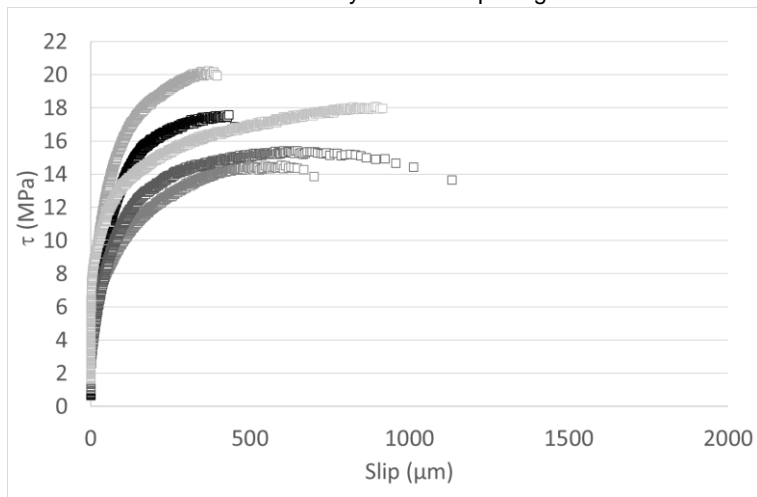


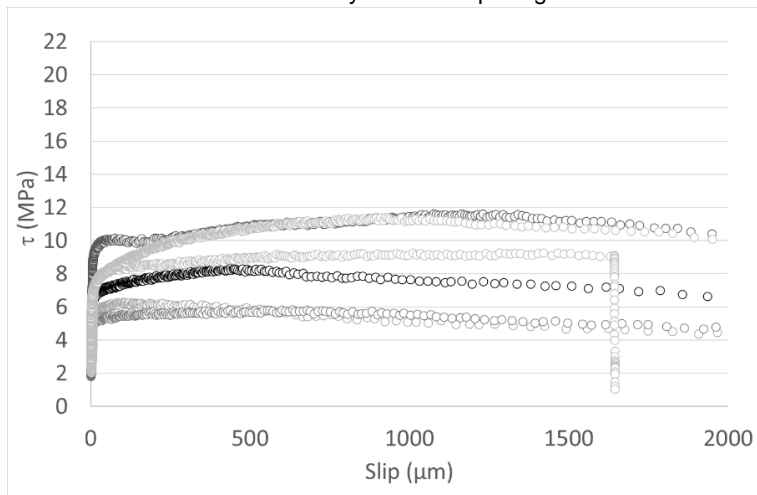
Figure 3-15 Residual crack width values for each prism, each degradation type of SCI, and each future storage conditions.



w1: failure by concrete splitting



w2: failure by concrete splitting



top bar effect with crack width w1: failure by rebar slipping

Figure 3-16 Evolution of shear stress vs slip of steel rebar for each reference pull-out test samples without carbonation and for each degradation type of SCI.

To improve the precision, the residual crack width had been measured on the two sides at the bottom of cracks using a video microscope. Experimental problems occur during tests for two prisms. There are no values of crack width for w1-ref-3 and TP-w2-ref-3.

Globally, the residual crack width values correspond to the interval of values desired:

- w1 \approx 200-300 μm (targeted): 227 μm (\pm 58 μm) for w1 and 258 μm (\pm 31 μm) for w1 with top bar effect
- w2 \approx 400 μm (targeted): 373 μm (\pm 113 μm)

However, the spread of the results is not negligible. Then, the samples have been gathered by group based on their future storage conditions. The samples with the highest values of crack width are subjected to phases A and B to induce more steel corrosion.

The Figure 3-16 presents the evolutions of shear stress value vs the slip between steel rebar and concrete for each reference pull-out test samples, after autogenous curing and without carbonation, for each family: w1, w2, and w1 with top bar effect. The shear stress is calculated from the force value and anchorage length of the rebar (60 mm) in concrete.

The curves are classical for pull-out tests with a linear phase followed by a second one characterized by a progressive decrease of the rate until a maximum value of the shear stress and a plateau. A greater variability is observed for pull-out test sample with w2 and top bar groups of samples, compared to w1 group (except for 2 tests).

The failure is by concrete splitting for w1 and w2 group whereas the rebar slips for top bar effect group revealing the presence of decohesion at SCI.

3.2.2 Effect of corrosion according to exposure conditions and the initial state of the concrete (top bar effect and/or level of crack opening)

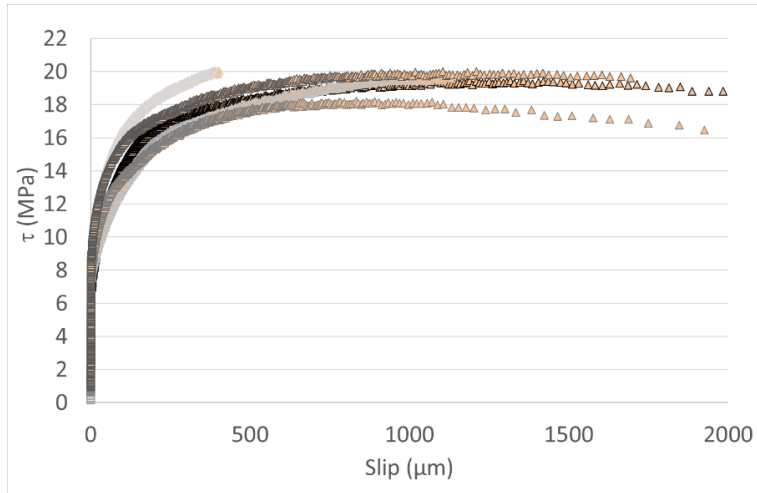
During the phase A of accelerated atmospheric carbonation, a rainbow pH indicator was used to analyse the carbonation depth on concrete block cast with other samples, and also at the SCI after pull-out testing. This indicator is more precise and non-toxic compared to phenolphthalein (Thiel and Gehlen, 2019). It turns green when the pH is lower than 11 and purple when higher, whereas with a phenolphthalein indicator, the non-carbonated part of the concrete turns purple at a pH above 9.

The measures on the concrete blocks stored in the same conditions of phase A show a carbonation depth of:

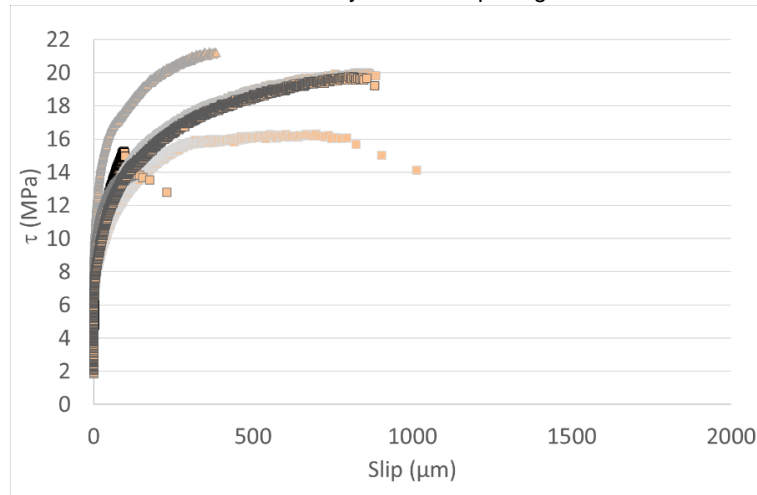
- 3 mm at 7 days
- 7 mm at 28 days
- 10 mm at 70 days, i.e. at the end of the phase A.

The analysis at the SCI using the rainbow indicator after breaking the samples following the pull-out test does not show carbonation. However, it takes more seconds to turn to purple in case of w2 and top bar effect groups in comparison with w1. This could demonstrate that the pH is closer to 11 in that case and that carbonation is more advanced due to SCI decohesion.

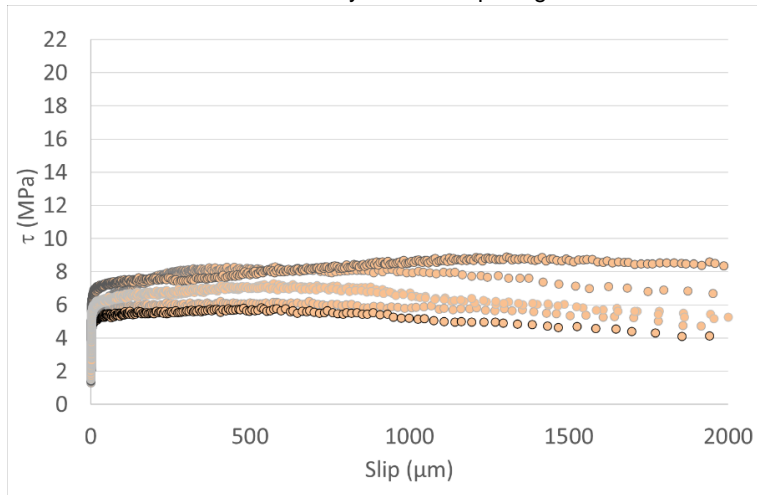
The Figure 3-17 presents the evolutions of shear stress value vs the slip between steel rebar and concrete for the pull-out test samples after phase A of atmospheric carbonation.



w1: failure by concrete splitting



w2: failure by concrete splitting



top bar effect with crack width w1: w1: failure by rebar slipping

Figure 3-17 Evolution of shear stress vs slip of steel rebar and for each degradation type of SCI after phase A.

The results are relatively similar to those for reference samples without carbonation in terms of curves forms, type of failure, and variability greater for w2 and top bar effects groups of samples.

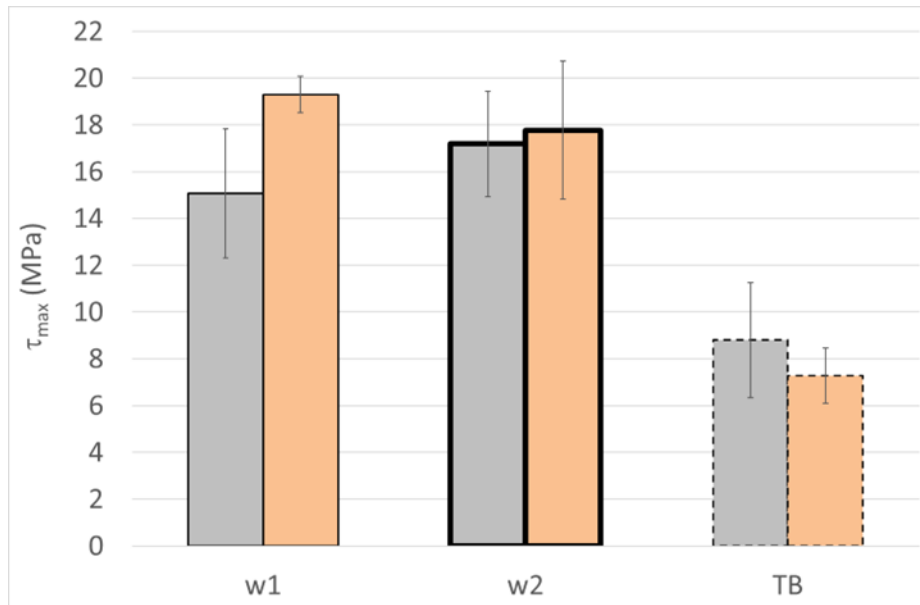


Figure 3-18 Comparison of the mean value of maximum shear stress (with standard deviation) for each degradation type of SCI (w1, w2 and top bar effect group “TP”), for reference samples (in grey) and after phase A (in orange).

Figure 3-18 synthesises the maximum values of the shear stress for each group, in cases of reference conditions without carbonation and after phase A of atmospheric condition.

The results for reference samples without carbonation show a slightly higher mean value of the maximum shear stress for crack width w2 compared to that of w1. The larger crack opening does not seem to have caused more damage of SCI. However, the difference and the variability of the results in case of w2 group of samples have to be taken into account to moderate this analysis. The probable higher damage around the crack tip could also induce presence of concrete particles which could increase the friction (maybe particles from mortar phase of the concrete or cement paste, since aggregates at SCI do not seem broken from specimens’ observation after failure). The results for top bar effect group clearly reveal the strong impact of the decohesion due to material behaviour at fresh state in case of reinforcement rebar located at height in a formwork.

After the phase A of atmospheric carbonation, the maximum shear stress increases significantly for w1 group and slighter for w2 group, whereas it decreases for top bar effect group.

These behaviours cannot be attributed to carbonation, as it is not detected at the SCI, or maybe with a lower pH for w2 and top bar effect revealing a beginning of carbonation. The explanation is probably the lower mean values of crack width for the w1 and w2 groups subjected to atmospheric carbonation compared to those of reference samples (Figure 3-15):

- w1 group: 198 μm for reference condition without carbonation, and 211 μm for phase A group
- w2 group: 354 μm for reference condition without carbonation, and 338 μm for phase A group

In case of top bar samples, it is the opposite since the mean value of crack width for reference group, 228 μm is lower than for the phase A group, 263 μm , explaining the lower value of the maximum shear stress instead of a carbonation effect.

3.3 Conclusion for part 3

The chemo-mechanical evolution of unsaturated concrete subjected to accelerated atmospheric carbonation has been investigated on concrete specimens (LaMCube) and on reinforced concrete ones (LMDC) with the same concrete. The mean values of its compressive strength and modulus of elasticity, after 28-day autogenous curing at 20 °C, were respectively $46.3 \text{ MPa} \pm 1.7 \text{ MPa}$ and $38.3 \text{ GPa} \pm 0.7 \text{ GPa}$. The porosity was $16.7 \% \pm 0.3 \%$.

The aim of the study at concrete scale (LaMCube) was to assess the effects of carbonation coupled with drying on uniaxial and triaxial compression. After the 20°C autogenous curing, the Ø37x74 mm specimens (cored from bigger beams) were successively stored during 7.5 months in lime-saturated water, 19 days at 20 °C and 65 %RH, 43 days at 45°C and finally 40 days in accelerated carbonation at 20 °C, 65 %RH, 50 % CO₂. Three states were studied: sound state, 50% and 100%+ carbonation (state 100% carbonated as detected by phenolphthalein plus additional days of carbonation, i.e. 40 days of carbonation for these samples). The main conclusions from uniaxial compression tests and triaxial compression tests with 3 MPa confining pressure, (compressive strength, modulus of elasticity, Poisson's ratio, compression behaviour law), are the following:

- Carbonation increases the modulus of elasticity, slightly for 50 % carbonation (+3 %) and (+10 %) at 100 % carbonation. Compressive strength at 50 % carbonation is rather similar to sound concrete one whereas it is strongly improved for 100 %+ carbonation (+25 %), but with a more fragile failure. This could be due to the calcite which fills the gaps and the microcracks limiting the formation of new ones. The differential carbonation shrinkage between the inner part and the outer carbonated part could also act as a confining pressure mitigating cracks nucleation and opening. The Poisson's ratio values do not seem influenced by carbonation.

- As expected for triaxial compression tests with 3 MPa confining pressure, the compressive strength is increased from around 55 % compared to uniaxial case, whatever the carbonation level. The effects of carbonation on modulus of elasticity and compressive strength with confining pressure are similar to uniaxial compression, with low effect at 50 % carbonation and a strong increase at 100 %+ carbonation. The Poisson ratio's values are rather identical for uniaxial and triaxial compression, and independent of carbonation state.

The objectives of the study of reinforced concrete behaviour (LMDC) were to analyse the coupled effects of previous steel-concrete interface (SCI) degradation, mechanical damage or top bar effect, on corrosion initiation and onset, and also the corrosion effects on steel-concrete bond. 100x100x400 mm reinforced concrete prisms with or without top bar effect were tested by three point-bending test to create a flexural crack favouring carbonation to reach the SCI. Two levels of loading were applied to induce two distinct mechanical damages of SCI, characterized by the residual crack width after unloading, w1 (200-300 µm) and w2 (400 µm). In case of top bar effect prisms, only the w1 residual crack width is applied. The accelerated atmospheric carbonation was 3 % ±0.5 % CO₂, 57 % RH ±3 % RH and 20 °C ±1 °C. The carbonation evolution was 3 mm at 7 days, 7 mm at 28 days and finally 10 mm at 70 days, end of the phase. Each prism was sawn to provide two pull-out test specimens used to characterize the steel-concrete bond. The main conclusions are the following:

- Control specimens without carbonation: the failure is by concrete splitting for w1 and w2 groups whereas the rebar slips for top bar effect group due to the presence of decohesion at SCI. A slightly higher mean value of maximum shear stress for w2 group is observed compared to that of w1 one. Higher SCI damage could induce the presence of concrete particles which could increase the friction. Top bar effect significantly decreases the maximum shear stress.

- Specimens subjected to carbonation condition: the failure and the shear stress vs slip curves are similar to those of control specimens. After 70-day carbonation condition, the maximum shear stress increases for w1 group and slighter for w2 group, whereas it decreases for top bar effect group. However, this tendency cannot be explained by carbonation since it is not detected at the SCI. It is probably due to differences in residual crack width values, and then differences in SCI mechanical damages, for control and carbonated samples.

3.4 References for part 3

- C. Thiel, C. Gehlen, On the determination of carbonation in cementitious materials, Proceedings of the International Conference on Sustainable Materials Systems and Structures (SMSS2019) Durability, Monitoring and Repair of Structures, Baricevic et al editors, Rovinj, 2019, 373-380.

4 Chemo-mechanical evolution of saturated concrete

4.1 Concrete ageing in contact with rock (Empa, PSI, SCK-CEN)

4.1.1 Non-Destructive Evaluation (NDE) measurements of specimens aged in contact with Opalinus Claystone (OPA)

4.1.1.1 Non-destructive mechanical characterization by Single-MODE Resonant Ultrasound Spectroscopy (SIMORUS)

Figure 4-1 till Figure 4-5 report the results for the complex-valued dynamic Young's modulus as obtained from the longitudinal SIMORUS measurements. Each figure is organized in the same way, comprising two insets: the left (or (a)) inset shows the actual Young's modulus (E^{dyn}) values while the right (or (b)) inset shows the longitudinal wave amplitude attenuation coefficient (α_L) ones. The values are sorted in distinct *ensembles*, labelled as *A*, *B* and *C*, based upon the respective specimen distance from the interface with the OPA, to allow for assessing any eventual influence of the latter variable. Notice that the *A* specimens were those directly in contact with the OPA interface, thus with zero distance. The distance for the *B* and *C* specimens is indicated in each figure's caption. The markers in these figures, pointed at by the green arrows, refer to the specimens, which underwent X-ray tomography. The vertical lines express the range of values either from multiple repeated measurements on the same specimens (e.g., 2274-A1 and 2274-B6 in Figure 4-1) or from measurements on specimens of the same *ensemble*. The letter *N* in the legend indicates either the number of repeated measurements on the same specimens or the number of specimens in an *ensemble*. The first range type provides an estimate of the data scatter due to measurement repeatability level. The second range type provides an estimate of the data scatter due to the material heterogeneity. All the values for the single specimens, reported in these 5 figures, are available in the corresponding data records curated within MAGIC's Interactive Database of Cement Properties (IDCP, files `FeatVars_2274_ESDRED_Concrete_14YearsOld.xlsx`, `FeatVars_2275_LAC_Concrete_14YearsOld.xlsx`, `FeatVars_2276_OPC_Concrete_14YearsOld.xlsx`, `FeatVars_2277_OPC_Mortar_9YearsOld.xlsx`, `FeatVars_2278_ESDRED_Mortar_9YearsOld.xlsx`).

Beyond providing the bare data about the investigated cementitious material types, some preliminary conclusions can be drawn from these results. They are preliminary because their reliable validation requires interpreting such data by considering also the microstructural and chemical characterization by SEM/EDX analysis, whose results are not yet available at the time of this report.

The first conclusion is methodological: independently of the material type, the E^{dyn} data scatter due to the material heterogeneity was larger than that due to the measurement repeatability level, while the two data scatter types were on average similar for α_L . Such difference can be recognized across Figure 4-1 and 4-2 by noticing that the E^{dyn} error bar for repeated measurements on single specimens is typically significantly shorter than that for the specimen *ensemble*. On the contrary, the α_L error bars of the two types are typically comparable, without evidence of any variation pattern. A possible explanation for such difference is that, on the one side, α_L strongly depends not only on the viscosity properties but also on the meso- and micro-structural ones, including, the eventual presence of cracks at multiple length scales (Saint-Pierre et al., 2007). On the contrary, E^{dyn} , as measured by longitudinal SIMORUS, is purely a macroscopic and bulk property, whose value is more strongly influenced by the average elastic moduli of the distinct material phases and by the air void content than by other meso- and microscopic features as cracks, porous patches and the capillary pore network (Philippidis et al., 2005, Gabrijel et al., 2020). Thus, on the one side, α_L is typically considered a more sensitive damage detection and evolution indicator than E^{dyn} , if it can be measured also at the reference material state. On the other side, E^{dyn} results are statistically more robust but mirrors just the bulk linear elastic properties of the composite material.

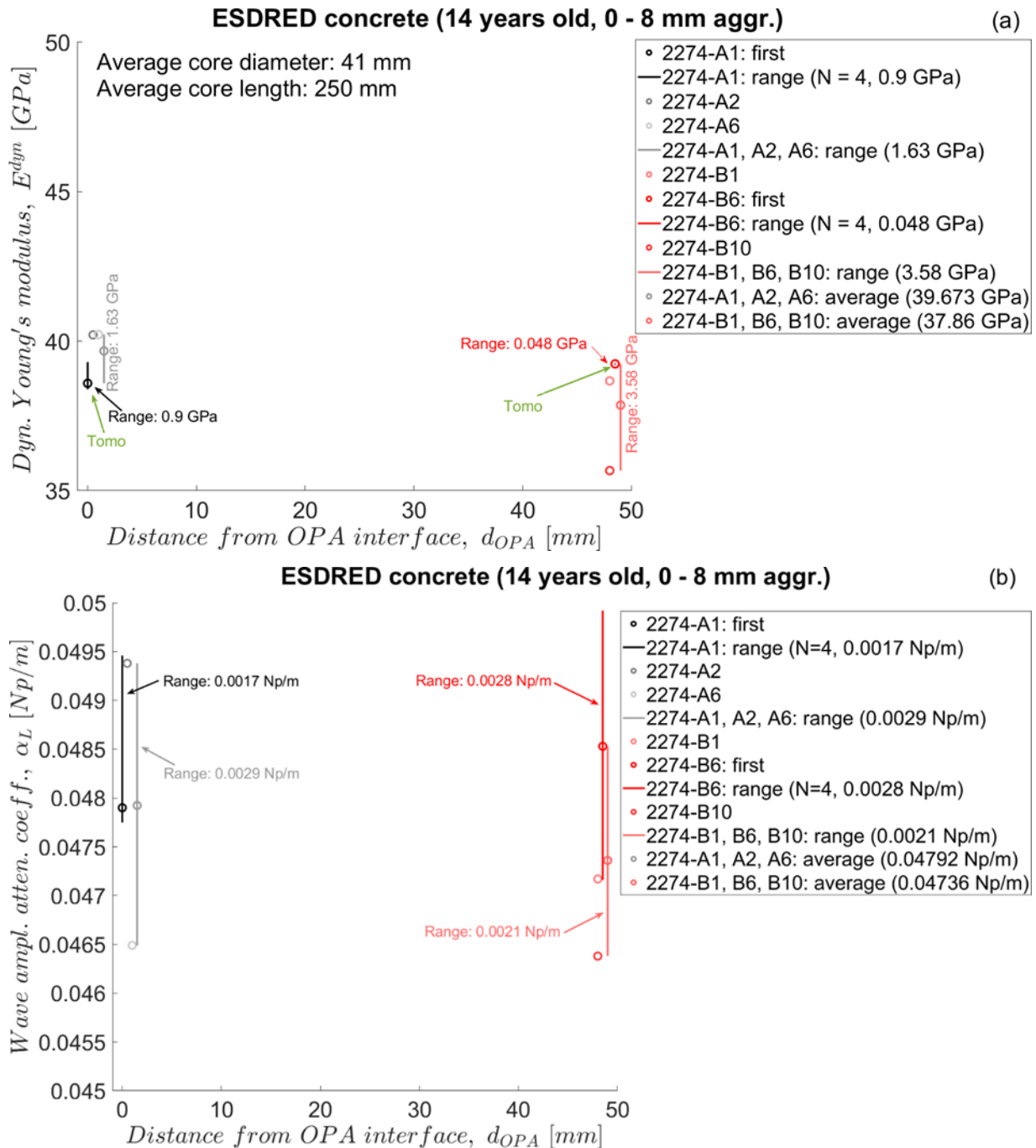
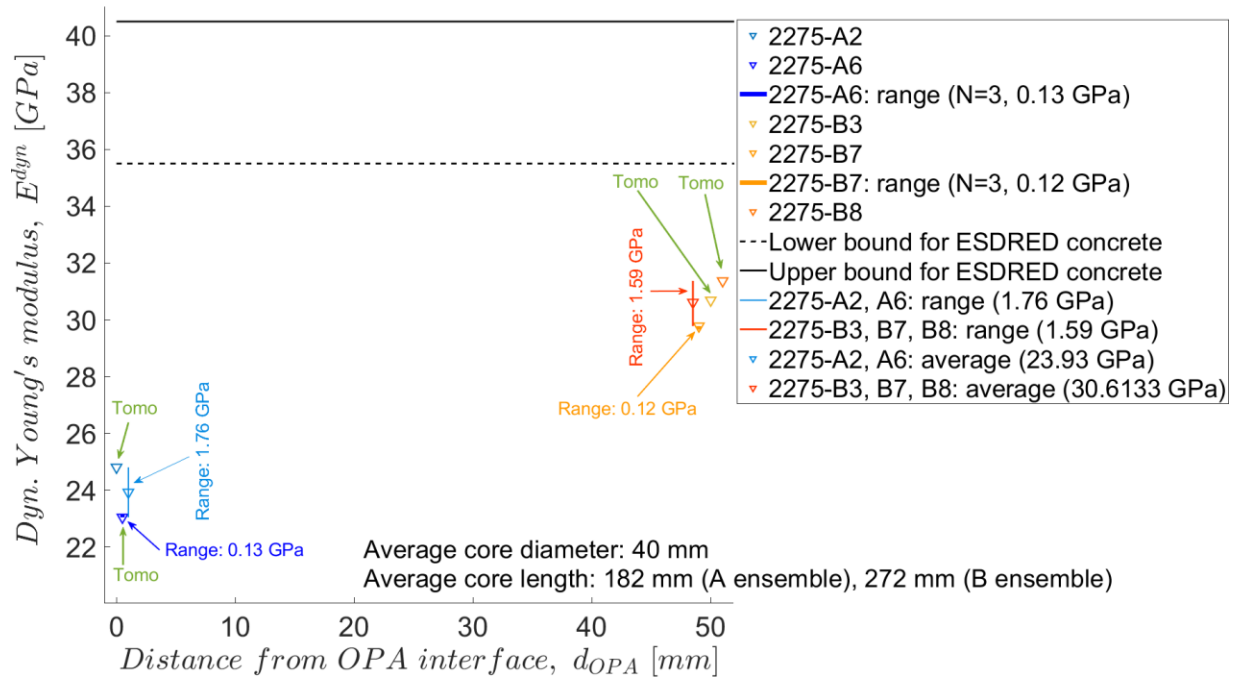


Figure 4-1 complex-valued, dynamic Young's modulus values (vertical axes) of the ESDRED (mix design Nr. 2274) concrete specimens, as a function of the specimen distance (d_{OPA} , horizontal axis) from the interface with the Opalinus Claystone (OPA). Each marker refers either to a single specimen or to the average value over the whole specimen ensemble. The 2274-A specimens all had a d_{OPA} value of 0 mm. Thus, their markers are artificially displaced horizontally, to improve their visibility. The 2274-B specimens had on average a d_{OPA} value of 47.2 mm. (a): real part of the complex-valued Young's modulus (E^{dyn}). (b): longitudinal wave amplitude attenuation coefficient (α_L), proportional to the imaginary part of the complex-valued Young's modulus and expressed in Neper per meter (Np/m).

LAC concrete (14 years old, 0 - 16 mm aggr.)

(a)



LAC concrete (14 years old, 0 - 16 mm aggr.)

(b)

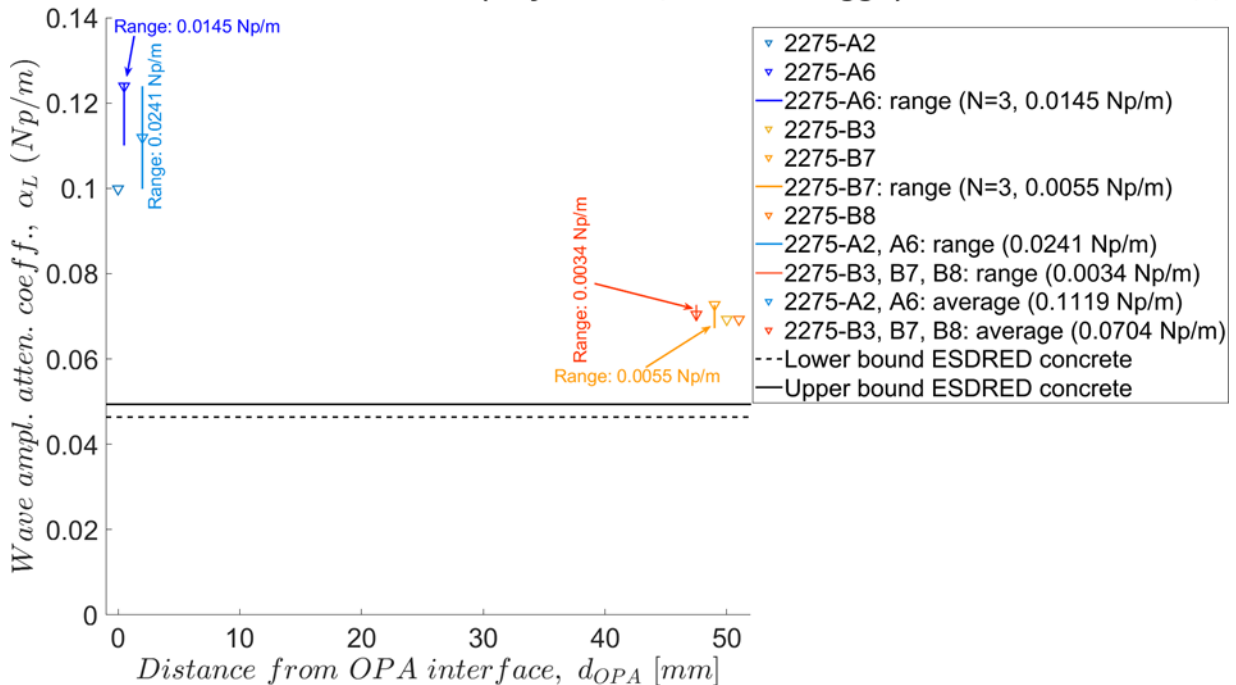
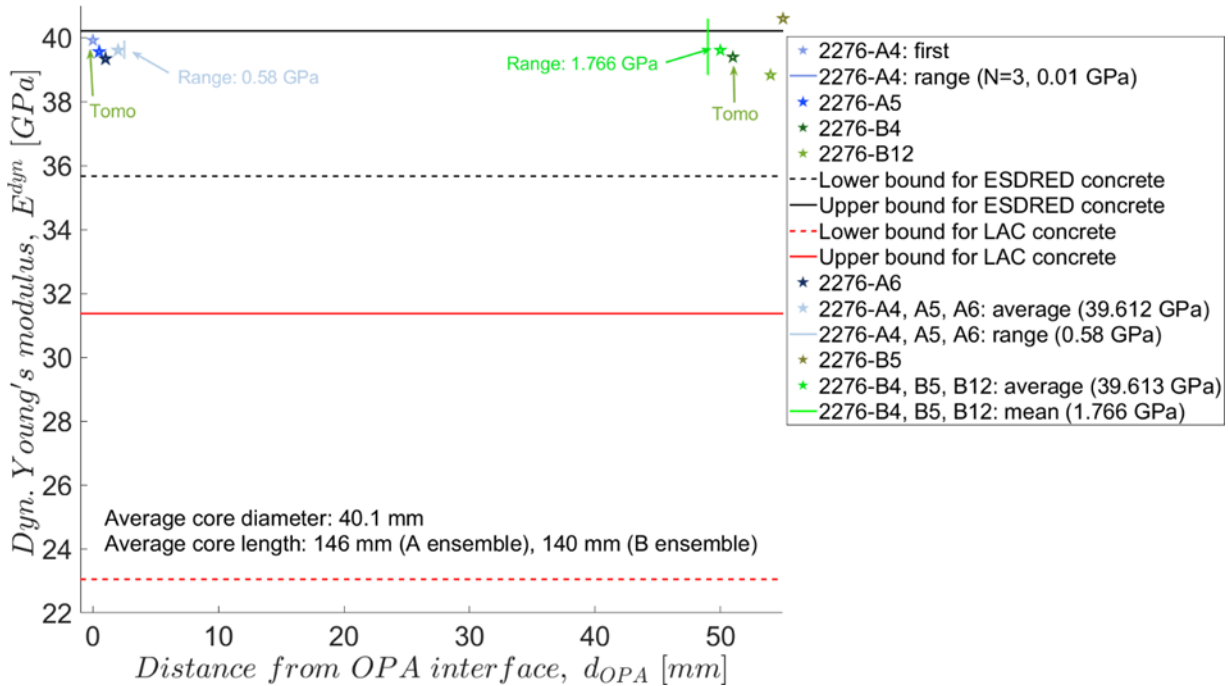


Figure 4-2 same as in Figure 4-1 but for the LAC concrete specimens (mix design Nr. 2275). In both (a) and (b), the dashed and solid horizontal lines indicate the lower and upper bounds, respectively, of the corresponding values for the ESDRED specimens (see Figure 4-1). For the 2275-B specimens, the average distance from the Opalinus Claystone's (OPA) interface was 49.9 mm. In both (a) and (b), when the vertical lines are not visible, it means that the range is smaller than the marker size.

OPC concrete (14 years old, 0 - 16 mm aggr.)

(a)



OPC concrete (14 years old, 0 - 16 mm aggr.)

(b)

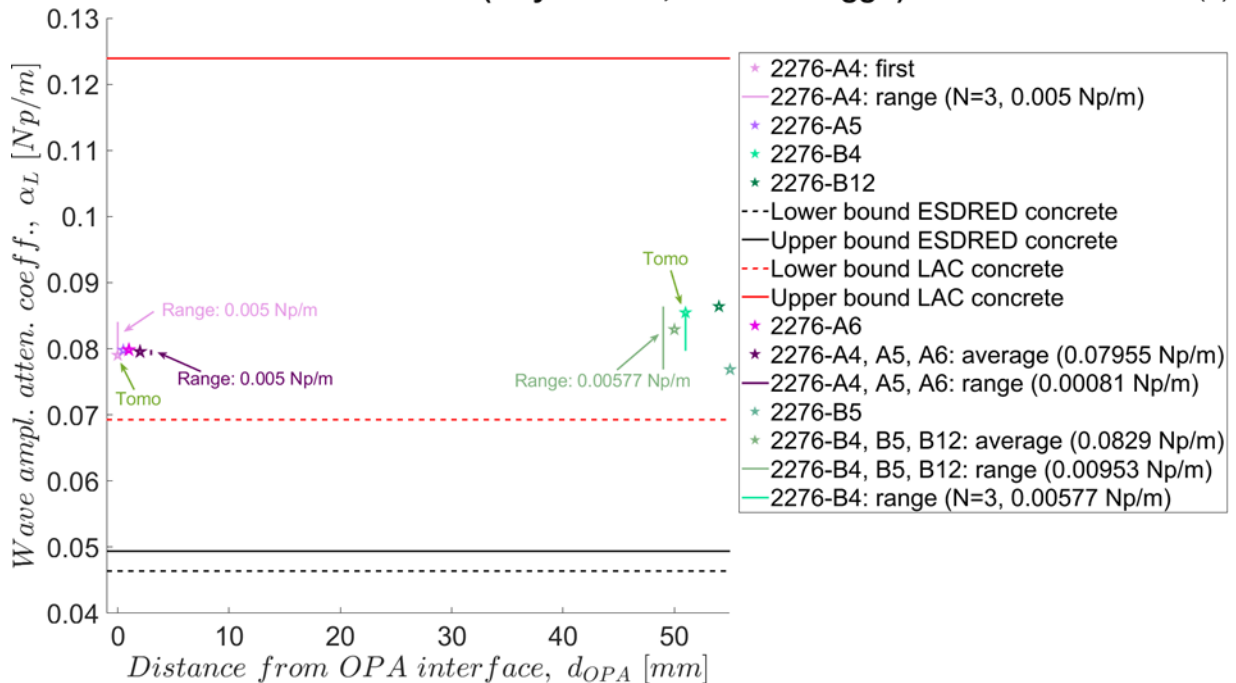
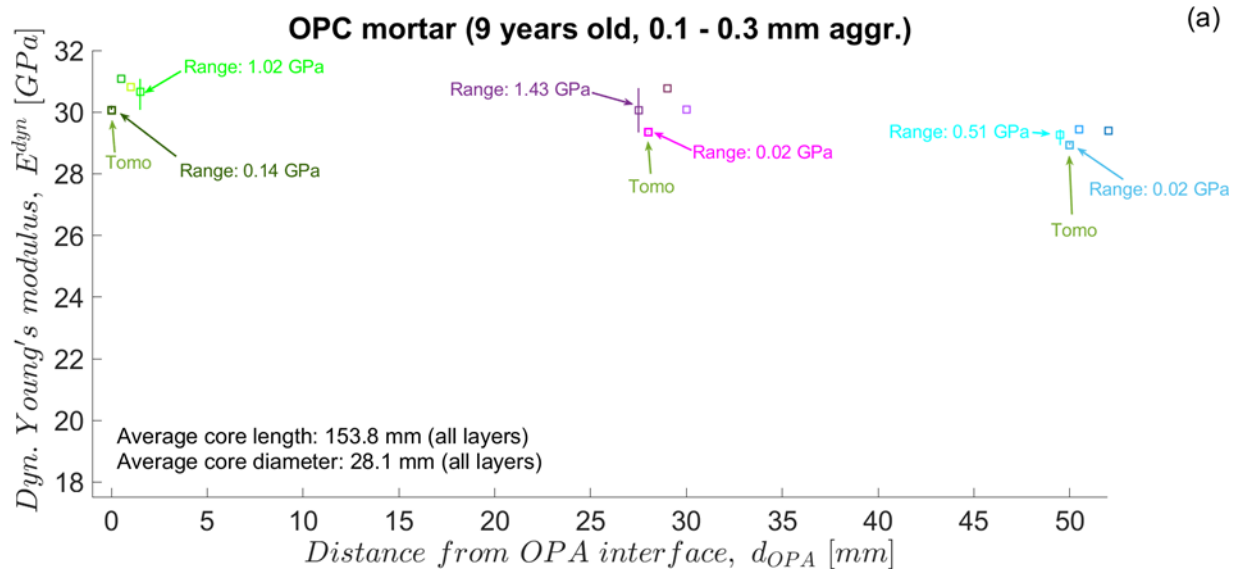
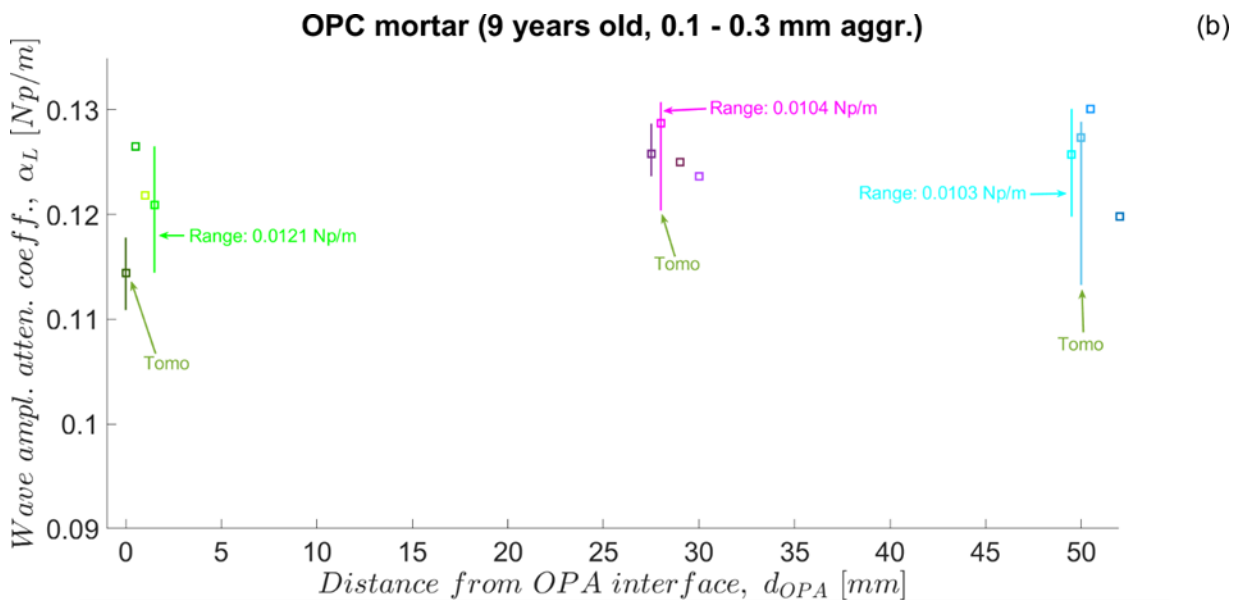


Figure 4-3 same as in Figure 4-1 but for the OPC concrete specimens (mix design Nr. 2276). For the 2276-B specimens, the average distance from the Opalinus Claystone's (OPA) interface was 49.2 mm. In both (a) and (b), the black, dashed and solid, horizontal lines indicate the lower and upper bounds, respectively, of the corresponding values for the ESDRED specimens (see Figure 4-1). The red, dashed and solid, horizontal lines indicate the lower and upper bounds, respectively, of the corresponding values for the LAC concrete specimens (see Figure 4-2). In both (a) and (b), when the vertical lines are not visible, it means that the range is smaller than the marker size.



| | | |
|-----------|-------------------------------------|--|
| ■ 2277-A2 | ■ 2277-C2 | ■ 2277-A2, A6, A8: average (30.66 GPa) |
| ■ 2277-A6 | ■ 2277-C4 | ■ 2277-B1, B4, B7: average (30.07 GPa) |
| ■ 2277-A8 | ■ 2277-C7 | ■ 2277-C2, C4, C7: average (29.25 GPa) |
| ■ 2277-B1 | — 2277-A2, A6, A8: range (1.02 GPa) | — 2277-A2: range (N=3, 0.14 GPa) |
| ■ 2277-B4 | — 2277-B1, B4, B7: range (1.43 GPa) | — 2277-B4: range (N=3, 0.02 GPa) |
| ■ 2277-B7 | — 2277-C2, C4, C7: range (0.51 GPa) | — 2277-C4: range (N=3, 0.07 GPa) |



| | | |
|-------------------------------------|-------------------------------------|---|
| ■ 2277-A2: first | — 2277-B4: range (N=3, 0.0104 Np/m) | — 2277-A2, A6, A8: range (N=3, 0.0121 Np/m) |
| — 2277-A2: range (N=3, 0.0069 Np/m) | ■ 2277-B7 | — 2277-B1, B4, B7: range (N=3, 0.005 Np/m) |
| ■ 2277-A6 | ■ 2277-C2 | — 2277-C2, C4, C7: range (N=3, 0.0103 Np/m) |
| ■ 2277-A8 | ■ 2277-C4: first | ■ 2277-A2, A6, A8: average (0.1209 Np/m) |
| ■ 2277-B1 | — 2277-C4: range (N=3, 0.0156 Np/m) | ■ 2277-B1, B4, B7: average (0.1258 Np/m) |
| ■ 2277-B4: first | ■ 2277-C7 | ■ 2277-C2, C4, C7: average (0.1258 Np/m) |

Figure 4-4 same as in Figure 4-1 but for the OPC mortar specimens (mix design Nr. 2277). For the 2277-B specimens, the average distance from the Opalinus Claystone's (OPA) interface was 29.11 mm. For the 2277-C specimens, it was 49 mm. In (a), when the vertical lines are not visible, it means that the range is smaller than the marker size.

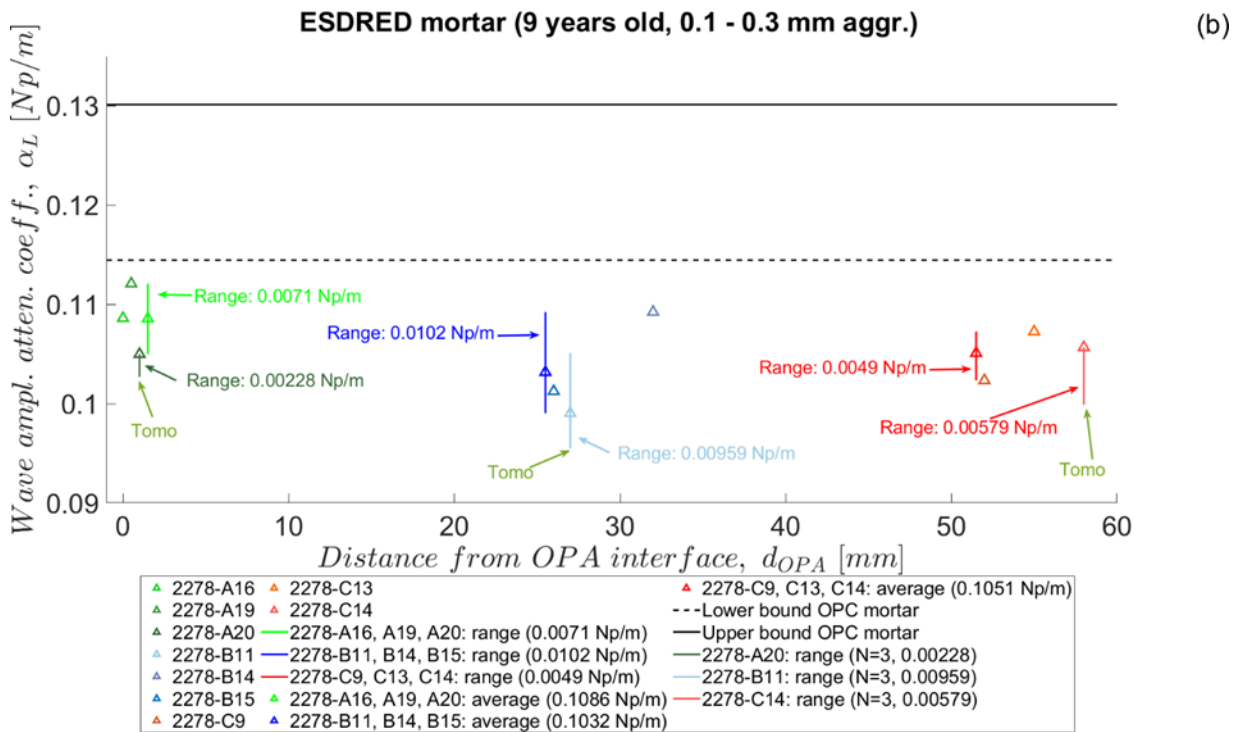
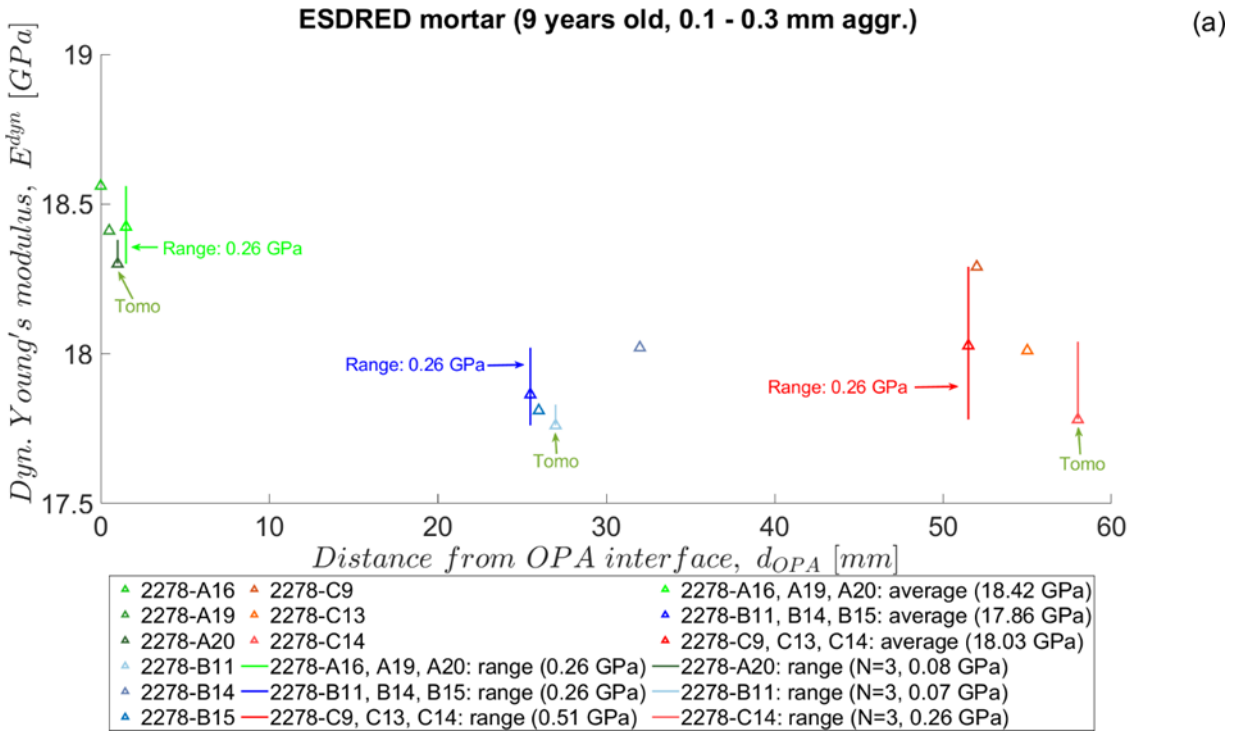


Figure 4-5 same as in Figure 4-1 but for the ESDRED mortar specimens (mix design Nr. 2278). For the 2278-B specimens, the average distance from the Opalinus Claystone's (OPA) interface was 29.2 mm. For the 2278-C specimens, it was 52.9 mm. Notice that repeated measurements on single specimens were not available at the time of this report. In (b), the dashed horizontal line indicates the lower bound of values for the OPC mortar (see Figure 4-4 (b)), while the solid one refers to the respective upper bound.

The second and most important conclusion is that the ESDRED and OPC specimens exhibited rather similar E^{dyn} values (38 – 40 GPa, average values) and about 33 % larger than the LAC ones (between 23 and 30 GPa, average values). The LAC specimens also exhibited the largest α_L values of all the 3 concrete types, followed by the OPC and ESDRED specimens. These results, considered alone, do not allow concluding that the LAC specimens were more mechanically degraded than the ESDRED and OPC ones, first, because the 3 concrete mix designs had distinct aggregate-to-binder (a/b) ratio (by mass) values (4.85, 7.25 and 8 for ESDRED, LAC and OPC, respectively). Second, the ESDRED concrete was cast with aggregate sieve size in the range 0 – 8 mm, while the LAC and OPC ones with 0 – 16 mm. Despite the three concrete types exhibited similar mass density values (measured on additionally cast 150x150x150 mm³ cubes at 90 days since casting, before compressive strength measurements, see Section 9.3.1.4 in the D16.3 Report), such difference may influence the aggregate spatial packing properties, thus the fluid transport ones, independently of the fact that, the aggregates were of the same type (round, stemming from river sediments). A more reliable comparison can be performed only between the LAC and OPC specimens, cast with more similar a/b values as well as identical aggregate sieve size range.

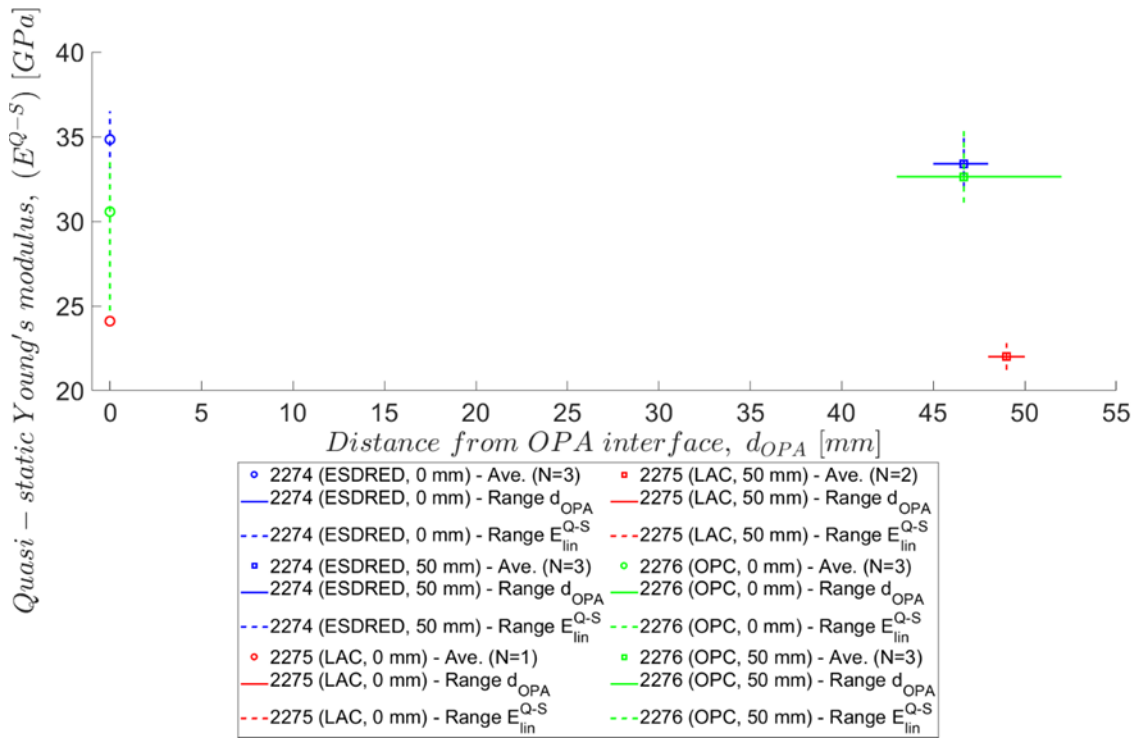
The third and last conclusion is that only the LAC specimens exhibited a clear and coherent spatial dependence of the mechanical properties on the specimen distance from the OPA interface: E^{dyn} was lower and α_L was higher for specimens directly at the interface than for specimens about 50 mm away. These two features may also point at a higher/faster degradation in the LAC concretes as in the two other ones.

Concerning the two mortar types, less clear conclusions can be drawn. While the ESDRED specimens exhibited much lower E^{dyn} values than the OPC ones, the opposite occurred for the α_L values. This apparently contradicting result may be explained by the extremely high air void content observed qualitatively by X-ray tomography in the ESDRED specimens, compared with the OPC ones (see below for details).

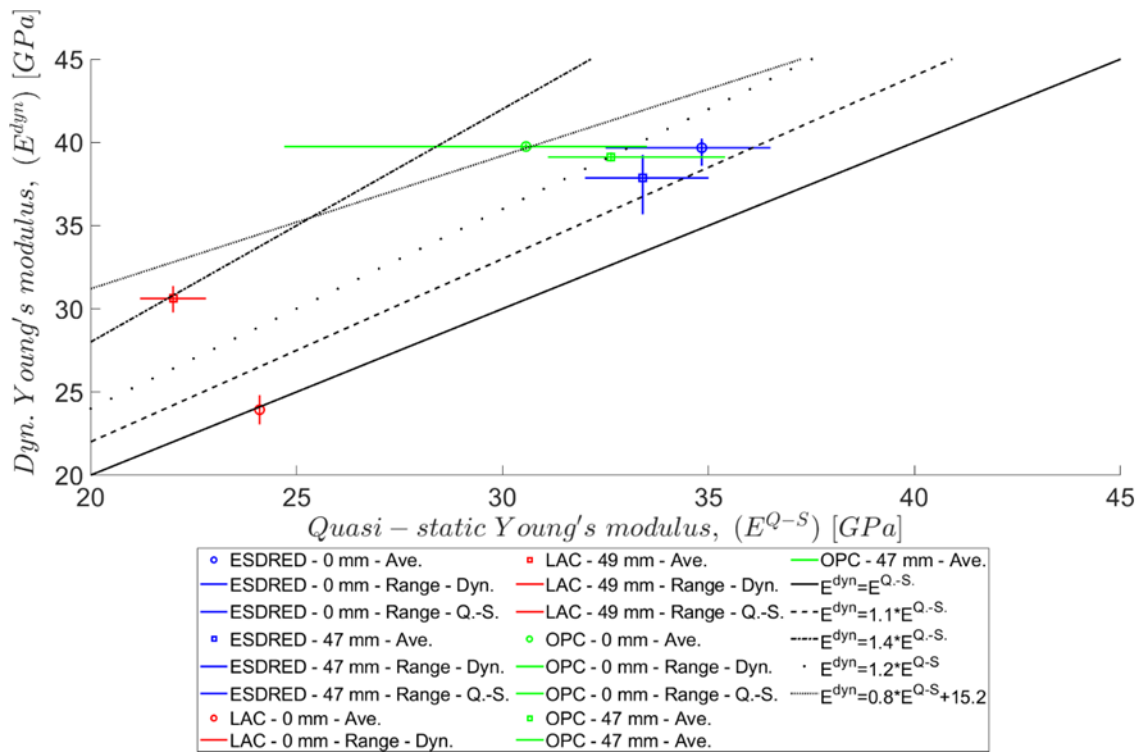
4.1.1.2 Destructive mechanical characterization: quasi-static Young's modulus and compressive strength

The quasi-static, compressive Young's modulus values for the 3 concretes are provided in Figure 4-6 (a). There, each marker refers to the average value over the respective specimen *ensemble*. Each horizontal, solid line indicates the range of values of the respective *ensemble*. Each vertical, dashed line indicates the range of values of the respective *ensemble*. The same applies to Figure 4-6 (b), which shows the correlation between the quasi-static (E^{Q-S} , horizontal axis) and the dynamic (E^{dyn} , vertical axis) Young's modulus values of the three concrete specimen *ensembles*. The lines in such figures provides some examples of theoretical relationships between the two variables. The solid line refers to the relationship E^{dyn} . The dashed and dashed-dotted lines refer to the $E^{dyn} = 1.1 \cdot E^{Q-S}$ and $E^{dyn} = 1.4 \cdot E^{Q-S}$ relationships, respectively. The coarsely and finely dotted lines refer to two phenomenological relationships originally proposed in Lydon and Balendran (1986) and in Swamy and Bandyopadhyay (1975), respectively, the latter adopted in the British testing standard BS8110 Part 2 (Neville, 2011).

Figure 4-6 (a) provides a similar picture as the dynamic ones, i.e., they hint at worse mechanical properties for the LAC concrete than for the two other types. No evident dependence from the OPA interface distance can though be inferred from the data available so far, which, for the specimens directly in contact with that interface, consists of a single point, thus no error bar could be estimated for such specimen *ensemble*. The qualitative analysis of the correlation between the dynamic and the quasi-static Young's modulus values (Figure 4-6 (b)) indicates that the dynamic values were up to 40 % larger than the quasi-static ones, a range in agreement with what reported in the literature (Popovics et al, 2008). The estimated values can thus be considered as meaningful proxies of the quasi-static ones.



(a)



(b)

Figure 4-6 (a): quasi-static, compressive Young's modulus values (E^{Q-S} , vertical axis) of the three concrete specimen ensembles (2274, 2275 and 2276), as a function of the specimen surface distance (d_{OPA} , horizontal axis) from the interface with the Opalinus Claystone (OPA). (b): correlation between E^{dyn} and E^{Q-S} values (markers), with some indicative theoretical models (lines) provided for reference.

Concerning the compressive strength (f_c) results, the data available so far adhere to the picture provided by the E^{dyn} and E^{Q-S} results: the LAC concrete exhibited the lowest values (about 24 MPa on average), followed by the OPC and ESDRED ones (about 36 MPa and 80 MPa, also on average, respectively); the ESDRED mortar specimens exhibited a lower value (about 40 MPa on average) than the OPC ones (about 80 MPa), again explainable based upon the extremely larger air void content of the former. No specific pattern for the dependence on distance from the OPA interface could be recognized.

4.1.1.3 Mesostructure non-destructive characterization by X-ray tomography

The qualitative inspection of the X-ray tomograms of the cored specimens allowed two essential observations. First, the LAC concrete cores were the only ones to exhibit evidence of resolvable (i.e., above 60 μm in size) damage features, mainly macroscopic cracks and disbonded Interfacial Transition Zones (ITZs), see Figure 4-7 for an example, while the ESDRED and OPC cores appeared completely undamaged above this length scale. The presence of these two damage features agrees well with the observation of lower E^{dyn} , E^{Q-S} and f_c values for the LAC concrete than for the two other concrete types. It is not possible for the Team either to exclude or to confirm that the sampling by coring induced such cracks, However, even in the case the coring did induce the observed cracks, their occurrence in the LAC concrete specimens and not in those of the two other concrete types still suggests that the former material was more degraded than the other two, given that the same exact workflow was followed for the coring and the three cast concrete volumes were subjected to the same exact boundary conditions.

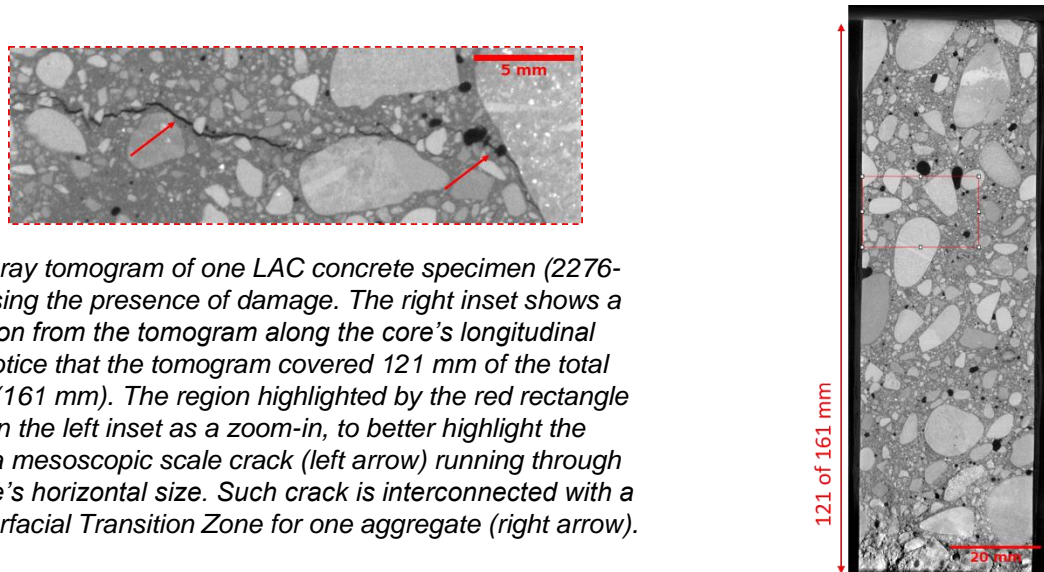


Figure 4-7 X-ray tomogram of one LAC concrete specimen (2276-A6), showcasing the presence of damage. The right inset shows a cross-section from the tomogram along the core's longitudinal direction. Notice that the tomogram covered 121 mm of the total core's length (161 mm). The region highlighted by the red rectangle is shown in the left inset as a zoom-in, to better highlight the presence of a mesoscopic scale crack (left arrow) running through half of the core's horizontal size. Such crack is interconnected with a disbonded Interfacial Transition Zone for one aggregate (right arrow).

The eventual gradient with the distance from the OPA interface could not yet be correlated with differences in tomographic features between specimens at the interface and about 50 mm far away. The mentioned future voxel value distribution analysis could further support such a validation. Second, both the ESDRED and OPC mortar cores showed no resolvable (i.e., above 44 μm in size) signs of damage and the ESDRED exhibited a significantly larger air void content, not yet quantified at the time of this report but to be performed before MAGIC's end.

Thus, overall, X-ray tomography could provide information that supports the interpretation of the results obtained from the mechanical characterizations, with clear evidence of severe damage at a length scale above 60 μm only in the LAC concrete specimens.

4.1.2 Physical properties of aged concrete from HADES URF

4.1.2.1 Quantitative autoradiography porosity mapping

Figure 4-8 illustrates autoradiography porosity maps of the interface along with various quantitative data, including metrics for total connected porosities and porosity profile histograms. The autoradiography porosity map offers insights into the distribution of porosity across a 4 × 8 cm surface. On the concrete side, the recorded porosity levels are influenced by the volume fraction of aggregates present within the probed regions. Specifically, the orange rectangular area represents the porosity arising from the intermingling of cement binder and small aggregates, which is approximately 20 %. Meanwhile, at the interface, regions with higher porosity readings are observed within the cement binder, with an average porosity of 35 % (indicated by the red rectangle) extending to the first 2 millimeters.

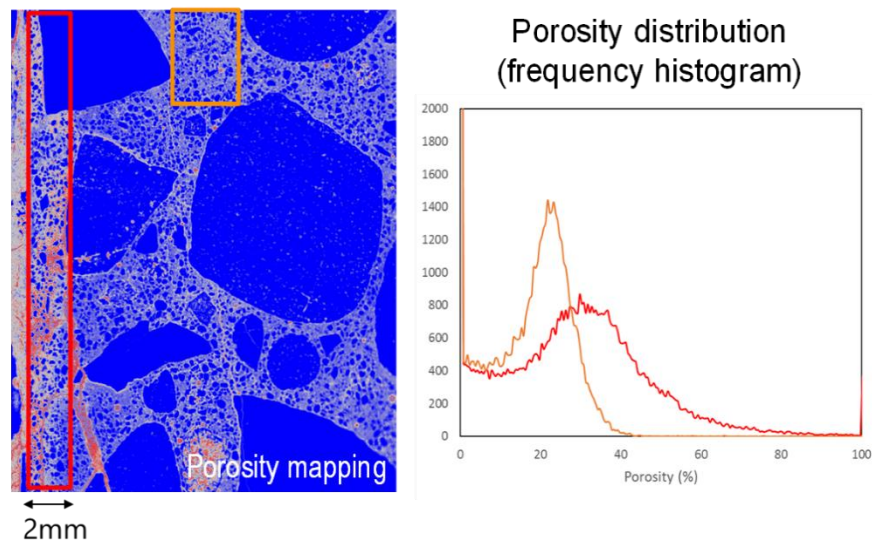


Figure 4-8 Autoradiography porosity map of the concrete-Boom Clay interface - Frequency histograms obtained from the rectangles plotted on the autoradiography.

4.1.2.2 Chemical and mineralogical characterization

Utilizing the autoradiography porosity maps and pinpointing regions with varying porosity levels, we conducted EPMA mapping to illustrate the chemical and mineralogical changes associated with the quantified porosity variations in specific areas of interest (Figure 4-9). These maps were generated within the concrete, within a one-centimeter proximity to the interface, and at the interface where porosity underwent alterations (Figure 4-8). Figure 4-9 showcases the diverse maps corresponding to concrete and their spatial alignment on the autoradiography porosity maps using red, green, and orange squares. Each map in Figure 4-9 includes a BSE image and essential element X-ray maps.

Analysis of the various EPMA maps and the associated elements reveals the evolving chemistry among the different probed regions, as demonstrated in Figure 4-9. To facilitate comparison, the same atomic weight % calibration was applied to the respective elements in each map, allowing for a straightforward assessment of false colour intensity.

In the concrete situated within a one-centimeter distance from the interface, Mg concentration displays a uniform distribution ranging from 0-3 wt% across the mapped area, with some grains exhibiting higher concentrations (~11.2 wt%). At the interface, there is noticeable Mg enrichment that coincides with the clay

contact, spanning a thickness of 500 μm (indicated by the green square in Figure 4-9). However, this enrichment is not consistently distributed along the Boom Clay interface, as evident from the orange square in Figure 4-9.

Furthermore, the increase in Mg concentration in the concrete is inversely correlated with calcium concentration, as observed in the green square of Figure 4-9. Notably, the mapping reveals the leaching of calcium in the concrete at the interface, which is evident when comparing regions near the interface (green square) and in the pristine concrete (red square).

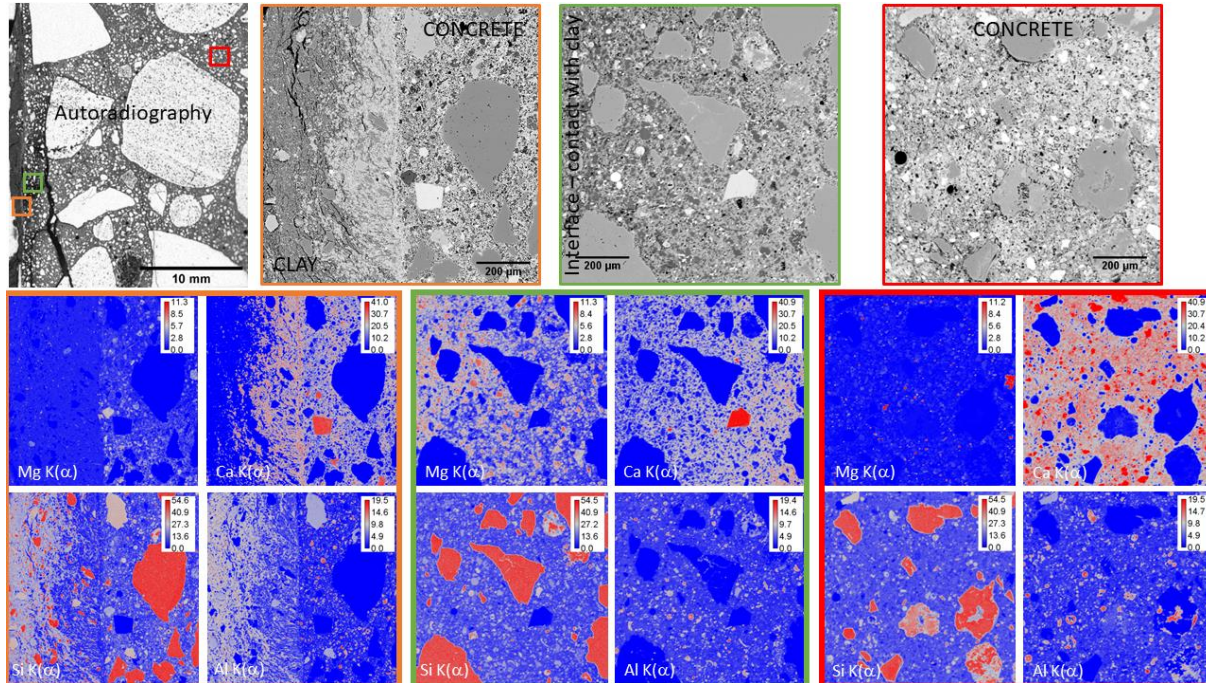


Figure 4-9 Localization of the mapped areas on the autoradiograph: The green, orange, and red outlines on the maps correspond to their positions on the autoradiography, and at the bottom, BSE images and quantitative chemical maps are presented. Atomic weight % is used for calibration, ensuring a consistent scale for the analyzed elements across all maps.

4.1.2.3 Mineralogical mapping

Figure 4-10 exhibits the following components: the BSE image of the mapped region, the associated mineral map, and ternary plots showcasing analyzed pixels. This analysis focuses on the concrete located within a one-centimeter proximity to the interface, as indicated in Figure 4-9. The Si-Ca-AlFeMg ternary diagram, also featured in Figure 4-10, enables the visualization of pixel clusters that are connected to cement and hydrates, in comparison to the end-members. The segmentation steps were elaborated in Gaboreau et al. (2017). Figure 4-10 outlines the final segmentation steps that identify the various chemical compositions of C-A-S-H (calcium-alumina-silicate-hydrate) phases.

The mineral map provides a breakdown of the distinct phases identified, along with their respective weight percentages (wt%) and chemical compositions. Among the fine aggregates, which encompass quartz, feldspar, and calcium carbonates, some residual cement grains have been identified. These cement grains include alite (C_3S), belite (C_2S), aluminat ($\text{C}_3\text{A}/\text{C}_4\text{AF}$), and fly ash (FA). The presence of fly ash amounts to 14 % of the studied area, or 18 % when normalized to the mass of hydraulic binder phases (excluding aggregates). This alignment with the initial cement composition is quite satisfactory.

Other phases observed are hydrates such as hydrogarnet and monosulphate (AFm-SO₄), and the variable chemical composition of C-A-S-H, as represented in Figure 4-10. The compositions of C-A-S-H are distinguished based on the atomic weight of calcium. Different clusters have been identified and segmented according to the calcium content within the C-A-S-H. In a magnified view presented in Figure 4-10 (highlighted by the red square), C-A-S-H with the highest calcium concentration (Ca > 40 wt%) is distributed around the residual grains of C₂S and C₃S, featuring a calcium-to-silica ratio (Ca/Si) of 1.47. The Ca/Si ratio of other C-A-S-H phases decreases as the distance from the residual cement grains increases, ultimately reaching 1.14. Notably, no portlandite was detected within this specific surface.

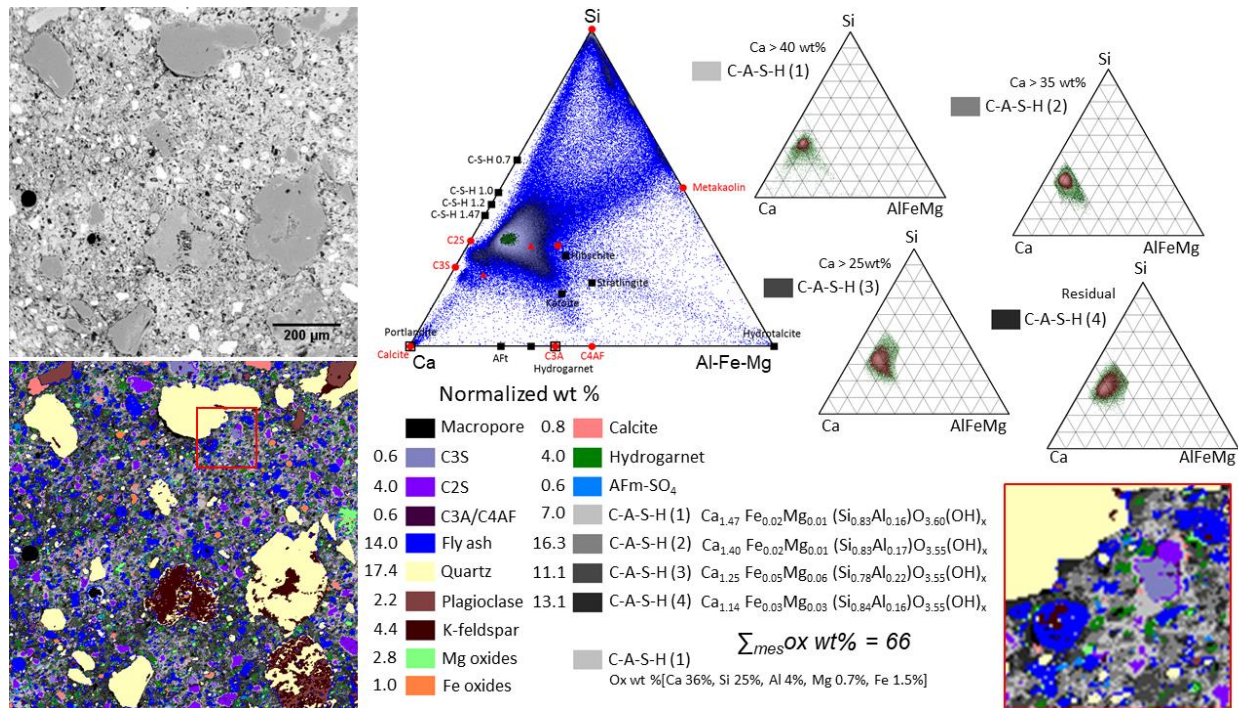


Figure 4-10 BSE image and a quantitative mineral map of the concrete. The Si-Ca-AlFeMg ternary diagram provides a projection of the elements examined within the mapped area.

Figure 4-11 depicts a map of the concrete near the interface in an area where porosity is on the rise. This mineral map clearly identifies the aggregates, which are consistent with those found in the "reference state" concrete shown in Figure 4-10. Notably, a prominent collection of pixels extends between the C-A-S-H and clay chemical compositions. After segregating the aggregates and residual fly ash (FA), the remaining pixels, representing the hydrates (components of the hydraulic binder), were plotted on either the M⁺-4Si-R²⁺ or Si-Ca-AlFeMg diagrams. In the Si-Ca-AlFeMg diagram, we can differentiate various clusters of pixels by imposing limits on the calcium and magnesium content (as seen in Figure 4-10). The two ends of this trend correspond to (i) pixels with the highest calcium content (Ca > 30 wt%), situated close to the C-A-S-H composition, and (ii) pixels with the highest magnesium content (Mg > 12 wt%), forming a tightly clustered group associated with the M-S-H, zeolites, and clay stoichiometry. These specific pixels appear as light blue grains with dimensions less than 50 μm on the mineral map (depicted in Figure 4-11). This elongated cluster of pixels signifies a chemical transformation that is dependent on the distance from the interface. Calcium and magnesium concentrations exhibit an inverse relationship, with an increase in magnesium observed in the concrete in contact with clay, resulting in a decrease in calcium concentration. This relationship varies with increasing distance from the interface.

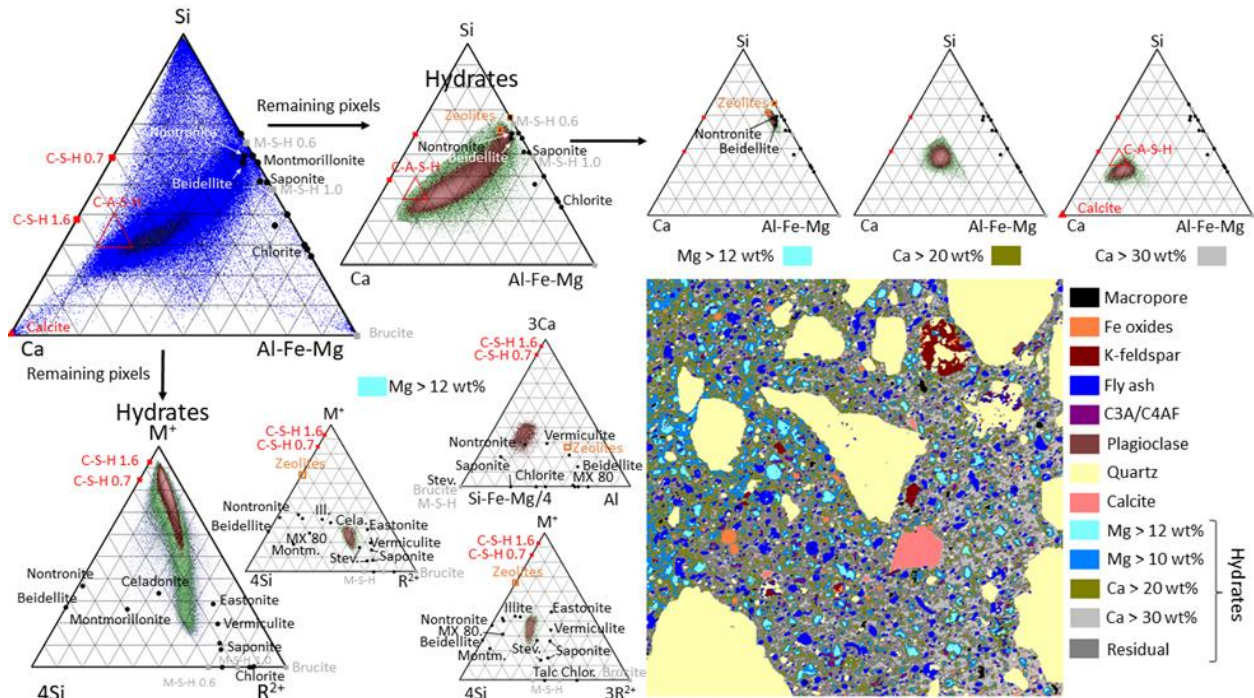


Figure 4-11 Mineral maps of the concrete adjacent to Boom Clay, featuring Si-Ca-AlFeMg ternary plots that encompass all the pixels within the map. Various segmentation steps were employed to distinguish the hydrates, with labels such as Stev. (stevensite), Ill. (illite), MX 80 (smectite MX80), Chlor. (chlorite), and Montm. (montmorillonite) corresponding to different mineral phases.

4.1.2.4 Change in water sorptivity of concrete

Figure 4-12 depicts the cumulative water absorption data for both undamaged (sound) and deteriorated (interface) concrete over a 40-day testing period. This data reveals a two-stage water absorption pattern, characterized by an initial rapid absorption phase, followed by a subsequent slower absorption phase. Intriguingly, for both types of concrete, the transition between these two phases occurs at roughly the same time, approximately 40 hours after the onset of measurements.

During the rapid absorption phase, water intake is primarily governed by capillary pores, which generate capillary suction, drawing water into the porous network. After this initial phase, most of the capillary pores become saturated with water, leading to the diffusion of water into smaller pores, including inter and intrapores within the C-S-H particles. The initial absorption phase is typically employed to estimate the water sorptivity coefficient using Eq. (1), which essentially involves determining the slope of the cumulative water absorption, as indicated on the right side of Figure 4-12. Notably, the water sorptivity coefficient of the interface concrete is found to be $0.151 \text{ mm/s}^{0.5}$, nearly three times higher than that of the sound concrete, which stands at $0.053 \text{ mm/s}^{0.5}$. This substantial increase in water sorptivity can be mainly attributed to the significant rise in porosity measured at the concrete interface, as demonstrated in Figure 4-8.

Using the porosity values measured at the interface and in bulk concrete (excluding coarse aggregates), an approximate estimation of the porosities for sound and interface concrete can be achieved by considering the volume fraction of coarse aggregate (porosity of the aggregates considered equal to zero). This estimation reveals porosities of 11.2 % and 19.3 %, respectively. It's worth noting that the estimated porosity of 11.2 % is slightly higher than the average value of 9 % measured by autoradiography, suggesting that the investigated area may have a slightly higher aggregate content compared to the bulk concrete.

$$S = \varphi r^{0.5} \left(\frac{\gamma \cos \theta}{2\eta} \right)^{0.5} \quad (1)$$

To explore whether changes in porosity alone contribute to the increase in water sorptivity or if other factors play a role, a theoretical relationship between water sorptivity, capillary porosity (φ), and average pore radius (r) can be established using Darcy's law in conjunction with the Lucas-Washburn equation, assuming cylindrical-shaped pores. The parameters involved in this equation, such as surface tension (γ), water viscosity (η), and the contact angle (θ) between concrete and water, are considered constant for both sound and deteriorated concrete. Therefore, the increase in water sorptivity can be attributed solely to changes in capillary porosity and average pore radius, which are linked to pore size distribution.

Based on the earlier rough estimation, where the porosity at the interface is approximately double that of sound concrete, achieving a threefold increase in water sorptivity implies that the average pore radius must increase by a factor of 1.52 (2.25 times) according to Eq. (1). Such a substantial increase in pore size is typically associated with conditions where the leaching process is significantly more pronounced than carbonation (as suggested by Phung et al. (2015)).

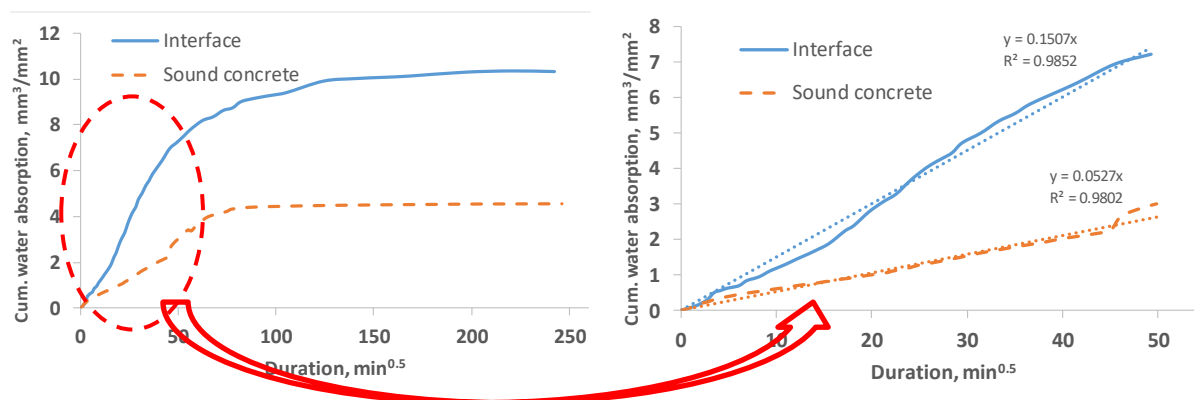


Figure 4-12 Increase in water sorptivity at the concrete interface.

4.1.2.5 Microbial analysis

To investigate potential microbial activity at the Boom Clay – concrete interface, we measured ATP and we tried to cultivate microorganisms from that surface (Figure 4-13).



Figure 4-13 Overview of the complete concrete core (left); the concrete-clay interface (middle) and the clay on the concrete core (right)

Currently, microbial analysis is still ongoing; however, first indications show that the amount of viable microbial cells on R2A in aerobic conditions is limited (Figure 4-14).

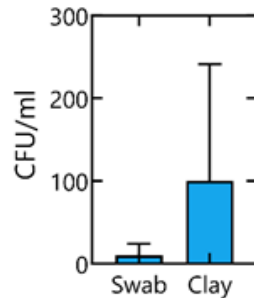


Figure 4-14 Total number of CFU/mL after 1 week of growth on R2A at 30°C in aerobic conditions from a swab taken from the concrete and from the remainder of the clay.

4.2 Evolution under multi-ionic chemical attack (SURAO/CTU/UJV/CVREZ, TUL, COVRA)

4.2.1 New ageing experiments under conditions representing operational disposal phase (Bukov URL)

4.2.1.1 AIR exposure as a reference

- o **Mechanical tests**

Each sampling campaign provided 6-12 samples for punch tests. The load at break and four values of rigidity (from four loading cycles) were determined for each specimen. The data sets were statistically evaluated (outliers, mean, std. deviation, k=2 interval). The following figures show the time evolution of samples from the air environment (Figure 4-15). Examples of min/max intervals are displayed on the right figure.

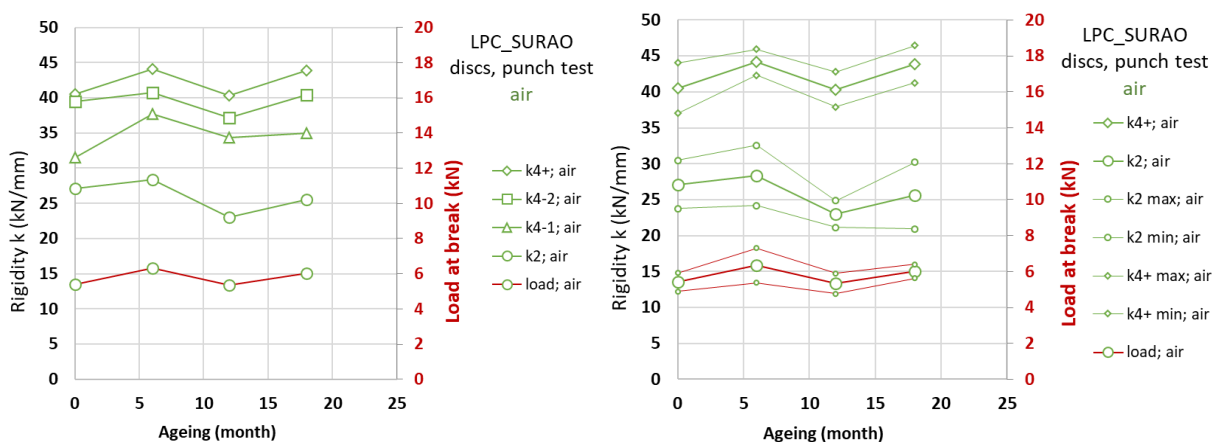


Figure 4-15 Results of punch tests - Load at break and rigidity evolution in time; air environment; average values (left); example of min/ max range of k2; k4+ and load at break datasets (right)

All parameters (load at break; rigidity in all loading steps; left figure) seem stable in time, with variations of average. The variations of most of the datasets (right figure; selection of rigidity in first and last loading step – k2 and k4+) seem significant, probably due to inhomogeneities (gravel in the concrete and its size related to sample size) but they are similar for all test sets. All observed values show a slight increase in the first period (6 months).

- **Nanoindentation**

The fragments resulting from mechanical tests were used for grid nanoindentation containing 1600 indents that was performed at the surface location (0-1 mm) and core location (1-4 mm). 0 mm means sample surface, 4 mm samples core. The data from all indents of E and H parameters were merged and separated into three (E) or two (H) mechanical phases by statistical deconvolution. The Young's modulus data were separated into three phases: #1 low stiffness hydrates affected by porosity, #2 main hydration products, #3 stiff particles (slag, clinker, silica fume, silicious aggregates) with E higher than 50 GPa. The phase of main hydration products was most frequently presented in volume fraction.

The micro-mechanical properties E and H at the core location were higher than on the surface location. After the exposition of 6 months in air, a small decrease of 6 % was observed for E values compared to the reference sample. However, the E increased by 28 % after 12 months of exposure to air conditions. In the case of hardness, the values increased in both exposure times 6 and 12 months by 63 % and 82 %, respectively (surface location).

Table 4-1 Results of Young's modulus (E) and hardness (H) of the samples exposed to air ventilation measured by nanoindentation at the surface and core locations.

| Exposure | Duration (months) | Surface location | | Core location | |
|-----------|-------------------|------------------|-----------|---------------|-----------|
| | | H (GPa) | E (GPa) | H (GPa) | E (GPa) |
| Reference | 0 | 0.94±0.28 | 18.3±3.0 | 1.33±0.30 | 24.0±4.9 |
| Air | 6 | 1.53±0.67 | 17.2±4.9 | 1.51±0.46 | 23.2±5.6 |
| Air | 12 | 1.71±0.92 | 23.5±4.2 | 2.35±0.42 | 31.0±3.6 |

- **SEM, XRD**

Samples were analyzed by SEM measurements on the exposed surface and from cross sections. The surfaces of the samples that were exposed to air were characterized by the local presence of microorganisms from the beginning of the exposure (Figure 4-16). A cross-sectional view showed that the presence of cracks was small and only near the surface during exposure. The influence of carbonation only became apparent after 18 months exposures penetrating to a depth of 87 μm (Figure 4-16).

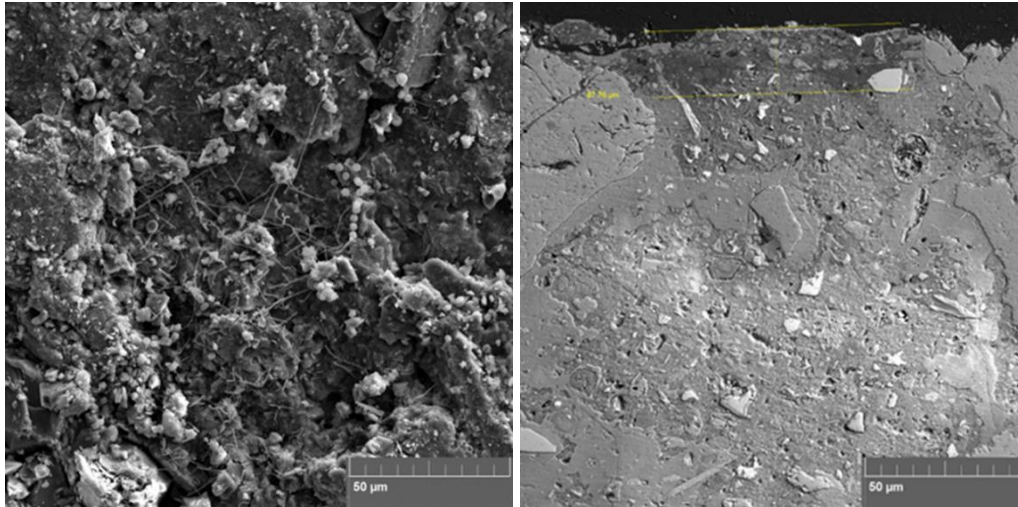


Figure 4-16 Scanning electron micrographs of the surface of samples exposed to air after 18 months (left) and showing penetration of the carbonation area observed only after 18 months (right).

Secondary phase formation on samples has been investigated using XRD techniques involving Grazing incidence X-ray diffractometry (GIXRD) and Powder XRD. The time evolution of the phase changes observed by XRD on samples exposed to air is shown in Table 4-2. The composition of the samples is an inhomogeneous mixture of minerals, where silica is the major phase, other minerals belong to the plagioclase group, and chlorite, muscovite, calcite, hornblende and hematite are present as minor phases. A new phase of vaterite and gypsum was observed for all aged samples compared to the initial reference sample.

Table 4-2 Phase composition of the samples by XRD and their percentages after 6, 12 and 18 months.

| Phase | 6 Months | 12 Months | 18 Months |
|---------------|----------|-----------|-----------|
| Silica | 59.6 | 61.3 | 61.6 |
| Albite | 10.2 | 9.1 | 10.9 |
| Microcline | 5.7 | 5.7 | 4.3 |
| Sanidine | 6 | 5.8 | 4.6 |
| Chlorite-IIb | 1.1 | 0.8 | 0.9 |
| Muscovite 2M1 | 4.7 | 4.8 | 4 |
| Calcite | 2.6 | 2.3 | 2.5 |
| Hornblende | 1.7 | 1.6 | 1 |
| Hematite | 0.3 | 0.2 | 0.2 |
| Vaterite | 7.7 | 7.9 | 9.1 |
| Gypsum | 0.7 | 0.7 | 0.9 |

GIXRD analysis was used to characterize the thin surface layers on the samples. Diffractograms of the surface of the samples (Figure 4-17) in air for each sample during exposure indicate the presence of gypsum, silica, vaterite, muscovite and albite.

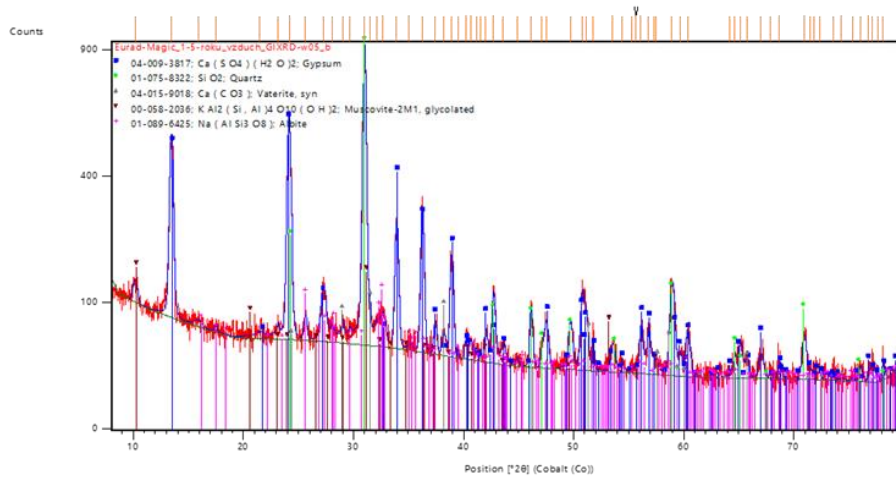


Figure 4-17 GIXRD analysis at an angle of 0.5° of the sample surface after 1.5 years.

o **Leaching and pH of samples**

The leachate pH of tested samples is evaluated according to SKB R-12-02 report (Alonso et al., 2012). The pH value of input material at experimental time T0 was evaluated as 10.6. The material at T0 was already approx. 3 years old and cured at the conditions of URL Bukov. Evolution of pH values from casting to experimental time T0 is shown in Figure 4-18. The evolution of pH values of the concrete samples from air environment after sampling campaigns is summarised in Table 4-3. A rainbow pH indicator was used to determine pH and visualize its changes in the cross-section of the (broken) samples (Figure 4-19).

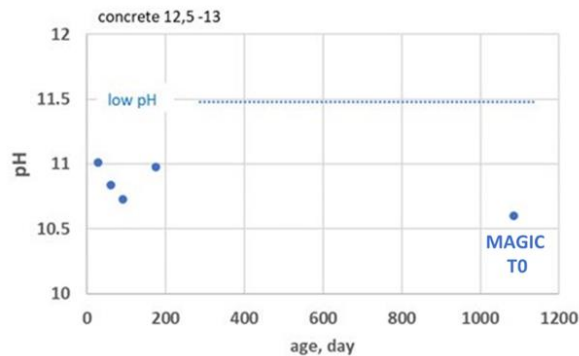


Figure 4-18 Evolution of pH values from casting to experimental time T0 of LPC SURAO material

Table 4-3 Evolution of pH values of the concrete samples from air environment.

| Time | Environment | pH |
|----------|-------------|------|
| 0 | | 10.6 |
| 0.5 year | air | 9.8 |
| 1 year | air | 9.6 |
| 1.5 year | air | 9.7 |



Figure 4-19 pH determination of LPC_SURAO by rainbow indicator (T3 – 18 months aged samples; broken discs after punch tests).

4.2.1.2 Underground water environment

o Mechanical tests

Each sampling campaign provided 6-12 samples for punch tests. The following figures show the time evolution of samples from the water environment. Examples of min / max intervals are on the right (Figure 4-20).

Load at break (left figure) vary in time but with similar average value and dataset variation after 18 months as initial. The rigidity values show a smooth but different time evolution. The rigidity k2 (1st loading step; largest effect of plastic deformation) decreases steadily (to about 55 % of the initial value), while k4-2 and k4+ (3rd and 4th loading step; elastic deformation dominates) increase slightly for two periods (6 and 12 months) followed by a slight decrease (18 months). k4-1 (2nd loading step) decreases after the initial increase at a similar rate as k2 (2nd largest effect of plastic deformation). The reason for this behaviour is likely due to two opposing phenomena - rehydration of the samples in aqueous environments (slight improvement in properties in most or all of the volume - 4-2; k4+; see nanoindentation results below) versus gradual disruption of the sample from the water interface/ sample surface inward (see following subchapters).

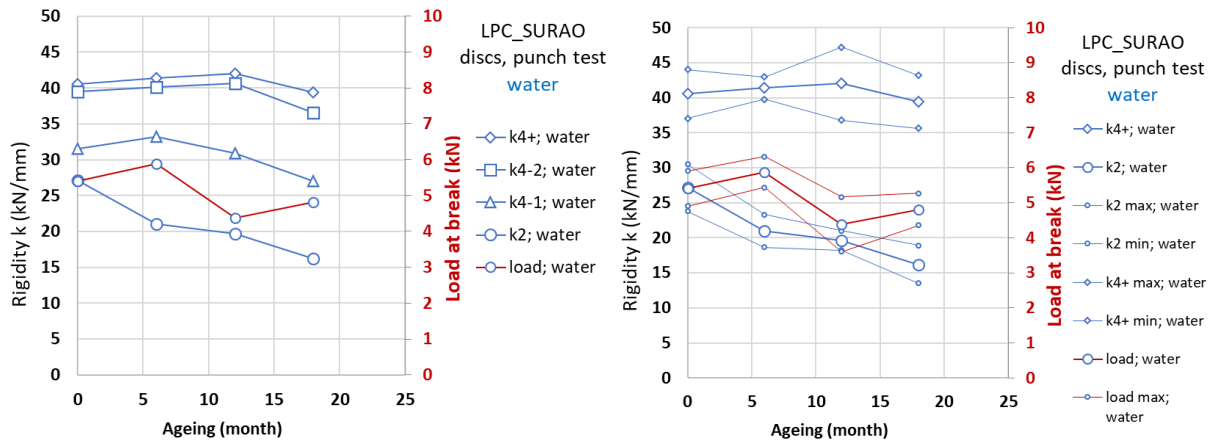


Figure 4-20 Results of punch tests - Load at break and rigidity evolution in time; water environment; average values (left); example of min/ max range of k2; k4+ and load at break datasets (right)

- **Nanoindentation**

The same measurement procedure as for samples exposed to air was performed.

Table 4-4 Results of Young's modulus (E) and hardness (H) of the samples exposed to underground water measured by nanoindentation at the surface and core locations.

| Exposure | Duration (months) | Surface location | | Core location | |
|-----------|----------------------|------------------|-----------|---------------|-----------|
| | | H (GPa) | E (GPa) | H (GPa) | E (GPa) |
| Reference | 0 | 0.94±0.28 | 18.3±3.0 | 1.33±0.30 | 24.0±4.9 |
| Water | 6 | 1.62±0.71 | 22.0±3.4 | 1.77±0.61 | 26.4±4.6 |
| Water | 12 | 1.74±0.52 | 26.1±5.1 | 1.87±0.35 | 30.8±4.9 |

The micro-mechanical properties E and H at the core location were higher than on the surface location. The increase of both mechanical parameters was observed for 6 months exposure to underground water by 20% (E) and 72% (H) at the surface location. An even higher increase was observed after exposure of 12 months by 43% (E) and 85% (H) compared to the reference sample. The most probable reason is due to renewed hydration reaction on the sample slices.

- **SEM, XRD**

In a water environment, SEM analysis showed microbial activity on the surface at all times (Figure 4-21). Metabolism products in the form of S on the surface was observed only after one year. (Figure 4-22).

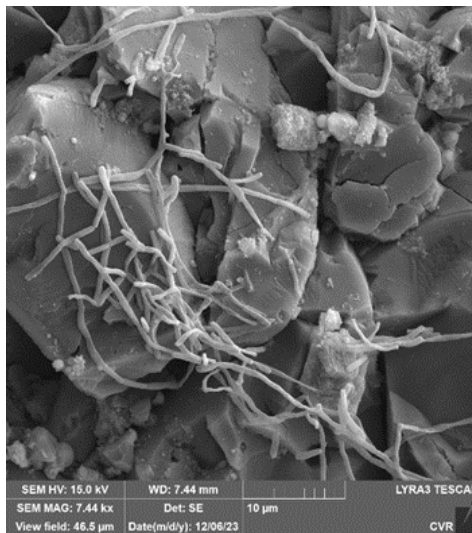


Figure 4-21 Scanning electron micrographs of the surface of samples exposed to water after 18 months.

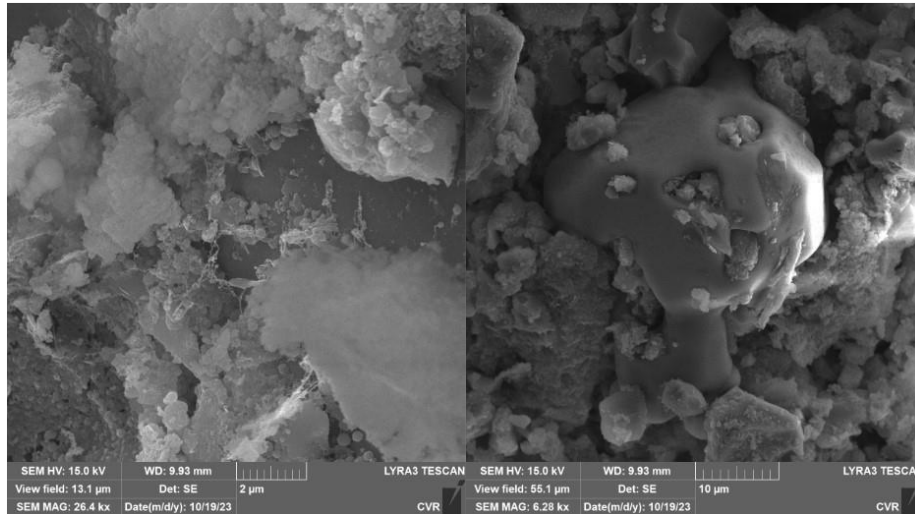


Figure 4-22 SEM measurement of LPC sample exposed to water environment indicating presence of organic matter and element sulphur after 12 months.

In a water environment, a process known as a carbonation attack occurs, which involves leaching. This process penetrates the area of degradation, as shown in Figure 4-23. As a result, the elements Ca and O in the cement matrix are depleted, based on EDS mapping and precipitation of CaCO_3 . This indicates both leaching and the degradation mechanism of carbonation in the second phase (decomposition of unstable C-S-H). The first phase of carbonation attack, due to undetected portlandite, was not observed. The occurrence of cracks is not very deep and appears in the degradation zone. The degradation zone in some cases penetrates up to 1 mm.

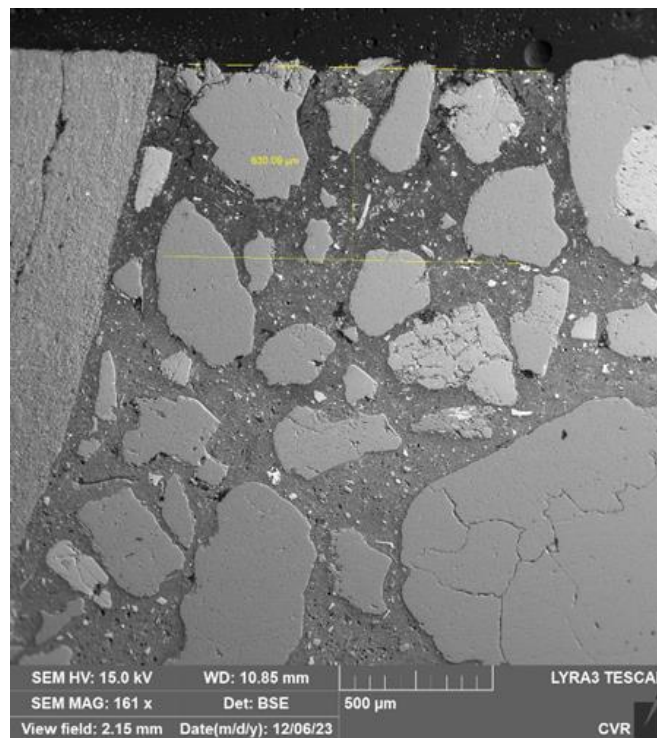


Figure 4-23 Scanning electron micrograph showing penetration of the carbonation area in water environment after 18 months.

The time evolution of the phase changes observed by XRD on samples exposed to water is shown in (Table 4-5). After 18 months, no vaterite was detected in the analysed sample. Hematite was also missing after 12 and 18 months. Compared to the air environment, no gypsum was observed.

Table 4-5 : Phase composition by XRD of the LPC samples exposed to water representing their weight percentages after 6, 12, 18 months

| Phase | 6 Months | 12 Months | 18 Months |
|---------------|----------|-----------|-----------|
| Silica | 66.1 | 61.8 | 66.4 |
| Albite | 10.9 | 12.7 | 13 |
| Microcline | 4.7 | 7.1 | 6.4 |
| Sanidine | 4.7 | 5.2 | 4.6 |
| Chlorite-IIb | 0.7 | 0.7 | 1 |
| Muscovite 2M1 | 5.4 | 4.8 | 2.9 |
| Calcite | 4 | 3.6 | 3 |
| Hornblende | 2.6 | 2.8 | 2.7 |
| Hematite | 0.3 | - | - |
| Vaterite | 0.7 | 1.5 | - |
| Gypsum | - | - | - |

The GIXRD analysis used to characterize the thin surface layers showed the presence of a new high temperature cristobalite phase after 18 months, that could be due to SiO₂ degradation by microorganisms (Xue et al., 2015).

Diffraction patterns of the surface of the samples (Figure 4-24) in water after 18 months indicate the presence of silica, calcite, cristobalite, albite and muscovite.

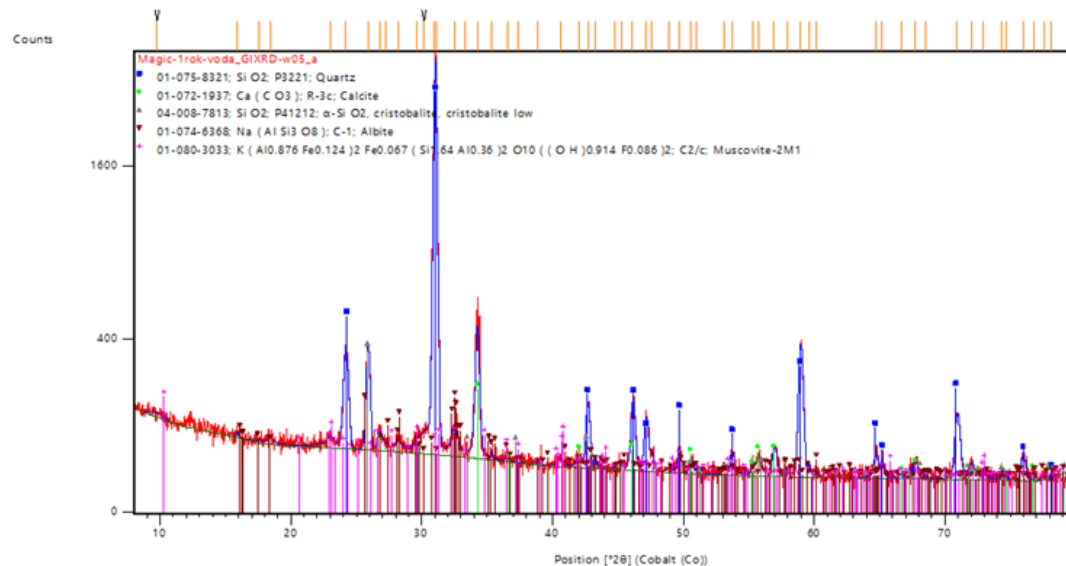


Figure 4-24 GIXRD analysis at an angle of 0.5° of the sample surface in water after 1.5 years.

o **Leaching and pH of samples**

For the leachate pH evaluation, the same procedure as for air environment samples was applied. Evolution of pH values of the concrete samples from URL Bukov groundwater environment after sampling campaigns is summarised in Table 4-6. A rainbow indicator was used to determine pH and visualize its changes in the cross-section of the (broken) samples (Figure 4-25).

Table 4-6 Evolution of pH values of the concrete samples from URL Bukov groundwater environment

| Time | Environment | pH |
|----------|-------------|------|
| 0 | | 10.6 |
| 0.5 year | groundwater | 10.1 |
| 1 year | groundwater | 10.0 |
| 1.5 year | groundwater | 10.0 |



Figure 4-25 pH determination of LPC_SURAO by rainbow indicator (T3 – 18 months aged samples; broken discs after punch tests).

4.2.1.3 Effect of direct contact with bentonite suspension

o Mechanical tests

Each sampling campaign provided 6-12 samples for punch tests. The following figure shows the time evolution of samples from the bentonite suspension environment (Figure 4-26). Examples of min / max intervals are displayed on the right figure.

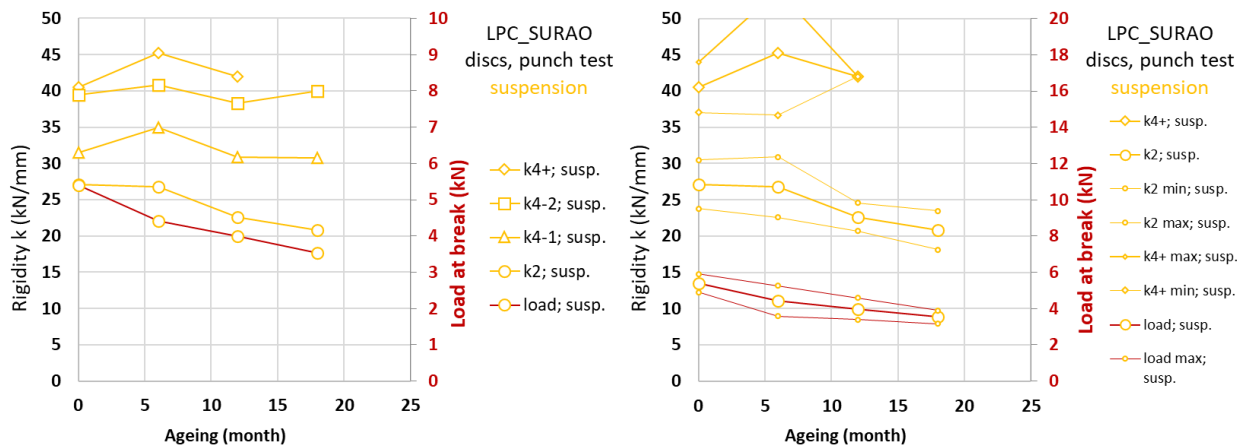


Figure 4-26 Results of punch tests - Load at break and rigidity evolution in time; bentonite suspension environment; average values (left); example of min/ max range of k2; k4+ and load at break datasets (right).

Load at break (left figure; red line) continuously decreases (down to 65 % of initial) in time with relatively low dataset variation (right figure; red lines). The rigidity either decreases continuously in the long term (k2; the largest effect of plastic deformation) or appears stable with a slight increase after 6 months and a subsequent decrease to the initial value.

A relatively important indicator is the number of specimens from each set (at least 7 pieces) that have withstood the stresses during mechanical testing up to the last loading step. In contrast to the air (at least 90 %) and water (at least 50 %) environment, where most samples survived, in the suspension environment the number of samples that survived decreased dramatically with the interaction time in suspension (50 %/ 6 months; 27 %/ 12 months; 0 %/ 18 months). Therefore, due to lack of data, the right figure does not show the k4+ value for 18 months or the variance of the data sets (after 12 and 18 months).

A comparison of evolution of parameters in all three environments (in %) is given in Figure 5-28.

o Nanoindentation

The same measurement procedure as for samples exposed to air was performed.

Table 4-7 Results of Young's modulus (E) and hardness (H) of the samples exposed to bentonite suspension measured by nanoindentation at the surface and core locations.

| Exposure | Duration (months) | Surface location | | Core location | |
|------------|-------------------|------------------|-----------|---------------|-----------|
| | | H (GPa) | E (GPa) | H (GPa) | E (GPa) |
| Reference | 0 | 0.94±0.28 | 18.3±3.0 | 1.33±0.30 | 24.0±4.9 |
| Suspension | 6 | 1.61±0.34 | 21.4±5.4 | 1.70±0.63 | 27.1±6.7 |
| Suspension | 12 | 1.92±0.65 | 26.9±4.7 | 2.04±0.42 | 31.4±6.0 |

The micro-mechanical properties E and H at the core locations were higher than on the surface location. The increase of both mechanical parameters was observed for 6 months exposure to bentonite suspension by 17% (E) and 71% (H) at the surface location. An even higher increase was observed after exposure of 12 months by 47% (E) and 104% (H) compared to the reference sample (Figure 4-27). The most probable reason is due to renew hydration reaction on the sample slices.

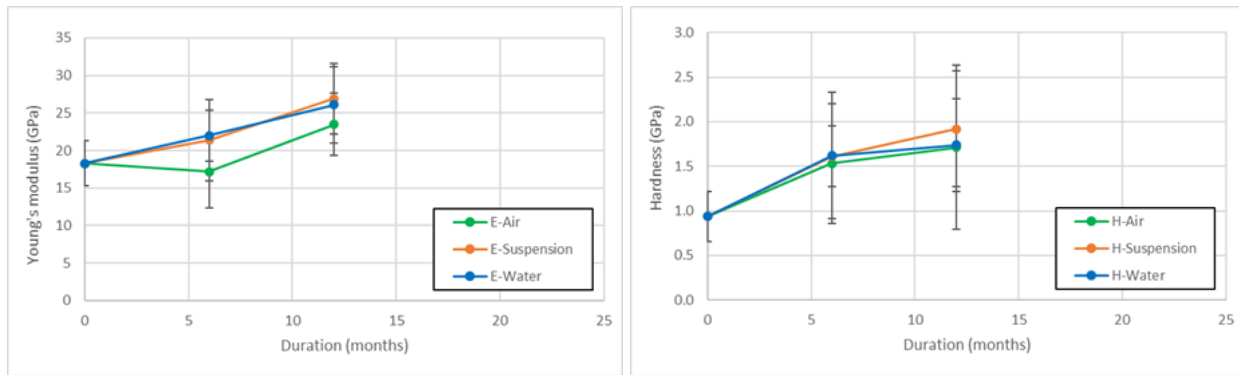


Figure 4-27 Evolution of Young's modulus (left) and hardness (right) of main hydration product over the different exposure time, measured by nanoindentation at the surface location.

o SEM, XRD

SEM analysis in the bentonite suspension environment confirmed the presence of higher Mg concentration and its penetration into the cement matrix mainly at the expense of Ca depletion (C-S-H phase changes to M-S-H phase). Here the most significant penetration and the appearance of cracks in the material is evident, showing in Figure 4-28. This penetration of magnesium into the cement matrix was observed in all samples. The presence of microorganisms on the surface was not detected during the exposures. The greatest penetration of cracks was observed in the bentonite suspension, reaching depths of up to 1.3 mm after 12 months.

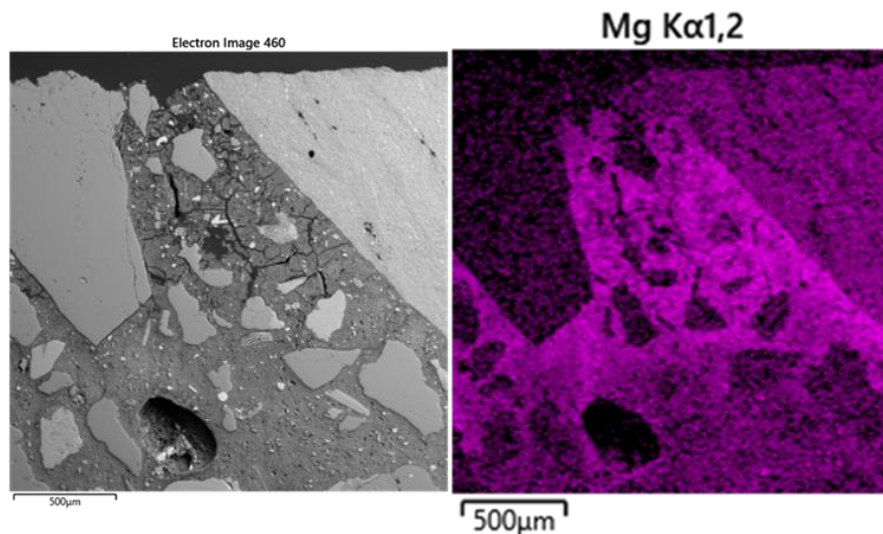


Figure 4-28 SEM showing the LPC samples cross-sections exposed to the bentonite suspension after 12 (left) and EDS elemental mapping of Mg (right).

The time evolution of the phase changes observed by XRD on samples exposed to bentonite suspension is shown in Table 4-8. The presence of vaterite was observed only after six months of exposure and no gypsum was detected in the analysed sample for all exposure times.

The GIXRD analysis used to characterize the thin surface layers showed the presence of silica, calcite, albite, vaterite and montmorillonite (Figure 4-29). No new phases were observed during exposure except montmorillonite, which was present due to the bentonite suspension.

Table 4-8 Phase composition by XRD of the LPC samples exposed to bentonite suspension, representing their weight percentages after 6, 12 and 18 months.

| Phase | 6 Months | 12 Months | 18 Months |
|---------------|----------|-----------|-----------|
| Silica | 65.7 | 68.2 | 71.2 |
| Albite | 10.8 | 10.1 | 9.6 |
| Microcline | 3.9 | 5.4 | 5.2 |
| Sanidine | 6.7 | 5.3 | 3.9 |
| Chlorite-IIb | 1.2 | 1.4 | 1 |
| Muscovite 2M1 | 4.5 | 4.3 | 3.7 |
| Calcite | 4.3 | 4.2 | 4 |
| Hornblende | 1.1 | 0.8 | 1.3 |
| Hematite | 0.4 | 0.3 | 0.2 |
| Vaterite | 1.6 | - | - |
| Gypsum | - | - | - |

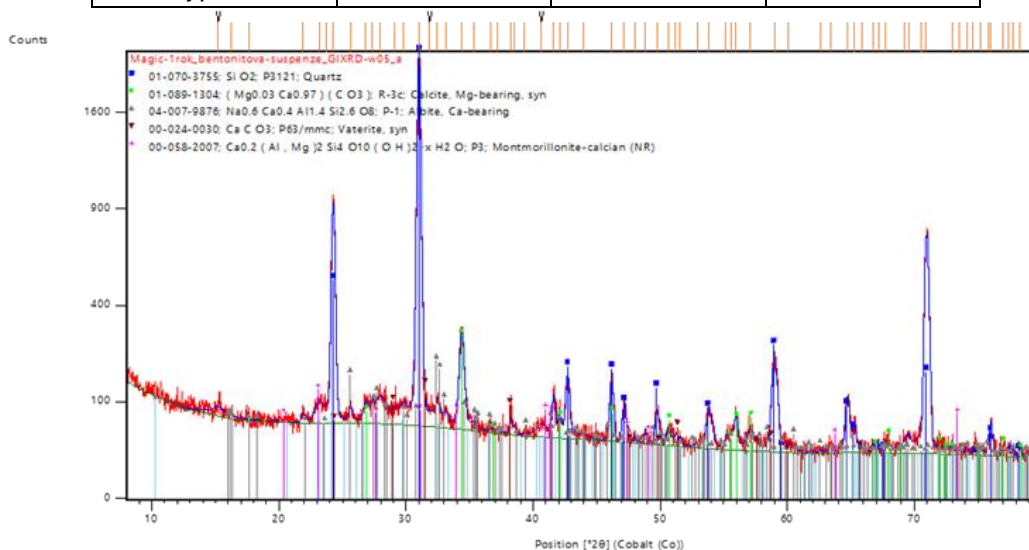


Figure 4-29 GIXRD analysis at an angle of 0.5° of the sample surface in bentonite suspension after 1.5 years.

o **Leaching and pH of samples**

For the leachate pH evaluation, the same procedure as for air and groundwater environment samples was applied.

Table 4-9 Evolution of pH values of the concrete samples from BCV bentonite suspension environment.

| Time | Environment | pH |
|----------|-------------|------|
| 0 | | 10.6 |
| 0.5 year | suspension | 10.1 |
| 1 year | suspension | 9.9 |
| 1.5 year | suspension | 10.0 |

Prior to testing, LPC specimens were cleaned of bentonite suspension residues on the surface. Evolution of pH values of the concrete samples from BCV bentonite suspension environment after sampling

campaigns is summarised in Table 4-9. A rainbow pH indicator was used to determine pH and visualize its changes in the cross-section of the (broken) samples (Figure 4-30).



Figure 4-30 pH determination of LPC_SURAO by rainbow indicator (T3 – 18 months aged samples; broken discs after punch tests).

4.2.2 Artificial ageing conditions through chemical multi-ionic attack (saline water).

4.2.2.1 Mechanical characterisation of certified specimens

As described in Deliverable 16.3, after 28 days of hardening, the CEM III/B buffer-like samples had an average compressive strength of 53.2 ± 1.3 MPa with an edge of 150 mm and 56.6 ± 0.9 MPa with an edge of 100 mm. Table 4-10 shows the measured compressive strength after submersion for $5\frac{2}{3}$ years in a solution as saline as seawater. The average compressive strength was measured to be 69.7 ± 1.8 MPa with an edge of 150 mm and 71.5 ± 3.6 MPa with an edge of 100 mm. In section 5.1.3, results of two samples with an edge of 50 mm are shown that had been measured on 28 September 2022 i.e. after an additional 5-month exposure. The compressive strength was 71.5 and 70.7 MPa. Consequently, although the average compressive strength after 6 years is larger than the average compressive strength after 28 days, the compressive strength may have been stabilized.

Table 4-10 Compressive strength measurements and weight of buffer-like materials (cement: CEM-III/B, coarse aggregate: 2-8 mm) after $5\frac{2}{3}$ years exposure to saline synthetic clay pore water. Measured on 11 April 2022 (cubical specimens with an edge of 150 mm and 100 mm) and casted on 13 July 2016.

| Sample (only casted) | Edge of samples [cm] | July 2016 after casting | 30 August 2016 & 1 September 2016 after submersion in tap water | 11 April 2022 after exposure to saline solution | Compressive strength [MPa] |
|----------------------|----------------------|-------------------------|---|---|----------------------------|
| | | Weight [gram] | | | |
| COV150_1 | 15 | 7804.0 | 7867.0 | 7901.6 | 68.3 |
| COV150_2 | 15 | 7650.2 | 7711.3 | 7746.4 | 71.7 |
| COV150_3 | 15 | 7636.5 | 7698.1 | 7730.5 | 70.6 |
| COV150_4 | 15 | 7568.5 | 7625.5 | 7658.7 | 70.6 |
| COV150_5 | 15 | 7706.8 | 7765.2 | 7801.7 | 67.5 |
| COV100_12 | 10 | 2226.38 | 2245.79 | 2260.52 | 70.9 |
| COV100_13 | 10 | 2269.56 | 2289.46 | 2301.69 | 71.2 |
| COV100_14 | 10 | 2311.86 | 2333.13 | 2347.78 | 70.7 |
| COV100_15 | 10 | 2297.48 | 2317.2 | 2330.79 | 68.6 |
| COV100_16 | 10 | 2187.63 | 2257.76 | 2270.73 | 66.6 |
| COV100_20 | 10 | 2315.19 | 2335.77 | 2347.99 | 76.1 |
| COV100_21 | 10 | 2307.03 | 2326.47 | 2340.33 | 76.3 |

The buffer-like concrete may still be in a hardening stage despite being almost 7 years old. A hardening stage requires not yet reacted cement. The presence of not yet reacted cement allows self-sealing of cracks

(Seymour et al., 2023). As explained in Deliverable 16.3, fractured surfaces of cracked samples have been put into close contact without additional pressure in order to study self-sealing of concrete. Figure 4-31 shows the re-assembled samples as submerged in saline water from 8 January 2021 until 23 October 2023 i.e. for almost 3 years. The fragments of the buffer-like specimen could not be removed by hand. Table 4-11 shows that this re-assembled specimen also had gained a strength of 34.4 MPa.

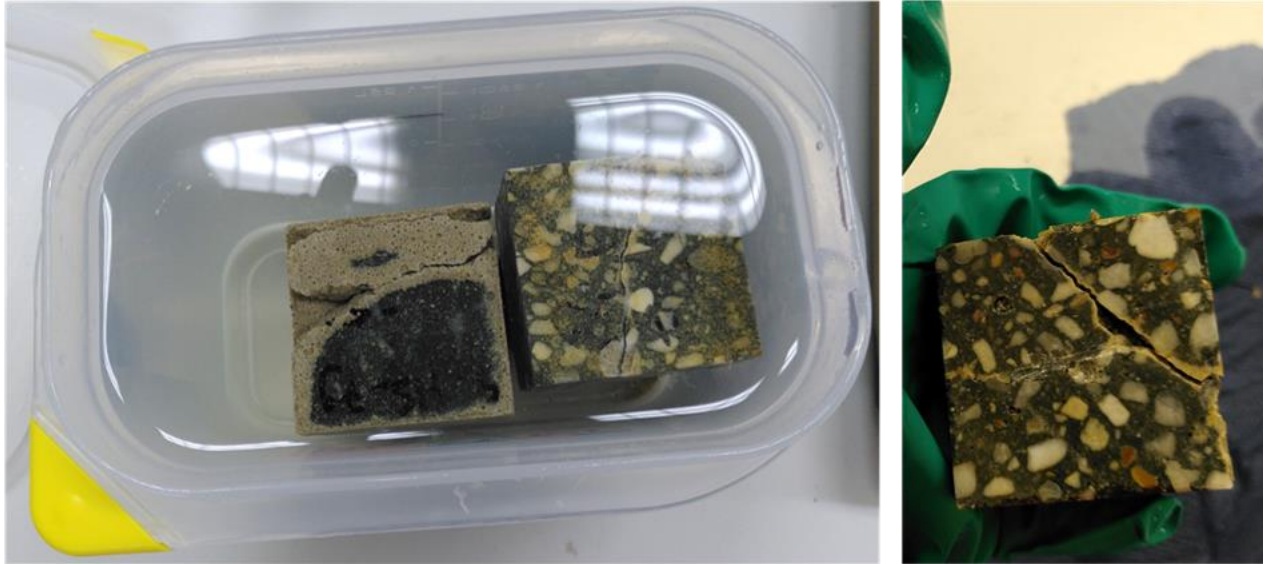


Figure 4-31 Re-assembled certified backfill-like concrete (left in box, 5_HS_79_50) and buffer-like concrete (right in box, 7_COV_59, and held by hand in right photo). Both casted and sawn samples.

Table 4-11 Compressive strength measurements and weight of buffer-like materials (cement: CEM-III/B, coarse aggregate: 2-8 mm) after 51/3 years exposure to saline synthetic clay pore water. Measured on 8 January 2021, 11 April 2022 and 23 October 2023, casted on 13 July 2016 and sawn after some months of exposure to tap water.

| Sample (casted and sawn) | Edge of samples [cm] | 18 January 2017 | 8 January 2021 (23 October 2023) | 11 April 2022 | Compressive strength 8/01/2021 (23 October 2023) [MPa] | Compressive strength 11/04/2022 [MPa] |
|--------------------------------|----------------------------|-----------------------|--|------------------|--|--|
| | | Weight [gram] | | | | |
| 7_COV50_52 | 5 | 301.10 | | 304.65 | | 52.6 |
| 7_COV50_53 | 5 | 299.86 | | 303.89 | | 57.9 |
| 7_COV50_54 | 5 | 303.54 | | 307.15 | | 54.0 |
| 7_COV50_55 | 5 | 298.46 | | 301.03 | | 64.7 |
| 7_COV50_58 | 5 | 293.85 | 298.39 | | 54.2 | |
| 7_COV50_59 | 5 | 296.39 | 300.11 (302.09) | | 63.1 (34.4) | |

Samples 7_COV_56 (51.7 N/mm²) and 7_COV_57 (40.5 N/mm²) were measured on 28 September 2022 (see section 5.1.3) i.e. 5 months later. Although these strengths are smaller, the variation due to sample preparation (sawing) is too large to conclude an effect of the exposure.

Fragments of the re-assembled backfill-like specimen in Figure 4-31 could easily be removed by hand i.e. no self-sealing of concrete had occurred. Consequently, unlike buffer-like concrete, a second compressive strength measurement was not possible. Table 4-11 shows the measurements of the weight and strength of the casted and sawn specimens.

Table 4-12 Compressive strength measurements and weight of certified backfill materials (cement: CEM-III/B, only fine aggregate: 0-2 mm)) after 51/3 years exposure to saline synthetic clay pore water. Measured on 13 April 2022, casted on September 2016 and sawn after some months of exposure to tap water.

| Sample (casted and sawn) | Edge of samples [cm] | 18 January 2017 | 13 April 2022 | 18 January 2017 (23 October 2023) | 13 April 2022 |
|-----------------------------|----------------------------|--------------------|------------------|--------------------------------------|---------------|
| | | Weight [gram] | | Compressive strength [MPa] | |
| 5_HS_79_50 | 5 | 212.20 (N.A.) | | 13.2 (N.A.) | |
| 5_HS_80_50 | 5 | 216.21 | | 13.0 | |
| 5_HS_81_50 | 5 | 197.30 | 210.39 | | 13.8 |
| 5_HS_82_50 | 5 | 210.22 | 214.34 | | 14.2 |
| 5_HS_83_50 | 5 | 197.46 | 215.00 | | 15.1 |
| 5_HS_84_50 | 5 | 200.11 | 215.89 | | 14.6 |
| 5_HS_85_50 | 5 | 198.42 | 212.98 | | 13.3 |
| 5_HS_86_50 | 5 | 202.69 | 218.87 | | 13.6 |

The strength of the only casted samples of certified backfill-like concrete after submersion in saline water has been measured in MAGIC. In Deliverable 16.3, only measurements of the compressive strength were available of casted and sawn specimens. As described in Deliverable 16.3, after 28 days of hardening, the CEM III/B backfill-like samples had an average compressive strength of 19.6 ± 1.7 MPa with an edge of 150 mm and 23.7 ± 2.3 MPa with an edge of 100 mm. The average compressive strength was increased into an average compressive strength of 28.6 ± 1.4 MPa with an edge of 150 mm and 29.4 ± 4.1 MPa with an edge of 100 mm after 5 years of submersion in the solution as saline as seawater. Table 4-13 shows the measured compressive strength after exposure for 5 and 5.5 years to the solution as saline as seawater. Also the backfill-like samples, like the buffer-like samples, may still have been in a hardening stage. However, considering the lack in sealing of cracks as explained earlier for this type of concrete, the hardening may have been completed.

All samples gain in weight after exposure to tap water or a saline solution. Sample HS_19_150 is of special interest since the main ingress of water is the saline solution and not tap water. Still the compressive strength is indifferent from the samples first exposed to tap water.

Table 4-13 Compressive strength measurements and weight of certified backfill-like materials (cement: CEM-III/B, only fine aggregate: 0-2 mm) after 5 and 5 1/2 years exposure to saline synthetic clay pore water. Measured on 11 and 13 April 2022 (cubical specimens with an edge of 150 mm and 100 mm) and casted on 6, 8 and 9 September 2016 and 14 June 2017.

| Sample (only casted) | Edge of samples [cm] | September 2016 after casting | 6 December 2016 after submersion in tap water | June 2017 after casting | 11 & 13 April 2022 after exposure to saline solution | Compressive strength [MPa] |
|-------------------------|----------------------------|------------------------------------|--|-------------------------------|---|----------------------------------|
| | | Weight [gram] | | | | |
| HS_2_150 | 15 | 5701.8 | 5912.7 | | 5894.3 | 28.7 |
| HS_3_150 | 15 | 5652.6 | 5771.3 | | 5794.5 | 27.6 |
| HS_10_150 | 15 | 5844.7 | 6066.0 | | 6068.1 | 28.2 |
| HS_11_150 | 15 | 5751.0 | 5958.2 | | 5974.1 | 27.3 |
| HS_12_150 | 15 | 5529.2 | 5758.5 | | 5794.6 | 26.1 |
| HS_13_150 | 15 | 5707.9 | 5844.8 | | 5886.7 | 28.5 |
| HS_14_150 | 15 | 5693.0 | 5824.1 | | 5867.1 | 28.8 |
| HS_15_150 | 15 | 5750.6 | 5853.0 | | 5939.9 | 28.6 |
| HS_16_150 | 15 | 5749.2 | 5856.8 | | 5931.4 | 30.9 |
| HS_17_150 | 15 | 5650.0 | 5798.5 | | 5812.4 | 29.8 |
| HS_18_150 | 15 | 5835.3 | 5983.1 | | 6012.4 | 30.5 |
| HS_19_150 | 15 | - | - | 5964.7 | 6144.5 | 30.6 |
| HS_22_100 | 10 | 1765.1 | 1812.3 | | 1815.0 | 32.5 |
| HS_23_100 | 10 | 1705.1 | 1748.9 | | 1762.6 | 27.4 |
| HS_24_100 | 10 | 1697.2 | 1742.6 | | 1751.9 | 28.1 |
| HS_25_100 | 10 | 1663.5 | 1706.4 | | 1717.3 | 23.0 |
| HS_26_100 | 10 | 1655.7 | 1693.5 | | 1704.0 | 23.8 |
| HS_30_100 | 10 | 1718.3 | 1789.5 | | 1796.1 | 29.6 |
| HS_31_100 | 10 | 1744.4 | 1802.7 | | 1809.2 | 32.8 |
| HS_32_100 | 10 | 1748.2 | 1798.8 | | 1811.4 | 33.4 |
| HS_33_100 | 10 | 1765.6 | 1802.9 | | 1813.0 | 33.8 |
| HS_34_100 | 10 | - | - | 1778.4 | 1853.5 | 28.0 |
| HS_35_100 | 10 | - | - | 1788.5 | 1864.2 | 30.4 |
| HS_95_50 | 5 | - | - | 225.83 | 241.30 | 23.1 |
| HS_96_50 | 5 | - | - | 222.18 | 237.83 | 26.0 |
| HS_97_50 | 5 | - | - | 231.47 | 246.18 | 31.2 |
| HS_98_50 | 5 | - | - | 231.92 | 246.79 | 26.7 |
| HS_99_50 | 5 | - | - | 230.02 | 244.96 | 29.2 |
| HS_108_50 | 5 | - | - | 221.29 | 238.52 | 25.3 |
| HS_109_50 | 5 | - | - | 223.57 | 238.92 | 24.1 |

4.2.2.2 Mechanical strength of non-certified samples

Table 4-14 Compressive strength measurements and weight of backfill-like materials (cement: CEM-III/B, only fine aggregate: 0-2 mm) after 52/3 years exposure to saline synthetic clay pore water. Measured on 13 April 2022 (cubical specimens) and casted in May 2016.

| Sample (only casted) | Edge of samples [cm] | 9 May 2016 after casting | 30 August 2016 after submersion in tap water | 13 April 2022 ^{after} exposure to saline solution | Compressive strength [MPa] |
|-------------------------|-------------------------|-----------------------------|--|--|----------------------------------|
| | | Weight [gram] | | | |
| H-S150_1 | 15 | 4950.3 | 5099.1 | 5296.3 | 9.1 |
| H-S150_2 | 15 | 5178.7 | 5317.3 | 5496.6 | 10.5 |
| H-S150_6 | 15 | 5578.1 | 5730.2 | 5888.0 | 13.5 |
| H-S150_7 | 15 | 5623.6 | 5761.6 | 5883.7 | 13.2 |
| H-S150_8 | 15 | 4896.6 | 5039.6 | 5278.0 | 10.3 |
| H-S150_52 | 15 | 4996.8 | 5147.9 | 5325.9 | 10.2 |
| H-S150_53 | 15 | 4864.8 | 5026.6 | 5252.7 | 10.0 |
| H-S150_54 | 15 | 4806.8 | 4969.7 | 5186.8 | 9.7 |
| H-S100_12 | 10 | 1664.6 | 1725.8 | 1807.2 | 10.9 |
| H-S100_13 | 10 | 1649.9 | 1706.7 | 1778.4 | 10.3 |
| H-S100_14 | 10 | 1663.7 | 1722.2 | 1797.9 | 14.1 |
| H-S100_15 | 10 | 1678.0 | 1729.0 | 1794.2 | 13.1 |
| H-S100_16 | 10 | 1590.6 | 1646.7 | 1725.9 | 10.4 |
| H-S100_20 | 10 | 1669.6 | 1720.8 | 1781.0 | 13.8 |
| H-S100_21 | 10 | 1630.2 | 1683.1 | 1756.4 | 12.3 |

As described in Deliverable 16.3, after 28 days of hardening, the CEM III/B backfill-like samples had an average compressive strength of 6.5 ± 0.5 MPa with an edge of 150 mm and 9.1 ± 1.2 MPa with an edge of 100 mm. These measurements are outside the calibration range of the used equipment i.e. a cubical specimen with an edge of 50 mm needs to have a minimum in compressive strength of 10 MPa. These results should therefore be treated with caution. Table 4-14 shows the measured compressive strength after exposure for $5^{2/3}$ years to the saline as seawater solution. The average compressive strength was measured to be 10.8 ± 1.6 MPa with an edge of 150 mm and 12.1 ± 1.6 MPa with an edge of 100 mm. Consequently, a detrimental mechanical effect on the compressive strength of concrete by submersion in a solution as saline as seawater has not been observed.

As described in Deliverable 16.3, after 28 days of hardening, the CEM I backfill-like samples had an average compressive strength of 11.5 ± 3.7 MPa with an edge of 150 mm and 18.6 ± 1.6 MPa with an edge of 100 mm. The measurements are outside of the calibration range of the used equipment. Table 4-15 shows the measured compressive strength after submersion for $5^{2/3}$ years in a saline as seawater solution. The average was measured to be 16.9 ± 6.3 MPa with an edge of 150 mm and 26.1 ± 2.9 MPa with an edge of 100 mm. Consequently, a detrimental mechanical effect on the compressive strength of concrete by exposure to a solution as saline as seawater has not been observed.

Table 4-15 Compressive strength measurements and weight of backfill-like materials (cement: CEM-I, only fine aggregate: 0-2 mm) after 5^{2/3} years exposure to saline synthetic clay pore water. Measured on 13 April 2022 (cubical specimens) and on 17 May 2016.

| Sample (only casted) | Edge of samples [cm] | 23 May 2016 after casting | 30 August 2016 after submersion in tap water | 13 April 2022 after exposure to saline solution | Compressive strength [MPa] |
|----------------------|----------------------|---------------------------|--|---|----------------------------|
| | | Weight [gram] | | | |
| P-S150_1 | 15 | 6388.5 | 6522.7 | 6519.8 | 23.9 |
| P-S150_2 | 15 | 5573.1 | 5722.1 | 5716.5 | 15.7 |
| P-S150_3 | 15 | 5369.9 | 5523.7 | 5491.4 | 13.0 |
| P-S150_4 | 15 | 6472.1 | 6606.2 | 6603.5 | 28.8 |
| P-S150_5 | 15 | 5933.0 | 6068.6 | 6060.7 | 16.9 |
| P-S150_6 | 15 | 5324.1 | 5475.7 | 5445.6 | 14.3 |
| P-S150_7 | 15 | 5107.3 | 5269.4 | 5271.6 | 9.9 ^x |
| P-S150_8 | 15 | 5221.1 | 5371.6 | 5367.3 | 12.7 |
| P-S100_12 | 10 | 1892.6 | 1948.7 | 1939.6 | 24.1 |
| P-S100_13 | 10 | 1829.7 | 1887.2 | 1875.8 | 21.0 |
| P-S100_14 | 10 | 1892.0 | 1947.4 | 1937.8 | 28.0 |
| P-S100_15 | 10 | 1857.8 | 1910.9 | 1902.9 | 27.9 |
| P-S100_16 | 10 | 1881.2 | 1938.1 | 1927.9 | 24.9 |
| P-S100_20 | 10 | 1911.6 | 1961.5 | 1957.6 | 27.8 |
| P-S100_21 | 10 | 1883.8 | 1937.1 | 1932.3 | 29.2 |

4.2.2.3 Chemical characterisation of certified samples

The cubical specimens with an edge of 5 cm were chiselled by hand in order to measure oxygen reaction fronts and carbonation profiles. Oxygen reaction fronts can only be observed for concrete made with a blended cement with Blast Furnace Slag. The non-oxidised part of concrete is dark blue and the oxidized part is light-grey. The extent of the wet oxidation front appeared to be too negligible to be able to make a carbonation profile of the chiselled samples. The fractured surfaces appear to be exactly as in Figure 6-23 in Deliverable 16.3 and are therefore not shown in this report.

Samples of concrete have been made in 2022 for X-ray diffraction (XRD) combined with Rietveld analysis, Thermal Gravimetric Analysis Differential Scanning Calorimetry (TGA-DSC), Energy Dispersive Spectroscopy (EDS), SEM and XRF. Samples of concrete for Inductively Coupled Plasma Optical Emission Spectrometry (ICP-OES) have also been prepared but the acid digestion of samples of concrete and resulting solutions that can be measured with ICP-OES are to be made. Ingress of magnesium has been measured for acid digested backfill-like concrete after 4 years of submersion in the solution as saline as seawater (Mladenovic and others, to be published) within 0.5 cm from the exposed surface.

4.2.2.4 Chemical characterisation of non-certified samples

The cubical specimens with an edge of 10 cm were chiselled by hand in order to measure oxygen reaction fronts and carbonation profiles. Concrete made with blended cement of portlandite and blast furnace slag contains traces of iron-sulphide. These traces give the freshly fractured concrete a dark blue appearance. This iron-sulphide reacts with ingressing oxygen. Despite that samples have been submerged, there can still be some dissolved oxygen entering the concrete specimen. The colour of the fracture surface then becomes light grey. Figure 4-32 shows that the rims of concrete made with CEM III/B that were oxidised were also carbonated.

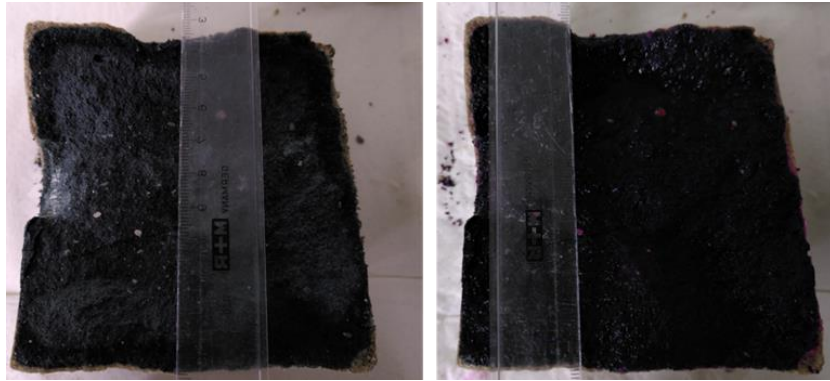


Figure 4-32 Chiselled cubical CEM III/B specimen with an edge of 10 cm without (left) and with sprayed phenolphthalein solution.

Cubical specimens with an edge of 10 cm made with CEM I could also be chiselled by hand. The ingress of oxygen within this sample cannot be monitored due to lack of reducing species in this concrete. Figure 4-33 shows that carbonation rims cannot be found since the specimens manufactured with CEM I have a too dark colour to observe carbonation fronts clearly.

Pieces of concrete for X-ray diffraction (XRD) combined with Rietveld analysis, Thermal Gravimetric Analysis Differential Scanning Calorimetry (TGA-DSC), Energy Dispersive Spectroscopy (EDS), SEM and XRF have been made in 2022. Pieces of concrete for Inductively Coupled Plasma Optical Emission Spectrometry (ICP-OES) have also been prepared. The sample preparation and the measurements are to be made if an ingress of magnesium and other elements from the saline solution can be measured with EDS.

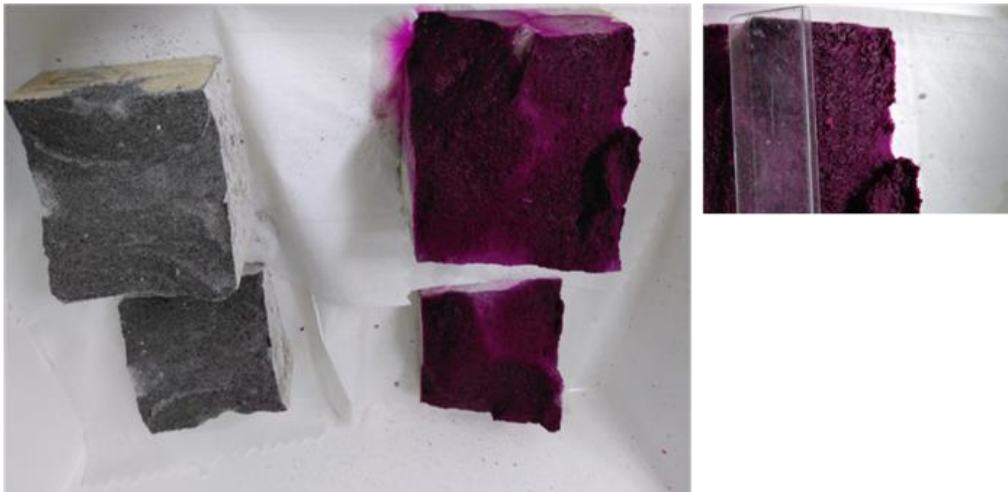


Figure 4-33 Chiselled cubical CEM I specimens with an edge of 10 cm without (left) and with sprayed phenolphthalein solution.

4.2.2.5 Concluding perspective

Self-sealing of cracks in concrete has only been observed and measured for buffer-like concrete with a porosity of 13% but not for backfill-like concrete with a porosity of 21%. An understanding of the difference between the two types of concrete is that the buffer-like concrete still had unreacted cement clinker by which the process of the seal-sealing of cracks was similar to Roman concrete.

Only an increase of the compressive strength has been observed for concrete samples submerged in clay pore water as saline as seawater despite ingress of magnesium. There were also initially unsaturated samples exposed to this clay pore water by which the ingress of magnesium may have taken place through the whole sample. Experimental evidence of ingress of magnesium over at least 0.5 cm from the exposed surface of concrete is however yet only available for the more porous concrete after 4 years of exposure. The use of the casted and sawn samples disturbs the mechanical interpretation of the effect of exposure too much to conclude a chemo-mechanical effect.

4.3 Degradation under water percolation (GRS, SCK CEN)

4.3.1 Batch/percolation experiments to mimic the Belgian disposal conditions.

The batch and percolation experiments are expected to accelerate the processes happening at the concrete-host rock interface. While the percolation experiment accounts for a pressure gradient (which is relevant for geological disposal), the batch type experiment only considers the diffusion as the main transport at the interface. Concrete used in these experiments have a similar formulation compared to the one of lining concrete at the HADES.

- Reference concrete properties:

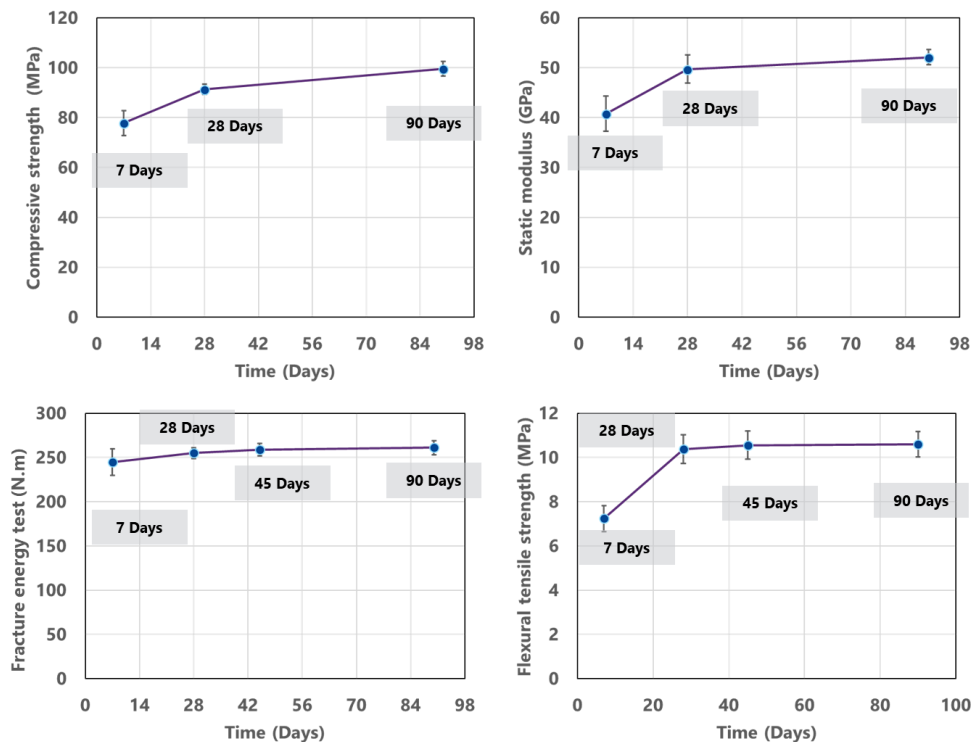


Figure 4-34 Mechanical properties of reference concrete.

Figure 4-34 illustrates the progression of concrete's mechanical properties up to 90 days of curing. At the 28-day curing, the compressive strength exceeded 90 MPa, similar to the concrete used in HADES (concrete class C80-90). Additionally, the flexural strength surpassed 10 MPa after 28 days of curing. By the 28-day curing, the fracture energy and static modulus were approximately 250 N.m and 50 MPa, respectively. Notably, these properties remained relatively stable from day 28 to day 90 of the curing process.

Figure 4-35 illustrates the concrete's remarkably low permeability. By 7 days of curing, the concrete exhibited a low permeability of $2.2\text{E-}13$ m/s, which further decreased to $4.5\text{E-}14$ m/s after 90 days of curing.

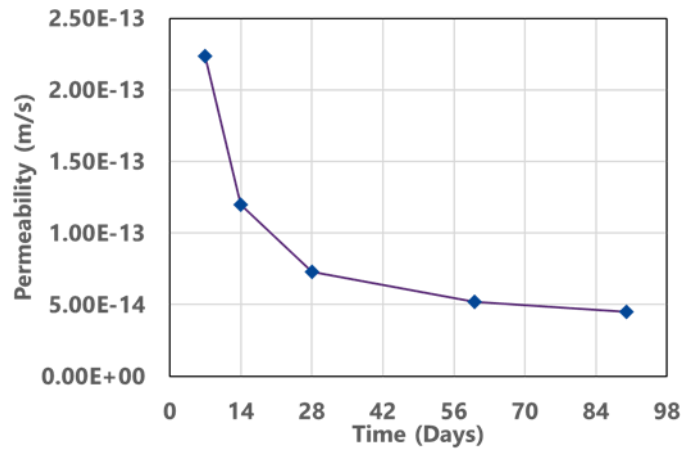


Figure 4-35 Water permeability of reference concrete.

4.3.2 Degradation of samples percolated with a “corrosive” solution (Konrad solution)

Currently, the THMC-test is in the thermal phase (pre-treatment) at a temperature of 70°C . Figure 4-36 shows the results for the first 58 days. Within the first days, a linear increase in axial strain is noticeable whose trigger cannot be identified yet. Following, axial and radial strains are constant until temperature is increased to 70°C . With the temperature increase radial strain increases a little for around 14 days. Afterwards, radial strain starts to decrease which may result in a radial contraction of the sample. In axial direction no significant changes are observed. Within the thermal load of 35°C an injection of 12 mL Konrad-solution to the sample is measured. After temperature was increased to 70°C , around 2 mL solution flowed back to the peristaltic pump. That may be caused by the solid volume increase inside the concrete which results in a decrease of the pore space.

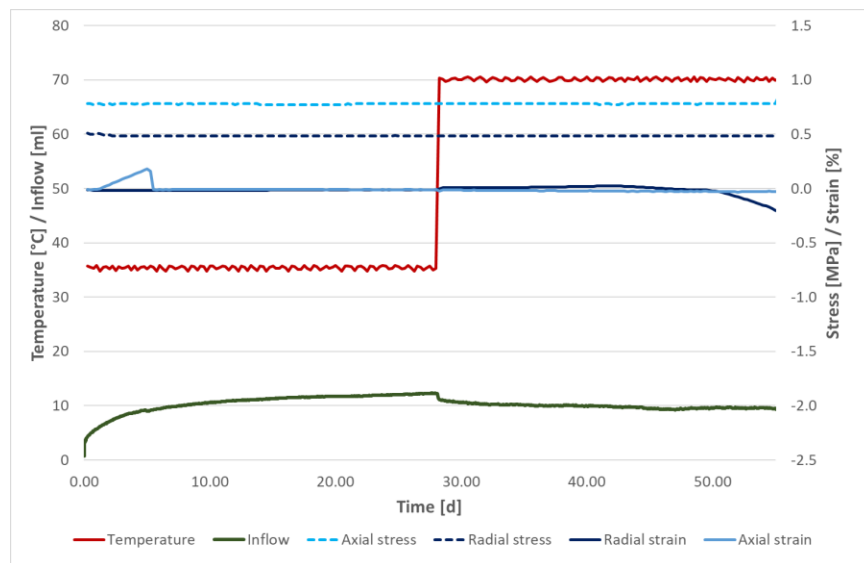


Figure 4-36 Primary results of the THMC-testing. The results refer to the thermal phase with load steps of 35°C and 70°C under nearly isotropic stress.

Currently, no more information regarding the THMC-coupled behaviour of low-pH S5 is available, caused by the sum of issues within the MAGIC project. Investigations of low-pH S5 will be continued at GRS, hence results will be available in future but not within the runtime of MAGIC.

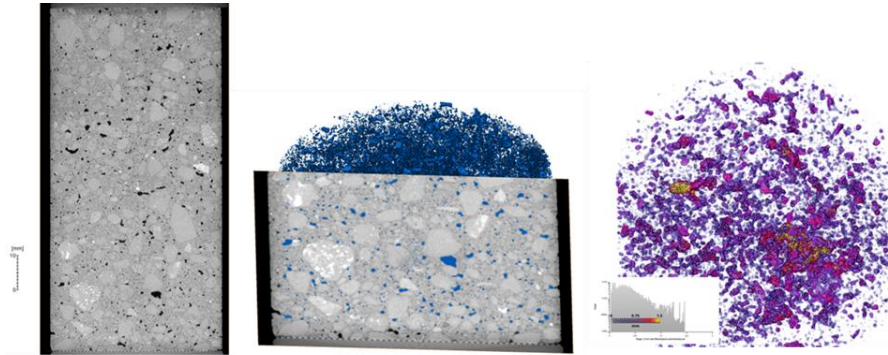


Figure 4-37 : Left: CT scan of low-pH S5 sample (voxel size = 20 μ m) Middle: Segmented pores (porosity = 0.04) Right: Thickness map (pore size distribution)

Figure 4-37 shows the results of the CT scan of the low-pH S5 sample which was conducted at HZDR during preparation of the GeoPET method. The CT scan was performed for about 15 hours with a voxel size of 20 μ m. Results show a high humidity of the sample. Indeed, there are a lot of pores at the grain boundaries of the aggregates, but a connection of the pore spaces could not be identified by CT.

4.4 Conclusion for part 4

- The first part focused on concrete ageing in contact with clay rocks:

In the PSI/Empa study, the mortars/concretes have, in increasing order, an average compressive strength of 24 MPa (LAC concrete), 36 MPa (OPC concrete), 40 MPa (ESDRED mortar) and 80 MPa (ESDRED concrete and OPC mortar). Concerning non-destructive tests, the E^{dyn} data scatter due to the material heterogeneity was larger than that due to the measurement repeatability level, while the two data scatter types were on average similar for α_L . The correlation between dynamic and quasi-static Young's modulus values indicates that the dynamic values are 10 to 40 % higher than the quasi-static ones. Only the LAC specimens exhibited a clear and coherent spatial dependence of the mechanical properties on the specimen distance from the OPA interface. This difference is consistent with the presence of cracks and debonded ITZs in the cores at 0 mm, but not in the cores at 50 mm.

In the SCK CEN study, the autoradiography porosity map shows that the porosity of OPC concrete increases by about 2 mm after 14 years of interaction in contact with Boom Clay (Hades URF). In the sound part, the porosity arising from the intermingling of the cement binder and the small aggregates is approximately 20 %, while in the surface the porosity is 35 %. The water sorptivity coefficient is then 3 times higher for altered concrete (at the interface) than for sound concrete. The cumulative water absorption data reveals an initial rapid absorption phase, followed by a subsequent slower absorption phase. A significant enrichment in Mg is observed in the concrete in contact with the clay, spanning a thickness of 500 μm . The mapping reveals the leaching of Ca in the OPC concrete at the interface and the increase in Mg concentration is inversely correlated with calcium concentration (mineralogical mapping). According to Darcy's law in conjunction with Lucas-Washburn's equation, the increase in water sorptivity can be attributed directly to changes in capillary porosity and mean pore radius.

- The second part focused on the evolution under multi-ionic chemical attack:

In the COVRA study, ageing of mortar/concrete in contact with poorly indurated clay simulants increased compressive strengths. A comparison of mechanical strengths is provided between samples hardened for 28 days and samples exposed for 5 years or more to a clay pore water salty as seawater. Following the saltwater immersion phase, the compressive strength of CEM III/B buffer-like samples increases by 26 to 31%, the compressive strength of CEM III/B backfill-like samples increases by 24 to 46 %, and the compressive strength of CEM I backfill-like samples non-certified samples increases by 40 to 47 %. The fractured surfaces of the cracked samples placed in close contact revealed a potential for self-sealing for the buffer sample, but not for the backfill sample. Regarding this increase in strength, it is not possible to separate the role of reactivity with the environment from that of hydration of the cement. The study of the oxygen reaction front by colour contrast, and the evaluation of carbonate thicknesses, gave the first indications about calcite formation and the degradation of C-S-H by carbonation, as well as the progression of Mg.

In the Czech team study, after three years, the initial pH of the interstitial solution is 10.6 (SKB procedure). After 18 months of exposure (air, ground water, suspension) in MAGIC, this pH rises to ~10. These are measurements for crushed samples and using distilled water. A reduction in mechanical properties was observed by punching test, especially in the case of water immersion and bentonite exposure for 18 months. After 18 months of conservation under water, a depth of decalcification/leaching was observed up to 1 mm. The samples show microcracks in the first few millimetres of the surface exposed to the bentonite. This could potentially be linked to drilling, cutting or sulphate attack (presence of sulphates in the bentonite slurry).

On the surface, the XRD gives results that are very similar to the initial state in terms of the main phases identified, but after 6 months there are new Ca mineral phases in samples exposed to Air. XRD measurements show that it is gypsum and vaterite.

➤ The third part focused on the degradation under water percolation:

In the SCK-CEN study, the percolation and batch treatment experiments are still in progress. SCK-CEN presented the properties of the reference concretes, having a compressive strength of 90 MPa and a permeability of $4.5E-14$ m/s after 28 days of curing.

In the GRS study, during the first phase at 35°C, an injection of 12 ml of Konrad solution into the low pH sample was measured. After increasing the temperature to 70°C, about 2 ml of solution flowed back to the peristaltic pump (TM effect). Increasing the temperature to 70°C slightly increased the radial deformation by dilatation and the sample then contracted radially. The CT scan of sample S5 at low pH showed the high presence of bubbles in the samples (porosity of 4 %).

4.5 References for part 4

- A.M. Neville, Chapter 9. Elasticity, shrinkage and creep, in: Properties of Concrete, 5th edition, Pearson Education Ltd., 2011.
- F. Saint-Pierre, P. Rivard, G. Ballivy, Measurement of alkali–silica reaction progression by ultrasonic waves attenuation, *Cement and Concrete Research*. 37 (2007) 948–956.
- F.D. Lydon, R.V. Balendran, Some observations on elastic properties of plain concrete, *Cement and Concrete Research*. 16 (1986) 314–324.
- I. Gabrijel, S. Staquet, M. Krüger, J. Carette, C.U. Grosse, G. Trtnik, Ultrasonic Techniques for Determination and Monitoring Various Properties of Cementitious Materials at Early Ages, in: *Advanced Techniques for Testing of Cement-Based Materials*, Springer International Publishing, 2020: pp. 23–68.
- J.S. Popovics, J. Zemajtis, I. Shkolnik, A Study of Static and Dynamic Modulus of Elasticity of Concrete, American Concrete Institute, 2008.
- L. M. Seymour, J. Maragh, P. Sabatini, M. Di Tommaso, J. C. Weaver, A. Masic. Hot mixing: Mechanistic insights into the durability of ancient Roman concrete. *Sci. Adv.*9, eadd1602(2023). DOI:10.1126/sciadv.add1602.
- R.N. Swamy, A.K. Bandyopadhyay, The elastic properties of structural lightweight concrete, *Proc. Inst. Civ. Engrs*. 59 (1975) 381–394.
- T.P. Philippidis, D.G. Aggelis, Experimental study of wave dispersion and attenuation in concrete, *Ultrasonics*. 43 (2005) 584–595.

5 Chemo-microbial impact on chemo mechanical evolution of concrete (SURAO/CTU/UJV/CVREZ, TUL, SCK-CEN, COVRA/FZJ, UNIMAN, HZDR)

5.1 Artificial ageing conditions due to salt water and microbial attack on old samples

5.1.1 Mechanical characterisation

Table 5-1, Table 5-2 and Table 5-3 show that the mechanical strength of the gamma-irradiated samples appears to be similar to the samples that were not gamma-irradiated. Certified backfill material is the best type of concrete to show this negligible effect by radiation since the variation in density is sufficiently small and all samples were prepared in the same way.

Table 5-1 Compressive strength measurements and weight of certified backfill materials (cement: CEM-III/B, only fine aggregated: 0-2 mm) after 5 years submersion in saline synthetic clay pore water. Measured on 28 September 2022 and casted on 14 June 2017. The edges of the samples is 5 cm. In brackets, the weight and compressive strength as measured on 23 October 2023.

| Sample | Characteristic | 20 June 2017 | 22 April 2022 | 28 September 2022 (23 October 2023) | Compressive strength [MPa] |
|-----------|--|---------------|---------------|-------------------------------------|----------------------------|
| | | Weight [gram] | | | |
| HS_106_50 | Casted | 216.66 | 237.20 | 237.24 (240.07) | 23.2* (27.7) |
| HS_107_50 | | 221.85 | 239.11 | 239.12 (241.66) | 25.8 (26.7) |
| HS_102_50 | Casted and γ -irradiated till a dose of 57.6 kGy (dose rate 6.4 kGy per hour) in Sep 2022 | 223.72 | 239.60 | 239.69 (241.83) | 23.2 (27.2) |
| HS_103_50 | | 220.75 | 237.56 | 237.45 (239.39) | 20.7 (18.6) |

*There may be an error in the installation of the equipment by which the measured compressive strength on 28 September 2022 is incorrect.

Table 5-2 Compressive strength measurements and weight of backfill materials (cement: CEM-I, only fine aggregated: 0-2 mm) after 61/3 years exposure to saline synthetic clay pore water. Measured on 28 September 2022 and casted on 17 May 2016. Edge of cubical samples is 5 cm. In brackets, the weight and compressive strength as measured on 23 October 2023.

| Sample | Characteristic | 23 May 2016 after casting | 30 August 2022 after submersion in tap water | 22 April 2022 after exposure to saline solution | 28 September 2022 (23 October 2023) after exposure to saline solution | Compressive strength [MPa] |
|----------|--|---------------------------|--|---|---|----------------------------|
| | | Weight [gram] | | | | |
| P-S50_28 | Only casted | 218.54 | 228.80 | 231.59 | 231.61 (235.88) | 16.6 (9.1*) |
| P-S50_29 | Casted and γ -irradiated till a dose of 57.6 kGy (dose rate 6.4 kGy per hour) in Sep 2022 | 192.75 | 205.04 | 201.47 | 202.06 (210.53) | 16.2 (8.1*) |
| P-S50_30 | | 233.65 | 242.49 | 240.77 | 241.13 (247.16) | 27.7 (15.5*) |
| P-S50_33 | Only casted | 238.50 | 246.96 | 247.35 | 247.10 (252.89) | 30.3 (26.2*) |

*Samples may have a too irregular surface for a reliable compressive strength measurement.

Table 5-3 Compressive strength measurements and weight of backfill materials (cement: CEM-III/B, only fine aggregated: 0-2 mm) after 61/3 years exposure to saline synthetic clay pore water. Measured on 28 September 2022 and casted in May 2016. Edge of cubical samples is 5 cm. In brackets, the weight and compressive strength as measured on 23 October 2023.

| Sample | Characteristic | 9 May 2016 | 30 August 2022 | 22 April 2022 | 28 September 2022 | Compressive strength [MPa] |
|---------------|---|---------------|-------------------------------|-----------------------------------|--|----------------------------|
| | | after casting | after submersion in tap water | after exposure to saline solution | (23 October 2023) after exposure to saline solution | |
| Weight [gram] | | | | | | |
| H-S50_22 | Only casted | 223.88 | 231.95 | 244.99 | 245.10 (244.94) | 20.3 (18.6) |
| H-S50_23 | Only casted | 225.62 | 234.02 | 242.72 | 241.97 (247.30) | 16.3 (19.1) |
| H-S50_24 | Casted and γ -irradiated till a dose of 57.6 kGy in Sep 2022 | 222.04 | 233.11 | 244.92 | 245.07 (246.89) | 18.2 (20.5) |
| H-S50_25 | | 222.28 | 229.11 | 240.42 | 240.57 (243.59) | 21.6 (23.5) |

*There may be an error in the installation of the equipment by which the measured compressive strength on 28 September 2022 is incorrect.

For buffer-like concrete, only a comparison was available with the casted and sawn samples (see Table 5-4). The sawing had a larger effect on the degradation of the strength of concrete. The only casted buffer-like samples may be better compared with the data in section 4.2.2 in which the average compressive strength was about 70-72 N/mm². The only casted but irradiated sample has a compressive strength of 71-72 N/mm². Again, similarly as certified backfill concrete, a negligible impact of gamma radiation was observed.

Table 5-4 Compressive strength measurements and weight of buffer-like materials (cement: CEM-III/B, coarse aggregate: 2-8 mm) after 6 years exposure to saline synthetic clay pore water. Measured on 28 September 2022 and casted on 13 July 2016a and on 30 June 2015b or 1 July 2015b. Edge of samples is 5 cm. In brackets, the weight and compressive strength as measured on 23 October 2023.

| Sample | Characteristic | 30 August 2016 | 18 January 2017 | 22 April 2022 | 28 September 2022 | Compressive strength 28/09/2022 (23 October 2023) [MPa] |
|-------------------------|--|----------------|-----------------|---------------|--------------------|---|
| | | Weight [gram] | | | | |
| 7_COV50_56 ^a | Casted and sawn | - | 297.62 | 301.92 | 304.65 | 51.7 (37.7) |
| 7_COV50_57 ^a | | - | 299.58 | 303.74 | 303.75 | 40.5 (66.9) |
| COV50_103 ^b | Casted and γ -irradiated till a dose of 57.6 kGy (dose rate 6.4 kGy per hour) in Sep 2022 | 293.09 | - | 295.46 | 294.84 (295.80) | 71.5 (61.1) |
| COV50_104 ^b | | 287.05 | - | 289.41 | 288.61 (289.58) | 70.7 (74.0) |

^aspecimen had been pulverised at the edges after measurement of the compressive strength. *There may be an error in the installation of the equipment by which the measured compressive strength on 28 September 2022 is incorrect.

Figure 5-1 shows that an irradiated sample became stacked to its sample holder after another year of submersion in the saline solution. This sticking did not have a large strength since the samples could be removed from their sample holder by hand. A chemical reaction does not seem likely and therefore microbial activity despite sterilization and cleaning with 70% ethylethanol is assumed to be the cause of this sticking. The water in which the concrete specimens were exposed to appeared to be sterile after irradiation. Any handling of the specimens, how carefully done, may introduce microbes. The samples made with CEM I

have the largest irregular surfaces. The surfaces of a sample need to be smooth for a credible compressive strength measurement.

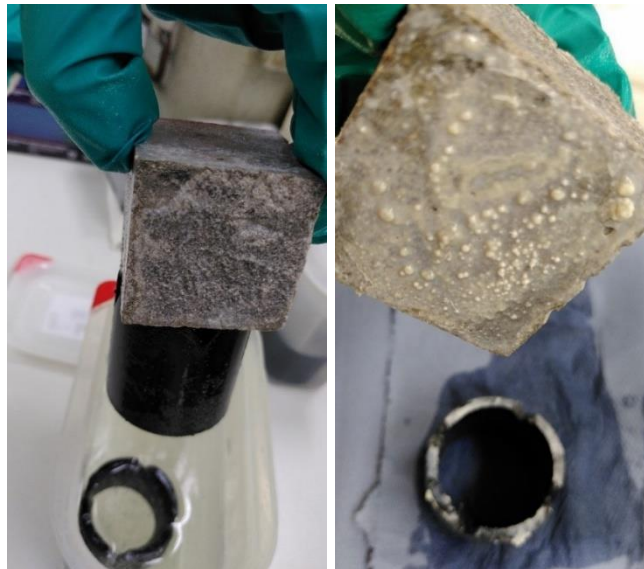


Figure 5-1 Irradiated sample sticking to the irradiated sample holder (left), irregular surface of the sample (right).

5.1.2 Chemical characterisation

The chemical characterisation of these samples is already described in section 4.2.2.3 and 4.2.2.4.

5.1.3 Microbial characterisation

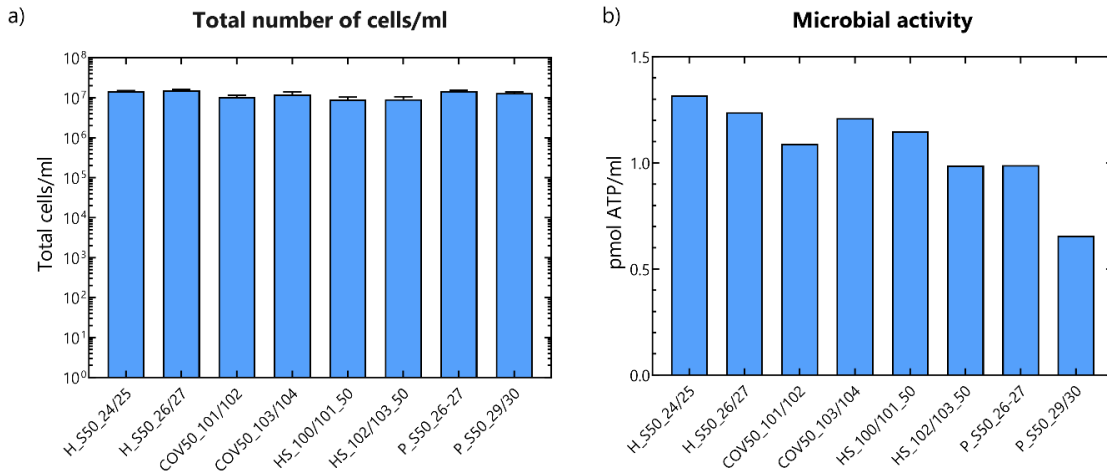


Figure 5-2 Bar plots representing a) total cell concentration determined with flow cytometry; b) microbial activity based on intracellular ATP. Values of flow cytometry measurements represent average and standard deviation of two technical replicates.

The concentration of the total number of microbial cells was similar in all Dutch clay water samples and ranged from $9.02 \times 10^6 \pm 1.40 \times 10^6$ cells/mL as minimum cell number in sample HS_100/101_50 to $1.52 \times 10^7 \pm 1.06 \times 10^6$ cells/mL in sample H_S50_26/27 (Figure 5-2). More variation in microbial activity was

observed with intracellular ATP measurements varying from 0.66 pmol ATP/mL in sample P_S50_29/30 to 1.32 pmol ATP/mL in sample H_S50_24/25 (Figure 5-2).

Comparison of the cell number with water samples from underground research facilities indicates that the total cell number is comparable with that observed for several piezometers in the HADES URF (Mol, Belgium) and is higher than that of water samples from the BN experiment at Mont Terri (Switzerland) (Hendrix *et al.*, 2022, Honty and Mijndonckx, 2022). On the other hand, ATP values are lower than most of the samples present in HADES but higher than most values observed in the BN experiment (Hendrix *et al.* 2022, Honty and Mijndonckx 2022). The discrepancy between total cell counts and microbial activity observed in samples studied here could indicate that cells are not highly metabolically active in these water samples.

To further confirm the presence of viable cells in the water, cells were grown in different media. One of the growth media that we used was R2A, a general growth medium used to monitor heterotrophic bacterial populations present in water samples (Reasoner and Geldreich, 1985). Colonies were counted after two weeks incubation at 30°C. Large differences are observed among the samples with samples P_S50_29/30 and P_S50_27/28 having the lowest number of CFU/mL, namely 30 CFU/mL and 250 ± 71 CFU/mL, respectively, and sample COV50_103/104 had the largest number, namely 10,200 CFU/mL (Figure 5-3). A variety of distinct colonies was present in the water samples (Figure 5-4). Colonies with different phenotypic characteristics (e.g. colour, morphology) were further purified. In total, 19 colonies were purified and identified representing nine different genera (Figure 5-5). Species from the genus *Phenylobacterium*, *Sphingopyxis* and *Sphingobium* are known for their ability to degrade xenobiotic compounds (Lingens *et al.* 1985, Sharma *et al.* 2021, Sato *et al.* 2023). The genus *Alcanivorax* comprises marine alkane-degrading bacteria able to use a variety of saturated alkanes in crude oil (Cappello and Yakimov 2010). They have been found in biofilms on reinforced concrete (Karacic 2021), which was also observed for species from the genus *Hyphomonas* (Karačić *et al.* 2022). Species from the genus *Pseudonocardia* have also been isolated from corrosive lesions of concrete structures (Rabab 2015). Contrary to the presence of aerobic heterotrophic microorganisms, only one sample – COV50_101/102 – was positive for growth of SRB.

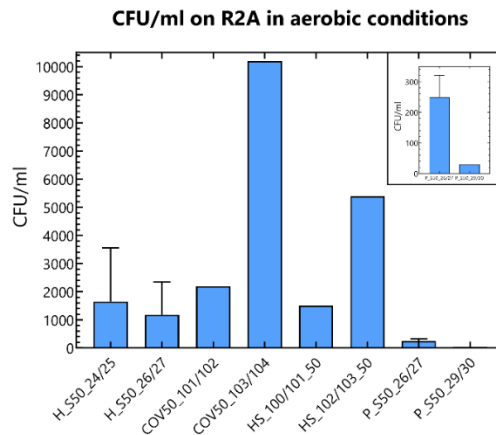


Figure 5-3 Bar plot showing the number of CFU/mL counted on R2A agar plates. Samples P_S50_26/27 and P_S50_29/30 are also shown in the small graph represented with a different scale.

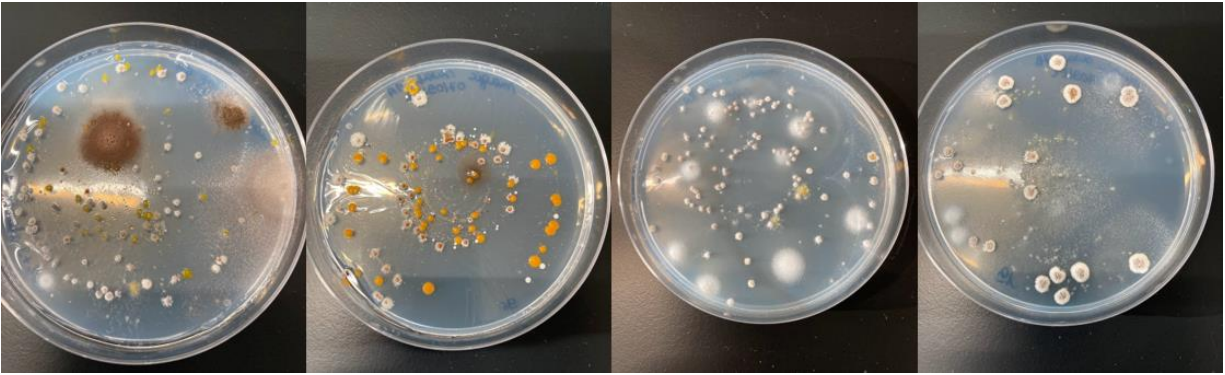


Figure 5-4 Example of different colonies from the water samples grown on R2A agar plates in aerobic conditions.

The number of CFU on R2A agar medium originating from the swaps taken from the concrete itself was generally lower than that of the number of colonies present in the water (Figure 5-5). Putatively, although to a lesser extent, the surfaces of the concrete cubes are colonized by bacteria. Similar as for the water samples, distinct colonies were purified and identified. Classification and sequence alignments showed that several of the identified colonies in the water were also isolated from the concrete cubes (Figure 5-5 and Table 5-5). For the samples without a representative of the colonies from water or on the concrete cubes, it is possible that either we did not select it for further purification, or it was not present on the concrete cubes.

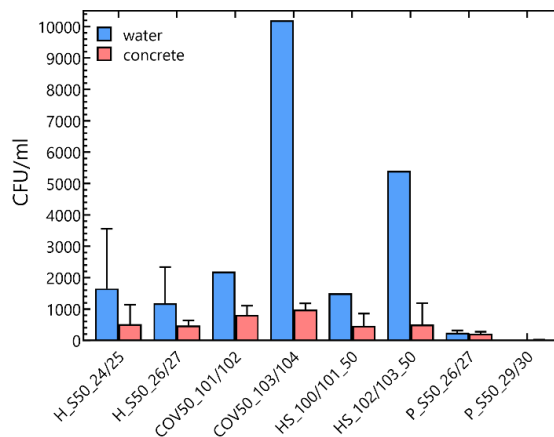


Figure 5-5 Bar plots showing the number of CFU/mL in water samples (blue) compared to the number of CFU originating from a swap taken from the concrete surface (red).

From these results, it is clear that all samples harbour a diverse microbial community. However, to enable studying the effect of microbial activity on the concrete samples, we needed abiotic controls. Therefore, we selected four samples (1 box of each sample: H_S50_24/25; COV50_103/104; HS_102/103_50; P_S50_29/30) for sterilization through γ -irradiation. Samples were irradiated at SCK CEN for 9 hours with a dose rate of 6.4 kGy/h corresponding to a total dose of 57.6 kGy. Sterility of the samples was confirmed by intracellular ATP measurements and growth in aerobic conditions. Both were negative therefore confirming sterility of the samples.

Table 5-5 Overview of the classification of the different colonies isolated from the water samples on R2A in aerobic conditions. Similar classifications are represented with matching colours for corresponding samples.

| Sample | Phylum | Order | Class | Family | Genus |
|---------------|-----------------------|----------------------------|--------------------------|---------------------------|-------------------------|
| H_S50_24/25 | <i>Proteobacteria</i> | <i>Alphaproteobacteria</i> | <i>Caulobacterales</i> | <i>Caulobacteraceae</i> | <i>Phenylobacterium</i> |
| | <i>Proteobacteria</i> | <i>Alphaproteobacteria</i> | <i>Caulobacterales</i> | <i>Caulobacteraceae</i> | <i>Brevundimonas</i> |
| H_S50_26/27 | <i>Proteobacteria</i> | <i>Alphaproteobacteria</i> | <i>Caulobacterales</i> | <i>Caulobacteraceae</i> | <i>Phenylobacterium</i> |
| P_S50_26/27 | <i>Proteobacteria</i> | <i>Alphaproteobacteria</i> | <i>Rhodovibrionales</i> | <i>Fodincurvataceae</i> | NA |
| | <i>Actinobacteria</i> | <i>Actinobacteria</i> | <i>Pseudonocardiales</i> | <i>Pseudonocardiaceae</i> | <i>Pseudonocardia</i> |
| | <i>Proteobacteria</i> | <i>Alphaproteobacteria</i> | <i>Caulobacterales</i> | <i>Caulobacteraceae</i> | <i>Phenylobacterium</i> |
| | <i>Proteobacteria</i> | <i>Alphaproteobacteria</i> | <i>Caulobacterales</i> | <i>Caulobacteraceae</i> | <i>Brevundimonas</i> |
| P_S50_29/30 | <i>Actinobacteria</i> | <i>Actinobacteria</i> | <i>Pseudonocardiales</i> | <i>Pseudonocardiaceae</i> | <i>Pseudonocardia</i> |
| | <i>Proteobacteria</i> | <i>Gammaproteobacteria</i> | <i>Oceanospirillales</i> | <i>Alcanivoracaceae</i> | <i>Alcanivorax</i> |
| | <i>Proteobacteria</i> | <i>Alphaproteobacteria</i> | <i>Caulobacterales</i> | <i>Hyphomonadaceae</i> | <i>Hyphomonas</i> |
| COV50_101/102 | <i>Actinobacteria</i> | <i>Actinobacteria</i> | <i>Pseudonocardiales</i> | <i>Pseudonocardiaceae</i> | <i>Pseudonocardia</i> |
| | <i>Proteobacteria</i> | <i>Alphaproteobacteria</i> | <i>Sphingomonadales</i> | <i>Sphingomonadaceae</i> | <i>Sphingopyxis</i> |
| | <i>Actinobacteria</i> | <i>Actinobacteria</i> | <i>Mycobacteriales</i> | <i>Mycobacteriaceae</i> | <i>Mycobacterium</i> |
| | <i>Proteobacteria</i> | <i>Alphaproteobacteria</i> | <i>Sphingomonadales</i> | <i>Sphingomonadaceae</i> | <i>Sphingobium</i> |
| COV50_103/104 | <i>Proteobacteria</i> | <i>Alphaproteobacteria</i> | <i>Sphingomonadales</i> | <i>Sphingomonadaceae</i> | <i>Sphingopyxis</i> |
| | <i>Actinobacteria</i> | <i>Actinobacteria</i> | <i>Pseudonocardiales</i> | <i>Pseudonocardiaceae</i> | <i>Pseudonocardia</i> |
| HS_100/101_50 | <i>Actinobacteria</i> | <i>Actinobacteria</i> | <i>Pseudonocardiales</i> | <i>Pseudonocardiaceae</i> | <i>Pseudonocardia</i> |
| | <i>Proteobacteria</i> | <i>Alphaproteobacteria</i> | <i>Sphingomonadales</i> | <i>Sphingomonadaceae</i> | <i>Sphingopyxis</i> |
| HS_102/103_50 | <i>Actinobacteria</i> | <i>Actinobacteria</i> | <i>Pseudonocardiales</i> | <i>Pseudonocardiaceae</i> | <i>Pseudonocardia</i> |

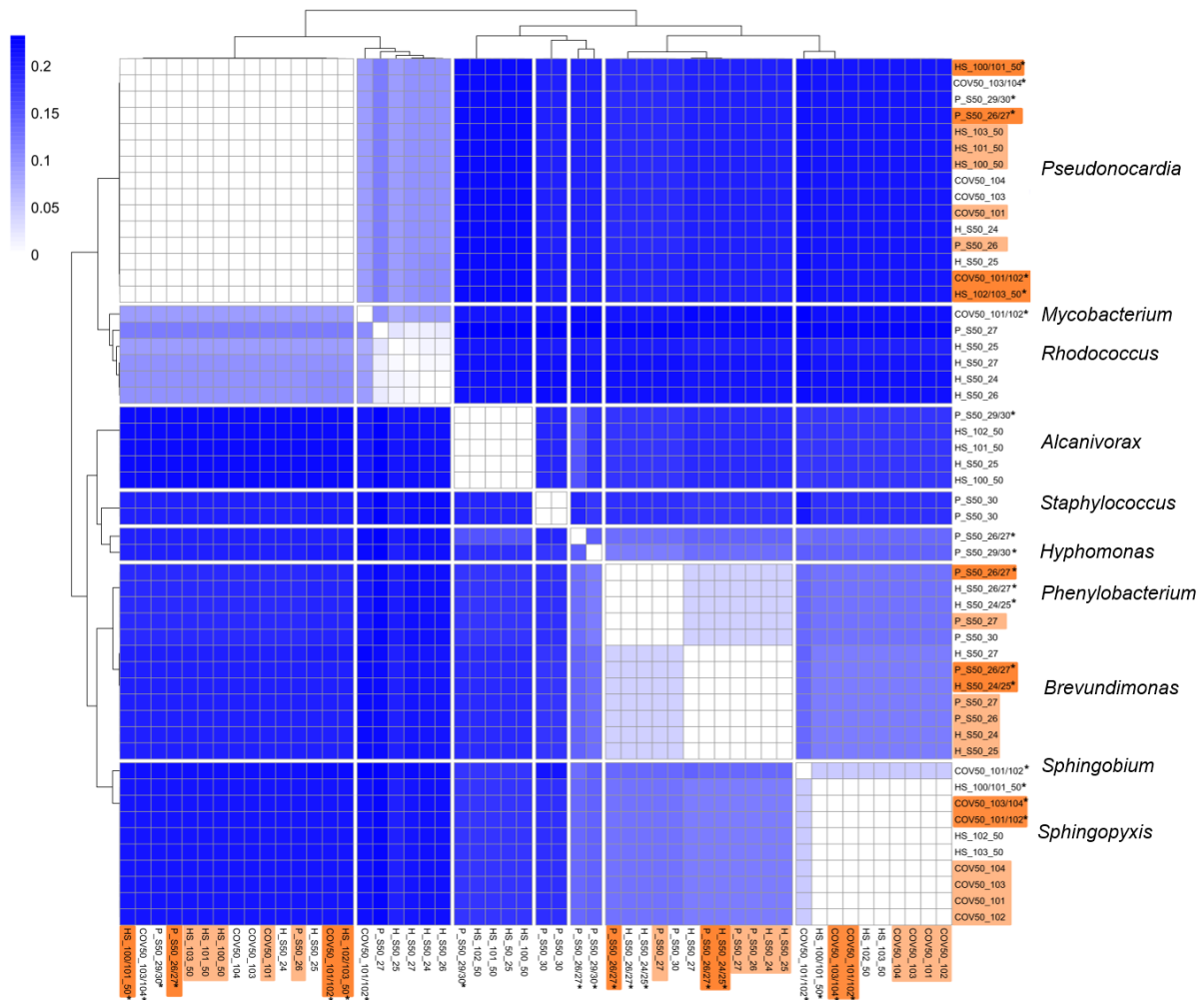


Figure 5-6 Distance matrix based on pairwise multiple sequence alignments of 16S rRNA amplicon sequences from colonies isolated from the water (marked with *) and concrete cubes. Samples from which the same genus was identified in the water and on the concrete cubes are designated in dark and light orange, respectively. The scale represents the dissimilarities between the sequences.

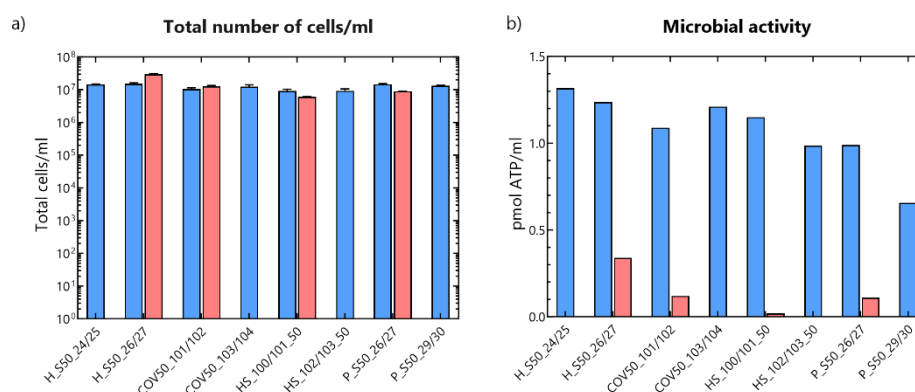


Figure 5-7 a) Total cell concentration determined with flow cytometry and b) intracellular ATP measured at the start of MAGIC (blue) and after 1.5 year (red). Samples without a value after 1.5 year were sterilized with γ -radiation.

Currently, the four biotic samples are analysed again in detail to see how the microbial community evolves in time. Analysis of the total cell concentration shows that the number is similar as at the beginning of the project. However, the amount of intracellular ATP is at least 3.5 times lower after 1.5

year, which indicates that cell activity decreased (Figure 5-7). Putatively, the amount of TOC in the samples becomes a limiting factor. Nevertheless, viable cells could be detected in all samples although some variability compared to the start of the experiment was observed (Figure 5-8Figure 5-9). Notably, the number of viable cells on the concrete cubes increased in all samples with a 25-times increase in sample HS_100/101_50 to a 680-times increase in sample H_S50_26/27 (Figure 5-8).

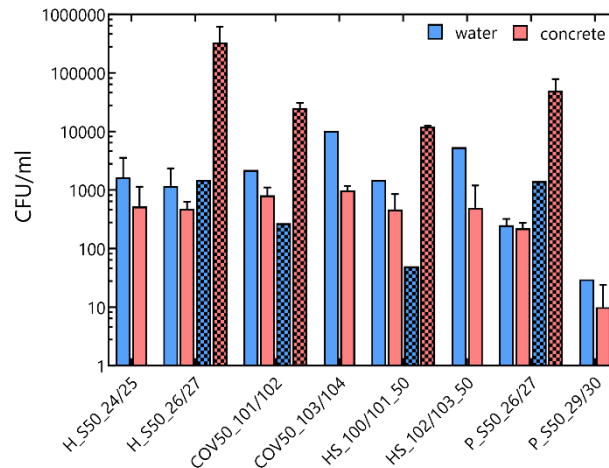


Figure 5-8: Bar plots showing the number of CFU/ml in water samples (blue) compared to the number of CFU originating from a swap taken from the concrete surface (red) at the start of the experiment (full bars) and after 1.5 year (blocked boxes).

The presence of a microbial community in all the samples raised questions about its origin. Therefore, To elucidate their possible origin, analyses were performed on water aliquots from large boxes with concrete samples (from certified and blend CEM), which was taken to prepare the concrete samples used during this project, as well as from tap water and sand used to prepare the concrete cubes. Total cell concentrations were determined on the water samples with flow cytometry. Total cell concentration in water from blend CEM was similar to that in the small boxes, while it was considerably less in the other samples (Figure 5-9). Similarly, ATP values were the highest in the water from samples with blend CEM: about 2.5 times higher compared to the water from samples with certified CEM and about 18 times higher compared to the tap water. However, they were about 10 times lower compared to the ATP values in the small boxes presented (Figure 5-9).

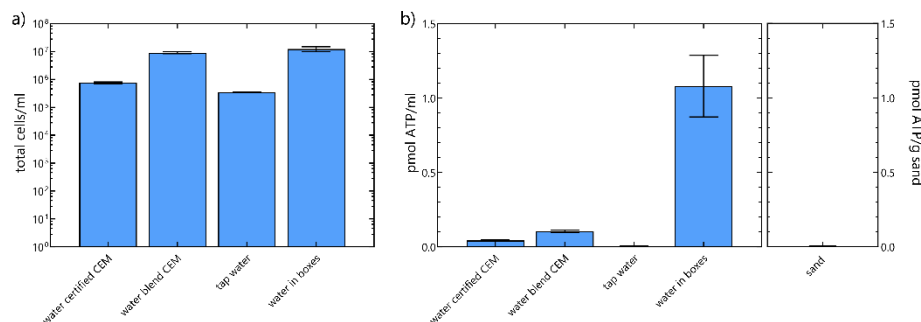


Figure 5-9 Bar plots representing a) total cell concentration determined with flow cytometry; b) microbial activity based on intracellular ATP of water originating from large boxes with certified CEM specimens; water from large boxes with blend CEM; tap water and sand to prepare the concrete cubes. Values represent average and standard deviation of three replicates.

Values are compared with the average ATP value from the water in the small boxes analyzed. Heterotrophic growth in R2A was low in the water samples (tap water and water from the large boxes) and was in the range of the lowest values observed for the eight water samples in the small boxes

presented above (Figure 5-7; Figure 5-9). Contrary, the number of colonies observed for the sand was > 10 times higher compared to those observed in the water samples (Figure 5-10). None of the samples was positive for SRB.

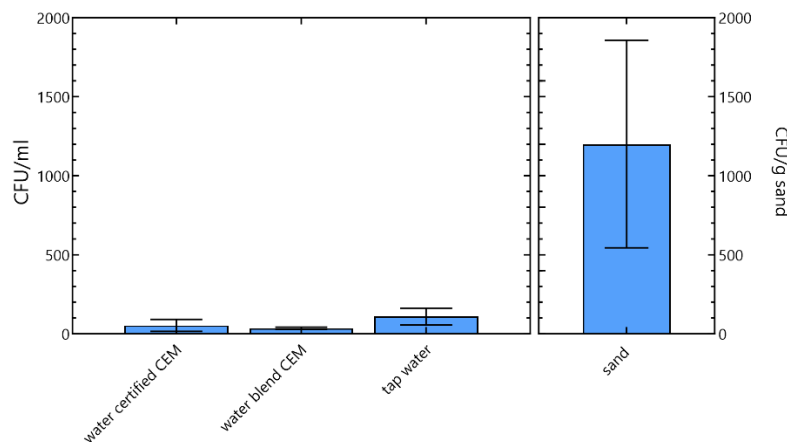


Figure 5-10 Bar plot showing the number of CFU/mL counted on R2A agar plates for water from large boxes with blend CEM; tap water and sand to prepare the concrete cubes. Values represent average and standard deviation of three replicates.

For these samples, some colonies were also selected for purification and identification through 16S rRNA amplicon analysis. Interestingly, a species from the genus *Rhodococcus* was isolated from the large boxes with water from certified CEM. Its 16S sequence closely resembled those found in colonies from the concrete surfaces of samples P_S50_27 and H_S50_24-27. Furthermore, another species, affiliated with the *Sphingomonas* genus, was isolated from the tap water. This genus shares a family with *Sphingophyxis* and *Sphingobium*, both of which were previously detected in the water and on the concrete surfaces. These results may shed further light on the origin of the microbial community within these environments. Nevertheless, the water in the small boxes is fundamentally the same as the water taken from the large boxes with certified or blend CEM specimens. However, the microbial community seems to more abundant and active in the small boxes. This suggests the presence of a factor that enhances the microbial community in the smaller containers.

We identified the complete bacterial community composition of the water samples, swabs and the sand by 16S rRNA amplicon sequencing.

Taxonomical characterization of the different ASV indicated the presence of a diverse microbial community comprised of ASV that belong to 19 different phyla (Figure 5-11). The most dominant phylum in all samples is Proteobacteria representing 41 – 81 % of the total community. In addition, Actinobacteria and Bacteroidetes are also abundant in the samples. Although Proteobacteria are abundant in the sand community, Firmicutes is the most dominant phylum in this sample. In addition, if data are zoomed to the genus level, it is clear that the most varying genera present in the water samples are not abundant or present in the sand (Figure 5-12).

Overall, the genus *Parvibaculum* is abundant in all samples except in H_S_24_25_2022 and a swab sample from the concrete surface of HS_100_50_2022. This genus is often associated with environments typified by hydrocarbon degradation (Schleheck *et al.*, 2011). In most samples, the water from the two boxes that were analysed in the beginning of the project are quite similar; however: the water sample H_S_24_25_2022 is completely different from all others (Figure 5-12). As we don't have a detailed chemical analysis of the water, we cannot link possible differences to the observed difference in the bacterial community. In addition, most genera that were observed in the water samples are observed on the swabs (except for HS_100_50_2022 and again the water sample H_S_24_25_2022 is very different compared to the swabs analysed from this box) but their relative abundance can be different. For example, the abundance of genus *Planktosalinus* is lower on the surfaces compared to its

abundance in the water sample, while the relative abundance of *Fodincurvataceae* on the concrete surfaces of samples from H_S and P_S was higher compared to its abundance in the water.

The bacterial community evolved during the 1.5 year of incubation. The clearest observation is the increased relative abundance of the genus *Alcanivorax* in samples where it was present in the beginning of the project (all samples except HS). Its relative abundance increased 30-fold in the sample P_S and up to 42-fold in samples indicated with COV50 and H_S. This increase was also observed on the concrete samples (Figure 5-12). Although its relative abundance was very low in the samples HS, we were able to isolate species from the genus *Alcanivorax* from the concrete surfaces in the beginning of the project (Figure 5-6). However, it is not clear why their abundance didn't increase in those samples. In fact, ASV among the order *Microtrichales* became one of the dominant ASV and also *Aliihoeflea* increased. On the other hand, in the water sample, HS_102_103_50, *Gimesiaceae* disappeared, while the abundance of *Legionellaceae* increased.

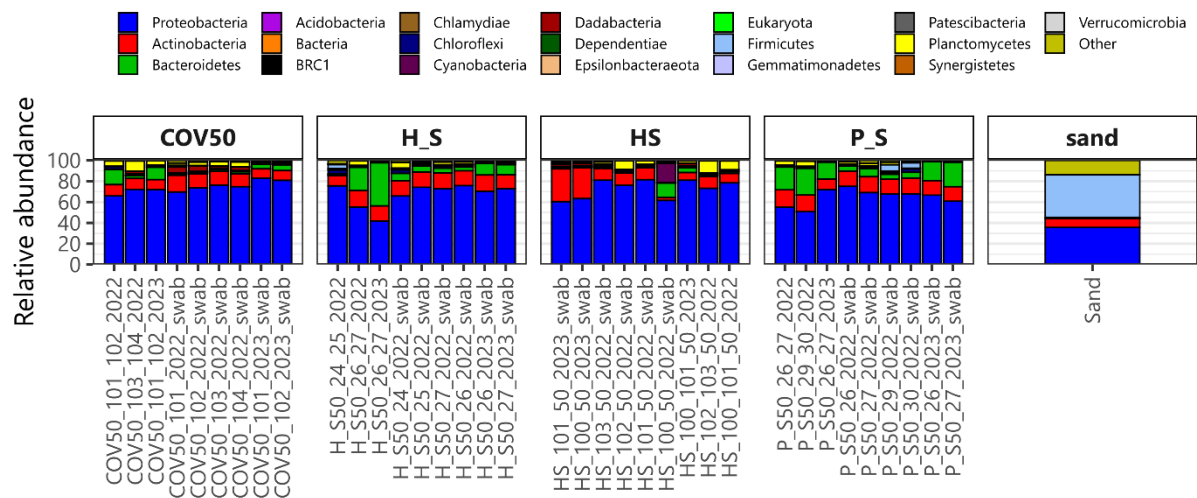


Figure 5-11 Microbial community profiles based on 16S rRNA amplicon sequencing showing the relative abundance (> 0.1%) of the different phyla in the different samples.

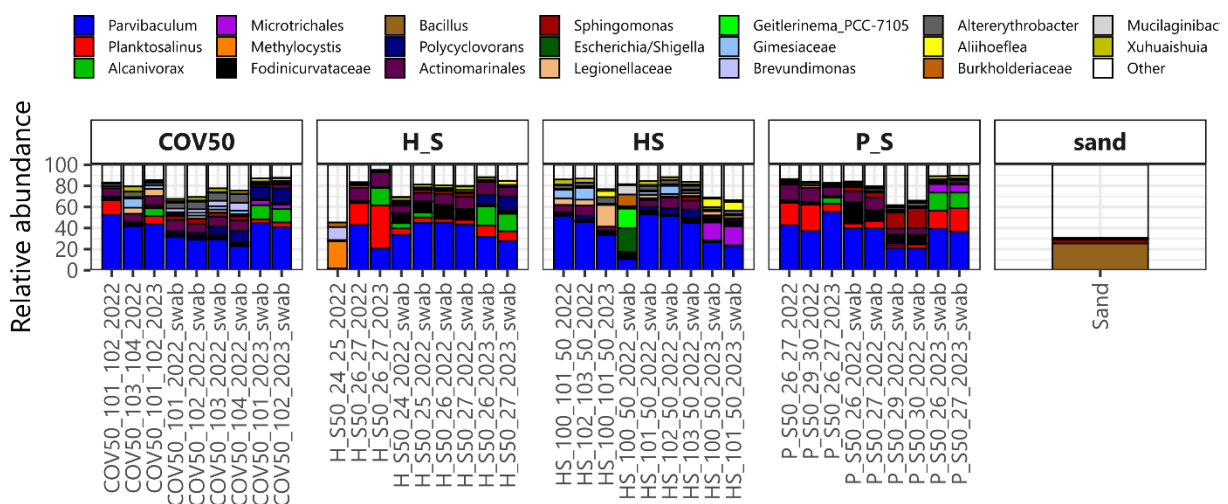


Figure 5-12 Microbial community profiles based on 16S rRNA amplicon sequencing showing the relative abundance (> 0.1%) of the 20 most varying genera in the samples.

Differences in the bacterial community between the different samples were further analysed through a beta diversity assessment. To this end, samples were first subsampled (rarefied) to the sample with lowest number of reads (i.e. 23,519 reads) to avoid sample-size dependencies in the diversity assessment. Rarefaction curves showing the number of ASVs in function of the number of reads were

made to examine if the sequencing depth (i.e. number of reads) was sufficient to map the full bacterial community diversity. Curve shape indicates community diversity while the maximum values indicate observed community richness. If the curve flattens towards the right, sufficient individual sequences have been analysed and it is unlikely to find many new additional species by increasing the number of sequences. Figure 5-13 indicates that sufficient sequences were collected for all samples, allowing correct interpretation of the bacterial diversity in the original sample.

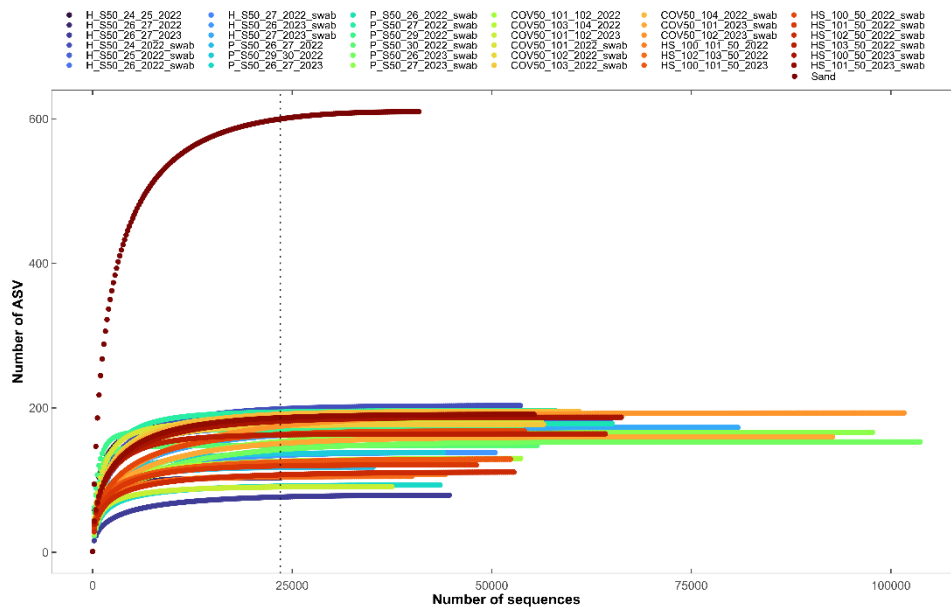


Figure 5-13 Rarefaction curves for the 16S rDNA gene amplicon sequencing data showing for each sample the number of OTUs in function of the number of reads. The dashed line represents the number of subsampled reads.

Beta diversity analysis was done via PCoA analysis based on the weighted unifrac as distance metric, which includes phylogenetic distances between the ASVs and their abundance (Figure 5-14). The closer the points are together, the more similar are the microbial communities between the samples. Samples that are obliquely from each other are more dissimilar. Results confirm that the bacterial community in the sand is different compared to that of the other samples (Figure 5-14). To investigate if the bacterial community is different between the different samples, PERMANOVA analysis followed by a permutation test of homogeneity of multivariate dispersions was performed. This indicated a significant difference between the bacterial community present in samples from certified and non-certified conditions ($p = 0.002$). More in detail, differences were observed between samples from P_S50 and COV50 ($p = 0.018$) and between P_S50 and H_S ($p = 0.018$). If the two samples that had a very dissimilar bacterial community (H_S50_24_25_2022 and HS_100_50_2022_swab (Figure 5-12) were removed from the dataset, differences were also observed between the bacterial community of H_S and COV50 ($p = 0.035$) and HS ($p = 0.009$).

All concrete cubes were submerged in the same synthetic clay pore water. One of the differences between the certified and non-certified conditions is the use of a superplasticizer in certified samples (COV50 and HS) while it is not present in non-certified samples (H_S50 and P_S50). Putatively, this difference could be one of the factors that explain the differences in the microbial community, but other factors could be at play as well. More detailed experiments and replicates are needed to confirm this hypothesis.

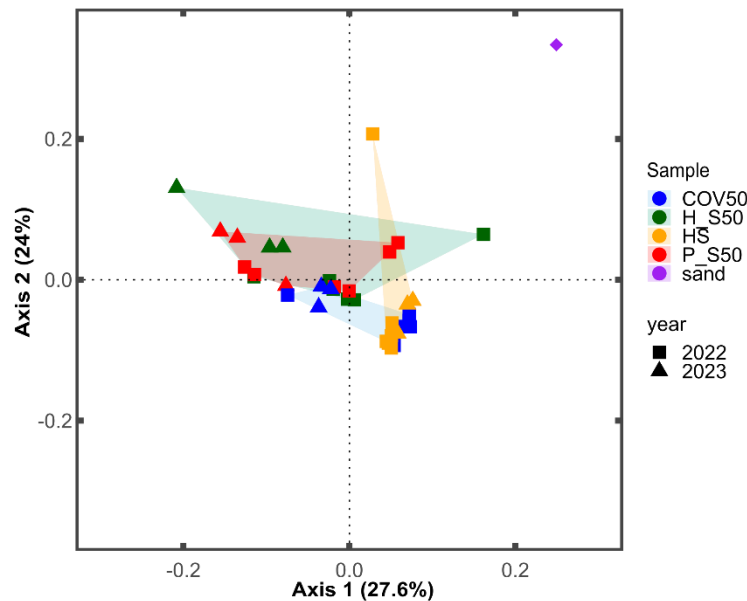


Figure 5-14 PCoA analysis based on weighted unifrac distances that show the dissimilarities between the bacterial community present in the different samples.

5.2 Artificial ageing to mimic the Belgian disposal conditions with microbial attack

5.2.1 Batch experiments at lab scales

Although samples were irradiated, there were some unforeseen manipulations, which caused a clear contamination of the batch experiments from the start of the experiments (Figure 5-15).

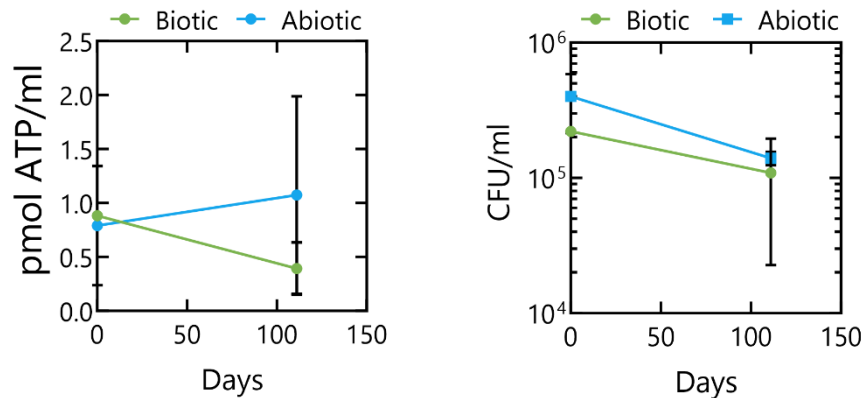


Figure 5-15: Intracellular ATP (left) and the number of CFU/mL on R2A in aerobic conditions after 1 week at 30°C (right) at the start and after 111 days of the experiments for the biotic (green) and abiotic (blue) sample. Results are the average and standard deviation of two technical replicates.

Consequently, it is impossible to draw firm conclusions regarding the effect of microbial activity on the concrete.

5.3 Artificial ageing to mimic the Czech disposal conditions with microbial attack

SURAO LPC samples exposed to three different conditions (air, underground water and bentonite suspension) in in situ conditions (URF Bukov, 15 °C) were studied in terms of microbial diversity. Sampling points of 6, 12 and 18 months are shown here (§ 3.1). Parallel, additional batch experiments were established as negative controls (Figure 2-17). These comprise of i) irradiated bentonite with irradiated concrete samples and sterile underground water and ii) native bentonite and underground

water with UV disinfected LPC samples. Control batch experiments were sampled at the time point of 18 months.

5.3.1 Microbiology at URF Bukov

The three-year old SURAO LPC cubes exposed to the underground ventilation were colonized by actinomycetal genera *Pseudonocardia* and *Promicromonospora*. These genera are common associates with earthen materials and were found to cause deterioration of ancient caves or Roman catacombs and mural paintings of tombs and churches (Diaz-Herraiz et al., 2014; Gurtner et al., 2000; Simons et al., 2020; Stomeo et al., 2008). After sample preparation, we have detected solely *Promicromonospora* in the concrete matrix using chloroform extraction, suggesting that this microorganism is present in the cementitious material. Microbial diversity of bentonite suspension at time 0 exhibited *Pseudomonas* and *Hydrogenophaga* genera. The latter is a representative of the underground water (borehole S25) that was used for the suspension preparation. As shown in Figure 5-16, this water inhabited sulphate-reducing bacteria (*Desulfotomaculum*, *Desulfatirhabdium* and *Thermodesulfovibronia*) in anoxic conditions. These genera are using different electron donors (mostly organic compounds or molecular hydrogen) to be able to reduce sulphate to sulphite and sulfane, eventually sulphide. The presence of hydrogenic genus *Hydrogenophaga* is in line with this. The reduced sulphur metabolites can be used in the presence of oxygen by sulphur oxidizing bacteria, such as *Thiobacillus*, detected in the water boxes (exposed to oxygen) 3 months after start-up of the Figure 5-16 *Hydrogenophaga* was more abundant under oxygenic conditions, but also present in the anoxic source water confirming its versatile nature.

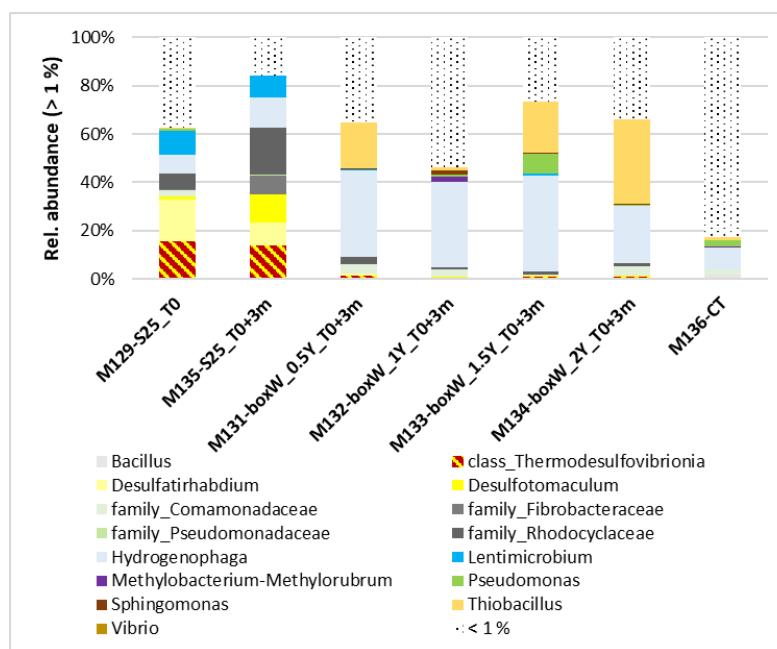


Figure 5-16 Relative abundance (> 1%) of microbiota present in the source water S25 and water in experimental boxes after 3 months of exposition to the underground in-situ conditions.

These microorganisms might alternatively use a different electron acceptor, such as e.g. nitrate or might use fermentation to digest organic matter in the absence of oxygen. According to very low concentration of nitrates in the S25 water, we assume that these bacteria solely use organic compounds to gain energy for its growth in anoxic environments. In the presence of oxygen, sulphate reducers sensitive to oxygen sporulate to overcome unfavoured conditions and become metabolically inactive. However, *Hydrogenophaga* could alternatively fix carbon dioxide autotrophically into organic matter (Taubert et al., 2021), similarly to *Thiobacillus*, or effectively assimilate organic carbon from chemolithoautotrophic primary production executed by *Thiobacillus*. Moreover, *Thiobacillus* could find metabolites from sulphate reduction such as thiosulphate and oxidize it to sulfuric acid that might be the main cause for deterioration of the concrete samples. In case of the genus *Hydrogenophaga*, the oxidation of sulphur compounds has not yet been described.

5.3.2 AIR exposure as a reference

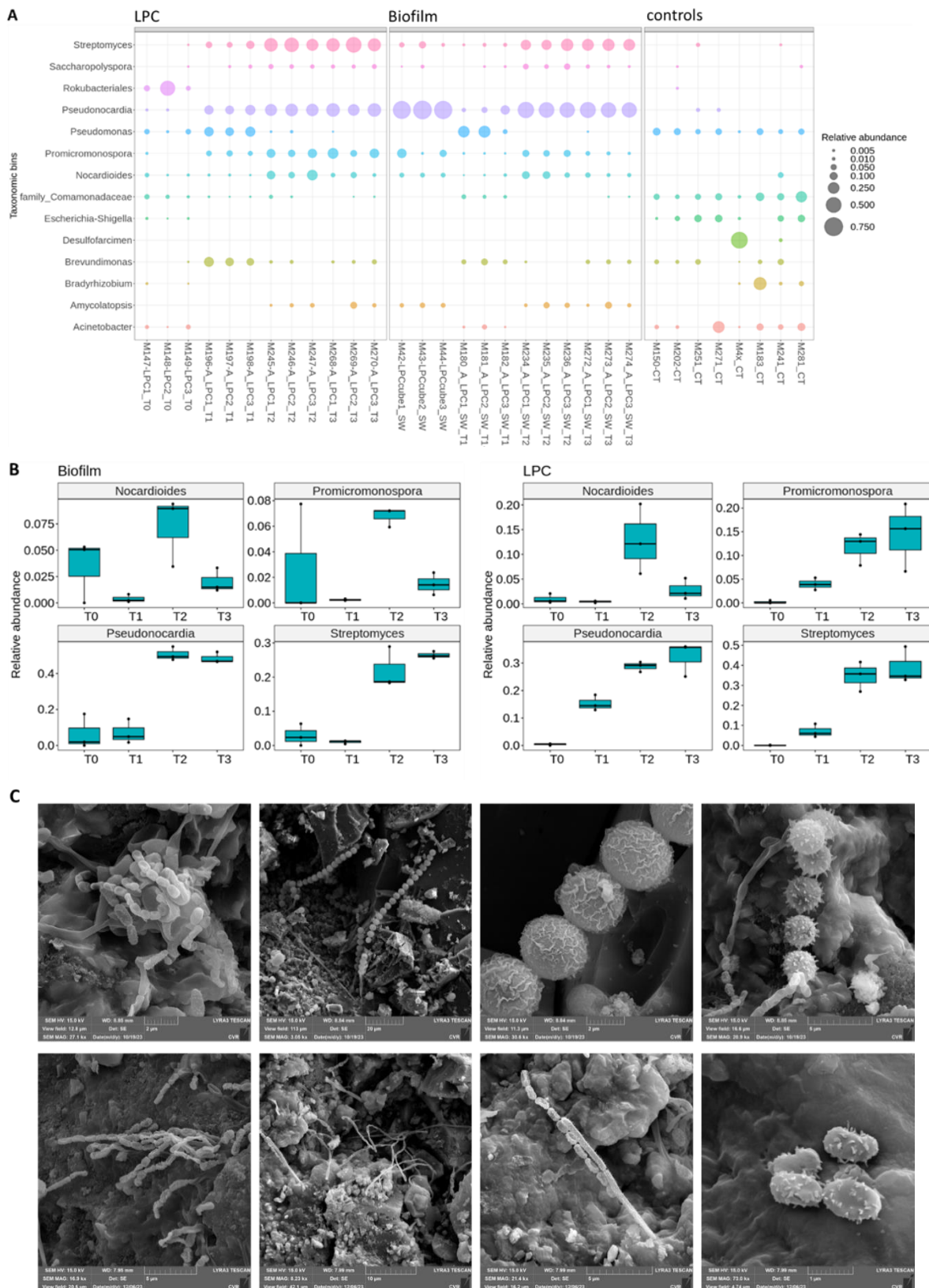


Figure 5-17 A) Relative abundance (>1%) of bacterial community on surface and interior of SURAO LPC samples exposed to underground air ventilation for 6, 12 and 18 months. B) Periodic changes of chosen microbes detected in and on the concrete exposed to the underground air ventilation. C) Surface SEM analysis of 1 (up) and 1,5-years-old (bottom) samples indicating *Streptomyces* genus and chains of fungal spores.

The microbial activity of samples exposed to the URF ventilation adopted similar patterns as the original SURAO LPC cubes with predominant occurrence of *Actinomycetota* and *Fungi* (Figure 5-17 and Figure 5-18). After 6 months of exposition, heterotrophic genera such as *Pseudonocardia* and *Streptomyces* were detected, and their relative abundance gradually evolved with increasing time of exposure (Figure 5-17 B). The presence of *Streptomyces*, fungal hyphae and spores, and other bacterial species was confirmed by SEM analysis of the 1,5-year-old air-exposed samples Figure 5-17 C).

Table 5-6 Relative quantity (RQ) of bacterial biomass inside (RQ_LPC) and on the surface (RQ_biofilm) of the SURAO LPC samples exposed to underground air at indicated time points after 6 (T1), 12 (T2) and 18 (T3) months in comparison to input samples (T0).

| | RQ_LPC | RQ_Biofilm |
|----|--------|------------|
| T0 | 1 | 1 |
| T1 | 61.04 | 4245.35 |
| T2 | 101.59 | 4820.61 |
| T3 | 309.76 | 5293.48 |

These data were proven by qPCR showing increasing relative quantity of bacterial biomass in the biofilm as well as in the interior of the samples (Table 5-6). Interestingly, the increase in the bacterial quantity in comparison to the input samples is robust and fast in these samples, especially in the biofilm. The growth of biofilm is faster and after 1.5 years reaches a plateau, however the growth in the matrix is slower (see further, Figure 5-18).

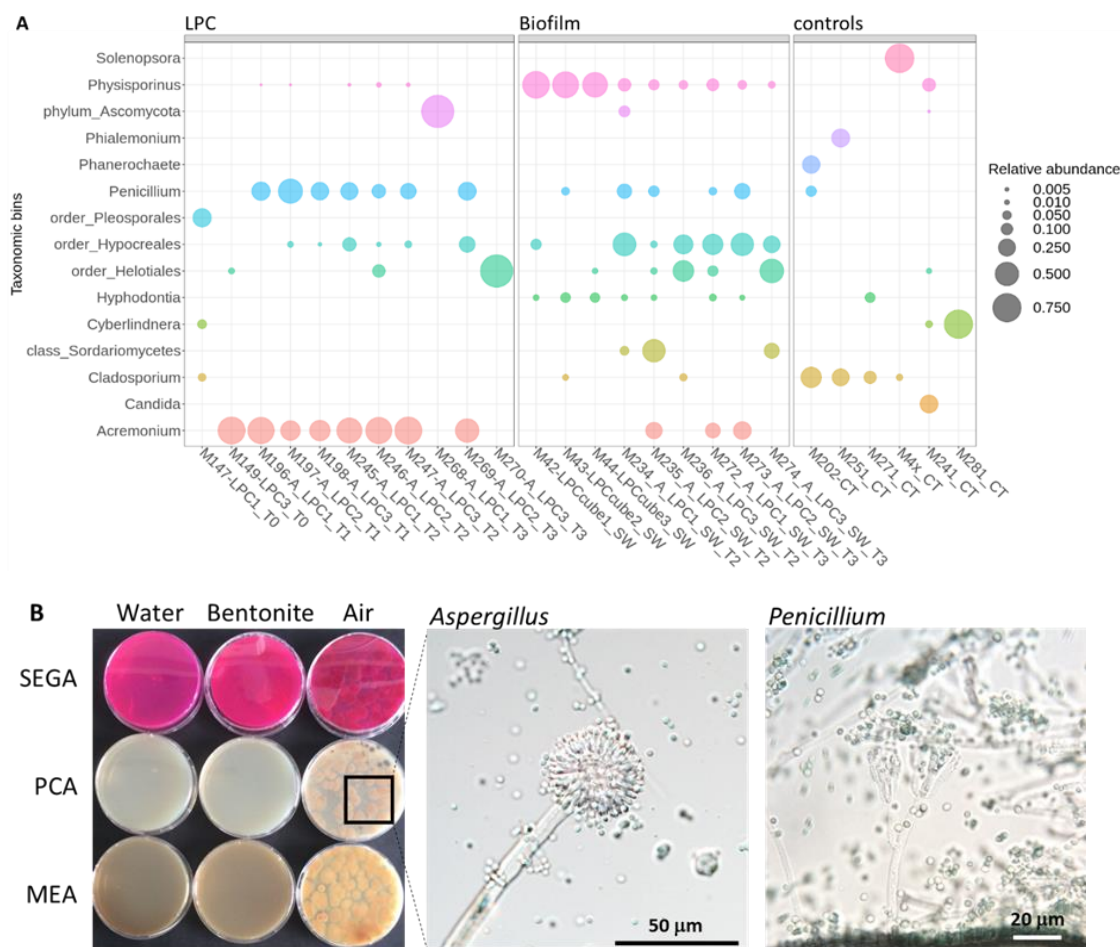


Figure 5-18 A) Relative abundance (> 1%) of fungal community on surface and interior of SURAO LPC samples exposed to underground air ventilation for different time points. CT – extraction control, SW – swab. B) Cultivation of fungi and their classification using microscopic analysis

As the analysis of the microbial communities of the LPC witness samples and the preliminary monitoring of the fallout showed, representatives of various fungi and molds, especially genus *Physisporinus*, were also abundant in the underground air. This genus was among the first colonizers of bare LPC samples, along with *Penicillium* and members of the *Hypocreales* order. After 1.5 year, the genus *Acremonium* was also detected on the surface. The detection of fungal communities in the samples exposed to underground ventilation showed some discrepancies between molecular-genetic and cultivation approaches were observed. Using a molecular-genetic approach, the genera *Acremonium*, *Penicillium* and *Pseudogymnoascus* were detected after 6-months of exposure inside the samples. However, the cultivation approach using antibiotics lead to observation of *Aspergillus*, *Cladosporium*, and *Penicillium* (Figure 5-18 B). Diminished abundance or absence of *Aspergillus*, and *Cladosporium* in the genetic profile can be explained by antagonistic effects of *Streptomyces* which can produce antifungal compounds against these fungi (Chevrette et al., 2019; Danial et al., 2020). Similarly, *Pseudonocardia* can produce antibiotics, particularly *P. endophytica*. This species might generate either antibacterial or antifungal antibiotics to suppress the growth of selected species of *Pseudomonas* and *Bacillus* or *Aspergillus* and *Penicillium*, respectively (Mangamuri et al., 2016). Antagonistic action of bacteria and fungi was probably the reason for the very weak evolution of biofilm in terms of bacterial diversity.

5.3.3 Underground water environment

The microbial activity of samples exposed to the underground water was influenced solely by the microbial diversity in the source water (see Figure 5-19). Although the underground water from the borehole S25 embodied constant nutrients with minimal fluctuations (Table 5-7), it comprises a diverse microbial community with consistent nature (Figure 5-19). The presence of sulphates determined the occurrence of species metabolizing sulphur compounds (as depicted in Figure 5-19). Interestingly, at the 1.5-years sampling point a significant increase in the relative abundance of *Desulfatirhabdium* was observed indicating a possible shift in nutrient availability. Alpha diversity analysis showed a significant difference between anoxic and aerobic water (Figure 5-19 B).

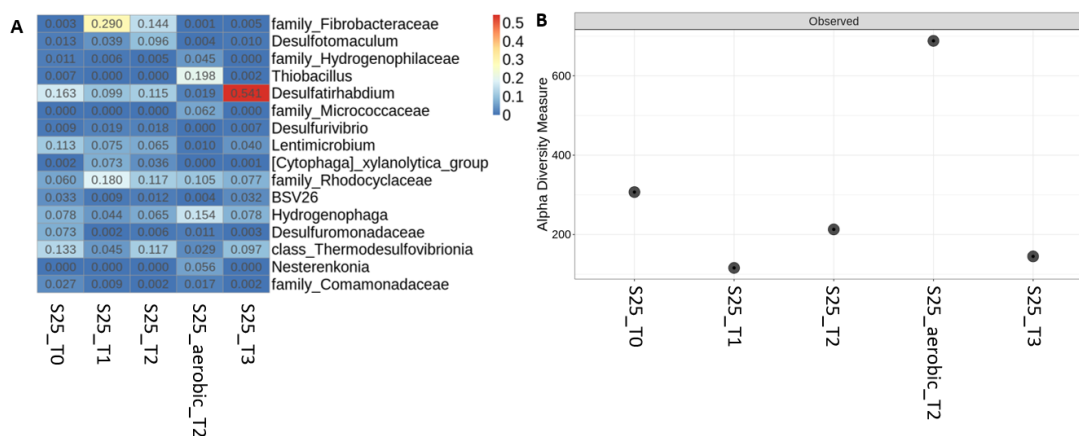


Figure 5-19 A) 16S sequencing heatmap of S25 underground water in anaerobic conditions for different time points (T0-T3). For sampling T2 (1 year) the water was taken directly from the borehole (S25_T2) and tested before entering the experimental box (S25_aerobic_T2). B) Alpha diversity of S25 source water at different time points.

The nature of the underground water influenced microbial activity of both the surface and interior of SURAO LPC samples (Figure 5-20Figure 5-21). The colonization of the concrete samples corresponds to a sequential evolution of biofilm including first colonization by autotrophic biomass producers such as *Thiobacillus*, followed by heterotrophic genera such as *Hydrogenophaga* or generally representatives of representatives of phylum *Pseudomonadota* (*Brevundimonas*, *Comamonas* etc.) that are capable of utilization of organic matter and finally infiltration of strictly anaerobic species such as *Lentimicrobium*. After 6 months of exposure, *Thiobacillus* was able to colonize the interior of the SURAO LPC samples, later, it was replaced by heterotrophic genera. The evolution of the biofilm was bigger and faster than in air-exposed samples (Table 5-6). The colonization of the concrete is slower with predominant occupancy

of *Hydrogenophaga* and *Brevundimonas* at the time point of 1.5-years exposure to the water environment. The sequential evolution of different metabolic groups as described above most probably relates to the carbon flux through microbial communities (Taubert et al., 2021), because organic matter as a major source of carbon in the system is the main energy source for most aerobic microorganisms.

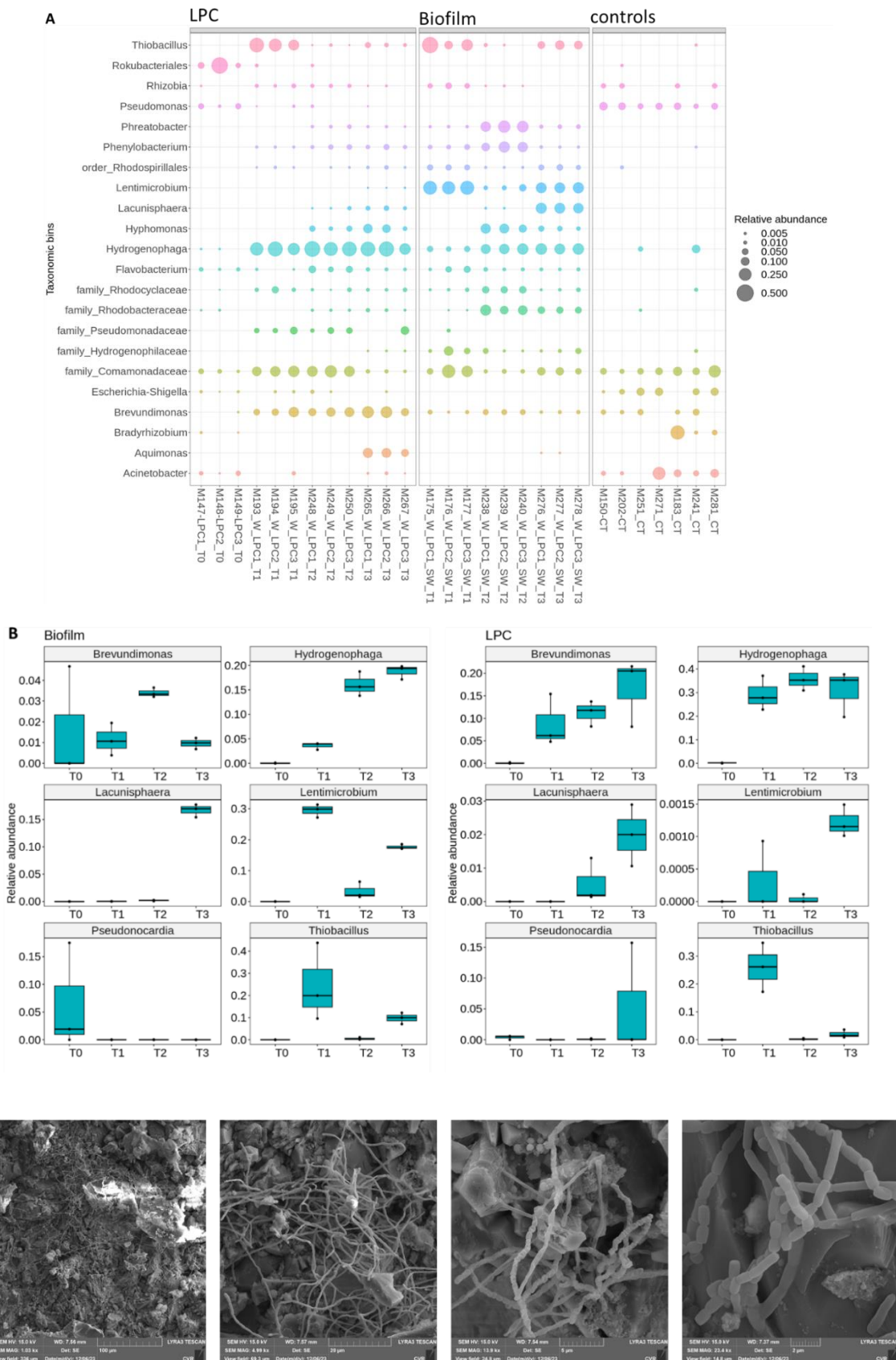


Figure 5-20 A) Relative abundance (> 1%) of microbial community on surface and interior of SURAO LPC samples exposed to underground water S25 for 6, 12 and 18 months, respectively. B) Periodic changes of chosen microbes detected in and on the concrete exposed to the underground water. C) SEM analysis of the biofilm after 1.5 years of exposure.

Table 5-7 Relative quantity (RQ) of bacterial biomass inside (RQ_LPC) and on the surface (RQ_biofilm) of the SURAO LPC samples exposed to underground water at indicated time points after 6 (T1), 12 (T2) and 18 (T3) months in comparison to input samples (T0).

| | RQ_LPC | RQ_biofilm |
|----|--------|------------|
| T0 | 1 | 1 |
| T1 | 2.75 | 80870.92 |
| T2 | 11.63 | 770.69 |
| T3 | 81.57 | 74330.50 |

The experimental setup to study the concrete/water interface was expected to hold even distribution of the underground water and thus even evolution of the microbial activity. However, the microbial diversity and biofilm formation on LPC samples was probably influenced by the formation of a biofilm inside the experimental boxes and mainly around the inlet tube. It seems that the outgrowth of the biofilm around the inlet tube slowed down the colonization of water exposed LPC samples or took up the incoming microorganisms more effectively (Table 5-7). Figure 5-21 shows bacterial diversity of such biofilm after 1.5 years. The biofilm inside the box inhabited a mixed microbial community including autotrophic (*Thiobacillus*), heter-otrophic genera (e.g. *Hydrogenophaga*, *Brevundimonas*, *Lacunisphaera*), and obligatory anaerobic (*Lentimicrobium*) microbes, suggesting a fully grown and stratified biofilm. The biofilm around the inlet tube was formed mainly by representatives from family *Hydrogenophilaceae* with relative abundance of 45.5 %, but no significant colonisation by the genus *Thiobacillus* was observed.

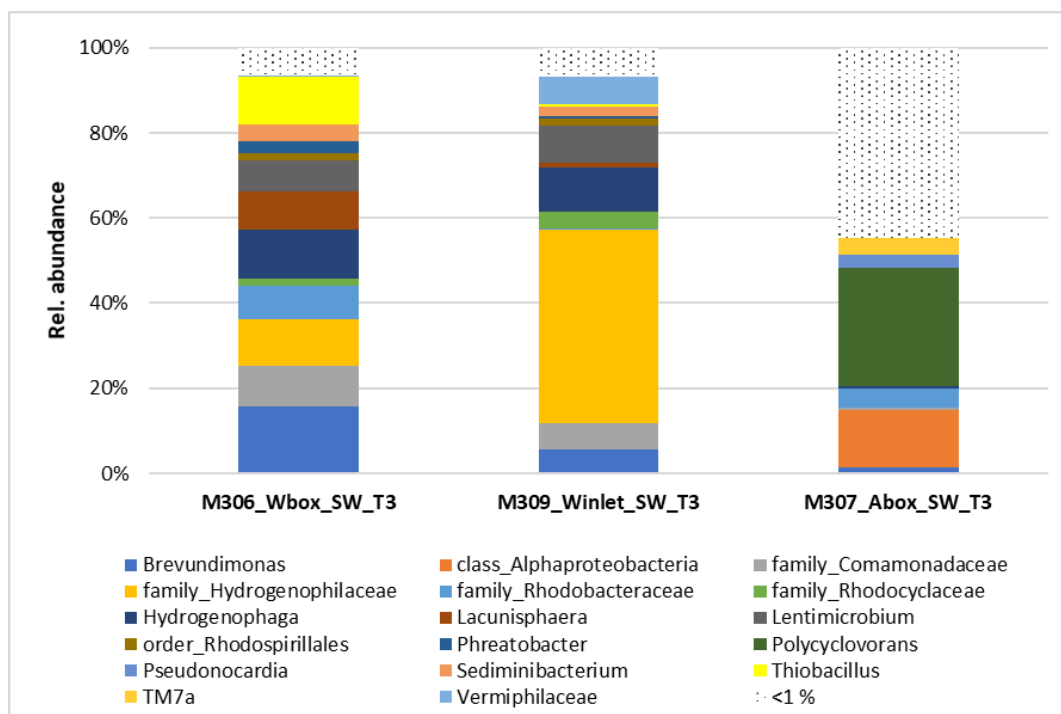


Figure 5-21 Relative abundance of present microbiota in biofilm of water box (1.5-years exposure), biofilm formed around the inlet tube and biofilm of the containers exposed to underground air, respectively.

5.3.4 Effect of direct contact with bentonite suspension

Similarly to the two previous environments, the microbial activity of the concrete samples in contact with bentonite is influenced by the indigenous microbiome of the bentonite suspension. The bentonite suspension was prepared one week before setting up the experiment at URF Bukov from Czech bentonite BCV and underground water from borehole S25. The microbial community remains unique with the persistent presence of dominant species *Pseudomonas* over the three sampling points (Figure 5-22 A). However, there is an increased abundance of representatives of families *Oxalobacteraceae* and *Pseudomonadaceae* in SURAO LPC samples treated with UV light. We assume that a significant release of sequences assigned to family grade is unspecific information. The UV light is one of the mutagenic factors that lead to changes in reading frame of such exposed DNA. The persistent presence of *Pseudomonas*, *Hydrogenophaga* in such treated samples is either a result of interior colonization or a result of insufficient surface disinfection due to residuals of bentonite suspension inside pores of the highly porous samples. The samples were not washed before UV treatment to avoid any additional contamination. Because there was no biofilm detected by using SEM analysis, we incline to believe that 2 hours of UV light treatment is not sufficient to disinfect the surface of these samples.

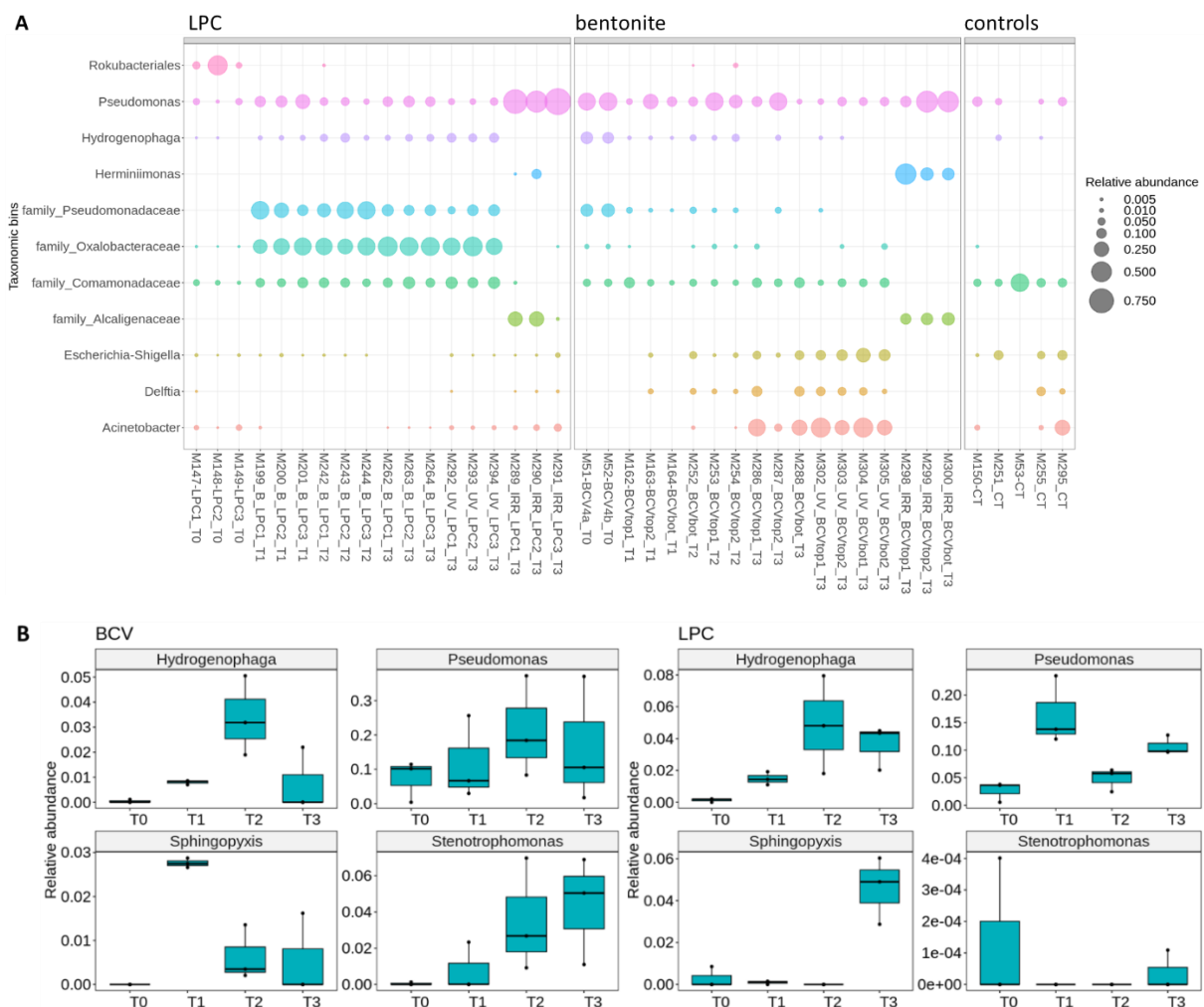


Figure 5-22 A) Relative abundance (> 1%) of microbial community interior of the SURAO LPC samples (LPC) exposed to bentonite suspension for 6 (T1), 12 (T2) and 18 (T3) months, respectively and microbial analysis of bentonite suspension at different time points. Each time three different concrete discs were used for separate extraction. BCV – Bentonite Cerny Vrch, CT – control extraction without input material; IRR – irradiated samples; UV – UV-treated LPC samples. B) Periodic changes of chosen microbes detected in bentonite (BCV) and in the concrete exposed to the bentonite suspension (LPC).

Additional control samples from irradiated and UV disinfected batches were collected and analysed at time point T3 and were set up to distinguish between chemical and biological concrete deterioration suggesting it might happen (Berns et al., 2008; McNamara et al., 2003). The UV-treated LPC samples exposed to native bentonite suspension embodied similar microbial activity as LPC not treated with UV light suggesting the microbial activity of bentonite suspension being responsible for their colonization. High relative abundance of *family_Pseudomonadaceae* and *family_Oxalobacteraceae* in samples treated with UV light most probably represents DNA fragmentation of the *Pseudomonas* genus (Figure 5-22) and thus its improper annotation in database as discussed above.

However, it appeared that the treatment of bentonite powder using γ irradiation was not effective with the calculated total dose of 58.44 kGy for bentonite. High relative abundance of *Pseudomonas* detected inside the irradiated SURAO LPC samples is proof of that because of its absence in T0 LPC samples. The genus *Pseudomonas* might originate solely from bentonite powder surviving ineffective treatment or high resistance for γ irradiation (Ito and Iizuka, 1971; Olanya et al., 2015; Soghomonyan et al., 2018). Consequently, after bentonite saturation *Pseudomonas* proliferated and infiltrated the LPC samples. Furthermore, there is a striking difference between irradiated and non-irradiated samples in the absence or presence of *family_Pseudomonadaceae*, respectively, suggesting the high abundance of species *Pseudomonas* inside the irradiated SURAO LPC samples.

The overall richness of described samples especially in samples exposed to bentonite suspension is rather very low. To prove the viability of present microorganisms in the bentonite suspension, the cell extraction and staining of living and dead cells was used as described in Hlavackova et al. (2023). Figure 5-23 shows that bentonite was colonized by metabolically active microbial cells. Similar numbers were observed in the upper and lower part of the bentonite mass in the experimental box, but more dead cells were observed in the bottom part of the bentonite suspension.

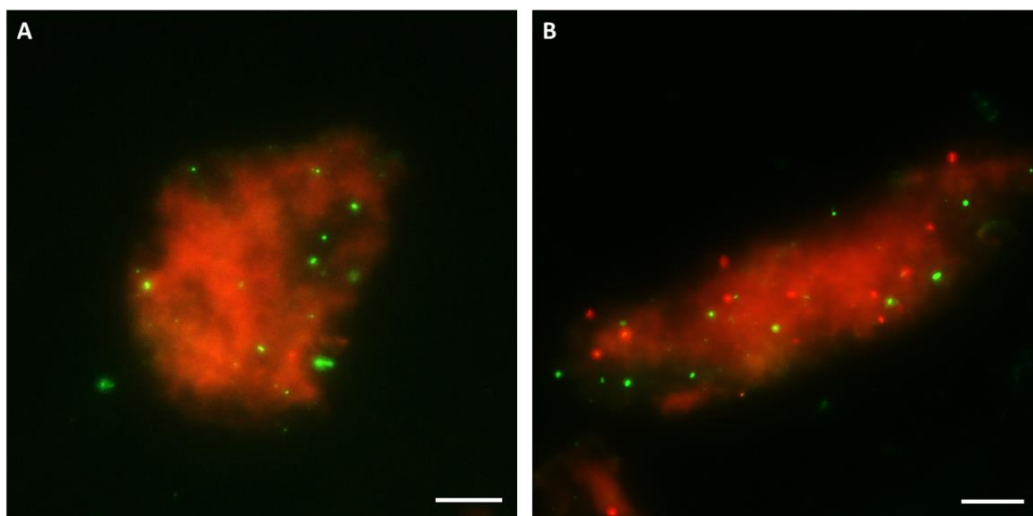


Figure 5-23 Determination of bacterial viability in bentonite extracts prepared from (A) top and (B) bottom (mostly in contact with LPC samples) of the bentonite suspension mass relative to the position in the experimental box (scale bar = 10 μ m, red fluorescence = light clay fraction and dead cells, green fluorescence = living cells).

5.3.5 Coupled multi-ionic and microbial (natural) attacks (conclusion)

The rapid decrease of **pH values** in MAGIC interaction experiments (Figure 5-24) after the time T0 in comparison to storing conditions after casting of low-pH concrete, is mainly caused by experimental sample (disc shape specimens) preparation and processing. For the experimental purposes the low-pH concrete material was core drilled and cut to obtain the experimental specimens. By these procedures the fresh reactive surfaces with newly opened pores were exposed to experimental conditions. The pH values for experimental time T0 and the previous time period were evaluated on unaffected material from internal parts of concrete cubes (15 cm edge). For samples after interaction with different

environments the specimen whole discs were crushed and milled for pH evaluation purposes. The degraded/interacted surfaces significantly affected the total volume of the specimen in comparison to the reference sample stored at relatively dry (laboratory) conditions (see Figure 5-25).

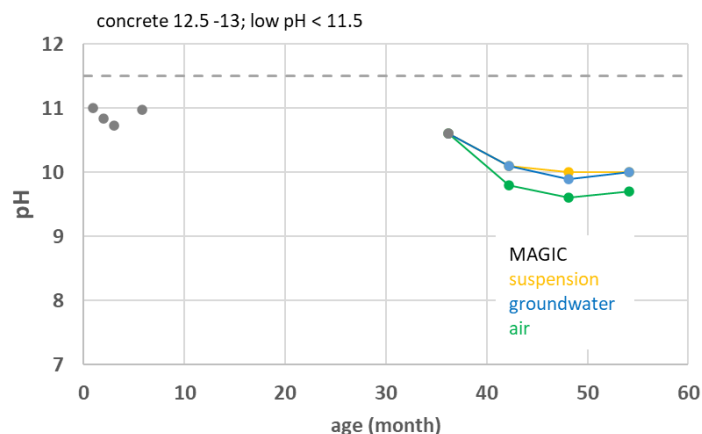


Figure 5-24 pH evolution in all three environments.



Figure 5-25 pH visualisation by rainbow indicator - cube cut edge (surface exposed to air for 3 years URL Bukov at 100% RH + 2 years at CTU lab with 30-50% RH).

Scanning Electron Microscope (**SEM**) analysis of the samples revealed distinct structural changes on the surfaces over time, varying according to the environment. In an air environment, a thin layer of organic products on the surface was observed. In a water environment, there was a penetration of the degradation area into the cement matrix, characterized by a decrease in the amount of calcium and oxygen, indicative of a disruption in the calcium-silicate-hydrate bond. In a bentonite suspension environment, the cement matrix showed an enrichment of magnesium and an increase in crack propagation. These unique surface characteristics for each environment over time are illustrated in Figure 5-26.

Primarily in the experimental environment of a bentonite suspension, an accelerated degradation by magnesium ions was observed. The degradation by magnesium ions was confirmed by SEM and EDX element mapping, demonstrating magnesium penetration in the cement matrix at the interface of the cement paste during exposure, shown in Figure 5-27. The concentration of magnesium ions in the pore water of the bentonite suspension was 0.695 mol/L, which is orders of magnitude higher compared to the concentrations found in groundwater (below 0.0027 mol/L). The pH of the low-alkali concrete was around 10, which corresponds to the conditions that lead to magnesium attack. A magnesium attack is observed when the concrete is exposed to a magnesium environment and when the pH of the concrete is below 11.5 (Dewitte et al., 2022). During this attack, there is mainly a destabilization of the C-S-H component to M-S-H, which occurs at the interface of the cement paste and the magnesium environment.

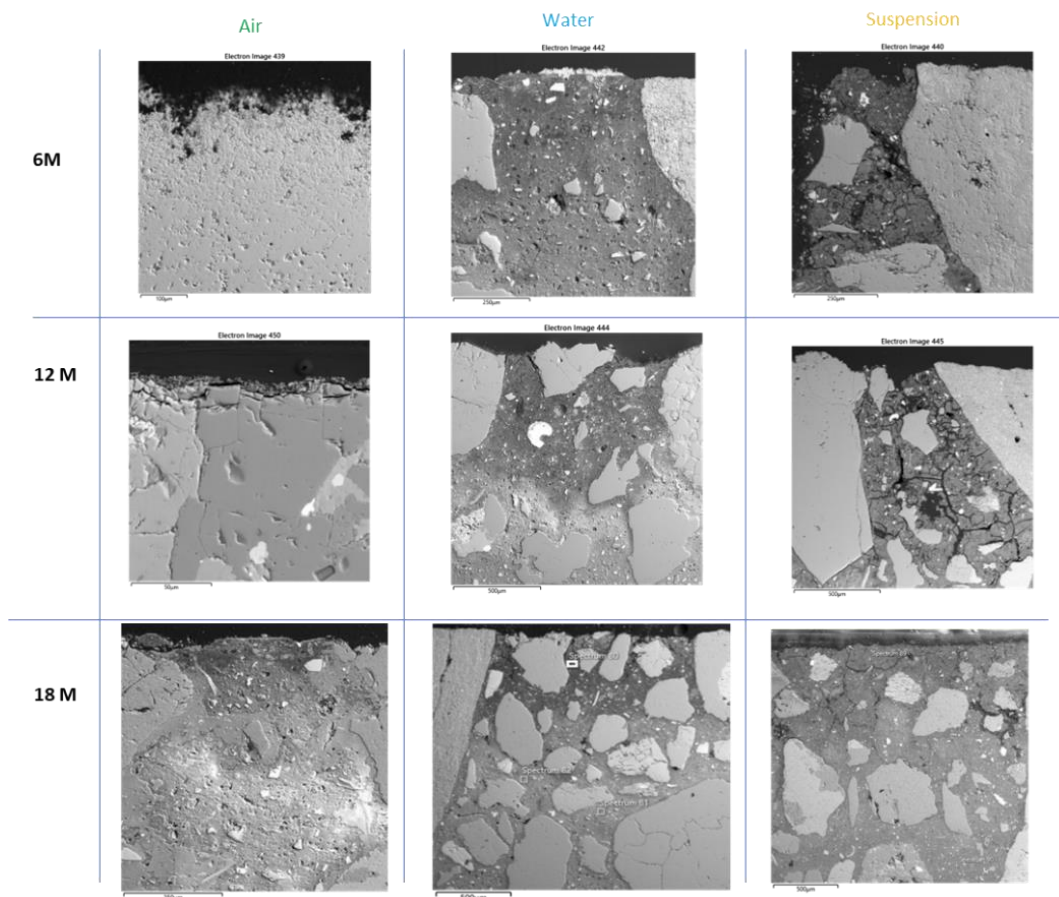


Figure 5-26 Specific characteristic surface changes for individual environments air, water and bentonite suspension after 6, 12 and 18 months.

In the case of a water environment, the main degradation mechanism is a combination of leaching and carbonation in the second phase due to the absence of portlandite. During degradation, there was a decrease in the amount of oxygen and calcium in the cement matrix forming degradation areas reaching a penetration of over 1 mm. Carbonation without leaching was observed in the air environment, penetrating to a depth of 87 μm , but only after 18 months. The degree of surface degradation of the samples was found to be the lowest in air environments, followed by water environments, with the highest degradation observed in bentonite suspensions.

Microorganisms were detected on the sample surfaces in both water and air environments from the beginning of the exposure period. After 12 months of exposure in the water environment, metabolic products in the form of elemental sulphur (S^0) were found on the sample surfaces.

Phase composition by XRD showed the presence of gypsum only in air environment. After 18 months, a new phase, indicative of a high-temperature cristobalite, was observed on the surface but only in the water environment. This new phase suggests the presence of microbial activity.

Microscale testing by **nanoindentation** was performed on selected intact areas of the cement matrix outside the aggregate area. The results therefore do not significantly take into account the influence of possible micro/macro cracks. The nanoindentation results show a slight improvement in mechanical resistance over time, independent of the environment. This can be explained by the rehydration of the sample after exposing the material during sample preparation from larger cubes (drilling, cutting). However, the resistance is slightly lower in the peripheral regions of the samples. This may be due to microcracks at the surface caused by sample preparation or microcracks/increased porosity caused by development/interaction with the environment.

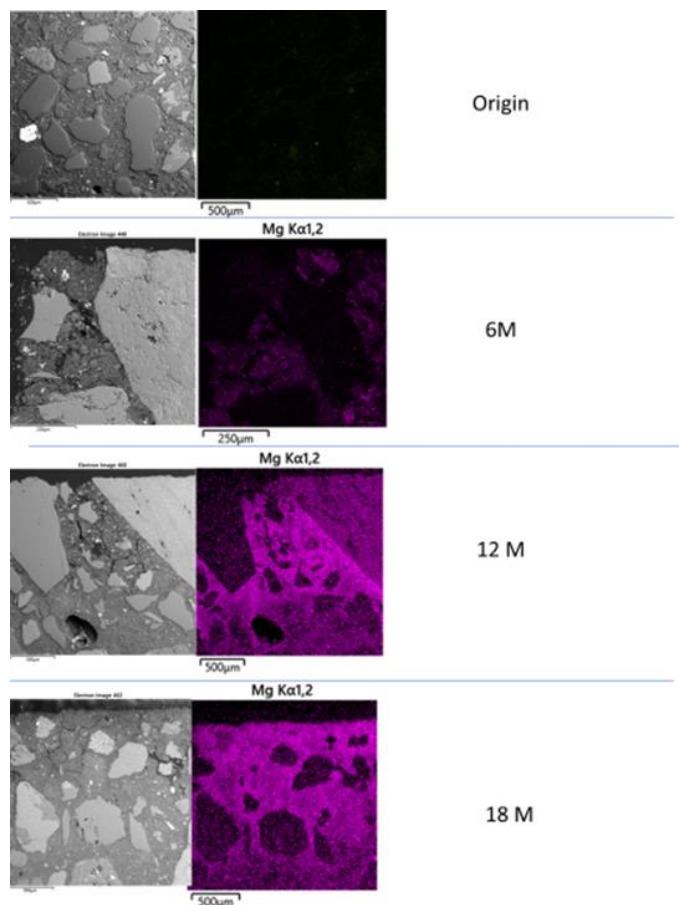


Figure 5-27 Scanning electron micrograph showing the penetration of magnesium into the cement matrix after 6, 12 and 18 months

The **punch test** (Figure 5-28) was carried out by pressing with punches in the middle of the disc. During compression with the punch, most of the volume of the specimen is thus loaded gradually in tension, in four steps until failure. The result is also influenced by micro/macro cracks, pores, etc.

From the evolution of the load branch directives (rigidity - k2, k4-1, k4-2, k4+), it is possible to infer the increase of plastic deformation at the beginning of the test (decrease of k2 and k4-1 for different periods and environments) while K4-2 and k4+ remain similar or slightly improve (compare to slight improvement of nanoindentation results). This effect is most visible for the aqueous environment, then for the suspension. In both cases, a persistent decrease (0-1.5y) is evident. This is probably due to the evolution of the micro/macrocracks in the sample. The cracks may be essentially unfilled (i.e., with zero mechanical resistance in tension) or filled with secondary fill partly maintaining mechanical resistance. The consequence of crack development and filling should be changes in strength. A significant change (decrease) in strength is observed for the suspension environment. The SEM analysis shows a significant range of unfilled cracks (depth to approx. 1.3 mm from the surface). The pH using the indicator shows a relatively large area of the sample (surface zone - approx. 1.5-2 mm) with a higher pH for the suspension samples. A similar but smaller effect is observed for the water environment samples (decrease in strength, SEM, pH). Also, the decreasing number of samples from each set that resisted the stresses in each step of the mechanical test (suspension < water < air) correlates with the crack formation and the decrease in mechanical resistance in each environment and time.

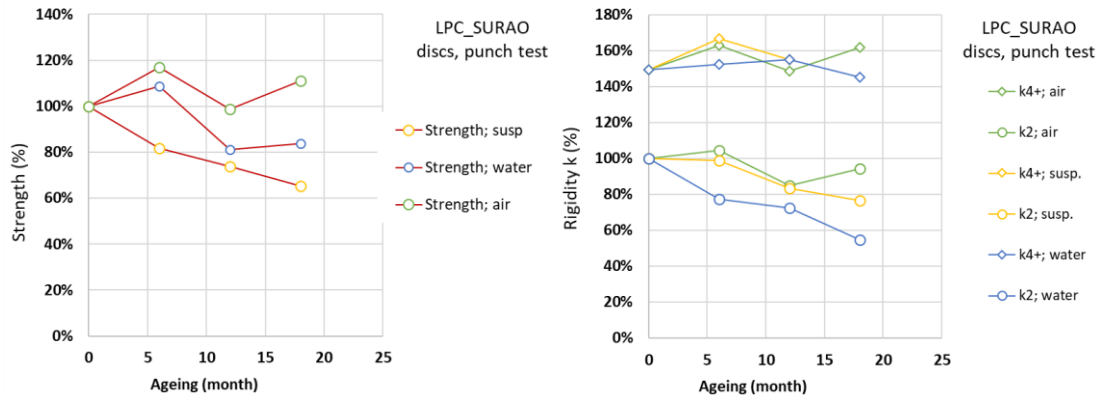


Figure 5-28 Time evolution of mechanical parameters in all three environments ((in %; strength left; rigidity k2 and k4+ right)

Exposure of SURAO LPC samples to different environments showed distinct behaviour in terms of loss of the mechanical strength that can be caused by local pH changes due to cation exchange or **biofilm** outgrowth (Figure 5-33).

Microbial activity in air

The pH of the SURAO LPC samples (10.6) did not inhibit microbial activity in the experimental set-up, as evidenced by the rapid growth of biofilm on the surface and the ability of microbes to infiltrate the matrix through microcracks (Figure 5-29). As described previously, local production of microbial metabolites causes a decrease in pH, leading to the dissolution of calcium and magnesium from the matrix and the formation of microcracks (Javaherdashti et al., 2009; Turick and Berry, 2016). The fast colonization of air-treated LPC samples by a mixed heterotrophic community led to local lowering of pH values in the surface layer (orange colour, rainbow pH indicator) as well as in LPC powder. The local production of acidic metabolites such as oxalic acid and acetic acid, likely caused the dissolution of calcium from the concrete samples and the formation of a calcium rich layer composed of gypsum and vaterite minerals, as confirmed by SEM and XRD analyses. The accumulation of gypsum suggests the presence of sulphur oxidizing microorganisms, despite the absence of sulphate-rich water and the low content of sulphates in the matrix (slag: 0.04 w%). Although known sulphur-oxidizing bacteria were not detected in air-exposed samples, the higher content of sulphides in slag (0.6 w%) and previous results indicating possible sulphur/sulphide oxidation by heterotrophic bacteria and fungi (Czaban and Kobus, 2000; Wainwright, 1984) support our findings. The high sulphide content in the slag used for SURAO LPC preparation (Pernicova et al., 2023) further corroborates our findings. Recent data shed more light on early-stage bacterial colonization driven by sulphide oxidation as a primary production force (Macey et al., 2020; Taubert et al., 2021), aligning with an early colonization of the “nude” LPC discs. In conclusion, the gypsum is considered to be a product of microbially induced deterioration. Although cracking did not occur within the studied timeframe, the increased “fragility” of the surface layer, as confirmed by NI, was notable. The faster colonization of air-exposed samples may be linked to the nature of colonizing species – fungi and actinomycetota – which spread and grow via filamentous protrusions that can intrude samples more effectively than a standard bacterial biofilm composed of cocci or rods.

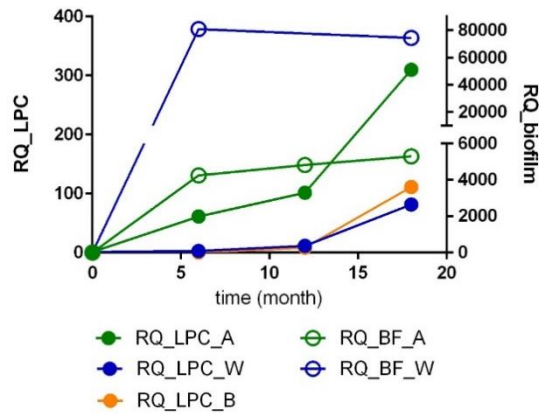


Figure 5-29 Relative quantification of bacterial biofilm (RQ_BF) on air- and water-exposed samples and biomass inside SURAO LPC samples (RQ_LPC) in time (0 - 18 months) and different environments (A – air, W – water, B – bentonite suspension). B) detection of biofilm on air-exposed samples using SEM cross section analysis

Microbial activity in water test environment

The pH of LPC leachate of water-exposed samples was less acidic than in air-exposed samples however, the growth of biofilm was faster and more robust (Figure 5-29). The formation of microcracks was confirmed by SEM in samples exposed to water and suspension and might result from a combined chemo-biological attack. In water, the cracks were eventually filled with calcium carbonate, suggesting that this precipitation is due to the high content of bacteria providing sufficient nucleation sites on the surface of water-exposed samples, as confirmed by high relative quantification and SEM. Carbonate precipitation in haloalkaliphilic and alkaliphilic terrestrial environments has been linked to a high relative incidence of the genus *Hydrogenophaga* (Ohlsson et al., 2019; Skorupa et al., 2019; Woycheese et al., 2015), suggesting its potential role in microbially-induced carbonate precipitation. Finally, the detection of strictly anaerobic species in the bacterial community of water-exposed samples is consistent with qPCR measurements and proves the existence of a fully developed and stratified biofilm.

Microbial activity in bentonite suspension

The growth of a biofilm in bentonite suspension-exposed samples could not be observed due to direct contact with the bentonite suspension. The colonization of the LPC samples was low and similar to that of the samples exposed to underground water (Figure 5-29). Given the presence of a single dominant species detected in aerobic bentonite suspensions, we expect that this species will prefer to metabolize and grow rather in its natural environment such as the suspension than in more alkaline concrete samples.

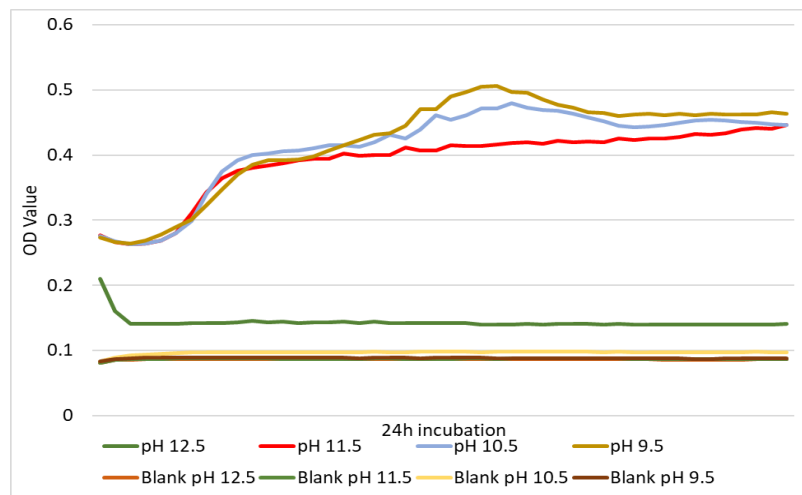


Figure 5-30 Growth kinetics of urease positive clone B62 at different pH.

Using epi-fluorescent microscopy we detected higher mortality rates around the concrete samples confirming our expectation. We suggest that the crack formation of the LPC samples is primarily a result of chemical magnesium/calcium exchange, with the biotic effect being rather insignificant in this case. Due to the dense environment of the bentonite suspension, it was impossible to heal the cracks formed in LPC samples. However, several heterotrophic species isolated from LPC samples exposed to bentonite possessed urease activity. Clone B62 in particular, tolerated higher pH levels and was capable of precipitating calcium carbonate (Figure 5-30). The results indicated that while clone B62 failed to thrive at pH 12.5, it exhibited growth in media with a pH of up to pH 11.5. This observation categorizes clone B62 as alkaliphilic, with ability to not only survive but thrive in high pH environments.

To summarize, from these experiments we can conclude that microbial presence can be either deteriorative or protective depending on the extent of water and local pH changes in environments dominated by heterotrophic microorganisms. Microbial assisted changes appear significant in both air and water environments, while chemical conversion of C-S-H to M-S-H is the main driving force of negative effects in contact with bentonite suspensions.

5.4 Interaction between low-pH cementitious material and microbes in low-carbon source groundwater

UNIMAN (Ananya Singh, Dirk Engelberg, Elizabeth Evan, Christopher Boothman, Katherine Morris, Sam Shaw, Jonathan R. Lloyd)

To study the impact of microbial activity in low-carbon groundwater on the cementitious material, microcosms were set up in triplicate under anaerobic conditions with N₂ in the headspace and incubated at 20°C in the dark for six months. For low carbon groundwater incubations containing low concentrations of yeast extract with nitrate (GYN) and without nitrate (GY), H₂ served as an electron donor, so the headspace was flushed with H₂ for 5 min every 14th day. There was a particular focus on microbially induced carbonate precipitation and changes in pore size distribution.

5.4.1 Geochemical analysis

pH is a crucial parameter influencing the composition of microbial communities. In this study, the initial pH of the system was 10, which increased to 10.5 after one week due to the dissociation of ions within the cement. Overall, the pH value for all the systems changed from 10 to 9.3 in 164 days, although the GLN (groundwater + lactate + nitrate system) had changed from 10 to 9 and showed the highest pH drop compared to other systems (Figure 5-31). A general decreasing trend was observed for pH in both no-nitrate and nitrate systems. This trend suggested that some microbial activity was ongoing in both systems, with and without nitrate, possibly due to the presence of sulphate in the groundwater, which served as a potential electron acceptor in both systems.

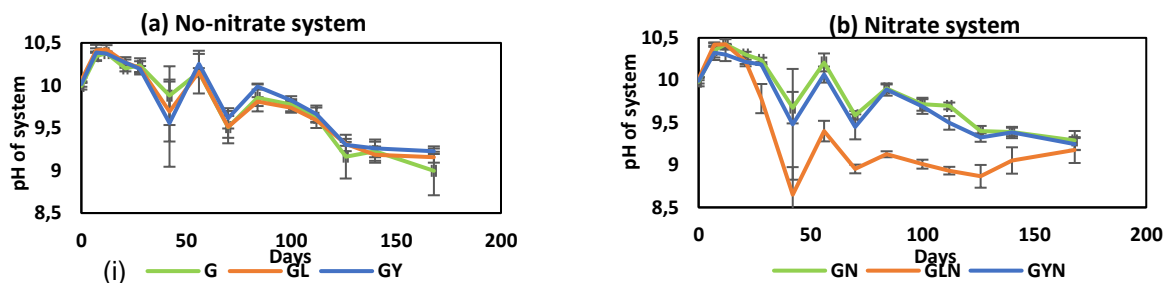
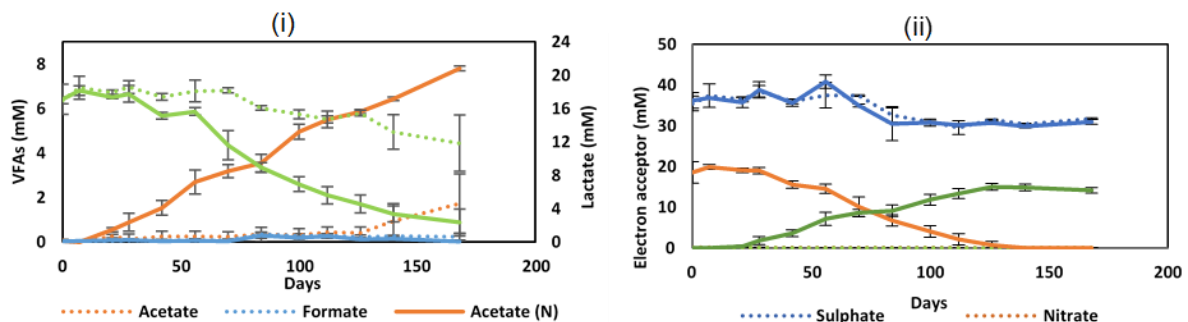


Figure 5-31: pH change in (a) no-nitrate system (GW, GL, GY) and (b) nitrate system (GWN, GYN, GLN).

Measuring the concentration of available nutrients is important for the evaluation and prediction of potential microbial activity within a sample. For groundwater without nitrate (G) and groundwater with nitrate (GN), the IC data for VFAs (lactate, acetate, formate) showed no significant changes over the

first 70 days. However, there was an increase in formate value from approx. 0.04 to 0.3 mM at day 70, accompanied by a minor increase in lactate (0.03 to 0.1 mM) and acetate (0.08 to 0.15 mM) value (Figure 5-32ai), most likely formed from the degradation of the low levels of organics present in the Harpur Hill sediment used in the system. For the same system, the sulphate value had decreased from 35 to 30 mM after 70 days, in addition to a decrease in nitrate values from 20 mM to 15 mM, and then remained constant (Figure 5-32aii). This suggested that slow microbial activity was ongoing using electron acceptors for the degradation of organic matter in the microcosms. Figure 5-32bi shows the IC data for the second system, i.e., groundwater and lactate without (GL) and with nitrate (GLN). For the GLN system, lactate concentrations decreased from 15 mM to 2 mM in 164 days and was degraded to acetate, whose concentration increased from 0 to 8 mM. This decrease in lactate concentration in GLN systems was accompanied by a decrease in nitrate concentrations from 15 mM to 0.02 mM, which was reduced to nitrite and accumulated over a 6-month period, along with a noticeable drop in sulphate concentrations (Figure 5-32bii), suggesting the microbial reduction of nitrate and sulphate occurred simultaneously. In contrast, the GL system (lacking the electron acceptor nitrate) showed a decrease in lactate concentration after day 70 with a smaller increase in acetate (Figure 5-32bi) as the concentration of sulphate dropped from 35 to 30 mM in the system (Figure 5-33bii).

(b) Groundwater + Lactate (GL) & Groundwater + Lactate + Nitrate



(c) Groundwater + Yeast Extract + Hydrogen (GY) & Groundwater + Yeast Extract + Hydrogen + Nitrate

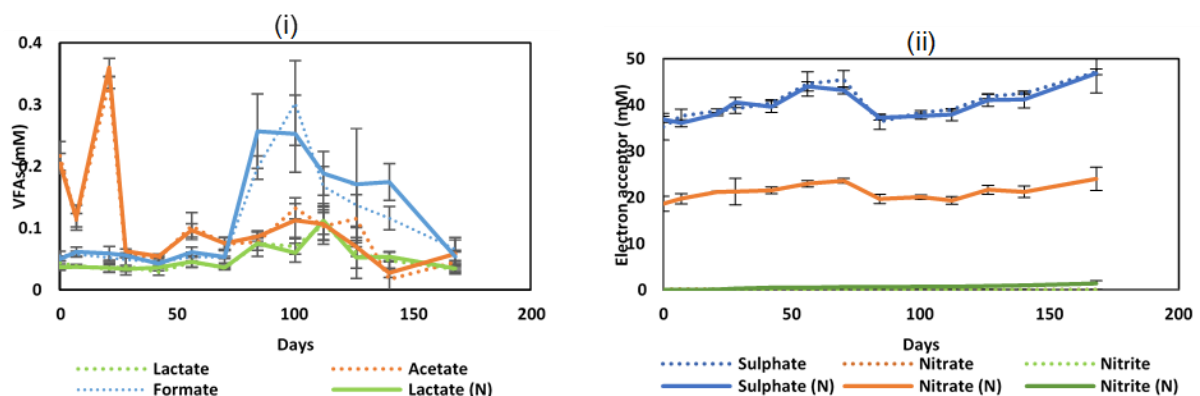
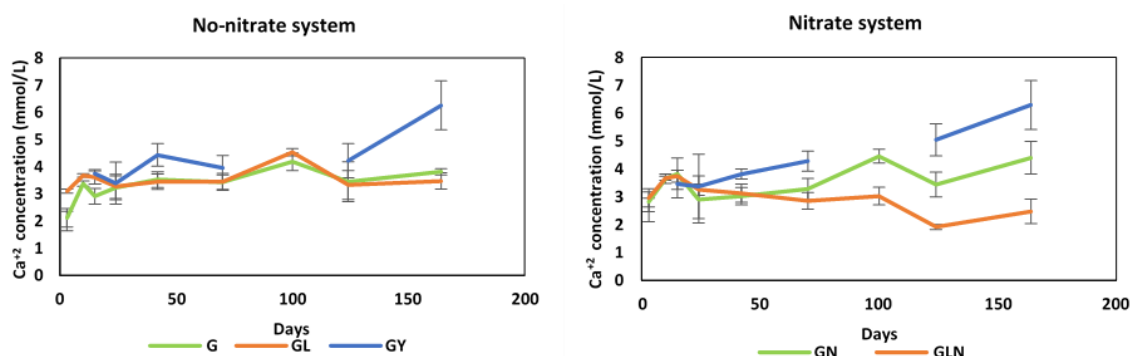


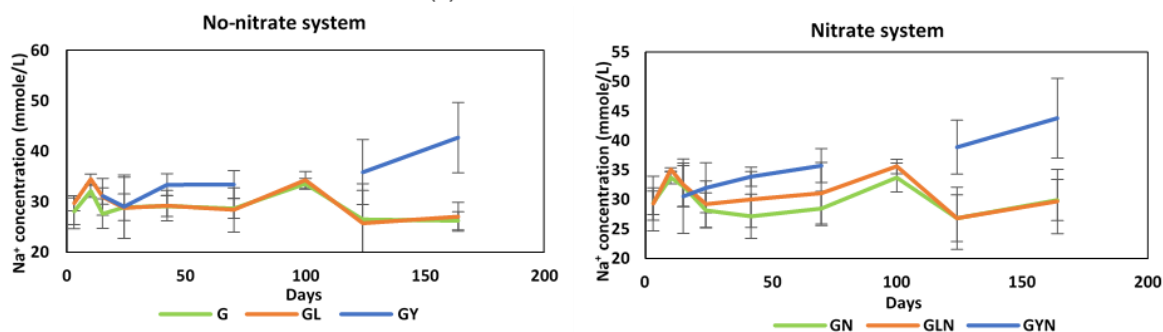
Figure 5-32: VFAs concentration and electron acceptor (sulphate, nitrate, nitrite) concentration for (ai & aii) Groundwater & Groundwater + Nitrate (GN), (bi & bii) Groundwater + Lactate (GL) & Groundwater + Lactate + Nitrate (GLN), (ci & cii) Groundwater + Yeast extract (GY) & Groundwater + Yeast extract + Nitrate (GYN) treatment of microcosm. For GL & GLN system, two axes represent lactate, which decomposes in acetate. The dotted line (...) represents no-nitrate, and the solid line (---) represents the nitrate system.

Formate values in the GL system also increased, suggesting degradation of the organics present, similar to the previous system. Figure 5-33c shows VFAs and electron acceptor concentrations in groundwater containing low concentrations of yeast extract without (GY) and with (GYN) nitrate. For this system also, the formate value increased suddenly after day 70 with a minor increase in lactate and acetate values similar to G and GN systems (Figure 5-32ci). Unlike for the other systems, sulphate concentrations were relatively stable over the duration of the incubation, although concentrations had increased from approximately 35 mM to 45 mM over the first 70 days for both GY and GYN systems, followed by a drop and again rise after day 126 (Figure 5-32cii), presumably due to abiotic factors in the system, e.g., dissolution of sulphate-containing cement phases. The other electron acceptor, nitrate, remained relatively stable, although there was evidence for limited microbial nitrate reduction with 0.6 mM nitrite detected after 126 days. Overall, the microcosms with a lower concentration of carbon showed less microbial activity, similar to no carbon source system, compared to those containing a higher concentration of carbon. Further investigation of calcium, magnesium and sodium ion concentrations in the system using ICP-AES revealed that, initially, the concentration of these ions increased due to the dissolution of ions from cement, and then remained constant till day 70 for all the systems (Figure 5-33).

(a) Calcium Concentration



(b) Sodium Concentration



(c) Magnesium Concentration

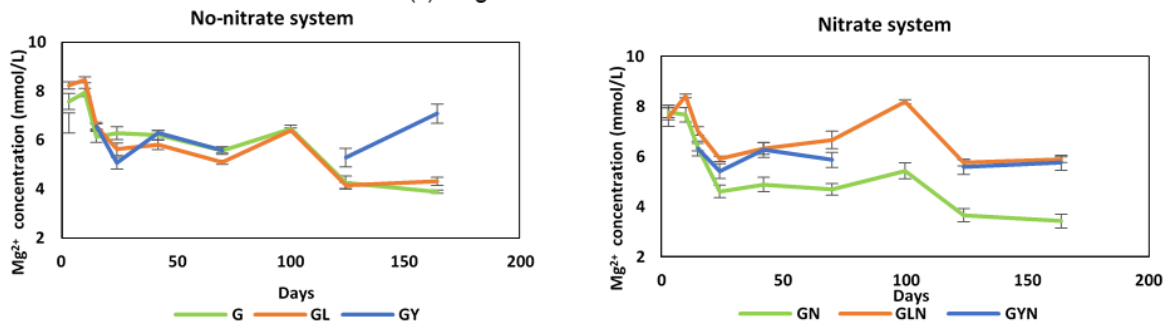


Figure 5-33: (a) Calcium ion concentration, (b) Sodium ion concentration, and (c) Magnesium ion concentration for the no-nitrate and nitrate system for 6 months.

For the GLN system, calcium concentration decreased after day 70, which indicates the formation of calcium carbonate (Figure 5-34a). This could be seen on the surface of cement tablets taken out after 3 months. The concentration of calcium ions was recorded to have increased for both GY and GYN systems (Figure 5-33c). This might indicate that cement dissolution occurred in the system after 3 months. A similar increase in the values of magnesium and sodium concentration was observed in that system.

5.4.2 2D-3D imaging processing analysis

The trend of IC and ICP data was supported by scanning electron microscopy (SEM) analysis. Microstructural investigation of surfaces and surficial cracks on cement tablets were studied for the first, second, third, and sixth month. It was challenging to make a definite judgment about healing time, speed, and form because of many external factors, e.g., variable width of surface cracks and orientation of cement tablets in the microcosms. Therefore, only cement tablets from the sixth month were compared and discussed here. The tablets were dried and analysed under a low vacuum of 1 mbar. Cracks on the surface were present in the samples after curing, and crack width varied between 2-6 μm . Backscattered images from the sixth month of each treatment are included in the described results.

For groundwater without nitrate (G) and with nitrate (GN) systems, the surface had rough and embedded calcite crystals in the sixth-month tablets. The cracks on the surface were not healed and were still prominent (Figure 5-34a & Figure 5-34b). There was no initiation of mineralization at the edge of cracks, which could have served as a potential surface for mineral nucleation and growth. For the groundwater and lactate without (GL) and with nitrate (GLN) system, the surface was covered with new minerals, including calcite, gypsum and vaterite (Figure 5-34c & Figure 5-34d). The deposition of these new minerals was more pronounced in GLN as compared to the GL system. Due to excessive carbonate and gypsum on the surface, the cracks were healed slowly from the edge towards the center of the crack for the nitrate supplemented GLN system (Figure 5-34d). The crack healing in the sample was generally superficial, but over a long time, it would be expected to decrease the permeability. Lastly, for groundwater and yeast extract without (GY) and with nitrate (GYN) systems, the surficial deposition of carbonate and gypsum was more pronounced than in the negative control (Figure 5-35e & Figure 5-35). The crack healing process for this system was slower than for GL and GLN systems. The surficial inspection under SEM suggested microbes were helping in crack healing and mineral formation, more in high (i.e., lactate system) and less in low carbon (i.e., yeast extract system) treatments. Apart from this, SEM images of GYN and GLN systems also showed different types of minerals on the surface like aragonite (CaCO_3), gypsum ($\text{CaSO}_4 \cdot 2\text{H}_2\text{O}$), ettringite ($\text{Ca}_6\text{Al}_2(\text{SO}_4)_3(\text{OH})_{12} \cdot 26\text{H}_2\text{O}$), and amorphous calcite (CaCO_3) (Figure 5-34g – Figure 5-34i). EDS on the new minerals formed on GYN showed that Ca, Mg, and O were present qualitatively in high amounts, which further confirmed the deposition of calcium-rich minerals like aragonite, calcite, gypsum, and magnesium-rich minerals e.g. magnesium hydroxide in the system.

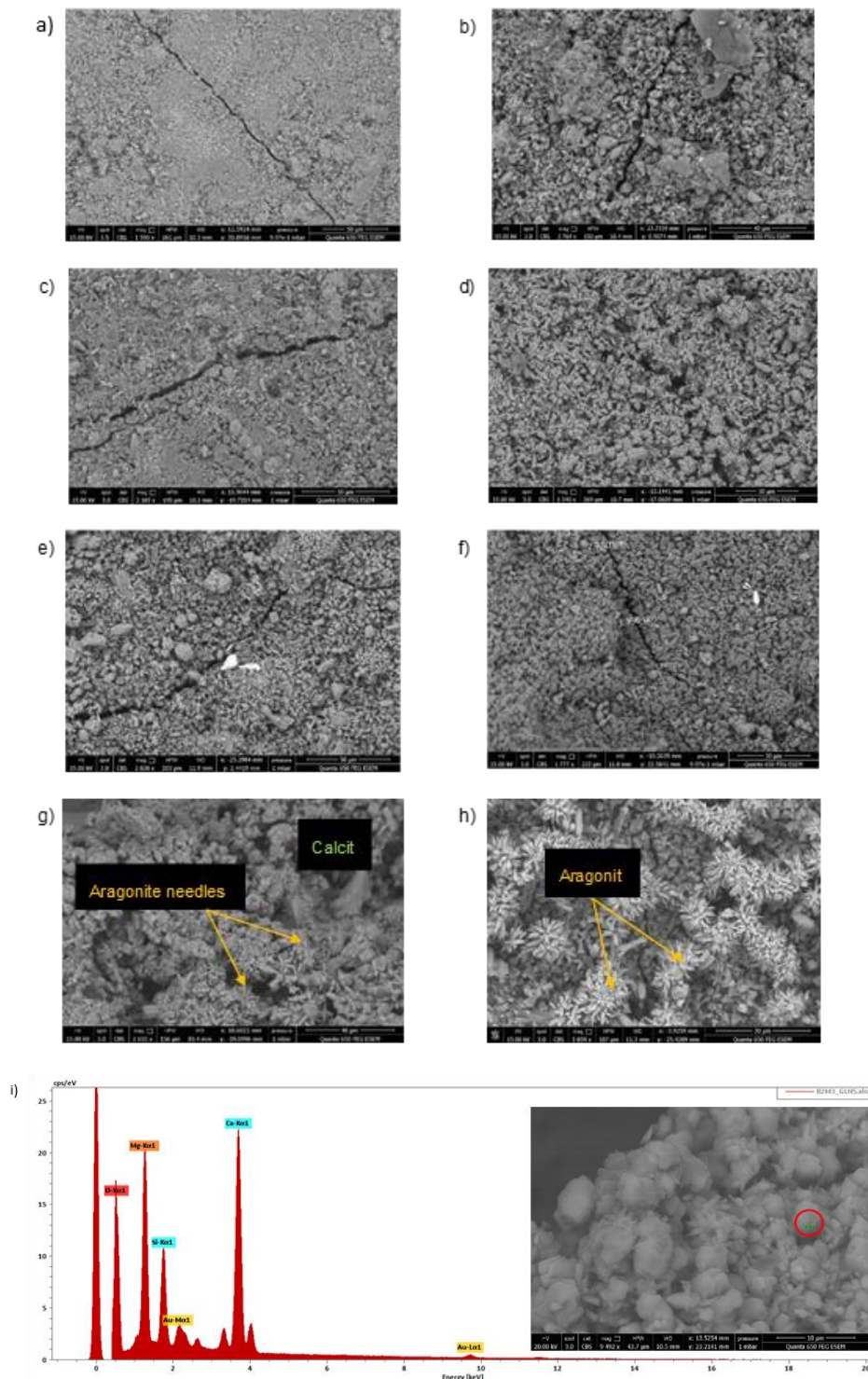


Figure 5-34: BSE image of crack healing material after three months in (a) Groundwater (G), (b) Groundwater + Nitrate (GN), (c) Groundwater + Lactate (GL), (d) Groundwater + Lactate + Nitrate (GLN), (e) Groundwater + Yeast extract (GY), and (f) Groundwater + Yeast extract + Nitrate (GYN). (g) & (h) Formation of calcite and aragonite minerals on the surface of cement tablets belongs to GYN system. (j) SEM-EDS for qualitative analysis of elements present on the surface cement tablet from GYN system.

After 2D surface analysis, samples were scanned under XCT for 3D images. The scanned images were cropped, and four different phases, including voids and carbonate deposited on the surface, were observed easily (Figure 5-35a). As expected, carbonate deposition on the surface was evident for the GLN system (Figure 5-35b and Figure 5-35c). The air voids were heterogeneously entrained in the

reference mortar matrix. This study mainly focused on pore filling and crack healing, so they were segmented using interactive and manual thresholding on the cropped volume. Most of the pore spaces were inside the silica fume used in the cement mix due to cracking during slurry mixing and curing. The change in pore diameter due to carbonation on the surface was evident in the volume of XCT images of cement tablets when comparing the first and sixth month of GL, GLN, GY, and GYN microcosms. The minimum detectable diameter was approximately 7.2 μm , and the maximum pore size was between 700 to 1000 μm . The 3D images of segmented pores according to their size are also shown with the semi-log graph of pore distribution, discussed in the paper, for better visualization.

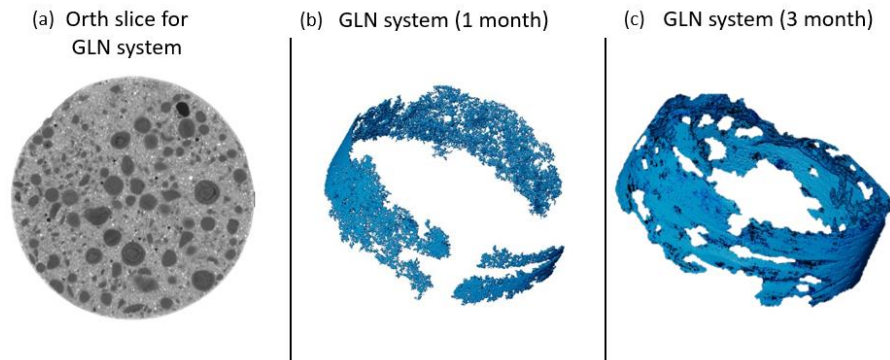
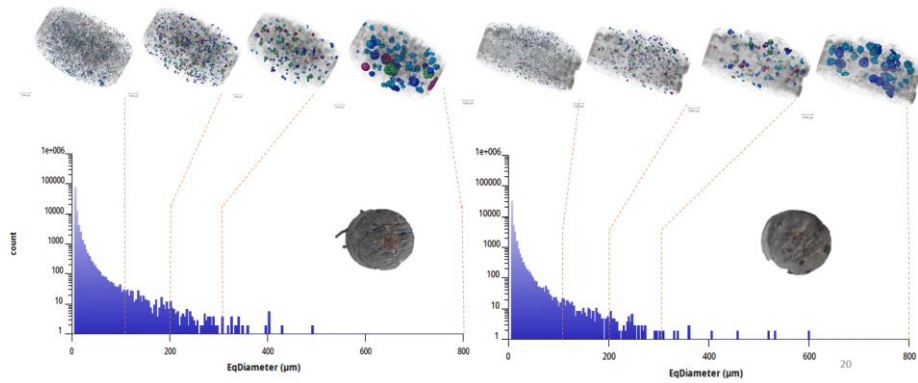


Figure 5-35: (a) Ortho slice of a volume section of GLN system. The different grey scales represent different phases present in the sample, Segmentation of the carbonate phase deposited on the surface of the GLN system in (b) 1 month and (c) 6 months.

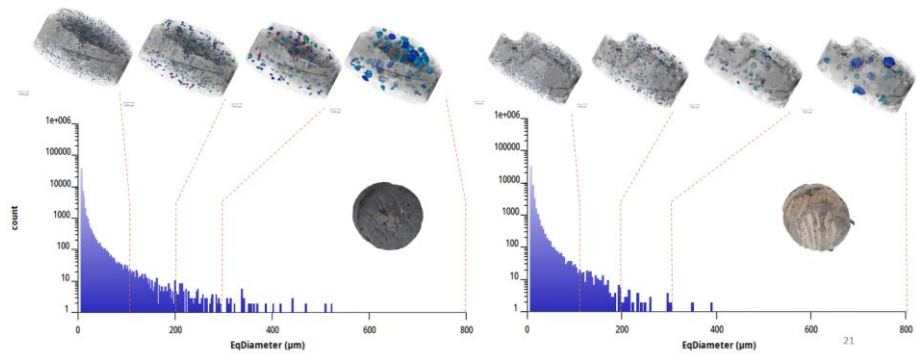
Figure 5-36a suggests that for one and six-month GL samples, there was a decrease in pore counts between 0-100 μm in the sixth month compared to the first-month sample. Apart from that, the pore densities between 200 to 300 μm also decreased. This was more prominent in the GLN treatment.

The pore density between 200 to 300 μm and 300 to 800 μm had decreased significantly, which can be easily compared with the respective 3D images (Figure 5-36b). For GY samples, there was a slight change in the pore distribution in the first and third month. However, figure 7c shows that in the third month, there was a decrease in the count of the smaller diameter of pores between 0-100 μm . On the other hand, the GYN sample shows a noticeable change in the pore size distribution between 200-300 μm and 300-800 μm (Figure 5-36d) as compared to the GY system. There was a thin layer of carbonation that was not detected by the XCT scan due to its limitations but was visible as a white layer on the samples. The decrease in the count or pore diameter in different systems indicates the filling of tiny pores or the lining of larger pores due to carbonation.

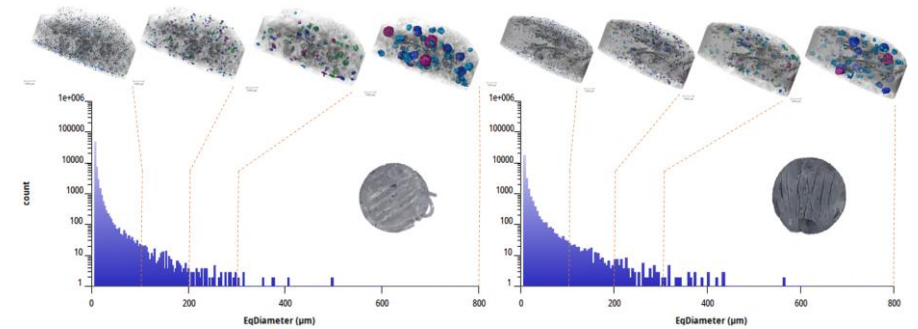
a) Groundwater
+ Lactate (GL)



b) Groundwater
+ Lactate +
Nitrate (GLN)



c) Groundwater
+ Yeast extract
(GY)



d) Groundwater
+ Yeast extract +
Nitrate (GYN)

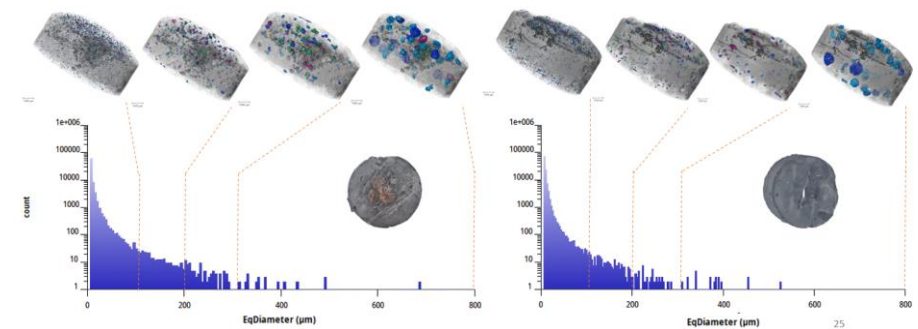


Figure 5-36: 1- and 6-month 3D XCT image and semi-log graph of pore diameter v/s count for (a) groundwater + Lactate (GL), (b) Groundwater + Lactate + Nitrate (GLN), (c) groundwater + Yeast extract (GY), and (d) Groundwater + Yeast extract + Nitrate (GYN)

5.5 Microbial influenced alteration of cement phases with natural waters

To evaluate whether microorganisms of natural groundwater of Cernon, France, lead to degradation or calcite precipitation of low-pH cements, microcosms incubating cement samples with two conditions of groundwater (with and without 2 mM of lactate) were conducted at the Tournemire Experimental Station of IRSN for up to 9 months with water renewing every 3 weeks.

5.5.1 Geochemical analysis

The pH of the natural groundwater from the Cernon fault (n = 2) is 7.80 ± 0.28 , containing 7.4 ± 0.39 mg/L of sulphate, 1.5 ± 0.45 mg/L of nitrate, 4.7 mg/L of total nitrogen, 4.9 ± 0.84 mg/L of total organic carbon and 41.2 ± 5.72 mg/L of total inorganic carbon (Table 5-8).

Table 5-8: The geochemical data from natural groundwater of Cernon, France collected in 2022 and 2023 (*data under detection limits from one replicate).

| ICP-MS | Concentration ($\mu\text{g/L}$) | IC | Concentration (mg/L) |
|--------|-----------------------------------|-----------------|----------------------|
| Ca | 81250 ± 7141.7 | Sulphate | 7.44 ± 0.39 |
| Mg | 17600 ± 1697.1 | Nitrate | 1.51 ± 0.45 |
| Na | 4015 ± 841.5 | Chloride | 4.29 ± 0.11 |
| U | 0.68 ± 0.52 | TN | 3.67 ± 1.04 |
| Ni | 0.397* | TIC | 41.75 ± 5.73 |
| Cu | 0.997* | TOC | 4.91 ± 0.84 |
| Fe | 1.61* | pH | 7.80 ± 0.28 |
| Ba | 4.0 ± 0.65 | | |
| Zn | 7.3* | | |
| K | 236 ± 26.87 | | |
| Si | 1235 ± 473.76 | | |
| Al | 1.02* | | |
| Mn | 2.25* | | |

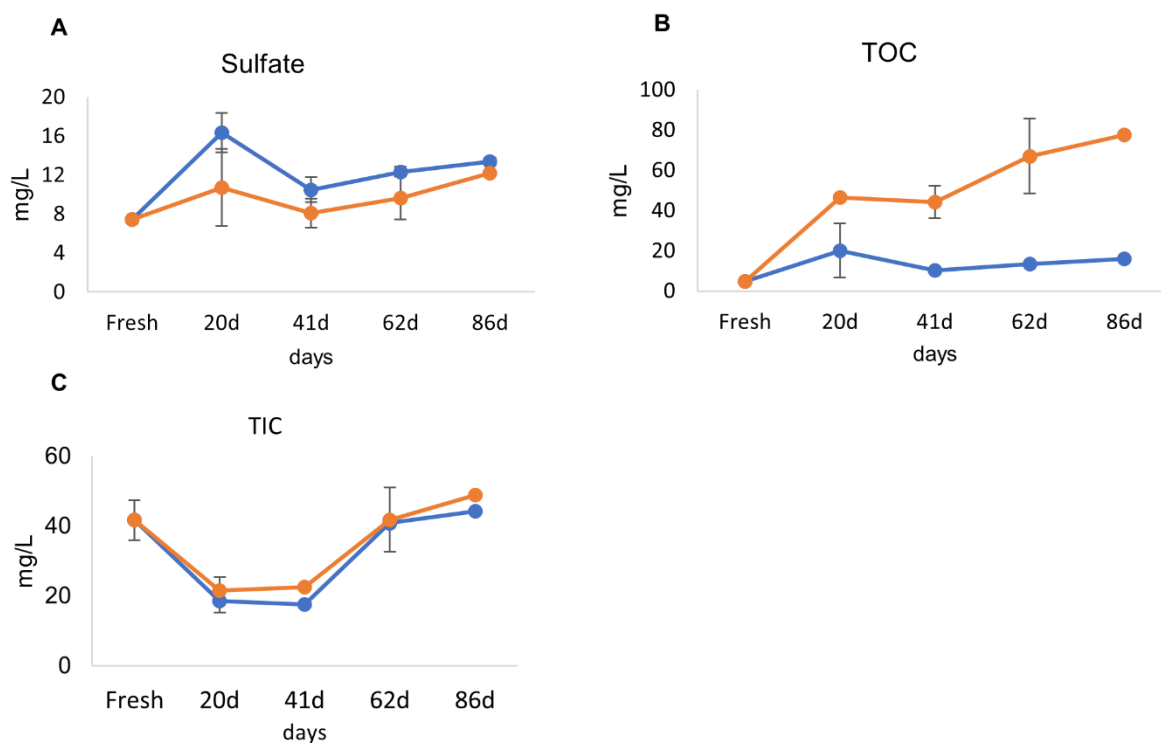


Figure 5-37: The evolution of sulphate concentration (A), total organic carbon (TOC) (B), and total inorganic carbon (TIC) (C) in water samples collected from condition 1 and 2 (Table 2-12) after different time frames analysed by High Performance Ionic Chromatography or Multi N/C 2100S.

This indicates that there are electron acceptors for anaerobic microorganisms (nitrate and sulphate) and for aerobic microorganisms (oxygen) available together with electron donors (TOC and TIC) as carbon source. On the other hand, Ca, Mg, Na and Si accounted for the most abundant elements (>1000 µg/L) in the fresh groundwater. Other minor elements, including K, Zn, Fe, Ni, Cu and U were also quantified via ICP-MS (Table 5-10).

During the 3 months of incubation, we observed that the content of TN and nitrate in each collected water samples under both conditions largely decreased to levels undetectable with Figure 5-37 A). Moreover, the TOC content in microcosms with 2 mM of lactate in the collected water samples ranged from 38.5 to 80.1 mg/L. However, the TOC content in microcosms without additional lactate was 2 to 5 times higher than that in fresh natural groundwater (Figure 5-37 B). The increase of TOC content in these microcosms may result from the dissolution of carbon from cement samples into waters or from the microbial activities stimulated by addition of lactate. The evolution of TIC content in both incubations was consistent, decreasing until 41 days of incubation and afterwards increasing to 44.3 ± 0.64 µg/l and 48.9 ± 0.57 µg/l Figure 5-37 C).

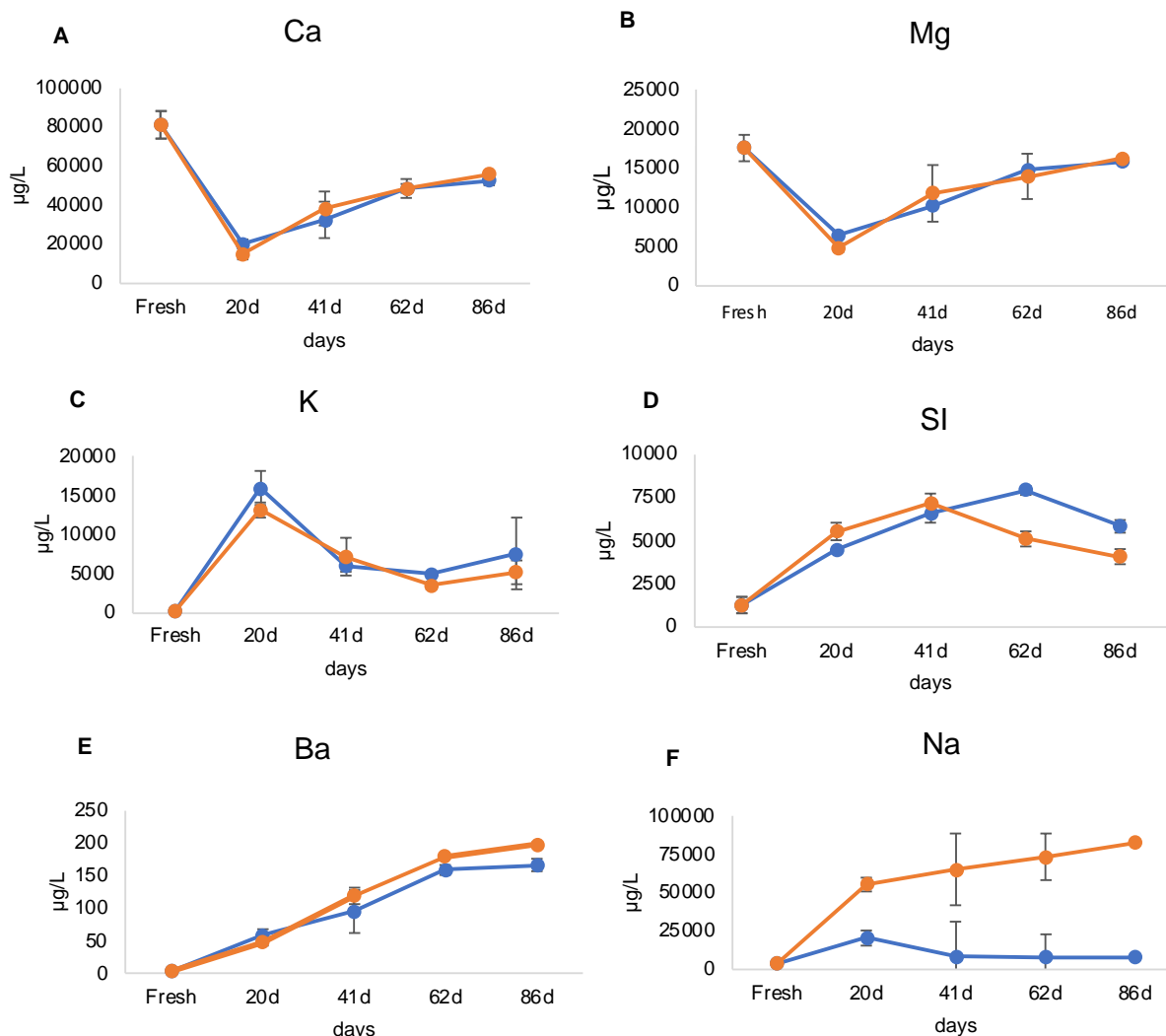


Figure 5-38: The evolution of elemental composition ((Ca (A), Mg (B), K (C), Si (D), Ba (E) and Na (F)) in waters collected from microcosms incubated with natural groundwater (blue) and additional 2 mM of lactate (orange) for up to 3 months and analysed by Inductively Coupled Plasma Mass Spectrometry. Fresh: fresh natural groundwater collected from source.

Changes in the elemental composition in collected water samples were also observed (Figure 5-38). The concentration of Ca and Mg in the fresh natural groundwater samples were $81250 \pm 7141.8 \mu\text{g/L}$ and $17600 \pm 1697.1 \mu\text{g/L}$, respectively. Their concentration greatly decreased in water samples collected after 20 days of incubation but gradually increased afterwards (Figure 5-38A and B). Conversely, the concentration of K largely increased to $5950 \pm 2192.0 \mu\text{g/L}$ and $13200 \pm 989.9 \mu\text{g/L}$ in microcosms without lactate and with additional lactate, respectively, after 20 days of incubation and decreased afterwards (Figure 5-38C). Similar observations were made for Si contents (Figure 5-38D). The concentration of Ba in freshly collected groundwater was $4.0 \pm 0.65 \mu\text{g/L}$ and gradually increased in waters of microcosms under both conditions (Figure 5-38E). The concentration of Na also gradually increased due to the addition of 2 mM of sodium lactate (Figure 5-38F).

5.5.2 Microbial diversity analysis of water and cement samples

The microbial diversity of fresh natural groundwater collected in 2022 and 2023 shows different dominant bacterial genera (relative abundance > 10%) *Pseudomonas* and *Rhodofera* are the major genera in groundwater from 2022, whereas in groundwater from 2023, *Hydrogenophaga*, *Alkanindiges* and *Rhodofera* are predominant. Other bacterial genera with abundance > 1% are listed in Table 509. Overall, up to 240 and 85 genera were identified in groundwater communities from 2022 and 2023, respectively. This indicated that the microbial communities of natural groundwater are highly diverse but variable at different points in time.

Table 5-9: Microbial diversity of natural groundwater of Cernon, France collected in 2022 and 2023. Only genera with relative abundance > 1 % in each year are shown in the table.

| Genus | Abundance in 2022 | Abundance in 2023 |
|---|-------------------|-------------------|
| <i>Pseudomonas</i> | 29.1% | 7.1% |
| <i>Rhodofera</i> | 24.1% | 18.8% |
| <i>Massilia</i> | 7.6% | 1.4% |
| Unidentified <i>Comamonadaceae</i> genus | 4.5% | 0.38% |
| <i>Rugamonas</i> | 2.9% | 0.14% |
| <i>Flavobacterium</i> | 2.63% | 0.013% |
| <i>Polaromonas</i> | 2.2% | 1.6% |
| <i>Hydrogenophaga</i> | 2.0% | 30.1% |
| <i>Duganella</i> | 1.7% | 7.1% |
| Unidentified <i>Sphingomonadaceae</i> genus | 1.6% | 0% |
| <i>Undibacterium</i> | 1.5% | 0.40% |
| <i>Acidovorax</i> | 1.1% | 0.47% |
| <i>Alkanindiges</i> | 0.002% | 18.9% |
| <i>Cavicella</i> | 0.02% | 9.7% |
| <i>Agitococcus</i> | 0.005% | 1.5% |

Water samples were collected from microcosms (number 2 & 3 with natural groundwater, and number 6 & 7 with groundwater plus additional lactate) after 20 and 41 days, together with fresh natural groundwater to compare microbial community changes. The biomass recovered from cement samples (incubated for 86 days in both conditions) was also subjected to microbial diversity analysis. Proteobacteria was the most abundant phylum in all microbial communities from water samples and cement surfaces, followed by Bacteroidota, Patescibacteria and Cyanobacteria in certain water communities (Figure 5-39 A).

Moreover, we observed that the gammaproteobacterial *Pseudomonas* largely enriched (up to 53.8%) in water communities incubated for 20 days under both conditions, except for the water from one microcosm with additional lactate (W7_20d), which was dominated by unidentified *gammaproteobacterial* genus (Table 5-10, Figure 5-39 B). However, microbial communities in water samples from 41 days incubation under both conditions were dominated by Alphaproteobacteria with relative abundance >50% except for one microcosm with natural groundwater (W2_41d) (Figure

5-39 C). Furthermore, the alphaproteobacterial *Azospirillum*, *Magnetospirillum* and *Caulobacter* were the most abundant taxa across all samples with various relative abundance (Figure 5-39 C). On the other hand, gammaproteobacterial *Dechloromonas* was the major genus in microcosm with natural groundwater (W2_41d), whereas in microbial communities from water samples with additional lactate, an unidentified gammaproteobacterial genus was the majority (Figure 5-39 B). Interestingly, gammaproteobacterial *Pseudomonas* dominated all microbial communities of the surface of cement samples despite the difference of the groundwater conditions (Figure 5-39 B). However, variances were also observed in microcosms under the same conditions. For example, in the microcosms (number 2 & 3) incubated with natural groundwater, the abundance of *Acinetobacter* on one of the cement surfaces (C2_86d) reached 51.6% but its abundance in another cement sample (W3_86d) was <1% (Figure 5-39 B). A similar observation was made for alphaproteobacterial *Sphingobium* on one of the cement surfaces (C3_86d) (Figure 5-39 C).

Altogether, we observed a pattern of dominant bacterial genera in the microbial communities of the water samples and cement surface based on different incubation times but both conditions of groundwater appeared to have minor effects on the microbial communities.

Table 5-10: Details of sample codes for microbial diversity analysis.

| Abbreviation | Sample | Microcosm | Condition | Days of incubation |
|--------------|--------|-----------|-----------|--------------------|
| W2_20d | Water | 2 | Natural | 20 |
| W3_20d | Water | 3 | Natural | 20 |
| W6_20d | Water | 6 | Lactate | 20 |
| W7_20d | Water | 7 | Lactate | 20 |
| W2_41d | Water | 2 | Natural | 41 |
| W3_41d | Water | 3 | Natural | 41 |
| W6_41d | Water | 6 | Lactate | 41 |
| W7_41d | Water | 7 | Lactate | 41 |
| C2_86d | Cement | 2 | Natural | 86 |
| C3_86d | Cement | 3 | Natural | 86 |
| C6_86d | Cement | 6 | Lactate | 86 |
| C7_86d | Cement | 7 | Lactate | 86 |

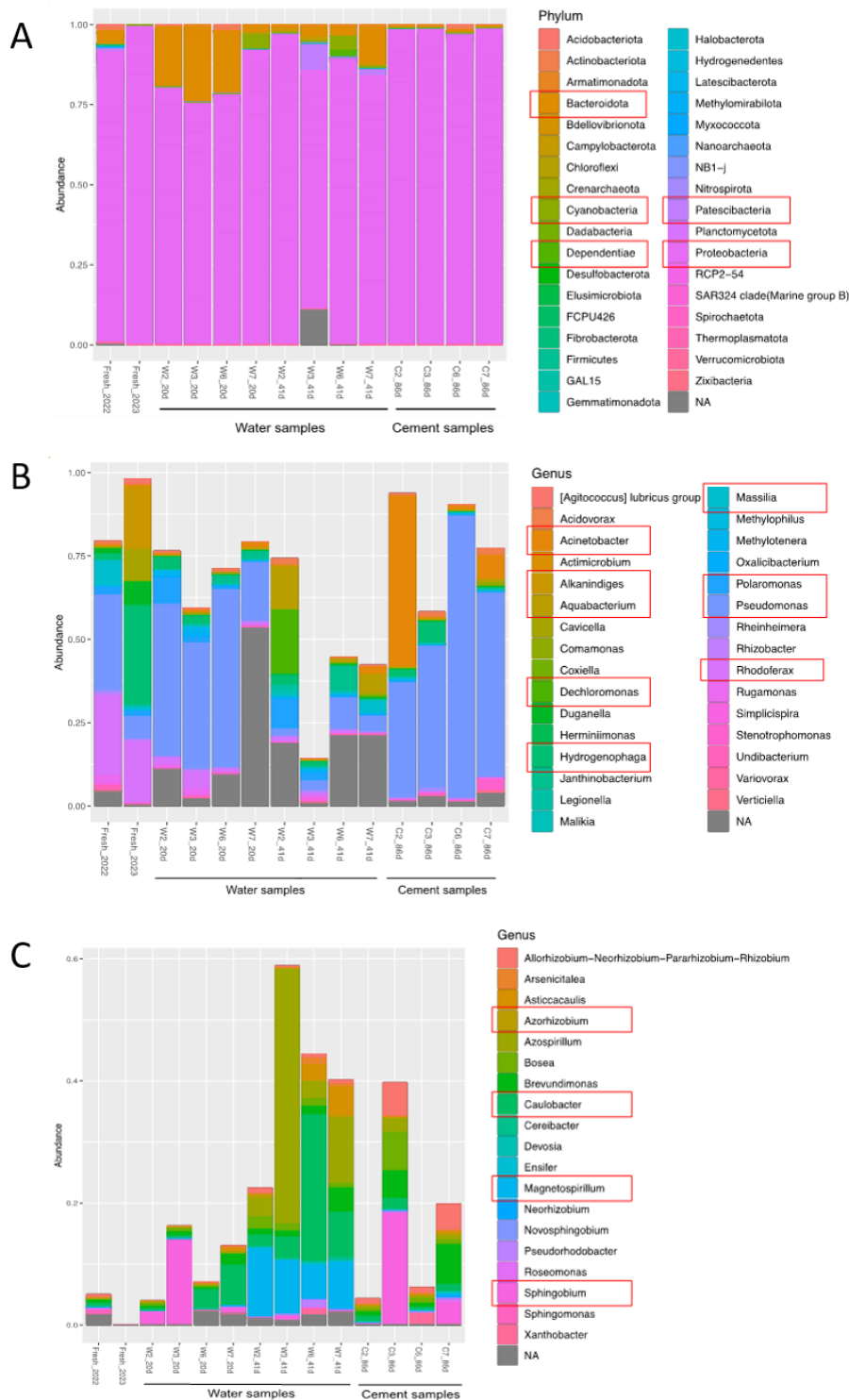


Figure 5-39: Microbial diversity of fresh natural groundwater collected in 2022 and 2023 (Fresh), water samples from 20 and 41 days of incubation with natural groundwater (W2 & W3), and with groundwater and additional lactate (W6 & W7), and surface of cement samples incubated with natural groundwater (C2 & C3), and with groundwater and additional lactate (C6 & C7) for 86 days at phylum level (A), genus level of Gammaproteobacteria (B) and genus level of Alphaproteobacteria (Classification based on Silva database). The red boxes highlight the dominant or common microbial taxa in all communities. Details about the sample codes are listed in Table 5-10.

5.5.3 Microbial colonization on cement surface

By using SEM bacterial shape-like aggregations associated with extracellular polymeric substances (EPS)-like structure were observed on the surface of a cement sample that was incubated in microcosms with additional lactate for 3 months (Figure 5-40 A). Instead of EPS-like structure, we observed irregular spikey shape of precipitation on the surface of the cement sample incubated with natural groundwater for 3 months (Figure 5-40 B).

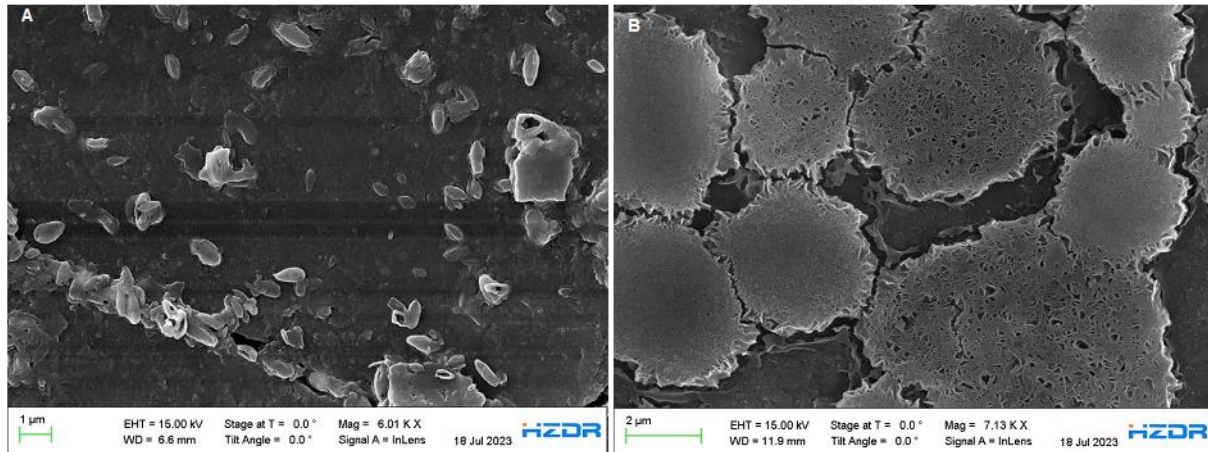


Figure 5-40: Scanning electron microscopic images of surface structure from cement samples incubated with groundwater supplied with 2 mM of lactate (A) and natural groundwater (B) for 3 months.

5.5.4 Analysis of the cement surface

Previous work was conducted on industrial low-pH concrete and cement paste immersed in solution (Neji et al., 2023), reporting that when the porosity is low, a layer of calcium carbonate precipitates at the interface, limiting the degradation mechanisms. Here, our EDS-SEM analysis showed a calcite layer on the surface of each sample incubated in different groundwater conditions (Figure 5-41). Moreover, no gradient degradation was observed, suggesting a clogging effect due to calcite precipitation that limits the leaching of species from the sample.

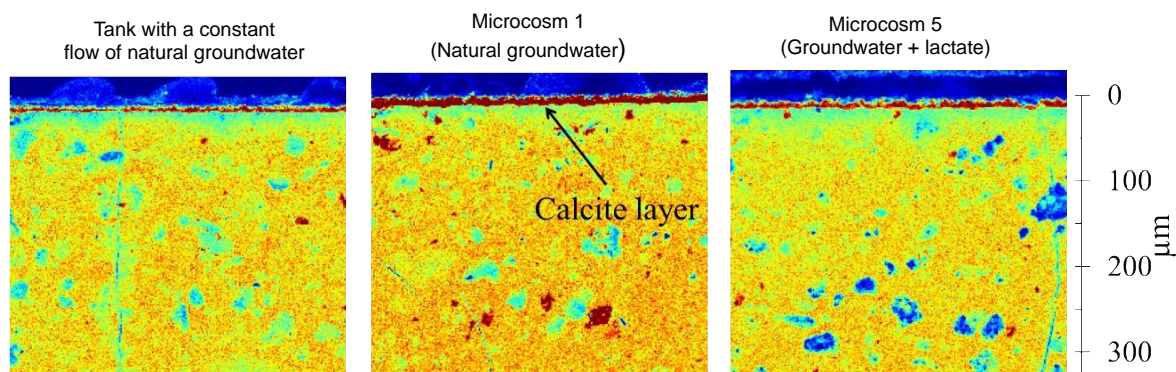


Figure 5-41: EDS mapping of calcium of low-pH cement samples incubated in a tank with constant flow of natural groundwater, in a microcosm with 300 ml of natural groundwater, and in a microcosm with 300 mL of groundwater supplied with 2 mM of Na-lactate. The rainbow colourmap denotes the high content (red) and low content (blue) of calcium.

The XRD analysis further confirmed the calcite precipitation on all the cement surfaces based on the diffractograms (Figure 5-42). The low sulphate content in all groundwater solutions suggests that the dissolution of ettringite (initially present in the sound material) can be used as a marker of degradation. In all cases, at a depth of 80 micrometers below the surface, ettringite is already observable, validating the barrier role of the calcite layer.

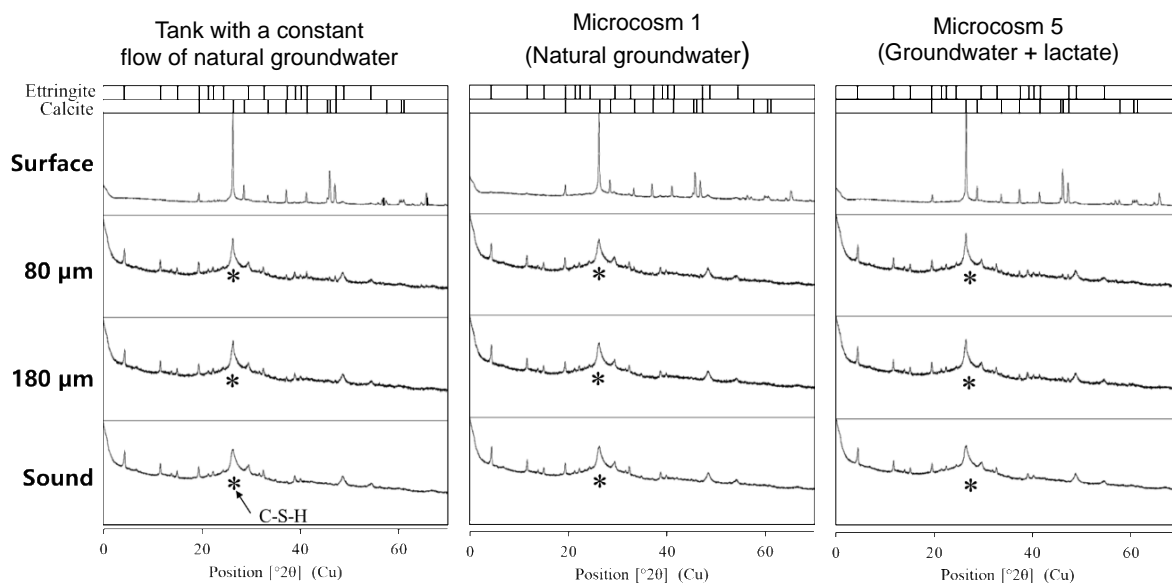


Figure 5-42: X-Ray diffractograms of surface of low-pH cement samples incubated in a tank with constant flow of natural groundwater, in a microcosm with 300 ml of natural groundwater, and in a microcosm with 300 ml of groundwater supplied with 2 mM of Na-lactate.

5.6 Conclusion for part 5

➤ Artificial ageing conditions

In the study performed by SCK CEN together with COVRA and FZJ where the Dutch concept was studied, a clear microbial community was present in the water and also on the concrete cubes. To obtain proper abiotic controls, samples were irradiated, which was shown to not negatively affect the mechanical strength of the concrete cubes. After 1.5 year, the amount of viable cells on the concrete cubes increased, putatively indicating that the microbial community could form a biofilm on the concrete. In addition, we also tried to explicate the origin of the microbial community by studying the water from large boxes with concrete samples (from certified and blend CEM), which was taken to prepare the samples used during this project, tap water and sand to prepare the concrete cubes. The water in the small boxes is fundamentally the same as the water taken from the large boxes with certified or blend CEM specimens. However, the microbial community seems to be more abundant and active in the small boxes. This suggests the presence of a factor that enhances the microbial community in the smaller containers. 16S rRNA amplicon sequencing demonstrated a very diverse microbial community in the samples, which is different than the sand used for the concrete samples. Differences are observed between the samples of certified and non-certified conditions, but more research is needed to explain the observed differences.

Regarding the Czech concept, it seems it is mainly water and the way how the samples are exposed to different sources of water (air humidity, continuous water flow or water suspending clay) that determines the fate of exposed LPC samples. The metabolic activity of microorganisms is above all driven by and dependent on the presence of water. Here we showed that the environmental microbial load designated the colonization of the LPC “nude” samples and was represented by mixed microbial community with dominant heterotrophic species in all three environments – air, water, and bentonite.

The fastest growth of biofilm detected by molecular-genetics methods was detected in water-exposed samples, followed by air-exposed samples. Samples exposed to bentonite could not adopt similar feature. It was probably the close **contact with bentonite suspension** and insufficient space around the samples that hindered to evolve rich biofilm. However, these were the least durable samples indicating that other than biotic factors control the durability of LPC (in contact with bentonite) such as the cation exchange between Mg type bentonite and LPC. The mentioned deteriorative effect is relatively strong with microfracture propagation rate of approx. 1 mm per year. Moreover, the cracks formed in surface layer were not healed despite the proved existence of urease-positive clones in LPC samples. We suggest this might be a result of insufficient number of nucleation sites due to slow biofilm formation and low availability of water that is taken by bentonite.

In **water environment** a different scenario was observed. Rapid and robust colonization of LPC samples in the water first by sulfur-oxidizing bacteria and by heterotrophic bacteria is most probably the reason for both LPC matrix deterioration in the first step and calcium precipitation in the second resulting in healing of formerly cracked samples. Fast growth of bacteria on the sample surface probably enable to form enough nucleation sites for calcium precipitation under these circumstances (water environment, higher pH, certain bacterial diversity), calcium being leached out from the cementitious matrix due to contact with acidic biofilm. This effect was observed in only 6-month-old samples, whereas in 12- and 18-month-old samples the relative crack penetration was low. However, the rigidity of surface layer in water-exposed samples declined rapidly in time and corresponded to fast outgrowth of surface biofilm. Similarly, the *de novo* crystallization of cristobalite in water-exposed samples after 1.5 year is also most probably microbially induced confirming the important role of bacteria in mineralization but also their potential to change concrete composition and structure.

Air-exposed samples are not in direct contact with water; however, the growth of biofilm is fast and vigorous and colonize better the interior of the samples. Local production of acidic metabolites most probably caused dissolution of calcium from concrete samples and formation of calcium rich layer composed of gypsum and vaterite minerals. The explanation of calcium sulphate precipitation without detection of sulfur-oxidizing species and sulphate present in surrounding environment is rather speculative suggesting sulphide oxidation as a driving force for primary matter production as observed in early colonizers. This effect would be attributed to the first stage of colonization of such samples that is in accord of our *de novo* drilled and cut samples. Moreover, the microbially-induced local precipitation of gypsum and vaterite might lead to strengthening of the exposed material despite lowering surface pH causing reduction in strength.

To summarize, from these experiments we can conclude that microbial presence can be either deteriorative as protective depending on the extent of water and local pH changes in environment where heterotrophic microorganisms dominate. Microbial assisted changes seem important in air and water environment while CSH to MSH chemical conversion is main driving force of negative effects on the contact with bentonite suspension.

- Interaction between low-pH cementitious material and microbes in low-carbon source groundwater

The work of UNIMAN showed that lactate in the high carbon source system with added nitrate (GLN) was degraded to acetate with a pH drop from 10 to 9.0 in 6 months. This was accompanied by a decrease in the concentration of nitrate, which was reduced to nitrite. Multi-technique analyses provided evidence that microbial carbon metabolism underpinned the reaction between carbonate and $\text{Ca}^{2+}(\text{aq})$ to form calcite and aragonite precipitates, which contributed to crack sealing. Pore size distribution and pore counts for this system also decreased significantly. In comparison, for the low carbon system with nitrate (GYN), there were very minor changes in measured VFAs and nitrate values, suggesting minimal nitrate reduction by the microbes. Interestingly, there was an increase in the calcium, magnesium, and sodium concentrations, which might be leached from the cement surface over time. However, 2D-3D images showed no significant change in pore size distribution or pore counts over 6 months in the low-carbon GYN system (in contrast to the GLN experiments).

Overall, this work provides evidence that bio-mineralization of calcite was prominent in the higher carbon GLN experiments, but very little microbial activity was observed in the lower carbon GYN system. There was no sign of biodegradation of cement for both systems. Microbial community analysis by 16S rRNA gene sequencing is ongoing to give a more holistic analysis of the system, highlighting key organisms and processes that may have promoted biomineralization in the higher carbon experiments. Additional tests are planned to identify impacts on the structure of the cement, including quantifying changes in water absorption capabilities in the treated samples by high-resolution XCT scanning. Future work could include follow-up longer-term studies using appropriate groundwaters, ideally in situ, dissected using the cross-disciplinary approach used in this study to discuss cement-microbe interactions.

➤ Microbial influenced alteration of cement phases with natural waters

In the experiments of HZDR and IRSN, low-pH cement samples were incubated under different conditions, mainly focusing on microbial impact of Cernan groundwater on cement degradation or Calcite precipitation. Despite the highly diverse microbial communities of natural groundwater (up to 240 genera), *Pseudomonas* species were the main microorganism recovered from the biomass of cement surface. This suggests that they are able to colonize on the surface of low-pH cement as *Pseudomonas* are known for biofilm formation on material surface by secreting EPS-based matrix. This is congruent with the SEM image of cement samples extracted from microcosm with additional lactate. Although *Pseudomonas* was also identified on the cement surface from the microcosms with natural groundwater, similar EPS-like structure was not observed. This may be due to lower microbial biomass not stimulated by exogenous lactate because the TOC content in the water of these microcosms was relatively low. On the other hand, the large decrease of calcium concentration in calcareous groundwater may result in calcium deposit on the cement surface supported by SEM-EDS and XRD analyses. The calcium layer precipitated on the surface may serve as a barrier to prevent cement degradation by attack solution such as calcareous groundwater. Although stimulation of microbial growth was attempted by addition of lactate, no impact on cement degradation for the 3 months' incubation period was observed.

5.7 References for part 5

- A.E. Berns, H. Philipp, H.-D. Narres, P. Burauel, Vereecken, H., Tappe, W., 2008. Effect of gamma-sterilization and autoclaving on soil organic matter structure as studied by solid state NMR, UV and fluorescence spectroscopy. *Eur. J. Soil Sci.* 59, 540–550. <https://doi.org/10.1111/j.1365-2389.2008.01016.x>.
- S. Cappello, and M. M. Yakimov (2010). *Alcanivorax*. Handbook of Hydrocarbon and Lipid Microbiology. K. N. Timmis. Berlin, Heidelberg, Springer Berlin Heidelberg: 1737-1748.
- M.G. Chevrette, C.M. Carlson, H.E. Ortega, C. Thomas, G.E. Ananiev, K.J. Barns, A.J. Book, J. Cagnazzo, C. Carlos, W. Flanigan, K.J. Grubbs, H.A. Horn, F.M. Hoffmann, J.L. Klassen, J.J. Knack, G.R. Lewin, B.R. McDonald, L. Muller, W.G.P. Melo, A.A. Pinto-Tomás, A. Schmitz, E. Wendt-Pienkowski, S. Wildman, M. Zhao, F. Zhang, T.S. Bugni, D.R. Andes, M.T. Pupo, C.R. Currie, 2019. The antimicrobial potential of *Streptomyces* from insect microbiomes. *Nat. Commun.* 10, 516. <https://doi.org/10.1038/s41467-019-08438-0>.
- A.M. Danial, A. Medina, M. Sulyok, N. Magan, 2020. Efficacy of metabolites of a *Streptomyces* strain (AS1) to control growth and mycotoxin production by *Penicillium verrucosum*, *Fusarium verticillioides* and *Aspergillus fumigatus* in culture. *Mycotoxin Res.* 36, 225–234. <https://doi.org/10.1007/s12550-020-00388-7>.
- M. Diaz-Herraz, V. Jurado, S. Cuezva, L. Laiz, P. Pallecchi, P. Tiano, S. Sanchez-Moral, C. Saiz-Jimenez, 2014. Deterioration of an Etruscan tomb by bacteria from the order Rhizobiales. *Sci. Rep.* 4, 3610. <https://doi.org/10.1038/srep03610>.
- C. Dewitte, A. Bertron, M. Neji, L. Lacarrière, A. Dauzères, Chemical and Microstructural Properties of Designed Cohesive M-S-H Pastes, (2022) *Materials*, 15 (2), art. no. 547, DOI: 10.3390/ma15020547.
- C. Gurtner, J. Heyrman, G. Piñar, W. Lubitz, J. Swings, S. Rölleke, 2000. Comparative analyses of the bacterial diversity on two different biodeteriorated wall paintings by DGGE and 16S rDNA sequence analysis. *Int. Biodeterior. Biodegrad., Biodeterioration of Culture property 2, Part 1* 46, 229–239. [https://doi.org/10.1016/S0964-8305\(00\)00079-2](https://doi.org/10.1016/S0964-8305(00)00079-2).
- V. Hlavackova, R. Shrestha, E. Hofmanova, P. Kejzlar, J. Riha, D. Bartak, A. Sevcu, K. Cerna, 2023. A protocol for the extraction of viable bacteria for identification of bacterial communities in bentonite. *Appl. Clay Sci.* 232, 106809. <https://doi.org/10.1016/j.clay.2022.106809>
- K. Hendrix, K. Mijndonckx, N. Bleyen, H. Moors, N. Leys and E. Valcke (2022). BN Experiment: Chemical and microbial analysis of phase 27. TECHNICAL NOTE. 2022-22.
- M. Honty and K. Mijndonckx (2022). Boom Clay pore water chemistry and microbiology around HADES, SCK CEN.
- H. Ito, H. Iizuka, 1971. Taxonomic Studies on a Radio-resistant *Pseudomonas*. *Agric. Biol. Chem.* 35, 1566–1571. <https://doi.org/10.1080/00021369.1971.10860119>
- S. Karacic, (2021). Microbial biofilm communities associated with degradation of sprayed concrete in subsea tunnels, Chalmers Tekniska Hogskola (Sweden).
- S. Karačić, O. Modin, P. Hagelia, F. Persson and B.-M. Wilén (2022). The effect of time and surface type on the composition of biofilm communities on concrete exposed to seawater. *International Biodeterioration & Biodegradation* 173: 105458
- F. Lingens, R. Blecher, H. Blecher, F. Blobel, J. Eberspächer, C. Fröhner, et al. (1985). *Phenylobacterium immobile* gen. nov., sp. nov., a Gram-Negative Bacterium That Degrades the Herbicide Chloridazon. *International Journal of Systematic and Evolutionary Microbiology* 35: 26-39
- U.K. Mangamuri, V. Muvva, S. Poda, B. Chitturi, V. Yenamandra, 2016. Bioactive natural products from *Pseudocardia endophytica* VUK-10. *J. Genet. Eng. Biotechnol.* 14, 261–267. <https://doi.org/10.1016/j.jgeb.2016.10.002>.

- J.A. Maresca, P. Moser, T. Schumacher, 2016. Analysis of bacterial communities in and on concrete. *Mater. Struct.* 50, 25. <https://doi.org/10.1617/s11527-016-0929-y>.
- N.P. McNamara, H.I.J. Black, N.A. Beresford, N.R. Parekh, 2003. Effects of acute gamma irradiation on chemical, physical and biological properties of soils. *Appl. Soil Ecol.* 24, 117–132. [https://doi.org/10.1016/S0929-1393\(03\)00073-8](https://doi.org/10.1016/S0929-1393(03)00073-8).
- O.M. Olanya, B.A. Niemira, J.G. Phillips, 2015. Effects of gamma irradiation on the survival of *Pseudomonas fluorescens* inoculated on romaine lettuce and baby spinach. *LWT - Food Sci. Technol.* 62, 55–61. <https://doi.org/10.1016/j.lwt.2014.12.031>.
- O. Rabab, (2015). Corrosive Lesions at Concrete Infrastructures as Promising Source for Isolating Bioactive Actinobacteria. *American Journal of Life Sciences* 3: 247-256.
- D.J. Reasoner, and E. E. Geldreich (1985). A new medium for the enumeration and subculture of bacteria from potable water. *Applied and environmental microbiology* 49: 1-7
- K. Sato, S. Take, S. A. Ahmad, C. Gomez-Fuentes and A. Zulkharnain (2023). Carbazole Degradation and Genetic Analyses of *Sphingobium* sp. Strain BS19 Isolated from Antarctic Soil. *Sustainability* 15: 7197.
- M. Sharma, H. Khurana, D. N. Singh and R. K. Negi (2021). The genus *Sphingopyxis*: Systematics, ecology, and bioremediation potential - A review. *Journal of Environmental Management* 280: 111744.
- D. Schleheck, M. Weiss, S. Pitluck, D. Bruce, M.L. Land, S. Han, E. Saunders, R. Tapia, C. Detter, T. Brettin, J. Han, T. Woyke, L. Goodwin, L. Pennacchio, M. Nolan, A.M. Cook, S. Kjelleberg, T. Thomas. Complete genome sequence of *Parvibaculum lavamentivorans* type strain (DS-1(T)). *Stand Genomic Sci.* 2011 Dec 31;5(3):298-310. doi: 10.4056/signs.2215005.
- A. Simons, A. Bertron, J.-E. Aubert, C. Roux, C. Roques, 2020. Characterization of the microbiome associated with in situ earthen materials. *Environ. Microbiome* 15, 4. <https://doi.org/10.1186/s40793-019-0350-6>.
- D. Soghomonian, A. Margaryan, K. Trchounian, K. Ohanyan, H. Badalyan, A. Trchounian, 2018. The Effects of Low Doses of Gamma-Radiation on Growth and Membrane Activity of *Pseudomonas aeruginosa* GRP3 and *Escherichia coli* M17. *Cell Biochem. Biophys.* 76, 209–217. <https://doi.org/10.1007/s12013-017-0831-4>.
- F. Stomeo, M.C. Portillo, J.M. Gonzalez, L. Laiz, C. Saiz-Jimenez, 2008. Pseudonocardia in white colonizations in two caves with Paleolithic paintings. *Int. Biodeterior. Biodegrad.* 62, 483–486. <https://doi.org/10.1016/j.ibiod.2007.12.011>.
- M. Taubert, B.M. Heinze, W.A. Overholt, G. Azemtsop, R. Houhou, N. Jehmlich, M. Bergen, P. von, Rösch, J. Popp, K. Küsel, 2021. Sulfur-fueled chemolithoautotrophs replenish organic carbon inventory in groundwater. <https://doi.org/10.1101/2021.01.26.428071>.

6 Conclusion

6.1 Conclusion of task 2 experimental work

Task 2 of the MAGIC WP covers a wide range of cementitious materials, the aim being to assess the ageing of concrete tunnel linings, sealing plugs, backfill materials and buffer-like materials.

➤ Task 2.1:

Under unsaturated conditions, the main chemical reaction in concrete is due to atmospheric carbonation. This phenomenon can be coupled with mechanical damage or, in the worst case, lead to depassivation of the steel reinforcement.

Effect of accelerated carbonation on concrete

In the case of CEM I concrete studied in Task 2.1, for a fully carbonated state obtained by accelerated carbonation, the mechanical properties tend to increase the material's mechanical properties (+ 10 % modulus of elasticity and + 25 % compressive strength). For an intermediate level of carbonation (50%), the effect on mechanical properties is not significant compared with sound concrete. These results can be explained by pore filling by calcite formation, and when the material is partially carbonated by a phenomenon of differential carbonation shrinkage that can act as a confining pressure. Knowing that, at the end of the operating phase, the carbonation of the tunnel segment concrete should be limited to one or a few centimeters, the impact on structural mechanical behaviour should therefore be limited. The results obtained in triaxial compression ($P_c = 3$ MPa) show that whatever the level of carbonation, the strength increases by around 55% compared with the uniaxial case.

Effect of accelerated carbonation on reinforced concrete

The LMDC pull-out tests study showed failure by concrete splitting for samples whose steel-concrete interface (SCI) had previously been mechanically damaged by a bending test led on prisms and characterized by two residual crack widths w_1 (≈ 200 - 300 μm) and w_2 (≈ 400 μm), whatever the level of damage. The differences between maximum shear stress depending on the level of SCI damage are low. On the other hand, failure occurred by rebar slip in case of material defect presence at the SCI, i.e. top bar effect, with a strong decrease of the maximum shear stress value. After a phase of 70 days of accelerated atmospheric carbonation, the maximum shear stress increases slightly more in the case of a pull-out sample resulting from w_1 crack opening prisms, compared to the case of a w_2 . This trend appeared to be due to differences in residual crack width and thus variability of damage at the SCI, given that carbonation is not detected at this interface. The maximum shear stress decreased for the samples with top bar effect. The second phase of humidification/drying cycle phase intended to induce a steel corrosion phenomenon and characterize the post-corrosion steel-concrete adhesion is still in progress.

➤ Task 2.2:

Ageing in contact with clay rock

Under saturated conditions, the first group of partners focused on concrete ageing in contact with clay rocks. Among the mortar/concrete (OPC and blended cement) in the PSI/Empa study, only the LAC specimens exhibited a clear and coherent spatial dependence of the mechanical properties on the specimen distance from the OPA interface. This difference is consistent with the presence of cracks and debonded ITZs in the cores at 0 mm, but not in the cores at 50 mm. Quantitative analysis of the measurements by X-ray tomography and microstructural characterization by SEM/EDX should provide a better explanation of the mechanical variations. In the SCK CEN study, the autoradiography porosity map shows that the porosity of OPC concrete rises from 20 % in the sound part to 35 % in the leached part. This increase is observed over a depth of 2 mm, after 14 years of interaction in contact with Boom Clay (Hades URF) due to Ca-leaching dominating over carbonation.

The water sorptivity coefficient is then 3 times higher for altered concrete (at the interface) than for sound concrete, with an initial rapid absorption phase, followed by a subsequent slower absorption phase. In addition, a significant enrichment in Mg is observed in the concrete in contact with the clay, spanning a thickness of 500 μm . *Multi-ionic chemical attack*

The second group of partners focused on the evolution under multi-ionic chemical attack. In the COVRA study, ageing of mortar/concrete (CEM I and CEM III/B) in contact with poorly indurated clay simulants increased compressive strengths. A comparison of mechanical strengths is provided between samples hardened for 28 days and samples exposed for 5 years or more to a clay pore water salty as seawater, despite ingress of magnesium. The increase in compressive strength is between 24% and 47% depending on the material. The fractured surfaces of the cracked samples placed in close contact revealed a potential for self-sealing for the buffer sample, but not for the backfill sample. By the end of the project, the SEM/EDS and XRD analyses at FZJ should provide an assessment of the chemical changes and thus explain the mechanical evolution of the materials. Performing compression tests at intermediate time intervals would have provided an indication of whether the changes in compressive strength were exclusively increasing. In the Czech team study, after 18 months' exposure (air, groundwater, suspension), a reduction in low pH concrete rigidity and mechanical strength was observed by punching test, especially in the case of immersion in groundwater and exposure to bentonite. The reduction in strength and rigidity is around 20 to 40%. The samples show microcracks in the first few millimeters of the surface exposed to the bentonite. This is attributed to Mg ingress showed by EDS elemental mapping, however, the influence of sulphates from the bentonite slurry and the impact of drilling and cutting operations cannot be excluded. New Ca mineral phases appear on surface of samples exposed to air. According to XRD measurements, these are gypsum and vaterite. Whatever the type of exposure, nanoindentation show increase in modulus of elasticity of cementitious matrix according to time, probably caused by hydration. Modulus of elasticity measured by nanoindentation is systematically worse closer to surface. SEM shows carbonation of $\sim 100 \mu\text{m}$ deep in air and carbonation/leaching of $\sim 1 \text{ mm}$ in water. In the LMDC study, after a first phase of accelerated atmospheric carbonation, the reinforced concrete prisms which provide pull-out test samples were stored under CO_x water with humidification-drying cycles to investigate coupled effects of corrosion and state of steel-concrete interface on steel corrosion onset and steel-concrete bond behaviour.

Degradation under water percolation

In the SCK-CEN study, the batch/percolation experiments to mimic the Belgian disposal conditions are still in progress. Experimental results are available for pastes (task 3) but not for mortars (task 2). The test consists of exposing the mortar sample to water representative of Boom Clay injected with 3 bar of pressure or immersing it in a Boom Clay slurry. In both cases, the in-situ conditions are reproduced by CO₂ bubbling. The aim is to determine the evolution of the chemical and transfer properties of the mortar at different time intervals. In the GRS/HZDR study, a THMC test is also in progress. In this deliverable, some preliminary results are presented, but the chemo-mechanical degradation of low pH concrete percolated with a saline solution (Konrad mine) is not yet available. Several experimental difficulties were encountered, especially problems of homogeneity during preparation, sample damages during removal from the percolation cell, and pathway between the inner and outer jacket.

➤ Task 2.3:

Multi-ionic chemical attack and microbial attack

The collaborative study by COVRA, SCK CEN and FZJ on the Dutch concept revealed a diverse microbial community in both water and concrete cubes, which is different than the community in the sand used to prepare the concrete cubes. The microbial community evolved in 1.5 year and more viable cells were observed on the concrete cubes suggesting the possibility for biofilm formation.

There seems to be a different microbial community present in the certified samples compared to that present in the non-certified samples but the major factor explicating these differences is not yet clear. Putatively, the superplasticizer used in the certified conditions could be an explaining factor. Furthermore, the experiments showed that gamma irradiation did not adversely affect the mechanical strength. Currently, the descriptive nature of the microbial results hampers a conclusive assessment of their impact on mechanical strength.

Experiments related to the Czech concept demonstrated that mainly water and the way how the samples are exposed to different sources of water (air humidity, continuous water flow or water suspending clay) determines the fate of low-pH concrete. In addition, metabolic activity of microorganisms is primarily driven by and dependent on the presence of water. Depending on the extent of water and local pH changes, microbial activity can be either deteriorative or protective. However, microbial-induced effects are not always as important as chemically induced changes. In air and water environments, microbiology seems to be the main driver whereas in bentonite, the chemical conversion of CSH to MSH is the most important parameter that induces negative effects.

Microbial effect in natural waters and low-carbon groundwater

In the experiments that applied a mechanistic approach, no effects on concrete samples were detected in most cases. The collaborative work of HZDR and IRSN, showed no effects of biodegradation on cement samples incubated with Cernan groundwater after 3 months, even if the microbial community was stimulated with lactate. Putatively, this time period is too short to induce some measurable effects. In addition, the decrease of calcium concentration in calcareous groundwater may result in calcium deposit on the cement surface, which may serve as a barrier to prevent cement degradation. Also, no effects of biodegradation on cement was observed in nitrate reducing conditions in experiments performed by UNIMAN. Nevertheless, different microbiologically induced processes were observed in high- versus low-carbon environments. Formation of calcite and aragonite precipitates were observed in high-carbon environments, which contributed to crack sealing and also pore size distribution and pore counts decreased.

The time period of the experiments carried out by SURAO/CTU/UJV/CVREZ and TUL was considerably longer compared to that of HZDR/IRSN and UNIMAN, which could explain why microbial-induced effects were observed or not.

6.2 Identification of knowledge gaps and future development needs

Calcite formation induced by the carbonation process and the resulting clogging of pores can have a positive effect on mechanical properties, as shown by the LaMcube study. Previous research enabled the modelling of these microstructural changes using a micromechanical model implemented in Abaqus. A possible continuation of this work could be the development of a new module to integrate a chemical calculation code. The results of Task 2.1 could be used as input data for the models, knowing that experimental research to investigate the mechanical properties of carbonated concretes needs to be extended to a wider range of cementitious materials. The aim is to anticipate future developments in cement materials, triggered mainly by the carbon tax and difficulties in sourcing raw materials.

Concerning the bond between steel and concrete under accelerated degradation conditions, research could be extended by increasing the duration of the humidification-drying phase to obtain a higher corrosion level than that realised in MAGIC. To standardise the tests proposed by the LMDC, accelerated corrosion could be used to reduce test duration. For example, the application of electrical current density is a way of accelerating corrosion, although the representativeness of the test is still in question. Concerning the link between the state of steel-concrete interface (SCI) and corrosion onset, the use of biodegradable adhesive tape is a potential way of creating a SCI defect similar to top bar effect to avoid casting concrete walls. The creation of mechanical damage of SCI to investigate the coupled effects of corrosion and damage requires experimental method improvement.

Reinforced concrete structure durability is linked to many factors, including fluid transport properties (e.g., permeability and diffusion coefficients of distinct fluid types) variations due to the ongoing reactive transport processes. One possible perspective of Empa/PSI's work could be to assess the chemical equilibrium between the investigated clayey rock and the cementitious materials cast in contact with it and what such equilibrium implies for the cementitious materials' microstructure (especially for the pore space), both at the interface and within several cm away from it towards the inner cementitious volume. The water sorptivity measurements and quantitative porosity mapping by autoradiography used by SCK-CEN could provide interesting means of assessing the degradation of concrete at the interface with the geological environment. These methods should be used on a wider range of materials and geological environments. This kind of water exchange can be encountered during the construction phase of underground structures, when a water balance is established between the host rock, which has been dried after excavation, and the concrete cast in place. In addition, the influence of water availability is cited by the Czech team as a factor that could influence the healing of cracks observed on the surface, as water is retained by the bentonite. It might be useful to assess the influence of the water content of the bentonite slurry on this process.

In the COVRA study, only an increase of the compressive strength has been measured for concrete samples submerged in clay pore water as saline as seawater despite ingress of magnesium. This conclusion is based on a comparison between compressive strengths at 28 days and after 5 years and even more in saline solution. More regular compressive strength tests could confirm that the compressive strength of the cementitious materials studied is only increasing between these two widely spaced time scales. Investigations concerning the self-healing capacity of cementitious materials could also be extended, by assessing the mechanical regain or creep-healing coupling. In general, the mechanical regain is significant mainly for a low curing age (high proportion of non-hydrated cement) and more important for stiffness than for mechanical strength.

Biohealing, using bacteria-induced calcium carbonate precipitation, effectively sealed micro-cracks in nuclear reactor enclosures during laboratory tests and a 1/3 scale replica (VERCoRs) pressurized to 500 kPa (ITM and EDF research projects). Future applications could refine the process for wider use in microcrack repair, by testing different types of cement, extending the range of environmental conditions and varying the methods of application of the bioprocess.

Chemical degradation processes such as carbonation, leaching or decalcification and multi-ionic attack lead to the gradual alteration of materials from the exposed surface to the sound part of the material. A continuation of the Czech team's study could be to evaluate the degradation of low-pH concrete

according to thickness by highlighting the chemical and mechanical evolution of the materials by zone. In addition, knowing that the degraded thicknesses are, in the worst case, in the millimetre range, ideally it would be necessary to perform tests with exposure durations around ten years. This appears essential to detect any changes on a macroscopic scale.

In the microbiological study, microbes were studied separately on bentonite and sand. Further investigations could be carried out on a mixture of the two materials. For example, in Andra's CIGEO concept, the closure structures consist of a swelling core made up of both clay and sand. The study of microbial activity and its influence on cementitious materials could focus more specifically on the coupled effect with carbonation, and on the evaluation of the progression of microbes in cementitious materials according to thickness. In addition, it could be interesting to assess microbial activity in the pore water of cementitious materials, by mechanical extraction of the interstitial solution.